Use of a Novel Two Color PALM Method to Examine Structural Properties of Drp1 Helical Rings during Mammalian Mitochondrial Fission *In Situ*.

by

Alyssa Blair Rosenbloom

A dissertation submitted in partial satisfaction of the
requirements for the degree of

Doctor of Philosophy

in

Molecular and Cell Biology

in the

Graduate Division

of the

University of California, Berkeley

Committee in charge:

Professor Carlos Bustamante, Chair
Professor Jasper Rine
Professor Jan Liphardt
Professor Jodi Nunnari

Fall 2012

Use of a Novel Two Color PALM Method to Examine Structural Properties of Drp1 Helical Rings during Mammalian Mitochondrial Fission *In Situ*.

Abstract

Use of a Novel Two Color PALM Method to Examine Structural Properties of Drp1 Helical Rings during Mammalian Mitochondrial Fission *In Situ*.

by

Alyssa Blair Rosenbloom

Doctor of Philosophy in Molecular and Cell Biology

University of California, Berkeley

Professor Carlos Bustamante, Chair

Visual observation is a powerful way to examine a biological structure. Since the development of the basic microscope, scientists have attempted to get a closer look at smaller and smaller biological systems and molecules. Until recently, the greatest technical challenge to visualization with visible light has been the diffraction limit. With the advent of photoactivatable light microscopy (PALM), the diffraction limit barrier has been circumvented, allowing for improved resolution by an order of magnitude and a much closer observation of cell organelles and individual proteins.

We set out to elucidate the structural properties of one component of the mammalian mitochondrial fission complex: the Drp1 helical ring. The mitochondria are the powerhouses of the cell, with important roles to play in cellular metabolism and apoptosis. The dynamic balance of mitochondrial network fission and fusion are critical for the health of a cell. The Drp1 helical ring is the main dynamic component of fission and is responsible for membrane scission. In order to visualize the structural properties of Drp1 on mitochondrial tubules *in situ*, we need a technique to visualize with sub-diffraction resolution. Although the sub-diffraction limited nature of PALM microscopy has enabled the observation of individual proteins, the technique's biological relevance has not yet been recognized. A large part of this lack of recognition is likely due to the limited efficiency of currently published green photoactivatable (or photoswitchable) fluorescent proteins and two-color PALM methods. For a fluorescent imaging technique to truly achieve wide use in biology, at least two useful fluorescent protein colors are required. In this thesis, we accomplish two goals: 1) we develop a novel two color PALM method for imaging in mammalian cells and 2) we explore our original biological question and discern the structural properties of the Drp1 helical ring during fission.

We established that mitochondrial membranes can be distinguished with the available photoactivatable fluorescent protein mEos2. However, we were not able to use any of the published photoactivatable and photoswitchable green fluorescent proteins, predominantly

because of an inability to identify individual fluorescent events due to rapidity of the photoswitiching. Based on published crystal structures, we created novel Dronpa variants with increasing steric hindrance around the chromophore, likely partially inhibiting the isomerization. We replaced Val157 with isoleucine, leucine, or phenyalanine. DronpaV157F showed no fluorescence and was discarded. DronpaV157I and DronpaV157L showed photoswitchable green fluorescence, with individual fluorescent events that were more easily discerned. DronpaV157L in particular had bright fluorescent events that were well separated when imaged in mammalian cells at 20 Hz. We named this new variant rsKame. Using PALM we successfully imaged rsKame expressed and localized to the mammalian mitochondrial inner membrane.

In order to characterize rsKame, we purified the protein and performed both bulk spectroscopic and single molecule studies. Purified rsKame shared a similar excitation and emission spectra to Dronpa, but had a reduced quantum yield and brightness. Single molecule studies of the kinetic rates of rsKame and Dronpa uncovered the source of the increased separation of the individual fluorescent events of rsKame, and the cause of the original difficulties with the published photoactivatable or photoswitchable fluorescent proteins. We also proposed and validated a kinetic model for the activation and excitation of Dronpa and rsKame. The time spent in the dark state, T_{OFF}, of rsKame was significantly increased as compared to Dronpa, indicating that the new variant spends an increased amount of time in the trans (OFF) isomerization of the chromophore. This allows for increased temporal separation of the individual fluorescent events, resulting in a super resolution PALM image. In addition, we observed photoswitching of individual Dronpa and rsKame in the absence of 405 nm activation, demonstrating that Dronpa and rsKame can be both activated and excited by 488 nm. In addition, the cis to trans isomerization of the Dronpa/rsKame chromophore was unaffected by increasing 405 nm and 488 nm laser power densities, demonstrating that the chromophore either relaxes into the trans configuration (dark state) spontaneously or is affected by an unknown variable. We also performed single molecule studies on PAmCherry1 and quantified the photoactivation rate. We noted that under the most intense activation of rsKame, less than 2.5% of PAmCherry1 molecules would be activated.

With the novel photoswitchable fluorescent protein, rsKame, available, we returned to the development of a novel two color PALM method. We chose PAmCherry1 as the partner for rsKame since PAmCherry1 has distinct and well separated excitation/emission spectra from rsKame and is not activated by low 405 nm laser power density. We first imaged rsKame with 405 nm activation at (0.61 mW/mm^2) and 488 nm activation/excitation (5.87 W/mm^2) to completion. We then imaged PAmCherry1 with increasing 405 nm activation (0.6-6.0 W/mm^2) and 561 nm excitation (22 W/mm^2). With the novel PALM imaging method, we labeled the inner and outer mitochondrial membranes with large populations of membrane bound rsKame and PAmCherry1 in HeLa and EpH4 cells. We were able to observe and clearly differentiate the two mitochondrial membrane structures and their various morphologies *in situ*.

With the functional two-color PALM method, we returned to our original investigation of the Drp1 fission ring *in situ*. In fixed HeLa cells, we continued to label the outer membrane with PAmCherry1 and fused rsKame to the N-terminus of Drp1, separated by a linker. The resultant PALM images allowed for the observation of two previously observed and one hitherto unseen distinct Drp1 morphologies: Constrict, Terminal, and Split. The Constrict morphology was defined as the Drp1 structures that clearly encircle the mitochondrial tubule at various stages of membrane constriction. The Terminal morphology was defined as the Drp1 structures found at the termini of mitochondria, presumably post membrane scission. The Split morphology is a

novel morphology and was defined as two Drp1 foci flanking the mitochondrial tubule but not completely encircling it. Quantification of the diameter and length of the Drp1 helical ring structures showed that the mean length of the Drp1 helical rings was consistent between all three morphologies, though a slight decrease was observed for the Terminal morphology, likely due to degradation. We observed a decrease of approximately 40 nm between the Constrict and Terminal mean diameters, consistent with a dynamic change in the Drp1 ring size due to membrane constriction towards membrane scission during mitochondrial fission. The Split morphology had a wide distribution of diameters and warrants further study.

Our earlier difficulties with the large cytoplasmic population Drp1 led to the development of bifurcated complementation PALM imaging (BiFC PALM). We established that PAmCherry1, Dendra2, and rsKame could be bifurcated, and upon complementation, maintain both their fluorescence and photoactivatability or photoswitchability. In ongoing work, we label two subunits of the ATP synthase stator section with the bifurcated halves of PAmCherry1 and attempting to demonstrate that, upon co-expression and complementation, the ATP synthase enzyme complexes along the mitochondrial inner membrane can be PALM imaged. BiFC PALM is a novel technique that still requires significant controls and improvements. However, BiFC PALM has the potential to solve difficulties with determining protein-protein co-localization. Complementation is dependent on the linker length separating the bifurcated half and the protein of interest, and gives relative localization of two proteins to each other. Combining the relative localization of BiFC and the absolute localization of PALM defines the clear interaction of two proteins within the resolution limits of a single PALM fluorescent event. This innovation could make PALM an even more powerful tool for biological investigations.

Over the course of this thesis, we developed and characterized a novel photoswitchable green fluorescent protein, rsKame, and a novel two-color PALM method to accompany it. With the new method, we examined the structural properties of Drp1 helical rings during mitochondrial fission *in situ* and are developing a method, BiFC PALM, for definitively determining protein-protein co-localization with PALM imaging. Our studies have spanned basic molecular biology, biochemistry, microscopy, and single molecule photophysics.

To my parents, who gave me love and support in both success and difficulty.
To Dr. Sumana Datta, who taught me to be passionate about science.
To the love of my life, Shawn, who is my rock, my shoulder, my hand to hold.

CONTENTS

LIST OF FIGURES

LIST OF TABLES

LIST OF SYMBOLS

α	ratio of populations with rate k_{r2} compared to k_{r1}
β	ratio of populations with rate k_{r3} compared to k_{r2}
ε	molar extinction coefficient
6XHis	6 histidine tag
AA	amino acid
Abs	absorbance
AIF	apotosis inducing factor
ATP/ ADP	adenosine triphosphate/adenosine diphosphate
ATP5F1	F_1F_0-ATP synthase stator subunit
ATP5O	F_1F_0-ATP synthase stator subunit
Avi	avidin
Bax	Bcl-2-assocated X protein
Bcl Xl	Bcl-2 X protein
BCA assay	bicinchoninic acid assay
BCS1L	mitochondrial chaperone protein
BFP	blue fluorescent protein
Bid	BH3 interacting-domain death agonist
BiFC	bimolecular fluorescence complementation
Caf4	CCR4-associated factor 4
CCD	charge coupled device
CMV	Cytomegalovirus
Cox5A	cytochrome c oxidase subunit Va
DNA	deoxyribonucleic acids
Dnm1	dynamin-related GTPase
Dox	doxycycline
Drp1	dynamin related protein 1
EGFP/GFP	enhanced green fluorescent protein/green fluorescent protein
ER	endoplasmic reticulum
EYFP/ YFP	enhanced yellow fluorescent protein/yellow fluorescent protein
FAD/FADH2	flavin adenine dinucleotide
FBS	fetal bovine serum
FMN	flavin mononucleotide
FPLC	Fast protein liquid chromatography
FRET	fluorescence resonance energy transfer
GED	GTPase effector domain
GTP	Guanosine triphosphate
hFis1/Fis1	*Homo sapiens* fission protein 1/*Saccharomyces cerevisiae* fission protein 1
HR/HR1/HR2	heptad repeat
HRP	horse radish peroxidase
Hs	*Homo sapiens*
Hz	hertz
Ile	isoleucine
IMM	inner mitochondrial membrane
IPTG	Isopropyl β-D-1-thiogalactopyranoside
$k_{activation}$ (k_a)	rate of photoactivation
Kan/Neo	kanamycin/neomycin
kb	kilobase

k_{bleach} (k_b)	rate of photobleaching
kDa	kiloDalton
k_{dark} (k_d)	rate of entry to the dark state
k_{r1} (k_{r2}, k_{r3})	rate of fluorescence recovery/rate of photoactivation (photoswitchable fluorescent protein)
$k_{triplet}$	rate of entry to the triplet state
Leu	leucine
Lk	linker
Mdv1	mitochondrial division protein 1
Mff	mitochondrial fission factor
Mfn1/Mfn2	mitofusion 1/mitofusion 2
MiD49/51	mitochondrial dynamic proteins 49 kDa and 51 kDa
MLS/ MTS	mitochondrial localization sequence/mitochondrial targeting sequence
mPEG/Bio-PEG	m-polyethylene glycol/biotin-polyethylene glycol
MPT	mitochondrial permeability transition pore
NAD+/NADH	nicotinamide adenine dinucleotide
N_{Blink}	number of times a fluorescent protein blinks or photoswitches
nm	nanometer
OD	optical density
OMM	outer mitochondrial membrane
Opa1	optic atrophy 1
OX/PHOS	oxidative/phosphorylation
PA-FP	photoactivatable fluorescent protein
PALM	photoactivatable light microscopy
PBS	phosphate buffered saline
PCR	polymerase chain reaction
Phe	phenylalanine
PHEM	PIPES/HEPES/EGTA/$MgCl_2$
PS-CFP2	photoswitchable cyan fluorescent protein 2
PSF	point spread function
PS-FP	photoswitchable fluorescent protein
QY	quantum yield
RFP	red fluorescent protein
ROI	region of interest
rRNA	ribosomal ribonucleic acid
ROX	reactive oxygen species
SDS-PAGE	sodium dodecyl sulfate polyacrylimide gel electrophoresis
Smac	second mitochondria-derived activator of caspases
SSIM	saturated structured illumination microscopy
STED	stimulated emission depletion microscopy
STORM	stochastic optical reconstruction microscopy
TIM	translocation complex in the inner mitochondrial membrane
TIRF	total internal reflection fluorescence
TNF	tumor necrosis factor
TO/Tet-on	tetracycline on
T_{OFF}	time spent in the OFF/dark state
Tom20	translocation complex in the outer mitochondrial membrane protein 20
T_{ON}	time spent in the ON/dark state
tRNA	transfer ribonucleic acid
Val	valine
W/mm^2 (mW/mm^2)	watts per millimeter squared/milliwatts were millimeter squared

ACKNOWLEDGEMENTS

There is a reason the scientific community uses the term "we" when discussing research. The best science is neither conceived nor performed in isolation. Because of this truth, I must extend my profound thanks to those who help, insight, and guidance were instrumental in my journey through graduate school and through this research.

I must, of course, first extend my thanks to my mentor, Carlos Bustamante, for his guidance and continual support. Carlos taught me how to see the entire path of the research, and encouraged me to reach for the big ideas, even when they seemed difficult or unlikely.

I must also extend my thanks to my thesis committee, Jasper Rine, Jan Liphardt, and Jodi Nunnari for their guidance and new ideas. My especial thanks to Jasper for suggesting I contact Jodi. Jodi has proven to be an incredible mentor both on mitochondrial research and on life in general.

As mentioned previously, no research is performed in isolation. My colleagues in the greater Bustamante lab kept the days mostly fun and were wonderful brains to pick for information. I owe a special thanks to a few colleagues, most importantly to two postdoctoral fellows: Sanghyuk Lee and Jae Yen Shin. Sanghyuk is the "microscope" whisperer and wonderful brain to bounce ideas off of. I think our conversations were some of the most productive of my graduate tenure and the success of my research is entirely due to his help. Jae Yen offered valuable advice in the biological side and her attention to detail was most helpful. Antony Lee is the graduate student continuing the BiFC research and I thank him for his help and wish him good luck. Jean-Charles Blouzard was my benchmate and a wonderful friend who listened to all my crazy ideas, and instead of telling me I was crazy, helped me work through them mentally. And lastly, Brad Zamft, my labmate who started on this long path with me, I thank so much for conversation, for support on the hard days, and for a wonderful continual friendship.

This graduate experience has taught me great lessons, exposed my weaknesses, and challenged my strengths. But the most important lessons were to ask for help and reach out for other ideas. I could not have completed this doctorate as an "I". So my thanks to the "we".

Chapter 1: Introduction

"Science is the poetry of reality." -Richard Dawkins

The world was not always full of oxygen. In fact, life on Earth began under a cloud of carbon dioxide. As life evolved and early plant-like organisms slowly transformed the Earth's atmosphere from a predominantly carbon dioxide atmosphere to an oxygen rich one, the earliest bacteria faced a crisis.[1] To these bacteria, oxygen was poison and the atmosphere was becoming hostile. Some bacteria evolved into aerobic bacteria, with chemical factories to use the oxygen to make energy and protective measures against dangerous free radicals. Other bacteria remained anaerobic and engulfed aerobic bacteria developing a symbiotic relationship. These symbiotic relationships were both a first step to the eukaryotic cells that make much of modern day flora and fauna, and also a first step to organelles, specifically mitochondria.[2]

Mitochondria are a stunningly complex organelle network that affects very important aspects of cellular metabolism and apoptosis.[3,4,5] In some multicellular organisms, such as *Homo sapiens*, mitochondria have known impacts on aging and cancer.[6,7] Mitochondria are unique among eukaryotic organelles, maintaining a separate genome and two complex membranes, reminiscent of alpha proteo-bacterial ancestors.[2] These observations of mitochondrial and bacterial similarities have long been associated with the theory of endosymbiosis, proposed by Lynn Margulis in 1967.[8,9]

MITOCHONDRIAL EVOLUTION

Early mitochondrial endosymbionts likely had similar genomes to alpha proteobacteria. As eukaryotic cells and organisms evolved, the mitochondria lost the majority of their genes to the nuclear genome. There are several theories as to the cause of this loss including horizontal gene transfer and deletions.[2,9] Modern mitochondria depend on the nuclear genome for the majority of their proteome. However, across the higher eukaryotic spectrum, most mitochondrial genomes maintain a similar set of genes. These genes predominantly code for proteins associated with oxidative phosphorylation, the production of iron-sulphur complexes, and translation within the mitochondrial matrices. Mitochondrial networks may contain hundreds to thousands of copies of the mitochondrial genome.[10,11,12] The resulting redundancy purportedly mitigates the damage caused by the reactive oxygen (ROX) species produced in the mitochondrial matrices as a result of the mitochondrial metabolic activity.[6]

Like their alpha proteobacterial ancestors, mitochondria maintain a double membrane composed of two lipid bilayers.[13,14] These membranes divide the mitochondria into multiple compartments. The matrix is the very center of the organelle, completely encompassed by the inner mitochondrial membrane. The space between the outer mitochondrial membrane and the inner mitochondrial membrane is termed the intermembrane space. The outer mitochondrial membrane encompasses the organelle in a rounded or elongated tubular shape.[15] The inner mitochondrial membrane is divided into three sections: the inner boundary membrane (IBM) that lies close to and along the outer mitochondrial membrane, the deeply invaginated tubular intrusions into the matrix termed cristae, and the crista junctions that connect the cristae to the IBM .[16,17,18,19] It is theorized that the inner mitochondrial membrane is folded so as to increase

the surface area available for the protein complexes responsible for oxidative phosphorylation and other metabolic processes.[20,21]

Though mitochondrial networks are common to the majority of eukaryotic cells, we will discuss predominantly mammalian mitochondria with some references to previous research performed in yeast. Mammalian mitochondria have some of the most compact mitochondrial genomes. At 16 kb, these small circular genomes have no introns and only one small space of non-coding DNA, the D-loop, set between the two promoters and near the origin of replication. The genome itself contains thirteen protein coding genes, twenty-two tRNAs, and two rRNA subunits. All of the mRNA transcripts code for proteins involved in oxidative phosphorylation or RNAs involved with translation within the mitochondrial matrix. Mammalian mitochondria are not known to import tRNAs. It is unclear whether recombination occurs between mammalian mitochondrial genomes, but if so, it is likely infrequent. Mammalian mitochondrial genomes are transcribed as three long RNA transcripts and undergo extensive splicing before being translated into protein.[22–26]

MITOCHONDRIA AND METABOLISM

As go the mitochondria, so goes the cell. The mitochondrial network is critical in maintaining cell metabolic homeostasis. The majority of adenosine triphosphate (ATP) is made in the mitochondrial matrix through the breakdown of glycolytic end products and the transfer of electrons across mitochondrial inner membranes through the four complexes of oxidative phosphorylation and ATP synthase.[27] These electrons eventually power the numerous ATP synthase enzymes lining the cristae. For every molecule of glucose taken in by the cell, 2 ATP are produced from glycolysis itself. Through oxidative phosphorylation, another 30 ATP are created from the 2 NADH produced by glycolysis and by the passage of the glycolytic products, 2 pyruvates, through the Krebs cycle.[28,29,30] Genetic errors in mitochondrial genomes often result in gross errors in oxidative phosphorylation and disrupted cellular metabolism.[7,31,32]

KREBS CYCLE

The Krebs cycle, also known as the citric acid cycle or tricarboxylic acid cycle, was first described in the 1930s by Albert Szent-Gyorgyi and Hans Adolf Krebs.[32] This important aerobic metabolic process is used by all aerobic organisms to produce energy in the form of ATP through oxidation of substrates derived from the breakdown of carbohydrates, fatty acids, and, in the case of starvation conditions, proteins. The primary subject of oxidation is acetate in the form of acetyl-CoA, generally derived from pyruvate, the end product of glycolysis.[27,32] The cycle is regenerative for all other substrates with the exception of acetyl-CoA which must continually be fed into the cycle to keep it going. Oxaloacetate can also be fed into the system to increase energy production but it must be done in conjunction with increased acetyl-CoA. One acetyl-CoA and one oxaloacetated molecule are combined into citrate and, in subsequent conversions, undergoe 4 major oxidations through one turn of the cycle.[1,27,29] Two CO_2 molecules are produced. The oxidation reactions are coupled with three reduction reactions of NAD^+ to NADH and one reduction reaction of FAD to $FADH_2$. NADH is used by Complex I to produce 2.5 ATPs per NADH. $FADH_2$ is fed into oxidative phosphorylation through Complex II, bypassing Complex I, and produces 1.5 ATPs per $FADH_2$ molecule.[33,34] Overall, one turn of the cycle will produce 9 ATPs after all the NADH and $FADH_2$ is processed through oxidative

phosphorylation. Oxidative phosphorylation crosses over with the Krebs cycle directly with the dual involvement of Complex II in both processes.[35] In the Krebs cycle, Complex II serves as succinate dehydrogenase, oxidizing succinate into fumarate and reducing $FADH_2$. However, Complex II is embedded in the inner mitochondrial membrane and can therefore feed the electrons from $FADH_2$ directly to coenzyme Q and into oxidative phosphorylation.

OXIDATIVE PHOSPHORYLATION

Oxidative phosphorylation was described initially in the 1940s but it took almost 60 years before it was more fully elucidated. Even now, much is not known and the research is ongoing. Oxidative phosphorylation is the metabolic process by which electrons are moved through a set of protein complexes in the inner mitochondrial membrane. This movement is coupled with the movement of protons across the inner mitochondrial membrane. This movement creates a proton gradient and electrical potential across the membrane which creates the energy necessary to drive ATP synthase, the enzyme responsible for phosphorylating ADP back into ATP.[27,29] Five complexes make up the metabolic process of oxidative phosphorylation. Four are involved in the electron transport chain and the fifth, ATP synthase, finishes the process with the production of ATP.[34,36]

Complex I

Complex I, also known as NADH-coenzyme Q oxidoreductase, is made up of forty-six subunits with a combined molecular mass of 1000 kDa. The majority of Complex I is embedded in the inner mitochondrial membrane, spanning the membrane with a large section of the complex jutting out into the mitochondrial matrix.[37,38,39] The matrix part of Complex I oxidizes a molecule of NADH. The 2 electrons are carried through Complex I via flavin mononucleotide or (FMN) and several iron-sulfur clusters to coenzyme Q, reducing it.[40] During reduction, coenzyme Q also picks up 2 H^+ ions from the mitochondrial matrix. While the electrons are passed through Complex I, 4 protons are pumped from the matrix to the intermembrane space. The mechanism by which this happens is not well understood.[41] Coenzyme Q and reduced coenzyme Q are thought to move freely within the inner mitochondrial membrane.[38,42]

Complex II

Complex II, also known as succinate dehydrogenase, is part of the Krebs cycle as well as oxidative phosphorylation. It is smaller with only four protein subunits.[43] Flavin adenine dinucleotide (FAD) is bound to Complex II. Complex II also contains Fe-S clusters that help pass the electrons through the complex, reducing Coenzyme Q. Complex II is also unique in that it does not pump protons across the inner membrane and therefore, its activity has no effect on the proton gradient.[44]

Complex III

The mobile reduced Coenzyme Q transfers its electrons to Complex III, also known as Q-cytochrome *c* oxidoreductase, in two steps.[39,41] Complex III is made up of eleven protein subunits and is found as a dimer in mammals.[45] The electrons are passed to cytochrome *c*, a heme containing protein, found in the intermembrane space but only loosely associated with Complex III. Cytochrome *c* can only carry one electron at a time. When mobile reduced

Coenzyme Q transfers its electrons to Complex III, one is transferred to cytochrome *c* and one is transferred to another bound Coenzyme Q, semi-reducing it.[29] Two protons are released into the intermembrane space in this step. A second mobile Coenzyme Q is then bound, transferring one electron to the semi-reduced Coenzyme Q and one to a second cytrochrome *c*, reducing both of them. The semi-reduced coenzyme Q picks up two protons from the matrix during this step and two more protons are transferred into the intermembrane space when the electron is transferred to cytochrome *c*.[21,42]

Complex IV

Complex IV, or cytochrome *c* oxidase, accepts electrons from reduced cytochrome *c* and reduces oxygen to water. Four reduced cytochrome *c* (or four electrons) are needed to reduce one O_2 molecule. During this process, four protons are pumped across the complex from the matrix to the intermembrane space, adding to the proton gradient. Complex IV has thirteen subunits and multiple co-factors.[46–49]

Complex V

Complex V, or ATP synthase, is the active enzyme that couples free phosphates to adenosine diphosphate (ADP). The ATP synthase enzyme has two major sectors, the F_0 and the F_1. The F_0 sector actively rotates a stalk.[50] The rotation is driven by the proton gradient created by the first four complexes of oxidative phosphorylation. The subunits of F_0 can only mechanically move if protonated. The protons enter through a channel, drive the rotation of the F_0 subunit, and then exit through a second channel into the matrix.[51,52] The F_0 sector driven stalk rotation movement is translated to the F_1 sector causing repeating subunit conformational changes. The F_1 subunits also bind ADP and free phosphates. The conformational changes of the F1 subunits bring ADP and free phosphates in close proximity and allow for the formation of ATP, which is then released into the matrix. ATP is exported to the cytoplasm via the adenine nucleotide translocase.[50–53]

MITOCHONDRIA AND APOPTOSIS

The other crucial cell processes that mitochondria play a huge role in is programmed cell death and apoptosis. Apoptosis is a type of programmed cell death. It differs from cell death caused by trauma or disease in that apoptotic cells produce small enclosed fragments of cell debris that are quickly and easily engulfed by phagocytes before they can cause an inflammatory response. Apoptosis is a normal and necessary part of mammalian development and maintenance.[3,5,54] There are two major apoptotic pathways that share some interconnectivity: the extrinsic pathway and the intrinsic pathway. The extrinsic pathway involves activation by external stimuli often related to the Tumor Necrosis Factor (TNF) superfamily at the cell surface transmitted across the cell membrane via death receptors.[4,55] The intrinsic pathway involves stimuli that are not transmitted by receptors but instead alter the cell's internal environment directly. Stimuli include radiation, high free radical concentration, toxins, temperature fluctuation, infection, oxygen starvation, the lack of growth factors, etc.[56,57,58] Mitochondria are central to the proper functioning of the intrinsic apoptotic pathway and are involved in the extrinsic pathway further downstream.[59]

The above mentioned intrinsic pathway stimuli all have a similar downstream function: the alteration of the mitochondrial transmembrane potential, generally by opening up a hole in the outer mitochondrial membrane known as the mitochondrial permeability transition pore (MPT). These membrane pores result in the loss of membrane potential and releases several pro-apoptotic proteins that are normally sequestered away in the mitochondria.[60,61] These proteins include, most famously, cytochrome *c* as well as caspase 8, second mitochondria-derived activator of caspases (Smac), apoptosis inducing factor (AIF), and endonuclease G. These mitochondrial proteins continue down subsequent pathways that promote and ultimately complete apoptosis. In the extrinsic pathway, one of the downstream occurrences of external ligands binding to the death adaptor proteins is the activation of caspase 8.[4] Caspase 8 cleaves a pro-apoptotic protein BH3 interacting-domain death agonist (Bid). The truncated Bid moves to the mitochondria and releases cytochrome *c*, meeting up with the intrinsic pathway.[54,62] Both the extrinsic and intrinsic pathways converge at the release of the sequestered mitochondrial pro-apoptotic proteins.

MITOCHONDRIAL MEMBRANE DYNAMICS

As mentioned previously, the mitochondrial network is incredibly dynamic. This dynamic behavior is the key for maintaining the health of the network and of the cell. Mitochondrial dynamics have been shown to play a role in apoptosis, stress response, aging, and disease. The dynamics of the network are controlled by two major opposing events: fission and fusion. The balance of these two morphological changes maintains the homeostatic cellular environment. Disruption of the balance often imposes major problems within the cell, including death.

FUSION

Fusion of mitochondria allow for the exchange of matrix contents, including metabolic intermediates and mitochondrial DNA as well as intermembrane space and membrane contents. Fusion requires that both membranes, the outer mitochondrial membrane and the inner mitochondrial membrane, fuse independently and almost concurrently.[15,63] The majority of the mammalian mitochondrial fusion machinery is made up of three proteins: optic atrophy 1 (Opa1), mitofusion 1 (Mfn1), and mitofusion 2 (Mfn2).[63] Mfn1 and Mfn2 are both outer mitochondrial membrane embedded proteins that perform basically the same function. The proteins have an N-terminal GTPase region followed by a hydrophobic heptad repeat region (HR1). The C-terminal region has a transmembrane region followed by a second hydrophobic heptad repeat region (HR2). The transmembrane region adopts a U shape that allows for both the N-terminal and C-terminal regions to face the cytoplasm. The C-terminal HR2 domains bind to each other, tethering the mitochondrial outer membranes to each other within approximately 9-10 nm. The downstream fusion events post tethering are GTP hydrolysis driven but otherwise have not been determined.[15,64,65] Opa1 is the best candidate for the protein responsible for inner mitochondrial membrane fusion. Opa1 has an N-terminal mitochondrial targeting sequence (MTS) followed by a transmembrane domain and hydrophobic heptad repeat region (HR) close to a GTPase region. The C-terminal region of Opa1 also has a coiled coil domain that may function as a GTPase effector domain (GED). The MTS targets Opa1 to the intermembrane space and the translocation complex in the inner mitochondrial membrane (TIM).[66] The N-terminal end of Opa1 is inserted into the inner membrane across the hydrophobic domain directly

following the MTS. The MTS is cleaved off the N-terminus, keeping Opa1 anchored in the inner membrane. The GTPase domain and the GED domain remain in the intermembrane space. Various isoforms of Opa1 have been found in the intermembrane space and demonstrated to form hetero-oligomeric structures. The exact mechanism of inner membrane fusion by Opa1 has yet to be determined but likely involves significant remodeling of the mitochondrial inner membrane.[67–69,70]

FISSION

Mitochondrial fission is essential for mobility and distribution around the cell and has a critical role in apoptosis. The mammalian mitochondrial fission machinery is made up of multiple proteins and has recently undergone a revolution in understanding. In our current understanding, mitochondrial fission sites are determined by interaction with the endoplasmic reticulum (ER). The ER wraps around a mitochondrial tubule, constricting the membrane.[64,71] The receptors on the mitochondrial outer membrane are thought to be mitochondrial fission factor (Mff) and fission 1 protein (hFis1), though the relative importance of each protein to the fission process is somewhat controversial.[72] The actual dynamic fission process is carried out by dynamin related protein 1 (Drp1), a GTP hydrolysis driven oligomeric protein.[73] Endophilin B also may play a role in maintaining the curvature of the mitochondrial constriction sites.[74] Mitochondrial dynamics proteins (MiD49/51) are new purported players to the fission machinery and their function is not yet well defined.[75]

Mitochondrial fission factor (Mff) is a mitochondrial outer membrane protein, anchored to the membrane C-terminally via a transmembrane domain. The N-terminally of the transmembrane domain is a coiled-coil region followed by two short repeats.[65,76] hFis1 is also a mitochondrial outer membrane protein anchored C-terminally in the membrane via a transmembrane domain. The majority of hFis1 faces the cytoplasm and is made up of six helices with two tetratricopeptide repeats central to the helical bundle.[60,77] Drp1 is a cytoplasmic protein with an N-terminal GTPase and a C-terminal GED. These two domains are divided by a central structural domain. Drp1 exists pre-dominantly in the cytoplasm as dimers or tetramers and is recruited to mitochondrial fission sites. The mechanism of this recruitment is as of yet unknown.[78,79] Once at the recruitment site, Drp1 interacts with Mff and potentially hFis1 to form a helical ring around the outer mitochondrial membrane. GTP hydrolysis has been shown to activate constriction of the Drp1 helical rings *in vitro* and is thought to play a similar role *in vivo*.[65,80] Endophilin B1 is fatty acyl transferase predominantly localized in the cytoplasm. It can be recruited to the mitochondrial outer membrane during fission by an unknown mechanism. Knockdown of Endophilin B1 results in gross morphological changes of the mitochondrial membranes, including, at times, a dissociation of the outer and inner mitochondrial membranes.[74,81] MiD49/51 are mitochondrial outer membrane proteins N-terminally anchored. The majority of the protein body lies in the cytoplasm and purportedly forms rings at punctate locations on mitochondria. MiD49/51 knockdowns and over expression have been shown to have some affect on mitochondrial morphology and co-localize with Drp1.[65,82] The exact nature of the interaction between MiD49/51 and Drp1 is currently unknown.

The current mechanism of mitochondrial fission as we currently understand it is as follows. The ER constricts mitochondria at specific "fission sites".[71] Mff and potentially hFis1 are recruited to those sites. Drp1 is then recruited from the cytoplasm to form a helical ring. Endophillin B1 stabilizes the membrane curvature. The role of MiD49/51 is not yet known. The

Drp1 helical ring dynamically constricts the mitochondrial outer membrane through GTP hydrolysis, scissioning the outer membrane. The mechanism for inner mitochondrial membrane fission is as yet unknown.[64]

PURPOSE

Mitochondrial fission is a complex interaction of various moving parts where the overall mechanism and dynamics are still very much a mystery. Fission can be driven forward by apoptotic signals, cell stress, or other disease factors as well as cell growth and division. Disruption of fission can affect the proper timing of apoptosis and lead to organismal defects. In this thesis, we hope to take a closer look at the major player of mitochondrial fission, Drp1. Though the *Saccharomyces cerevisiae* homologue, Dnm1, and Drp1 helical ring structures have been elucidated and shown to undergo dynamic constriction on liposomes *in vitro* via electron microscopy, no one has yet been able to examine the helical ring structure and overall constriction by a change in diameter *in vivo* or *in situ*.[83,84] We will demonstrate that by using photoactivatable light microscopy (PALM)[85], we can observe structural characteristics of the Drp1 helical ring and the end result of a dynamic constriction by measuring the helical ring diameter before and after mitochondrial membrane constriction.

In Chapter 2, we discuss the necessity of creating a novel photoactivatable fluorescent protein, rsKame, in order to properly make use of PALM imaging in two colors. We will also characterize the novel protein in bulk and at the single molecule level, revealing new insights into the reversibly switchable photoactivatable fluorescent protein Dronpa and our reasoning for mutating Dronpa into rsKame. In the process we discover that both Dronpa and rsKame can be activated and excited simultaneously by illumination with 488 nm laser. We find that by increasing the steric hindrance around the Dronpa chromophore, resulting in rsKame, we are able to slow down the isomerization such that clean PALM imaging was possible. We also discuss how increased sterics and the resulting single molecule rate constants may give insight on the Dronpa/rsKame switching mechanism and propose and validate a novel kinetic model.

In Chapter 3, we discuss the development of a novel PALM imaging protocol. We demonstrate the necessity of this imaging protocol for PALM and its increased effectiveness over published two color PALM protocols. We altered the published protocol to take into account the new activation information about rsKame that we determined in Chapter 2 as well as the single molecule determined photoactivation rates of rsKame and PAmCherry1. By illuminating rsKame at low 405 nm laser power density first and following with PAmCherry1 at high 405 nm laser power density, we are able to produce clean reproducible two-color PALM images of mammalian mitochondria *in situ*.

In Chapter 4, we demonstrate the use of the novel PALM imaging protocol to image Drp1 helical rings on mitochondria in HeLa cells during fission *in situ* and determine structural characteristics and an overall dynamic constriction of the Drp1 helical ring. We image Drp1 helical rings in various stages of mitochondrial fission and measure the outer diameter of the helical ring as well as the length of the helix. We determine that the helical length is consistent but a significant change in diameter can be observed between helical rings in the middle of fission and rings that have completed the fission process. We also note a novel Drp1 morphology and discuss its possible implication in mitochondrial fission.

In Chapter 5, we discuss a method to overcome the co-localization uncertainty inherently present in two-color PALM imaging. We demonstrate that three different photoactivatable

(photoswitchable) fluorescent proteins can be bifurcated, complemented, and continue to maintain their photoactivatable (photoswitchable) properties. These proteins are PAmCherry1, Dendra2, and rsKame and, when used in this context, are termed "BiFC PA(PS)-FPs". We also discuss ongoing work to demonstrate that by using bifurcated and complemented photoactivatable fluorescent proteins, we could potentially show definitive co-localization of two proteins within the resolution limits of PALM.

In short, this thesis demonstrates the development of true two-color PALM using a novel green photoswitchable fluorescent protein, rsKame, and a novel imaging protocol. We also demonstrate that this method can be used to elucidate structural information about a biological event such as Drp1 helical ring formation and constriction dynamics during mitochondrial fission. Finally, we demonstrate our "collateral science" or the development of BiFC PA(PS)-FPs for use with PALM imaging and solving some of the issues with determining co-localization via PALM imaging methods.

Chapter 2: The Development of the Photoactivatable Fluorescent Protein rsKame

INTRODUCTION

Mitochondria are magnificent organelles, dynamic and essential for aerobic life. However, we are just beginning to understand and appreciate their complexity. Fluorescent light microscopy is one way to study biological interactions such as those within mitochondria. However, one of our major limitations in studying the mitochondrial network is the size of the mitochondrial tubules of the network. Mitochondrial tubules range in diameter from less than 200 nm to over 1 μm.[83] The limit of diffraction for conventional fluorescent microscopy is approximately 200-250 nm. Therefore, any substructures of mitochondria are difficult to distinguish from each other. Visualizing sub-organelle structures was out of the question until recently. Now, new advances in super resolution fluorescent light microscopy technology can allow us to elucidate structural information *in situ*, which was previously only possible by electron microscopy or cryotomagraphy. Photoactivatable light microscopy, or PALM, is a super resolution fluorescent microscope technique that makes use of photoactivatable fluorescent proteins (PA-FPs) and high speed cameras.[86–88] We wanted to demonstrate that we could use the new technology to determine structural information about an important aspect of mitochondrial fission, the oligomeric Drp1 helical ring. For our investigation and for biological relevance, PALM with two colors was absolutely necessary. However, we quickly discovered that we could not visualize sub-mitochondrial structures at sub-diffraction resolution using the published methods with existing PA-FPs. Therefore, to gain structural information about Drp1 fission helical rings, we had to develop a new green PA-FP.

MICROSCOPY

Epifluorescence Microscopy

Fluorescence is a property of certain molecules which emit light of a particular wavelength after absorbing light of a specific shorter wavelength. This absorption of light is termed excitation. The electrons of excited molecules jump to a higher energy state upon absorption of the excitation light. As those electrons fall down to their ground state, energy is released as photons of a specific wavelength (instead of as heat).[89,90,91] If these photons fall in the visible spectrum, we can visualize specific wavelengths by filtering with appropriate emission filters. The use of cameras can allow for visualization with higher sensitivity. Biological fluorescence is most often found in molecules with alternating double bonds, such as benzene rings, a common feature in the chromophores of fluorescent proteins.[90] The maximum resolution of conventional and confocal fluorescence microscopy is limited by the Abbe limit of diffraction.[89,92]

$$d = \frac{\lambda}{2(n \sin\theta)}$$

Where lambda (λ) is the wavelength of the excitation light and *d* is the minimum distance between points that can be resolved, the numerical aperture, $n \sin\theta$, is dependent on the index of refraction of the medium through which the light is being transmitted (n) and the angle at which the light illuminates the sample (θ). It is, at best, 1.5 for today's optical setups. Therefore, the limit of diffraction is roughly determined by dividing the excitation wavelength by 2. Green light (561 nm) and blue light (488 nm) are commonly used excitation wavelengths for fluorescence microscopy of biological samples, making the maximum resolution approximately 250 nm. Shorter excitation wavelengths can be used to decrease the diffraction limit, but wavelengths below ultraviolet are generally not useful for biological specimens due to a loss of contrast. In addition, prolonged exposure to UV and below UV wavelengths can damage biological samples.[90,91]

Fluorescence microscopy is a powerful biological tool that has been steadily improving in resolution for several hundred years. Both the microscope instrument and the biological labeling techniques have undergone significant changes. Biologically relevant fluorescent microscopy began when August Kohler noticed that tissue specimens glowed under ultraviolet light, the first instance of auto-fluorescence. In 1941, Albert Hewett Coons used antibodies labeled with fluorescein to perform the first immunofluorescence.[90,91]

Fluorescence microscopy underwent a revolution as a technique with the development and use of green fluorescent protein (GFP). GFP was discovered by Osamu Shimomura and further studied by Martin Chalfie.[93] Roger Tsien made the key GFP mutation S65T in 1995, creating the enhanced version, EGFP.[94,95] The S65T mutation dramatically increased the brightness and photostability of GFP.[94] The use of EGFP fused to proteins of interest dramatically increased the biological relevance of fluorescent microscopy. Over the subsequent years, a large color palette of fluorescent proteins was developed.[96,97,98] In 2008, Roger Tsien, Martin Chalfie, and Osamu Shimomura were awarded a Nobel Prize for the discovery of GFP.[99] Fluorescent dyes have also undergone dramatic improvement in the last 30 years, improving immunofluorescence labeling cells as well. While the fluorescent microscope began as a simple light microscope making use of ultraviolet light, several different fluorescence microscopy techniques have come to the forefront of biological research.

Conventional fluorescence microscopy has one of the simplest setups. The technique makes use of a basic light microscope with the addition of a mercury arc lamp. The mercury arc lamp emits a broad spectrum of light. Excitation filters determine specific wavelengths of light that are allowed to pass through the filter and onto the sample, blocking the other wavelengths. Most conventional fluorescence microscopy setups make use of epifluorescence, in which the filtered excitation light passes through the objective on its way to the sample. The reflected light is then passed through the emission filter, which blocks most wavelengths, including light form the excitation band. The light that is transmitted goes on to the binoculars or camera for observation.[90–92] Each fluorescent protein or dye has an excitation and emission spectra.[98,100] It is the combination of the right excitation wavelengths and the collection of the right emission wavelength that allows for visualization.

Conventional fluorescence microscopy is excellent for tissue sections and whole cell applications.[90,91,98] However, conventional fluorescence microscopy can only give a two dimensional image of what is always a three dimensional sample. Therefore, the resolution of the technique is always somewhat limited due to out of focus fluorescence of the sample above and below the focal plane.

Confocal Fluorescence Microscopy

Confocal microscopy was developed to improve the resolution of conventional fluorescence microscopy by eliminating fluorescence outside of the focal plane. The ability to image narrow focal planes quickly led to three dimensional imaging by imaging many consecutive narrow focal planes in the vertical (Z) direction and compiling the stack into a single three dimensional image.[101] This type of optical sectioning is created by using small focused laser illumination and passing the light emitted by the sample through a pinhole, blocking the majority of the out of focus fluorescent light. The same focal plane can also be imaged multiple times with high precision for time lapse imaging. The size of the pinhole and the brightness of the fluorophore determine resolution.[101]

There are two common types of confocal microscopes: scanning laser and spinning disk. The scanning laser microscope uses oscillating mirrors, automatically controlled by servomotors and software, to move the laser across the sample. All light coming off the sample, including fluorescent emission, is deflected off the movable mirrors a second time.[102] This "descanned" light is then directed through an emission filter for wavelength specificity followed by a fixed pinhole to eliminate out of focus light.[101]

The spinning disk microscope involves the Nipkow disk, which consists of a series of small pinholes in Archimedean spirals. The disk is spun as a high speed. The excitation laser passes through the pinholes before illuminating the sample, dividing the laser into many smaller parallel excitation beams. These beams all hit the sample at once, as opposed to a single beam that is moved mechanically. The emission light of the sample is directed back through the spinning disk before passing through emission filters to the detectors, eliminating the out of focus light.[103,104]

The most important variables to take in to account, when deciding to use a scanning versus spinning disk confocal fluorescent microscope, are time and image resolution.[105] Because laser scanning microscopes require a mechanical movement of mirrors, the speed of imaging is related to the speed at which the mirrors can be made to oscillate precisely. The image is built pixel by pixel. This makes scanning confocal microscopy often incompatible with most video imaging. However, most laser scanning confocal microscopes can sample at various densities due to adjustable pinholes, which can dramatically improve spatial resolution.[101]

Spinning disk confocal microscopes excel at high speed imaging, as images are built all at once, due to the parallel excitation beams. This makes the spinning disk confocal microscope ideal for imaging quick cellular occurrences or at video speed. However, because of the fixed pinhole size, the spinning disk setup has a fixed sampling density and so can lose some spatial resolution. Therefore, laser scanning is best for high spatial resolution while spinning disk is best for high temporal resolution.[101] Both offer resolution improvements over epifluorescence imaging. However, all three methods are still confined by the limits of diffraction. Recently, several new fluorescence microscopy techniques have opened doors into super resolution imaging, circumventing the diffraction limit barrier.

Stimulated Emission Depletion Microscopy and Saturated Structured Illumination Microscopy

Stimulated emission depletion microscopy (STED) and saturated structured illumination microscopy (SSIM) are two relatively new methods of super resolution microscopy that image samples at resolutions below the diffraction limit without the use of specialized fluorescent small molecules or proteins.[92] STED microscopy narrows the effective point spread function (PSF) of an existing fluorophore by using stimulated emission to silence fluorescence around the center of an excitation spot.[106] Generally, when a fluorophore is excited, ground state electrons (i.e. electrons in energy level S_0) jump up to a higher energy level (S_1). The spontaneous relaxation of the electrons back to S_0 results in photon emission. If the electron encounters a second photon with a wavelength that is equal to the energy difference between S_1 and S_0, then it returns to ground state without releasing photons, effectively silencing the photon emission before it can occur. This process is called "stimulated emission".[106,107] STED microscopy involves two lasers: an excitation laser and a second STED laser that overlaps the excitation laser spot and matches the wavelength needed for stimulated emission. The STED laser spot is shaped such that it has an almost zero intensity center, with an increased intensity in a doughnut shape around the zero intensity centroid. Therefore, for each excited fluorophore, the emission periphery is silenced by stimulated emission, leaving only the center emitting photons and able to be detected. The diameter of the point spread function (PSF) post stimulated emission depletion is determined by the laser intensity of the STED laser. STED microscopy has achieved resolutions of 30-40 nm.[89,92,106,107]

SSIM depends on a computational extraction of information from the moiré fringes of the illumination pattern. SSIM illumination requires bright fluorescent molecules of high photostability.[89,92] The sample is illuminated with a strong excitation laser in a sinusoidal pattern which is created by passing the excitation beam through a diffraction grating. The excitation laser intensity needs to be strong enough such that the fluorophore is constantly in a highly excited state and giving off maximal emission. This creates a pattern with saturated emission peaks and wells of minimal emission in between. The sinusoidal pattern is then rotated slightly and the sample is reimaged. The image is created by combining the high resolution information at the fringes of the moiré pattern that results from the imaging pattern.[89,92] SSIM generally achieves a resolution of 100 nm and its effectiveness is highly limited by the stability of the sample and the fluorophore.[92]

Electron Microscopy

Electron microscopy is a type of microscopy that is commonly used for super resolution imaging of *in situ* and *in vitro* samples. Electron microscopy can achieve resolutions around the nanometer level. Electron microscopes use electrons instead of photons to illuminate a sample. Because the electron beam has a wavelength of five orders of magnitude shorter than ultraviolet light, the Abbe's limit of diffraction for light becomes significantly lower. Electron beams are produced using an electron source focused through magnetic lenses.[92] There are two common types of electron microscopy: transmission electron microscopy and scanning electron microscopy.

Transmission electron microscopy is ideal for imaging of the internal parts cells. Cells must be immobilized and sliced thinly enough for electrons to pass through them.[108] For transmission

electron microscopy, an electron beam is focused through magnetic lenses via current through the sample. Current also controls beam power. For the electron beam to travel straight through the sample, the beam must follow a perfectly straight column path under vacuum. The electrons passing through the sample are detected either by a fluorescent screen or, more modernly, by a charge coupled device (CCD) camera. The image is built based on the information gathered by measuring the differences in electron energy before hitting the sample and after passing through the sample.[109] Transmission electron microscopy is limited greatly by sample preparation. Immobilization by embedding samples in hard resin can cause morphological chances in the cellular sample. In addition, not every type of sample can be successfully thinly sectioned by microtomes. For these samples or for samples where the surface is the imaging target, scanning electron microscopy is a better technique.[92,108,109]

Scanning electron microscopy is useful for imaging surface structures of larger samples. An electron beam scans across the sample quickly in the X direction and slowly moves down in the Y direction.[110] The electrons interact with the sample and then lose energy in many processes including low-energy secondary electrons, heat, and X-ray emissions. The measurement of these energy losses are detected using electron detectors. Information from these energy losses are used to build the final image.[111] Scanning electron microscopy does not have as high a resolution as transmission electron microscopy but can handle more variation in vacuum and much larger three dimensional samples.[112,113]

Total Internal Reflection Fluorescence

High signal to noise ratio in any given focal plane is absolutely key for acquiring an informative image. One of the best ways to increase the signal to noise ratio is to remove the background. Confocal microscopy makes use of pinholes to filter out background but is generally limited to Z slices of approximately 1 μm thick. Within that single micrometer, depending on the density of the labeling, there can still be a significant number of fluorescent molecules and the setup is still subject to the diffraction limit barrier. For super resolution below the diffraction limit, imaging is vastly improved when the fluorescent molecules are spatially distant in the X, Y, and Z direction. To improve spatial separation in the vertical (Z) direction, an imaging method that allows for a thinner sectioning is necessary. One potential solution is physical thin sectioning as is done in sample preparation for electron microscopy.[111,114] However, not every sample can be embedded and thin sectioned and the use of a microtome requires significant technical skill. A second option is to optically thin section the sample using total internal reflection fluorescence (TIRF). TIRF makes use of an intrinsic optical property of light passing between two substances with slightly different refractive indices.[115] When a beam of light is directed through two mediums, generally glass and water or oil in light microscopy, the light will enter the first medium at a particular angle called the "incident angle". Upon entering the second medium of a different refractive index, the angle of the light is changed to the "refractive angle". The light path can be physically moved in regards to the sample, changing incident angle. When the incident angle moves past a certain "critical angle", a phenomenon termed "total internal reflection" occurs.[116] When total internal reflection occurs, the light no longer passes through the second medium but is instead completely reflected at the surface interface of the two mediums. When this happens, an electromagnetic field termed the "evanescent field" occurs at the interface between the two medium. The field penetrates the second medium with a Z depth of approximately 100 nm with perfect total internal reflection. If

the angle is not at or past the critical angle, then the propagating wave will penetrate several hundred nanometers. We term this non perfect total internal reflection "pseudo-TIRF". In terms of the microscopy, the two mediums are generally the immersion oil on the objective and the glass slide holding the sample.[115,116] In fluorescence microscopy, when total internal reflection is achieved, only fluorescent molecules within that 100-200 nm evanescent wave, beginning at the glass surface, will be excited. By nature, this is a phenomenon reserved for the surface interface between two mediums and so cannot be used to thin section a cell in steps increasing in the Z direction like a confocal microscope.[105] However, at the glass surface, it can create an optically thin section far superior to the capabilities of the confocal setup. TIRF is ideal for imaging fluorescent molecules close to the glass surface either on the cell membrane or in positions close to the cell membrane. Imaging of such a thin section removes a significant amount of background which can vastly improve the signal to noise ratio.[105] For super resolution imaging, TIRF can also spatially limit the number of fluorescent molecules that can be illuminated in the vertical (Z) direction, improving potential single fluorophore identification.[88,117,118]

Photoactivatable Light Microscopy

Both types of confocal microscopy are suitable for whole cell imaging, both *in vivo* and *in situ*, but are subject to the diffraction limit in regards to resolution. STED and SSIM imaging offer higher resolution but require specialized lasers and imaging software. Electron microscopy sample preparation is known to significantly alter mitochondrial morphologies and is technically difficult. Therefore we turned to another super resolution imaging technique that offers resolution of approximately 25 nm, superior to both STED and SSIM, and requires minimal sample preparation, thereby preserving the *in vivo* mitochondrial morphology.

Photoactivatable light microscopy (PALM) was developed by Eric Betzig in 2006.[118] The theory behind PALM is the separation of individual fluorescent molecules both spatially and temporally. Each fluorescent protein, upon excitation, emits photons. The photon emission produces an Airy disc point spread function (PSF). Individual absolute protein localization can be determined by calculating the center of this point spread function. However when multiple proteins' PSFs overlap, it then becomes all but impossible to determine the number of proteins, let alone the absolute localization of each individual protein. The overlapping PSFs are compounded with an increasing population of fluorescent proteins all being excited and emitting at the same time. However, if the PSFs of two neighboring proteins were to be excited and emit detectable photons at different times, then each individual point spread function can be back calculated to an absolute localization.[117,118] PALM therefore requires two parameters: a way to only excite a widely scattered small stochastic population of fluorescent proteins in a sample and a way to separate the detection by time. The second temporal separation parameter is easily met by using a high speed CCD camera. Various cameras will image from speeds at 20 Hz to 900 Hz. The first parameter requires that only a limited stochastic number of fluorescent proteins in a small spatial area are excited when an excitation laser is fixed upon it.[117,118] In order to achieve this, fluorescent proteins need to be "activated" before they are able to be excited. During imaging, each camera frame will contain a small scattered population of detected fluorescent PSFs. After removal of background and identification of fluorescent molecules, the frames can be compiled to form the complete image. PALM's most obvious limitation is the necessarily long imaging time, which currently precludes the use of live cells.[119] PALM images have been taken of whole cells under multiple *in situ* preparations, including cryo-fixation with sectioning

and basic fixation with paraformaldehyde.[85,88] A similar technique called stochastic optical reconstruction microscopy (STORM) was developed by Xiaowei Zhuang using fluorescent dyes and small molecules instead of fluorescent proteins.[120] Sample prep for STORM imaging uses classic fixation and membrane permeablization techniques associated with immunofluorescence.[120,121] In addition, a third technique, very similar to PALM, termed fluorescence PALM (FPALM) was reported by Samual Hess.[122] The imaging theory behind STORM and FPALM is very similar to PALM. The keys for all of these techniques are spatial and temporal separation of fluorescent "events" and the number of photons collected.

FLUORESCENT PROTEINS

Overview

Fluorescent proteins are generally β-barrel proteins containing a chromophore inside the β-barrel. Fluorescent proteins can be either monomeric or oligomeric. Fluorescent proteins are usually biologically inert and so are often excellent tags for individual proteins.[97,100] Various fluorescent proteins can be pH sensitive and so different fluorescent proteins will be more suitable for different cellular compartments.[98] The chromophores can vary widely among different fluorescent proteins, but the principle remains the same. Electrons within the chromophore are excited to a higher energy state by a particular wavelength of light. As the electrons fall back to their ground state, they emit photons at a longer wavelength. Those emitted photons are the detectable fluorescence. The range of wavelengths, or spectrum, which excites a fluorescent protein, can be narrow or broad and the strength of the excitation is dependent on the wavelength. The fluorescent protein will emit photons in a range of wavelengths and the number of photons detected will also be dependent on the wavelength examined.[96,97,98,100]

Each fluorescent protein has specific excitation and emission spectra. The excitation and emission wavelengths cover the UV-visible spectrum. The lifetime and brightness of the fluorescent protein varies and is dependent on multiple factors. After emission a fluorescent protein can take two paths. The fluorescent proteins can either enter a dark state where they can be re-excited or they can be photobleached and no longer be re-excited or emit any further photons.[123,124] Until recently, fluorescent proteins existed in three states: non-excited, excited or bleached. However, for PALM imaging, we need an additional state: "non-activated".

Photoactivatable and Photoswitchable Fluorescent Proteins

A new class of fluorescent proteins has recently emerged, termed photoactivatable (PA) or photoswitchable (PS).[125,126] These fluorescent proteins begin in a "non-activated" state. While these fluorescent proteins are in the "non-activated" state, the molecule cannot be excited or emit photons. In order to achieve a viable excitation state, these fluorescent proteins have to be "activated" by a third wavelength.[124] Therefore illumination of the fluorescent proteins in a sample with both the activation wavelength (using a low powered laser) and the appropriate excitation wavelength (using a middling to strong powered laser) will result in only small stochastic populations of fluorescent molecules emitting at any given time.[127] Some fluorescent proteins are activated irreversibly and some can be activated and excited in multiple cycles. These molecules are termed "photoactivable" and "photoswitchable" respectively.

There has been a lot of work in the last 10+ years to develop photoactivable and photoswitchable fluorescent proteins. The first photoactivable fluorescent protein was PA-GFP made by the Lippencott-Schwartz lab and published in 2002.[127] PA-GFP is a mutant variant of wild type GFP with the key mutation T203H.[125] PA-GFP was quickly followed by a slew of photoactivatible and photoswitchable fluorescent proteins that fall under several categories: green to red, dark to red, dark to green, and blue to green. We will not discuss all possible PA and PS-fluorescent proteins, but instead focus on the ones used or tested and discarded in our studies.

Green to red photoactivatable fluorescent proteins

While there are multiple available green to red photoactivatable fluorescent proteins, our studies used mEos2. mEos2 is a monomeric version of tetrameric Eos.[126] Wild type Eos was originally isolated from *Lobophyllia hemprichii*, a coral. Pre-activation, Eos has an emission maximum at 519 nm. It can be activated by 405 nm illumination. Post activation, Eos has an emission maximum at 584 nm and an excitation maximum of 573 nm.[85,97,128] Another coral protein, DendGFP, was isolated from *Dendronephthya sp.* and has a pre-activation emission maximum at 505 nm and a post-activation excitation maximum at 553 nm and an emission maximum at 573 nm.[98,128–130] Its activation wavelength is also 405 nm. Dendra2 is the monomeric form of DendGFP.[98] Dendra2 is not as bright at mEos2 but it folds more efficiently at 37ºC.[128]

Dark to Red photoactivatable fluorescent proteins

PamCherry1 was developed by the Vladislav Verkhusha. It is a mutant variant of mCherry with the mutations E26V/A58T/K69N/L84F/N99K/S148L/I165V/Q167P/L169V/I203R.[131] Prior to activation, PAmCherry1 exists in a dark state with no detectable fluorescence. Post activation by UV light (~405 nm), PAmCherry1 has an excitation maximum at 564 nm and an emission maximum at 595 nm, which is downshifted from the mCherry1 emission maximum of 610 nm.[131,132]

Dark to green photoswitchable fluorescent proteins

Dronpa is a monomeric mutant variant of 22G, which is a GFP-like protein isolated from the coral species *Pectiniidae*.[133] In its pre-activated state, Dronpa is dark with no detectable fluorescence. Upon activation with UV light, Dronpa has an excitation maximum of 503 nm and an emission maximum of 515 nm.[134–136] Instead of photobleaching, after excitation, Dronpa re-enters its dark state. It can be then be reactivated and go through the whole cycle again. Dronpa can go through the cycle up to thirty times.[137,138] Several mutations of Dronpa have been made including rsFastlime, which is a single point mutation of Dronpa at position 157, replacing a valine with a glycine.[139] The valine at position 157 is involved in the photo-induced cis to trans switching of the chromophore, though not directly part of the chromophore.[135,140] A glycine in place of the valine at position 157 reduces the steric hindrance around the chromophore, allowing rsFastlime to switch rapidly between cis and trans such that camera imaging speeds between 500 and 900 Hz are needed to perform high resolution microscopy with rsFastlime.[140,141,137]

SPECTROSCOPY

Each fluorescent protein, regardless of color, oligomerization, or photoactivatability, exhibits specific characteristic traits that can be easily measured by fluorimeters and spectrophotometers. Such parameters include excitation and emission spectra, a molar extinction coefficient, quantum yield, and brightness. We discuss the actual calculations later in this chapter, so here we will simply define terms. An excitation spectrum refers to the range of photon wavelengths the chromophore of a fluorescent protein can absorb at varying efficiencies and more specifically to photons that are absorbed by the chromophore and excite its electrons to higher energy states.[142,143] Its shape and range are generally similar to that of the absorption spectrum. An emission spectrum refers to the range of photon wavelengths emitted by the fluorescent protein via spontaneous relaxation of the excited chromophore electrons back down to the original ground state. The emission spectrum curve is indicative of the probability that a particular photon will be emitted at a given wavelength.[142,143] The techniques for obtaining spectra is described in the Results and Discussion section of this chapter. The molar extinction coefficient is a measure of the amount of light the chromophore can absorb at a particular wavelength. We generally measure the molar extinction coefficient at the maximum absorbance wavelength of a given fluorescent protein. Quantum yields are a measure of the efficiency of the chromophore, or how much of the absorbed photon energy emitted as photons and not lost to heat. In a perfectly efficient fluorescent protein, every photon that is absorbed by the chromophore results in an emitted photon. The reality is that a substantial amount of energy in many fluorescent proteins is lost to heat.[142,143] Brightness is basically a combination of the ability of the chromophore to absorb light (molar extinction coefficient) and the efficiency of photon emission versus heat loss of the same chromophore (quantum yield) and is generally compared to EGFP where EGFP has a given brightness of 100.[96] Calculations for each of these fluorescent traits are described in the Results and Discussion section of this chapter.

PHOTOPHYSICS AND KINETIC MODELS

With regards to the physics behind fluorphore excitation/emission (photophysics), we consider at least two kinetic steps, governed by the rate constants: k_{bleach} and $k_{triplet}$. The k_{bleach} or k_b rate constant refers to the rate at which the fluorescent protein is photobleached.[124] Occasionally, a fluorescent protein can return to a "triplet state" and be re-excited. We term this entrance to the "triplet state" $k_{triplet}$.[123,124] Photoactivatable fluorescent proteins have to be activated prior to excitation. Commonly the activation of photoactivatable fluorescent proteins requires a chemical change that directly or indirectly interacts with the chromophore. The activation step adds an additional rate constant, $k_{activation}$ or k_a which is generally considered irreversible as it is often due to a chemical change.[128,130] Some photoactivatable proteins such as mEos2 and Dendra2 have an additional "dark" state. The rate of entrance to the dark state, k_{dark} or k_d, and fluorescence recovery rate(s), k_{r1} (and k_{r2}, etc. if the recovery rate is of higher order) account for the observed "blinking" behavior.[130] The ratio of the populations inhabiting different recovery rates is described by the variable α (β, etc).[130] Photoswitchable fluorescent proteins generally switch between two physical states, either through isomerization or reversible chemical changes. Generally one state is "OFF" or dark and one state is "ON" or fluorescent. The activation of the photoswitchable chromophore switches it from the dark state to the fluorescent state.[137,139] In the photoswitchable fluorescent protein kinetic model we propose, the rate

constant(s) that describes the activation of the chromophore is now considered the k_{r1} (and k_{r2}, k_{r3}, etc. if the recovery rate is of higher order). In this case, the relatively rare "triplet state" is mostly indistinguishable from the activated chromophore isomerization in that it is difficult to differentiate between entering the triplet state and subsequent re-excitation versus fluorescence recovery via activation. The chromophore is then theorized to return to its physical starting state either through exposure to the excitation wavelength or spontaneous relaxation. This change from the fluorescent state to the dark state for photoswitchable proteins is given the rate constant term k_{dark} or k_d.[135] Therefore photoactivatable fluorescent proteins have at least one additional rate constant to account for and photoswitchable fluorescent proteins have two or more additional rate constants (Figure 1). Our photophysical studies used these rate constants to calculate the average time spent in the ON state (T_{ON}), the average time spent in the OFF state (T_{OFF}), and the average number of times the protein switches back and forth between the dark and fluorescent states before photobleaching (N_{Blink}). Actual calculations are discussed in the Results and Discussion of this chapter.

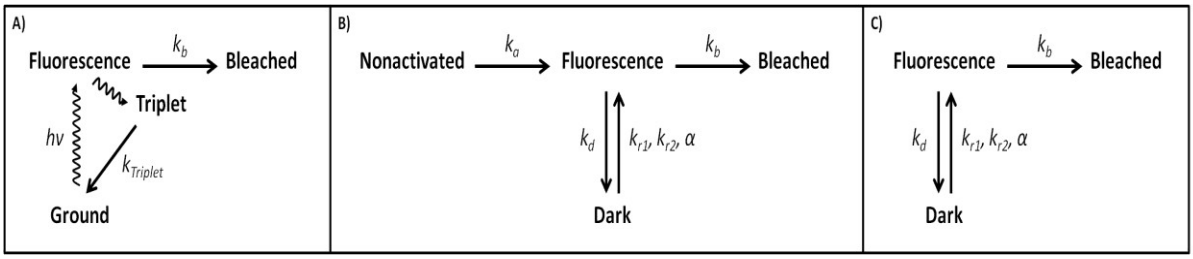

Figure 1: Kinetic models of fluorescent, photoactivatable fluorescent, and photoswitchable fluorescent proteins. A) The kinetic model of a conventional fluorescent protein. After excitation by the respective wavelength, the chromophore usually photobleaches (k_b) but can relax to a "triplet" state ($k_{triplet}$) before returning to the ground state where it can be re-excited. B) The kinetic model of a photoactivatable fluorescent protein. Photoactivatable fluorescent proteins begin in a nonactivated state. Upon activation (k_a) with 405 nm and excitation with the respective wavelength, the chromophore can either photobleach (k_b) or enter a "dark" state (k_d) and recover its fluorescence (k_{r1}, k_{r2}, α). C) The proposed kinetic model of a photoswitchable fluorescent protein. Photoswitchable fluorescent proteins can start either in their activated (ON) or dark state (OFF) based on the isomerization of the chromophore. After excitation of an activated chromophore by the respective wavelength, the chromophore can either photobleach (k_b) or isomerize back to the dark state (k_d). Photoactivation by 405 nm (k_{r1}, k_{r2}, α) will isomerize the chromophore back to its ON state for re-excitation.

RESULTS AND DISCUSSION

RESOLVING MITOCHONDRIAL MEMBRANE STRUCTURES VIA PALM IMAGING

Molecular cloning of mitochondrial membrane targeted mEos2 and Dronpa

Our initial attempts to verify our ability to use two-color PALM to image mitochondria were based on the published two color scheme detailing the use of mEos2 as the "red" fluorescent protein and Dronpa as the "green" fluorescent protein. We decided to target the two largest structures of the mitochondrial organelle, the inner mitochondrial membrane (IMM) and the outer mitochondrial membrane (OMM), to see if the increased resolution of PALM imaging could resolve these two structures from each other. For clear imaging of the membranes, we needed to "coat" the membranes with randomly inserted and membrane anchored PA-FPs. Nuclear encoded mitochondrial proteins are directed to mitochondrial network by way of mitochondrial localization sequences (MLS), most often found on the N or C terminus.[85] These sequences can direct mitochondrial proteins to different compartments of the organelle and/or determine specific membrane integration. Many MLSs have been characterized in the literature. We chose two proteins whose MLS and specific membrane integration had already been characterized by truncations fused to GFP and the resulting specific sub-organelle localization of the GFP fusion (Figure 2). By just using the N or C termini of such protein, we allow for random insertion in the respective mitochondrial membrane as opposed to fusions with full length and functional mitochondrial proteins, which may be more specifically localized due to that protein's specific function.

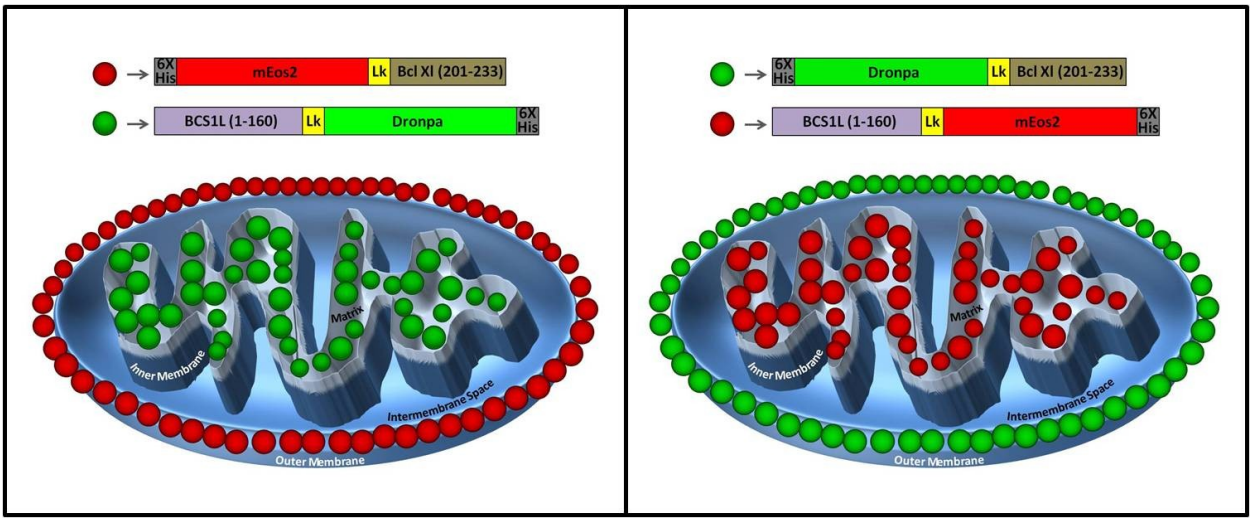

Figure 2: Genetic construction of mitochondrial membrane localized photoactivatable fluorescent proteins. Photoactivatable fluorescent proteins were localized to specific mitochondrial membranes using mitochondrial localization sequences and transmembrane domains of membrane specific mitochondrial proteins.

In order to coat the outer mitochondrial membrane with our PA(PS)-FPs, we chose murine BclXl, an OMM protein involved in apoptosis, which has the main body of the protein in the cytoplasm but is anchored to the OMM by a C terminal transmembrane region.[144] BclXl is localized to the OMM by a C-terminal MLS. We used the C terminal 32 amino acids (ESRKGQERFNRWFLTGMTVAGVVLLGSLFSRK). To coat the inner mitochondrial membrane, we chose murine BCS1L, a mitochondrial chaperone protein which is anchored N terminally in the IMM with the main body of the protein in the mitochondrial matix. BSC1L is localized to the IMM by a N-terminal MLS and anchored by the N-terminal 160 amino acids.[145]

We built mEos2 (or Dronpa) fused to the C-terminus of BclXl separated by the 25 amino acid linker by nesting PCR and cloned it into pCMV Kan/Neo for constitutive expression. We also included an N-terminal 6X histidine tag. We built mEos2 (or Dronpa) fused to the N-terminal 160 amino acids of BCS1L by obtaining commercial murine *BCSI1L* cloned into pCMV Kan/Neo from Origene and replacing the main body of BCS1L 161-418 with the PA-FP and a C-terminal 6X histidine tag (Figure 3).

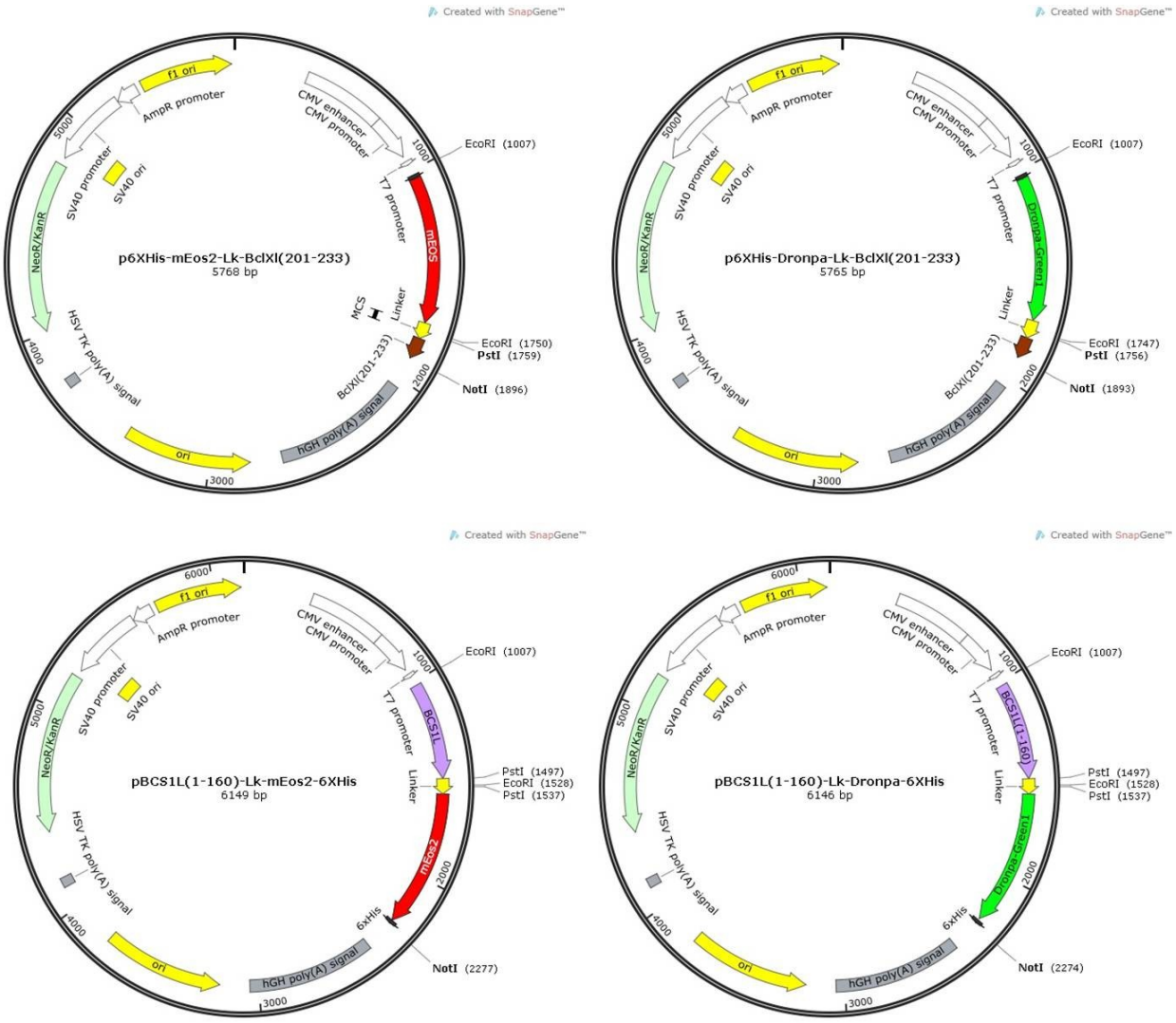

Figure 3: Cloning maps of mitochondria localized photoactivatable fluorescent proteins. 6XHis-mEos2-Lk-BclXl(201-233) or 6XHis-Dronpa-Lk-BclXl(201-233) was inserted into pCMV Kan/Neo with EcoRI and NotI. Lk-mEos2-6XHis or Lk-Dronpa-6XHis was inserted into pBCS1L on a pCMV Kan/Neo backbone using PstI and NotI.

Expression and imaging the OMM and IMM coated in PA-FPs *in situ*

To determine basic localization of mEos2 (Dronpa), we transfected C2C12 murine muscle cells via Lipofectamine with either p6XHis-PAFP-Lk-BclXl(201-233) or pBCS1L(1-160)-Lk-PAFP-6XHis. Cells were plated approximately 24 hours before on a MatTek imaging plate, treated to encourage cell adherence and containing a central #1.5 glass viewing window for microscopy. We used the C2C12 cell line due to its high mitochondrial content. Cells were incubated overnight and the mitochondria were labeled with MitoTracker Red CMXRos. The

transfected cells were then imaged *in vivo* in growth media. For basic mitochondrial localization, cells were imaged on a Nikon Eclipse TE2000-S confocal microscope. Images were taken without activation by 405 nm via mercury arc lamp since both fluorescent proteins can absorb blue light and emit in the green emission spectra in the pre-activated (mEos2) or randomly activated (Dronpa) states respectively. Both 6XHis-mEos2-Lk-BclXl(201-233) and BCS1L(1-160)-Lk-mEos2-6XHis showed clear co-localization with MitoTracker Red CMXRos (Figure 4). The same was shown for Dronpa. (Data not shown) Since mitochondrial localization was confirmed, we moved forward to PALM imaging of cells transfected with p6XHis-PAFP-Lk-BclXl(201-233) or pBCS1L(1-160)-Lk-PAFP-6XHis.

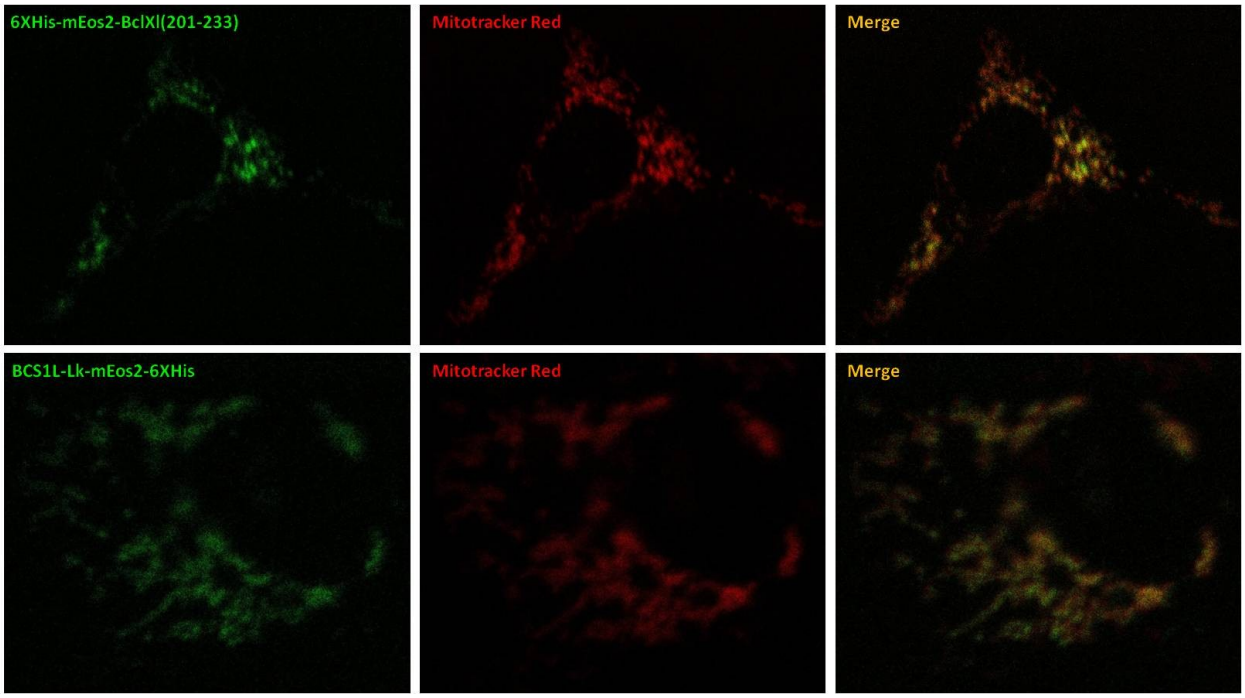

Figure 4: Photoactivatable fluorescent proteins fused to mitochondrial localization sequences and transmembrane regions are successfully localized to mitochondria. Cells were transfected with mEos2 fused C-terminally to BclXl(201-233) (*top row*) or N-terminally to BCS1L(1-160) (*bottom row*). Cellular mitochondria were labeled with MitoTracker Red CMXRos. mEos2 was not activated.

For PALM imaging, we had to take two more variables into account: sample illuminating laser angles for TIRF and fiducial markers. PALM imaging is most effective when performed under TIRF or pseudo-TIRF conditions. Pseudo TIRF conditions result in a propagating wave of 100-400 nm depth of excitation from the surface of the coverslip. Since mitochondria vary in diameter from 200 nm to 1 μm, it is necessary to have the mitochondria to be imaged close to the surface of the glass slide. Adherent cells attach to coated glass slides and are thickest near the

nucleus. Adherent cells thin near the edges of the cell. The flatter and more spread out a cell is, the larger percentage of mitochondria per cell will be close to the glass and better separated as a network. Therefore we decided to switch from C2C12 cells to the larger and flatter murine EpH4 cell line. In addition, 100 nm Au particles were coated in fetal bovine serum (FBS) and fed to the cells post transfection.[146] A percentage of Au particles are endocytosed and a percentage stick to the glass slide (Figure 5). The Au particles served as fiducial markers for correcting X and Y drift during analysis and to help set the sample illuminating laser angle for TIRF. Fiducial markers can also be useful to help set the focal plane in the vertical (Z) direction.

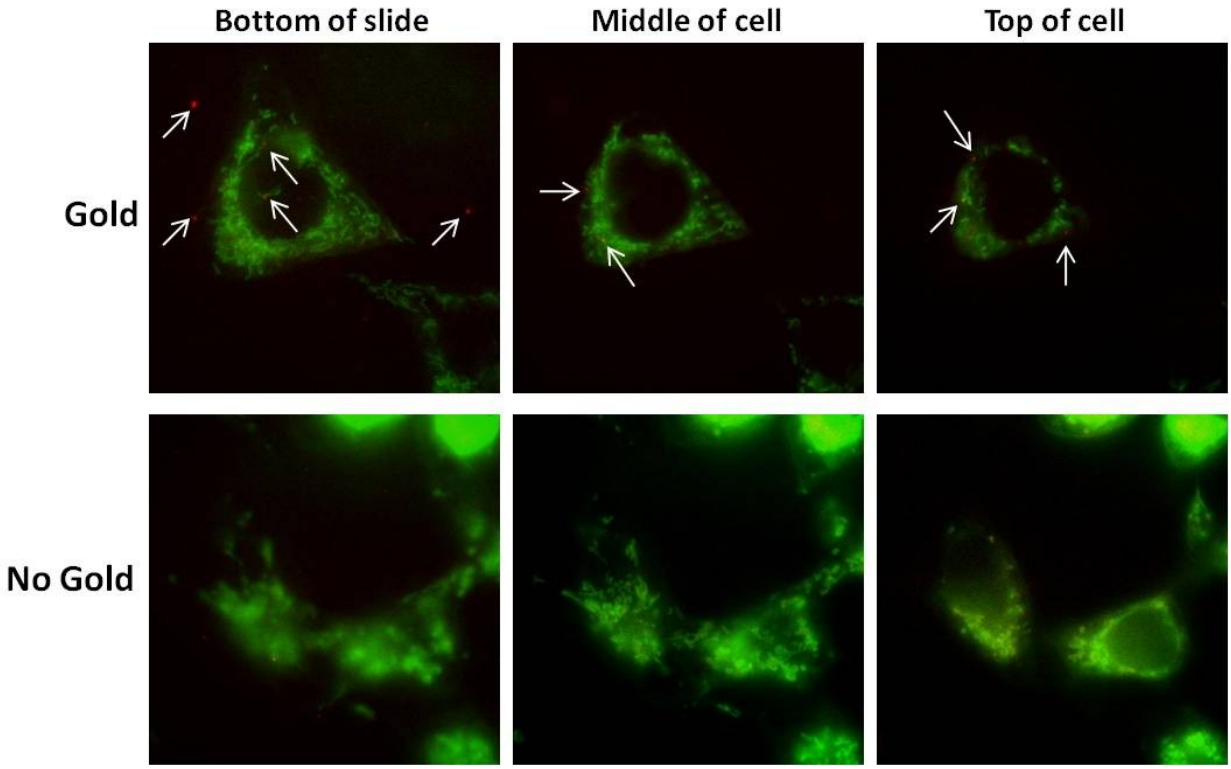

Figure 5: EpH4 cells engulf FBS coated 100nm gold fiducial markers for tracking XY drift and for use in setting focal planes. EpH4 cells were fed 50 µL of FBS coated 100 nm Au fiducial markers overnight (60,000 particles/mL), washed 6 times in 1X PBS, and imaged. Cellular mitochondria were labeled with MitoTracker Green. Different focal planes of specific cells were imaged.

EpH4 murine cells were plated on fibronectin coated #1.5 glass slides 24 hours prior to transfection. As described before, cells were transfected with p6XHis-PAFP-Lk-BclXl(201-233) or pBCS1L(1-160)-Lk-PAFP-6XHis via Lipofectamine and fed FBS coated 100 nm Au fiducial

markers. Cells were incubated overnight at 37ºC, washed in 1X phosphate buffered saline (PBS) and fixed in fresh 1% formalin in 1X PBS for 10 minutes. Cells were imaged on the PALM microscope using a specific sequence of events. Since mEos2 are fluorescent in the green channel by pre-activation and Dronpa is reversibly fluorescent in the green channel, we determined successful transfection and set focal planes by locating cells fluorescing in the green emission channel via low excitation with a mercury arc lamp. We set the sample-illuminating laser angle, always attempting to be as close to TIRF as allowable by the setup, by illuminating the cell with the 561 nm laser. The 561 nm laser reflects strongly off the 100 nm Au fiducial markers and allows for determination of even illumination across the field while staying near TIRF. Illumination at 561 nm has no downstream detrimental effects on the mEos2 or Dronpa, as mEos2 cannot be excited prior to activation and 561 nm is outside of the Dronpa excitation spectra. After setting the focal plane and sample-illuminating laser angle for TIRF, the imaging methods for mEos2 and Dronpa diverged. mEos2 transfected cells were imaged by turning on the 561 nm laser (22 W/mm^2) to bleach any pre-activated fluorescent proteins and setting the camera at 20 Hz. At this time, the Z feedback for automatic Z drift correction by the stage was set. The 405 nm laser was then turned on with low power density (0.60 W/mm^2) and slowly increased during the imaging process in order to maintain a constant and small stochastic population of activated molecules. Because the cells were exposed to the excitation and activation laser simultaneously, molecules were excited immediately upon activation. Cells transfected with mEos2 were imaged in this method until all fluorescent molecules were activated, excited, and bleached. Dronpa transfected cells were imaged by turning on 488 nm laser (5.87 W/mm^2) and setting the camera as described previously. After allowing the pre-activated Dronpa to return to its dark state, the 405 nm laser was turned on (0.60 W/mm^2) and imaging was completed as described previously.

We noted during the imaging itself, that, while mEos2 transfected cells produced clearly distinguishable events on the camera screen, Dronpa transfected cells showed no discernible events, instead resulting in a “shimmering” effect. In observing “shimmering” effect, we noted that all the molecules seemed to be activated and fluorescing at once, or were photoswitching with such rapidity that we could not distinguish individual events by eye or by analysis, though both were attempted. We also observed that while exposure to 561 nm laser had no effect on mEos2 prior to activation by the 405 nm laser, exposing Dronpa to the 488 nm laser prior to activation appeared to bleach the Dronpa fluorescence instead of returning it to the dark state for re-activation. Therefore, the addition of the 405 nm laser seemed unable to activate Dronpa molecules as they appeared to be already photobleached by the prior exposure to the 488 nm laser. Lowering both the 488 nm (0.54 W/mm^2) and the 405 nm (1.2 mW/mm^2) laser power densities did not result in improved event capture. Lowering the expression levels of Dronpa also did not improve individual event capture.

Analysis of the PALM images was completed using “peakfindtool”, a software program for MATLAB developed in our lab by postdoctoral fellow Sanghyuk Lee.[130] Individual fluorescent events per frame were chosen based on two parameters. Parameter 1 sets a threshold for individual pixel brightness over total background (peak to background). Parameter 2 sets a threshold for the summed number of photons within a 7 x 7 pixel square centered on each pixel identified by parameter 1 (total photon count) (Figure 6). Each pixel equals 106.6 nm; therefore, by applying the total photon count threshold, each event’s PSF center is separated spatially by at least 700 nm. Events that pass both thresholds are considered real and the 7 x 7 pixel square was fit by a 2-D Gaussian PSF. From these PSFs, the inferred position of the single PA-FP molecule

was calculated with higher accuracy than is possible with the diffraction limit. XY drift was tracked and corrected by identifying fiducial markers and tracking their paths. Fiducial markers were determined by identifying "events" that were consistent in every frame. The fiducial path was used to correct each individual event after identification. In the reconstruction of the final PALM image, each individual event was represented by its 2-D Gaussian. The center and the width of each 2-D Gaussian were given by the position and the uncertainty in the position, respectively, inferred from the PSF-fit. Within the final PALM image, each event, represented by a round "spot", theoretically represents one individual fluorescent protein. However, previous work has demonstrated that many of the PA-FPs that used in PALM imaging "blink", or enter a dark state and can be re-excited. Therefore, if XY drift is not carefully tracked, one fluorescent protein could show up as several "spots" on the final image. This is critical if attempting to perform quantitative analysis of the number of proteins but less important for simply visualizing larger protein or finer organellar structures and was not a critical factor in our investigations.

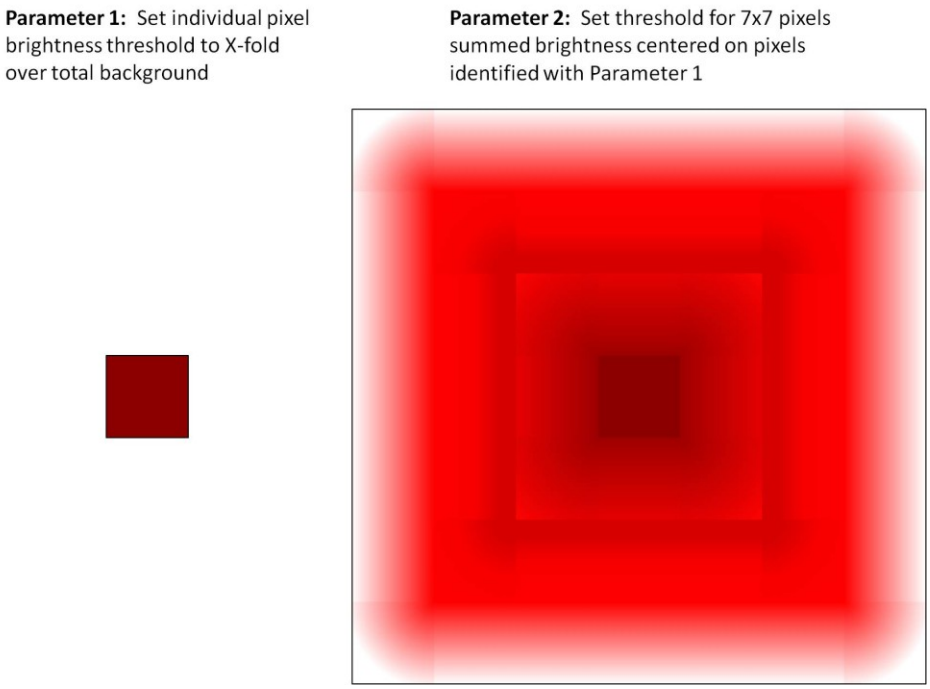

Figure 6: Two parameters are used to pick individual PALM events during analysis. Parameter 1 requires the user to set a threshold for individual pixel brightness that is X-fold over the total background of the frame. Parameter 2 requires the user to set a threshold for the sum of the number of photons within the 7 x 7 pixel square centered on the pixels chosen by parameter 1. Events that are above both thresholds are considered "real" and are used to compile the final image. Each event theoretically represents a single protein.

In cells transfected with p6XHis-mEos2-Lk-BclXl(201-233), photoactivatable fluorescent protein mEos2 showed clear localization to the outer mitochondrial membrane. The fluorescent proteins clearly outline the elongated tubular mitochondria and the more punctate mitochondria. No fluorescence is found in the center of the mitochondria, confirming localization to the outer mitochondrial membrane (Figure 7a). Our images are consistent with published STORM imaging of the outer mitochondrial membrane. In those images, Tom20, an outer mitochondrial membrane protein, was labeled with antibodies conjugated to STORM photoswitchable dyes.[121] In cells transfected with pBCS1L(1-160)-Lk-mEos2-6XHis, mEos2 showed clear localization to the inner mitochondrial membrane. We observed "lines" across mitochondria that are consistent with known cristae structures (Figure 7b). Our images are consistent with published isoSTED imaging of mitochondrial inner membranes treated with fluorescent dye conjugated antibodies against ATP synthase.[147]

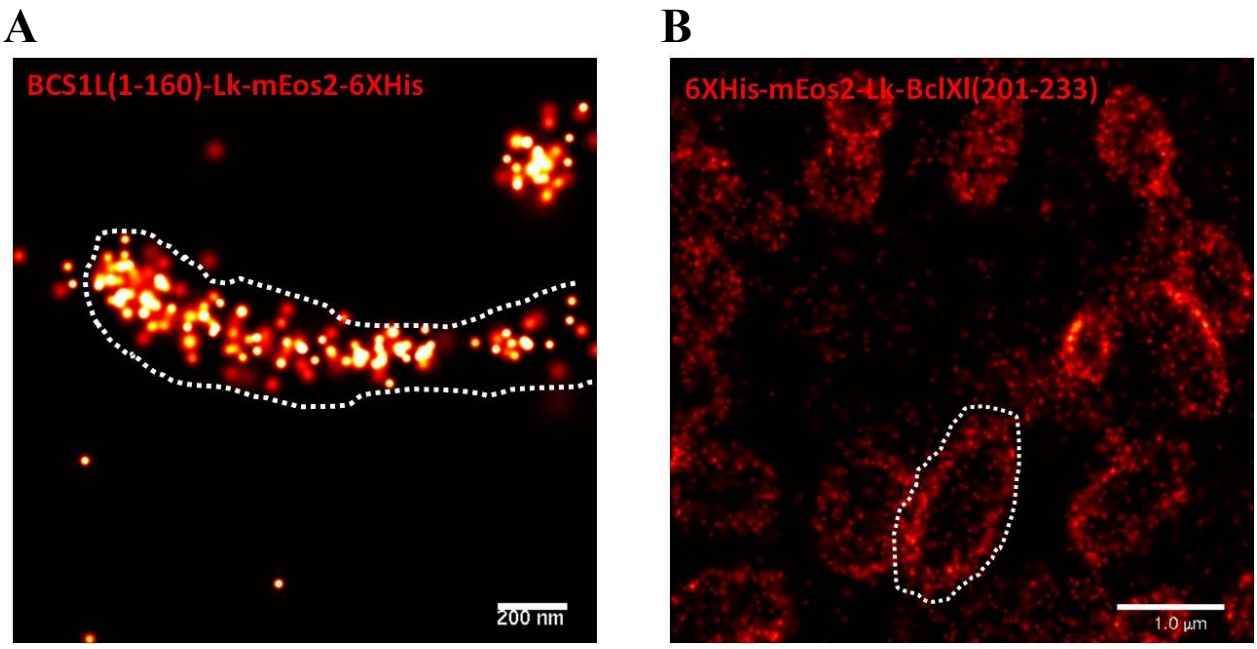

Figure 7: Analyzed PALM images of mitochondrial membranes labeled with mEos2. EpH4 cells were transfected with A) pBCS1L(1-160)-Lk-mEos2-6XHis or B) p6XHis-mEos2-Lk-BclXl(201-233). Mitochondria were PALM imaged with 561 nm at 22 W/mm^2 and 405 nm ranging from 0.60-6.0 W/mm^2 and analyzed using a 6-fold threshold for peak to background and a 2200 threshold for the total photon count. XY drift was corrected with 100 nm Au fiducial markers.

Because of the previously mentioned "shimmering" effect, we were unable to obtain a useful analyzed PALM image of either the inner or outer mitochondrial membranes when the membranes were coated with targeted wild type Dronpa. The inability to collect or subsequently identify individual events during PALM imaging or analysis meant we lacked confidence in the absolute localization of any Dronpa molecules. This created a great difficulty in our research. For PALM to be biologically relevant, two colors are a necessity and though published literature had detailed two-color PALM imaging, in our hands, their protocols were not effective.[132,148,149] We had confirmed that mEos2 could be used as one of the two colors (red) but we lacked a second color (green). Other PA-FPs emitting in the red part of the spectra were not useful because of the substantial overlap of the emission spectra. We explored other PA-FPs including photoactivatable green fluorescent protein (PA-GFP), photoswitchable cyan fluorescent protein (PS-CFP2), and enhanced yellow fluorescent protein (EYFP) as potential second colors. However, though the published literature seemed promising, all failed in our hands, often due to either dimness or the same "shimmering" effect we observed with Dronpa (confirmed through personal communication with Eric Betzig).[150]

DEVELOPMENT OF A VIABLE GREEN FLUORESCENT PALM PHOTOACTIVATABLE FLUORESCENT PROTEIN

Development of Dronpa Mutants via Mutagenesis

Previous work by Stefan Jakobs' group had demonstrated that the reduction in steric hindrance around the chromophore resulting from a valine to glycine substitution at position 157 in Dronpa resulted in a faster cis to trans isomerization (switching) of the chromophore. They termed this variant rsFastLime.[148] rsFastlime switched so quickly that it required imaging at over 500 Hz to catch individual photon bursts or "events". We obtained and tested rsFastLime as a potential "green" PA-FP for two-color PALM imaging, but our camera was not able to image at the high speeds necessary to catch individual events. The issue seemed to be that both rsFastLime and Dronpa were switching from cis to trans and vice versa so quickly that we could not capture individual events within one camera frame. We therefore reasoned that increasing steric hindrance at position V157 in Dronpa would result in slowed cis-trans switching of the chromophore, therefore allowing for easier capture of individual events at slower camera speeds (~20 Hz). We resolved to develop variants of Dronpa, exchanging the V157 for isoleucine, leucine, or phenyalanine (Figure 8). We purposely used amino acids that were nonpolar and similar in structure to valine, but with larger side chains. The phenylalanine mutation was included to determine if a large sidechain at V157 could prevent movement of the chromophore completely.

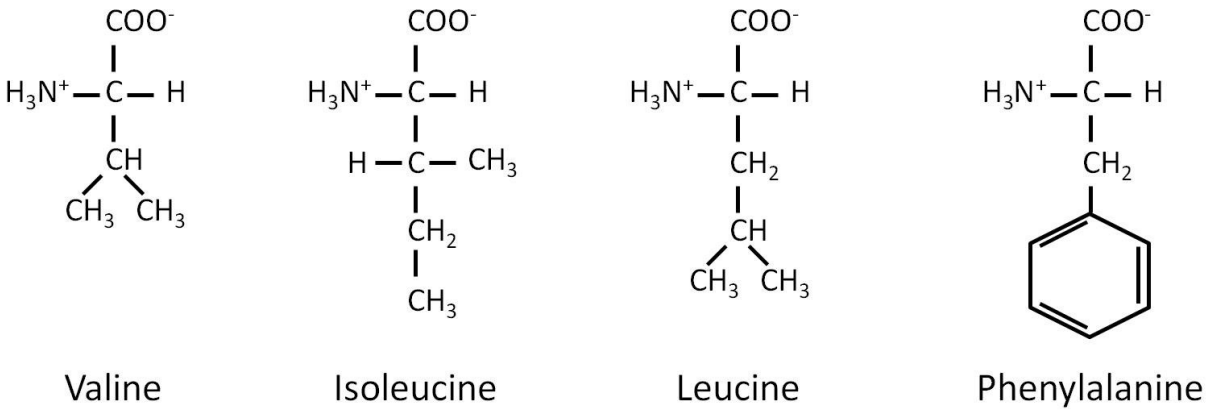

Figure 8: Amino acids side chain structures used for Dronpa mutagenesis. Amino acids of increasingly large nonpolar side chains were placed at position 157 of wild type Dronpa via mutagenesis.

In order to test the efficacy of the increased steric hindrance in the context of PALM imaging in mammalian cells, we developed a series of constructs designed to target the Dronpa mutants to the inner membrane of the mitochondria by fusing *Homo sapiens* Cox5A, an integral inner mitochondrial membrane protein, to the N terminus of DronpaV157X separated by a three amino acid linker for easier cloning.[46,47,151] Cox5A had previously been labeled C-terminally with GFP with no observed interruption of its integration into Complex IV or function therein.[152] This design scheme was chosen based on previous successful PALM imaging of mEos2 targeted to the inner mitochondrial membrane via fusion to the N-terminus of BCS1L, an integral IMM protein. By using this previous imaging, we had a basis of comparison for the quality of the images able to be obtained by our Dronpa mutants. Our mutants were termed DronpaV157I, DronpaV157L, and DronpaV157F. Wild type Dronpa was also examined for comparison (Figure 9). We also added a second cell line to our experiments; T-Rex HeLa cells (Invitrogen), in order to allow for finer control of expression levels. T-Rex HeLa cells are part of a Tet ON system and are stably transfected with a plasmid constitutively expressing a tetracycline repressor. For the following constructs we also used a Tet ON system cloning plasmid, pCDNA 5/TO (Invitrogen).

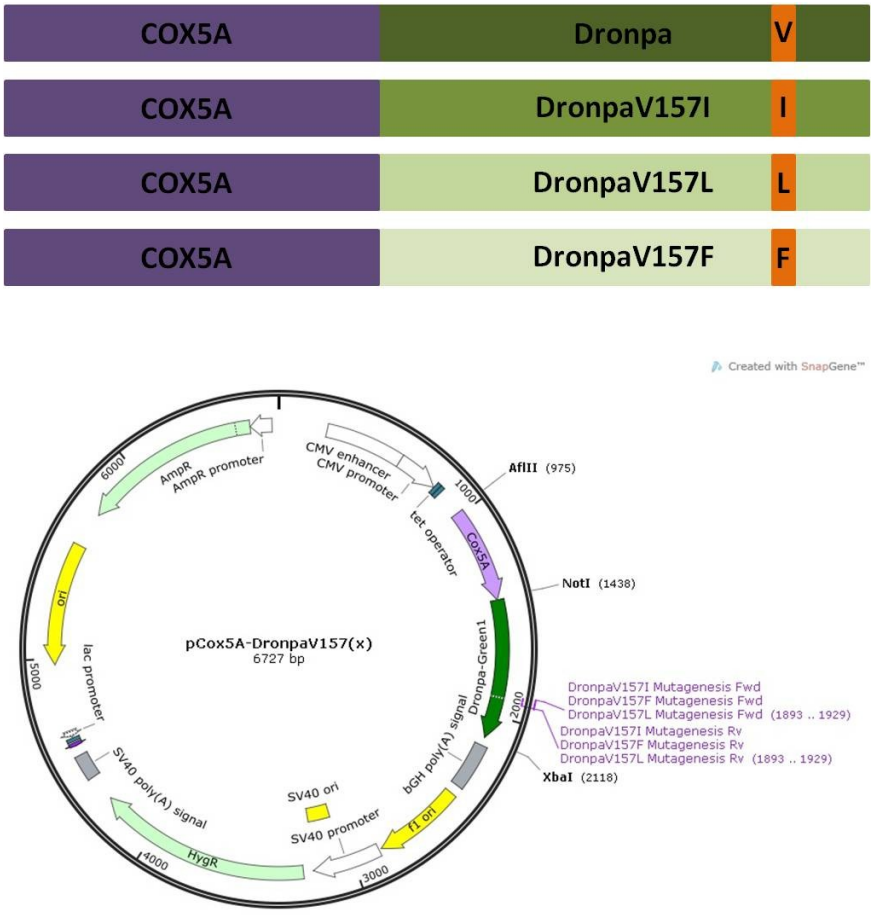

Figure 9: Genetic constructs and cloning map of inner mitochondria membrane localized DronpaV157X series. Dronpa was inserted into pcDNA5/TO with NotI and XbaI and *COX5A* with AflII and NotI. The valine at position 157 of Dronpa was exchanged for an isoleucine, a leucine, or a phenyalanine using site directed mutagenesis.

We began our two step cloning process by cloning Dronpa V157 (wt) into pCDNA 5/TO. We obtained the *COX5A* cDNA from Open Biosystems and cloned it to the N-terminus of Dronpa V157 (wt). We then took this wild type construct and mutated V157 to isoleucine, leucine, or phenylalanine using site directed mutagenesis. Plasmids were titled pCox5A-Dronpa, pCox5A-DronpaV157I, pCox5A-DronpaV157L, and pCox5A-DronpaV157F.

Expression and Imaging of DronpaV157X Series

In order to test expression and localization, EpH4 cells were plated in MatTek imaging plates as described previously. We transfected EpH4 cells with pCox5A-Dronpa using Lipofectamine as described previously. Cells were incubated overnight at 37°C. Since EpH4 cells do not contain the tetracycline repressor, the gene is under constitutive expression and is

therefore over expressed. We used the confocal microscope as described previously and labeled the mitochondria with MitoTracker Red CMXRos (Figure 10). Dronpa was activated by a 10 second 405 nm illuminatin via the mercury arc lamp. Cox5A-Dronpa showed clear co-localization with the MitoTracker Red CMXRos labeled mitochondria.

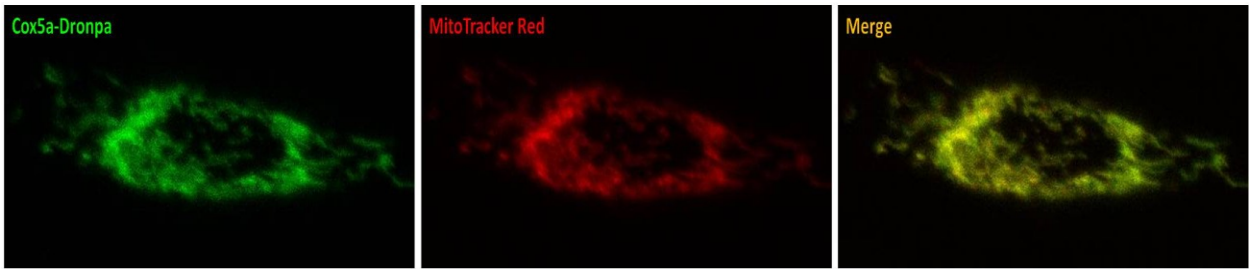

Figure 10: Dronpa fused to Cox5A localizes to the mitochondria. Dronpa was fused C-terminally to Cox5A and is shown in green. EpH4 cells were transfected with the construct and grown overnight. Mitochondria were labeled with MitoTracker Red CMXRos. Dronpa was activated with mercury arc lamp illumination at 405 nm. Resulting confocal images were overlaid directly using ImageJ.

In parallel we also built the mitochondrial membrane targeted genetic constructs, as described previously, with the DronpaV157X series and cloned them into pCMV Kan/Neo, creating pBCS1L(1-160)-Lk-DronpaV157X-6XHis and p6XHis-DronpaV157X-Lk-BclXl(201-233). In addition, we cloned the same constructs into pcDNA5/TO. This series of constructs were termed p(TO)BCS1L(1-160)-Lk-DronpaV157X-6XHis and p(TO)6XHis-DronpaV157X-Lk-BclXl(201-233) (Figure 11).

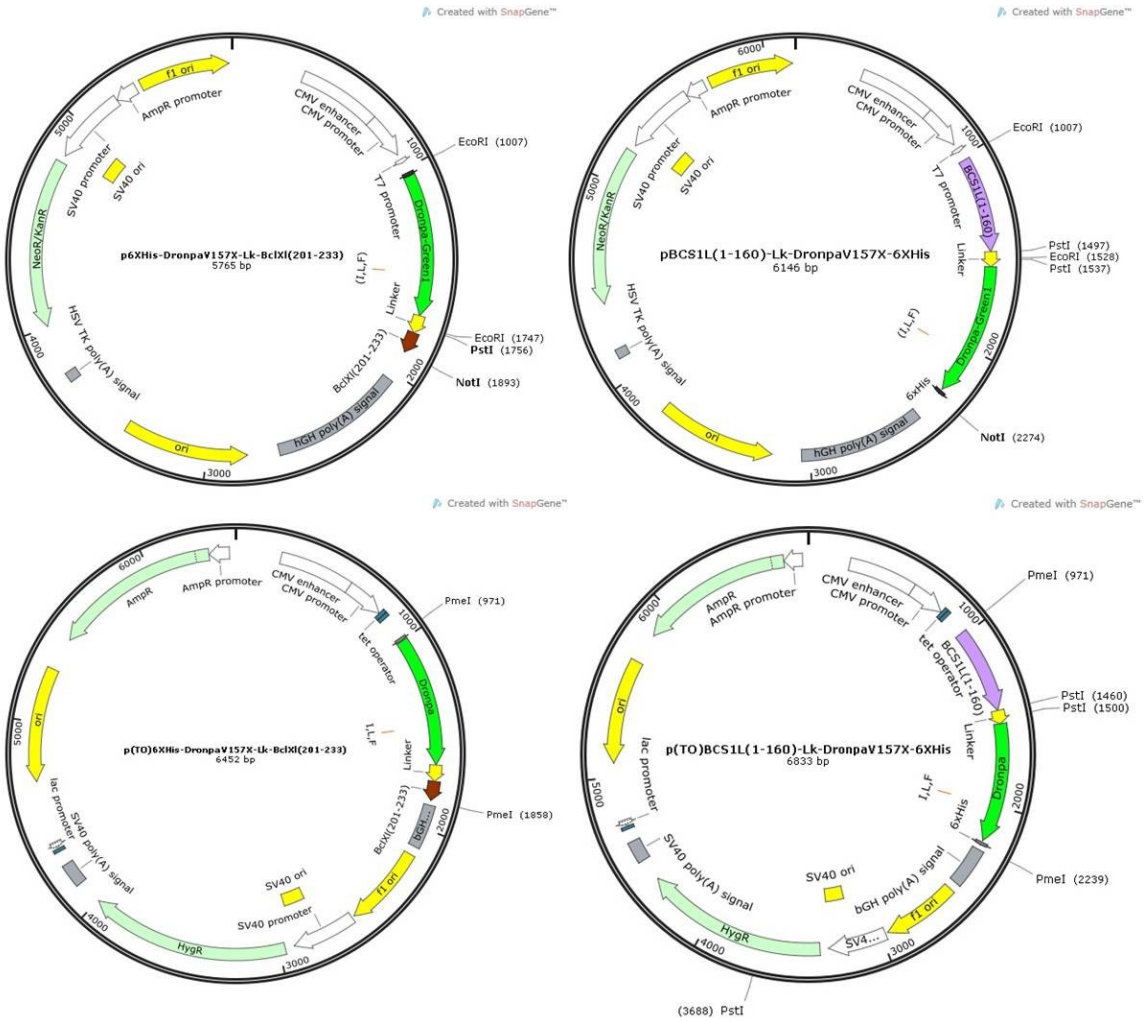

Figure 11: Cloning maps of mitochondria localized DronpaV157X series. 6XHis-DronpaV157X-Lk-BclXl(201-233) was inserted into pCMV Kan/Neo with EcoRI and NotI or into pcDNA5/TO with PmeI. BCS1L-Lk-DronpaV157X-6XHis was inserted into pCMV Kan/Neo using EcoRI and NotI or into pcDNA5/TO with PmeI.

Each of the p(TO)BCS1L(1-160)-Lk-DronpaV157X-6XHis and p(TO)6XHis-DronpaV157X-Lk-BclXl(201-233) constructs were transfected into EpH4 cells as described previously. Dronpa mutants V157I and V157L maintained fluorescence localized to the mitochondria (Figure 12). DronpaV157F showed no visible fluorescence. (Data not shown) Cells were not labeled with Mitotracker Red CMXRos as mitochondrial localization via the OMM and IMM targeting sequences had already been demonstrated and the DronpaV157X mutation would not affect said sequences.

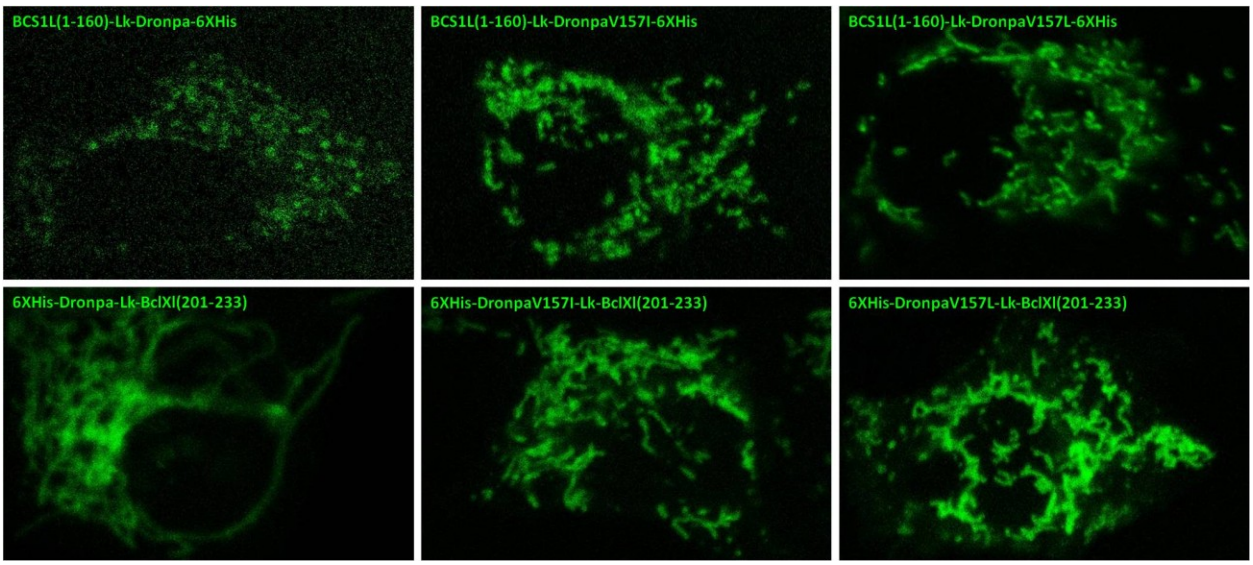

Figure 12: Dronpa mutants V157I and V157L maintain photoswitchable green fluorescence when activated by 405 nm and excited by 488 nm. EpH4 cells were transfected with p(TO)BCS1L(1-160)-Lk-DronpaV157X-6XHis or p(TO)6XHis-DronpaV157X-Lk-BclXl(201-233). Wild type Dronpa was used for comparison. Dronpa mutants with Phe substituted for Val showed no fluorescence and are not shown. Dronpa mutants with Ile or Leu substituted for Val were activated with arc lamp 405 nm illumination prior to excitation at 488 nm. Confocal images were analyzed in ImageJ.

Since the PALM microscope is more sensitive, we continued on with all four constructs to PALM imaging. For PALM imaging, EpH4 cells were plated on fibronectin coated #1.5 glass slides 24 hours prior to transfection. Cells were transfected with each of the four constructs with Lipofectamine as described previously and fed FBS coated 100 nm Au fiducial markers. Cells were incubated overnight at 37°C. Since mitochondrial localization had been confirmed for these constructs previously, cells were not labeled with MitoTrackers. Cells were rinsed with 1X PBS and fixed in 1% formalin. Cells were imaged using the PALM protocol for Dronpa as described previously, using activation by 405 nm (0.61 mW/mm^2) and excitation at 488 nm (0.54 W/mm^2). This experiment was repeated with T-Rex HeLa cells with some minor alterations. T-Rex HeLa cells were transfected with Clontech Xfect and, since the plasmid was under tetracycline repression, protein expression was activated with the addition of doxycycline (Dox), a tetracycline homologue. Tetracycline has been shown to affect mitochondrial morphology in higher concentrations. Doxycycline does not have the same affect and so is recommended for mitochondrial experiments using Tet ON/OFF systems. T-Rex HeLa cells were induced at 1 μg/mL Dox for 4 hours. Using the T-Rex HeLa cells allowed us to examine whether individual event separation could be improved if the protein expression itself were reduced.

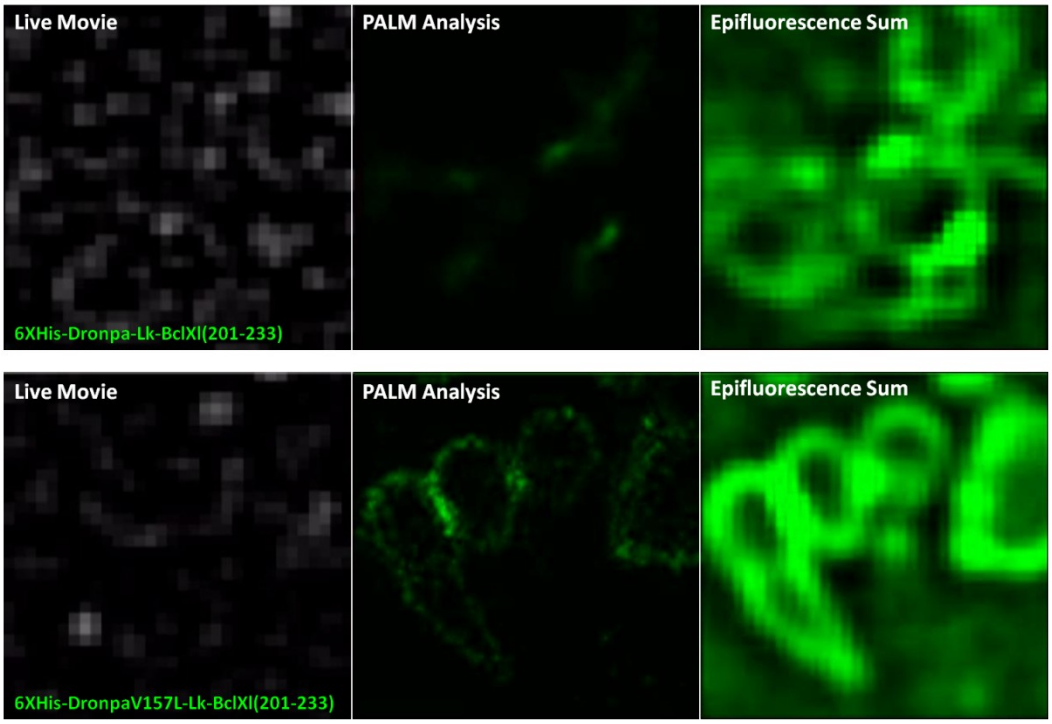

Figure 13: Movie screen captures of Cox5A-DronpaV157L show improved separation of fluorescent events as compared to Cox5A-Dronpa. EpH4 cells were transfected with pCox5A-DronpaV157X. Mitochondria were PALM imaged with 488 nm (0.54 W/mm^2) and 405 nm (0.61 mW/mm^2) and analyzed using a 6-fold threshold for peak to background and a 2200 threshold for the total photon count. XY drift was corrected with 100 nm Au fiducial markers. Each row of movie screen captures shows live PALM imaging of individual fluorescent events (*left*), the build of analyzed PALM figures (*center*), and the build of the same figures using the sum of their epifluorescence (*right*).

During imaging, Cox5A-Dronpa showed the same "shimmering" effect as was described previously. Cox5A-DronpaV157I showed improved separation of individual events and improved observed contrast over background. Cox5A-DronpaV157L showed an even greater improvement on the separation of individual events and observed contrast over background (Figure 13). Cox5A-DronpaV157F showed some minor dim fluorescence and switching. Because of the dimness of Cox5A-DronpaV157F, we determined that the bulkiness of the phenylalanine inhibited the fluorescence to such an extent that further investigation was not warranted. We analyzed the images using the previously described method and compared them to the previous images where we targeted mEos2 to the IMM. Only DronpaV157L resulted in a usable PALM image that clearly showed the IMM cristae structure (Figure 14). Over expression in EpH4 cells versus reduced protein expression via Dox induction in T-Rex HeLa cells had little effect on the quality of PALM imaging and post image analysis.

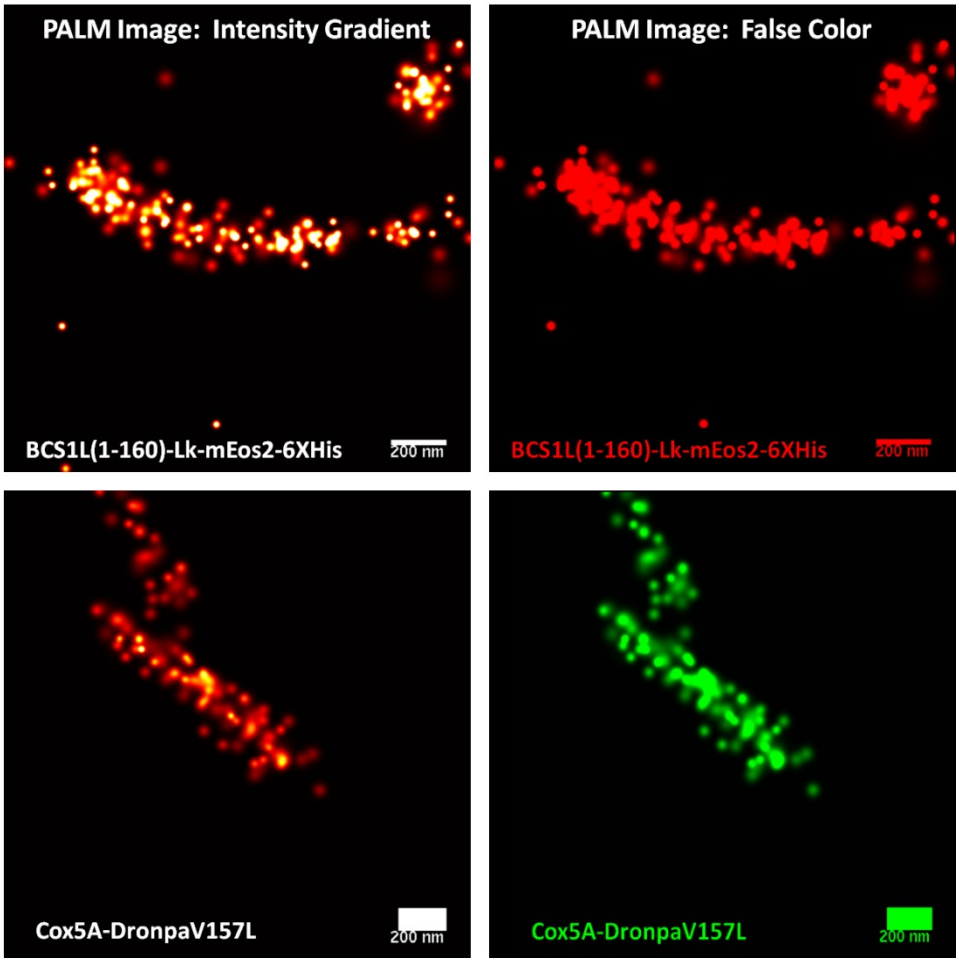

Figure 14: Dronpa mutant variant V157L allows for successful PALM imaging of single molecule green fluorescence. EpH4 cells were transfected with pCox5A-DronpaV157L and imaged via PALM. Individual fluorescent event thresholds were set at 6 and 2000 for peak to background and total photon count respectively for PALM analysis (*bottom row*). For comparison, EpH4 cells were transfected with pBCS1L(1-160)-Lk-mEos2-6XHis and PALM imaged as previously described (*top row*). Images were colored according to a fluorescence intensity gradient warm to hot (*left column*) or false color assigned by emission spectra (*right column*).

We demonstrated that DronpaV157L was a viable PA-FP in the green emission spectra for PALM imaging. The V157L mutation is a novel, previously uncharacterized, mutation of Dronpa; therefore, we set out to analyze the bulk spectroscopic properties and single molecule photophysics of DronpaV157L. We also analyzed Dronpa as our base of comparison and DronpaV157I for additional information on the effect of different amounts of steric hindrance at position 157. In addition, because DronpaV157L is a novel mutation, we renamed it rsKame. Dronpa was initially named for "dron" a Japanese ninja word for vanishing and PA for photoactivation.[153] rsKame is a combination of reversibly switchable (rs) and "kame", the Japanese word for turtle.

BULK AND SINGLE MOLECULE CHARACTERIZATION OF rsKAME, A NOVEL DRONPA MUTANT

Purification of Dronpa, DronpaV157I, and rsKame

To examine the spectral and photophysical properties of Dronpa, DronpaV157I, and rsKame, we first had to purify each protein. We began by cloning Dronpa, DronpaV157I, and rsKame into pJY00 using BamHI that allows for the addition of an N-terminal 6XHis tag and a C-terminal avidin tag (LGGGLNDIFEAQKIEWHE) in frame. These plasmids were termed p6XHis-Dronpa-Avi, p6XHis-DronpaV157I-Avi, and p6XHis-rsKame-Avi and can be maintained by selection with ampicillin (Figure 15). The 6XHis tag was added to allow for purification using a nickel coated sepharose column. The avidin tag was placed at the C terminus to allow for downstream applications. We used this particular sequence because it can be used in a biotinylation protocol based around BirA. BirA is an *E. coli* enzyme that will attach a biotin molecule to a particular enzyme in acetyl-CoA carboxylase. BirA has also been shown to attach biotin molecules to other specific amino acid sequences. The avidin tag is a consensus sequence such that proteins fused to the tag and expressed in BirA containing *E. coli* expression strains will be biotinylated in the presence of free biotin. AvB101 is one such strain. AvB101 contains a plasmid containing BirA and is maintained by selection with chloramphenicol. DNA constructs were transformed into DH5α *E. coli* cells and sequenced for correct coding sequences.

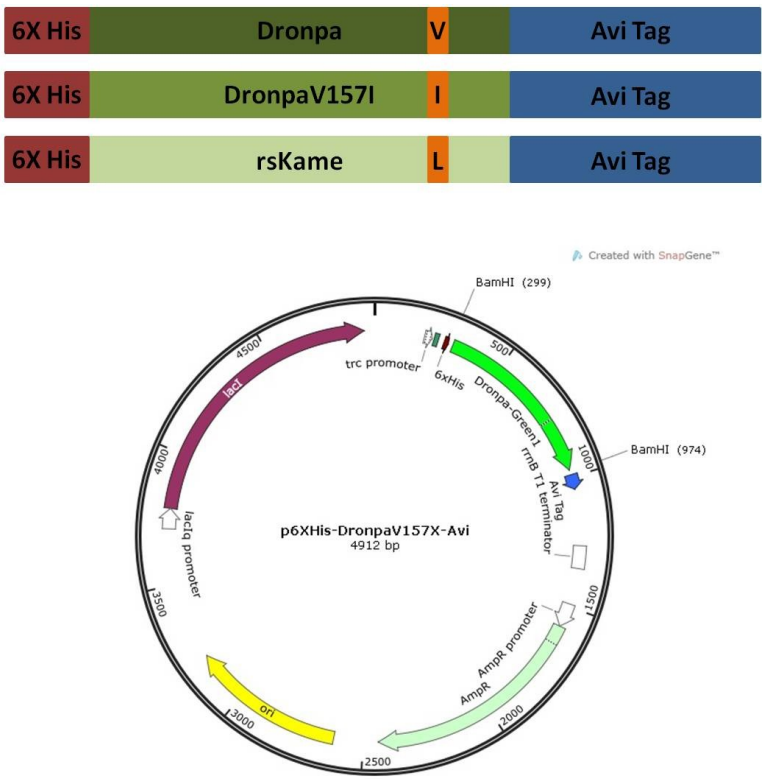

Figure 15: Genetic constructs and cloning map of Dronpa series (V, I, L) for purification. Each of the DronpaV157X mutant series was inserted into pJY00 bacterial expression vector with BamHI between an N-terminal 6XHis tag and a C-terminal avidin sequence. pJY00 has an IPTG inducible promoter.

In order to do both bulk spectral and single molecule photophysic characterization on the same purified protein sample, we transformed AvB101 *E. coli* cells with the constructs and plated them on Amp/Cam plates. Cells were inoculated overnight in 3 mL cultures grown at 37°C and then inoculated into 1 L cultures at a starting OD of 0.1. Cells were grown to an OD of 0.7 and induced with 1 μg/mL IPTG and 0.5 μM Biotin. Cells were grown for 12 hours at 37°C with agitation then pelleted and washed. Lysis was accomplished via sonication for five 20 second pulses with 1 minute intervals in lysis buffer (Table 5). Protein expression was confirmed with a polyacrylamide denaturing gel (SDS-PAGE). Cell lysate samples of either induced or uninduced were denatured with β-mercaptoethanol and heated prior to loading. A clear band at 30 kDa is shown on the induced lane. After transfer to a nitrocellulose membrane, protein samples were probed with αHis and Streptavidin antibodies conjugated to horse radish peroxidase. Horse radish peroxidase can cleave certain substrates to produce chemiluminescent compounds. All induced samples proved to be both His-tagged and biotinylated (Figure 16a). Significant bleed-through of expression was noted on the uninduced samples but, as expression of Dronpa, DronpaV157I, or rsKame is non-toxic to the cells, had no negative effects on purification.

A

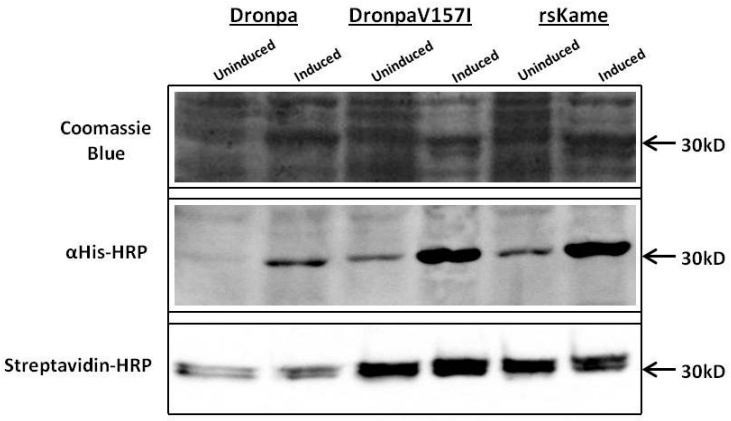
Dronpa
DronpaV157I
rsKame
Uninduced
Induced
Uninduced
Induced
Uninduced
Induced
Coomassie Blue
αHis-HRP
Streptavidin-HRP
30kD
30kD
30kD

B

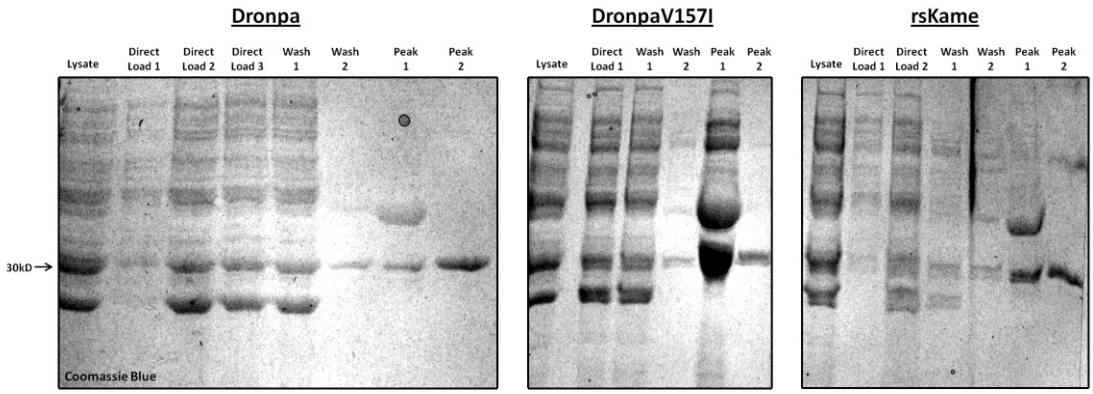
Dronpa
DronpaV157I
rsKame
Lysate
Direct Load 1
Direct Load 2
Direct Load 3
Wash 1
Wash 2
Peak 1
Peak 2
30kD
Coomassie Blue

C

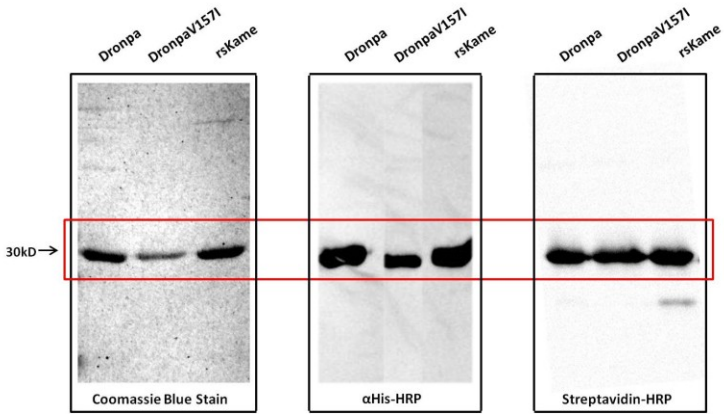
Dronpa
DronpaV157I
rsKame
30kD
Coomassie Blue Stain
αHis-HRP
Streptavidin-HRP

Figure 16: Expression and purification of DronpaV157X series. A) AvB101 *E. coli* cells transformed with p6XHis-DronpaV157X-Avi were induced and cultured with 1 μg/mL IPTG and 0.5 μM biotin for 12 hours prior to purification. Uninduced lanes were cultured with biotin but not IPTG. Samples were run on an SDS-PAGE gel and stained with Coomassie Blue for overall protein content or probed with αHis and Streptavidin-HRP conjugated antibodies. B) Cell lysate ("Lysate") of the induced AvB101 p6XHis-DronpaV157X-Avi cells was loaded on to a nickel column ("Direct Load1/2"). Unbound protein was washed away ("Wash1/2") with excess lysis buffer and eluted off the column with a gradient elution of increasing imidazole concentration in elution buffer in two peaks ("Peak 1/2"). Samples from each step were loaded onto a polyacrylimide denaturing gel and stained with Coomassie Blue showing increasing purity of the respective DronpaV157X protein sample. C) Purified samples of DronpaV157X from the second peak fractions were pooled and dialyzed to remove the imidazole. Samples of each purified protein were run on an SDS-PAGE gel and stained with Coomassie Blue for overall protein content or probed with αHis-HRP and Streptavidin-HRP conjugated antibodies. The samples showed high purity as well as robust biotinylation. A small degradation product was noted for rsKame when probed by Strepavidin-HRP post dialysis, but was not seen either with Coomassie Blue stain or αHis-HRP.

Purification of the cell lysates was accomplished based on established published affinity chromatography techniques on a Fast Protein Liquid Chromatography (FPLC) instrument.[130] Nickel coated sepharose bead columns (His-trap HP) were equilibriated with lysis buffer with 10 mM imidazole. The lysate was loaded onto the equilibriated column and unbound protein was washed off the column. The His tagged protein was eluted off using a gradient elution of increasing amounts of imidazole from 10 mM to 300 mM in elution buffer (Table 5). The protein eluted off the column in two peaks. The first peak contained high molecular weight contaminants. The second peak contained highly pure DronpaV157X protein. The fractions containing the second peak eluted off the His-trap HP columns were pooled and dialyzed in order to remove the imidazole. The samples were then aliquoted and snap frozen in liquid nitrogen. Samples were kept at -80ºC until use. SDS-PAGE was used to show the proteins that eluted off the column at each of the described steps, including dialysis (Figure 16b). Western blots of the samples were also probed with αHis-HRP and Streptavidin-HRP conjugated antibodies to confirm protein identity and successful biotinylation (Figure 16c). All isolated Dronpa and Dronpa mutants showed high purity and biotinylation.

Bulk Spectroscopy of Dronpa, DronpaV157I, and rsKame

Basic bulk spectroscopy is the core analysis of new fluorescent protein variants. The mutation position of Dronpa (V157X) is not part of the chromophore itself. However, the increasingly larger amino acid side chain of the mutants may interact directly with the chromophore or indirectly with the isomerization cascade. Therefore, we decided to examine the emission and excitation spectra, as well as determine the molar extinction coefficient, quantum yield, and brightness. We decided not to explore folding kinetics or pH dependency since our mutations are not amino acids involved in overall protein structure and are not charged.

Fluorescent proteins absorb large amounts of light at specific wavelengths. The absorbed light is used to excite electrons to higher energy levels. As the electrons fall back down to their ground state, photons are emitted as specific wavelengths. Three spectra can be obtained to characterize fluorescent proteins: excitation, emission, and absorption. Excitation spectra are obtained by bombarding the sample with a range of light wavelengths while holding the emission wavelength constant. The excitation spectrum is a measure of wavelengths that are able to be absorbed by the sample and result in emitted photons with a defined range of wavelengths. Emission spectra are obtained by bombarding the sample with a single constant wavelength and collecting the light emitted over a wide range of wavelengths. The emission spectrum is the plot of the distribution of photons emitted as a function of wavelength. Protein samples were loaded onto a fluorimeter at 1 μM concentration. Excitation spectra were taken by setting the emission wavelength at 525 nm and bombarding the sample with light from 350 nm to 530 nm through a 10 mm pathlength quartz cuvette. Emission spectra were taken by setting the excitation wavelength at 488 nm and collecting photons from 495 nm to 650 nm. The peaks of the spectral plots are the excitation and emission maxima (Figure 17b). Both spectra were taken in triplicate and averaged. Dronpa has a maximal excitation of 503 nm and a maximal emission of 515 nm. DronpaV157I has a maximal excitation of 504 nm and a maximal emission of 517 nm. rsKame has a maximal excitation of 503 nm and a maximal emission of 517 nm. The differences between Dronpa and the mutants are not significant.

A

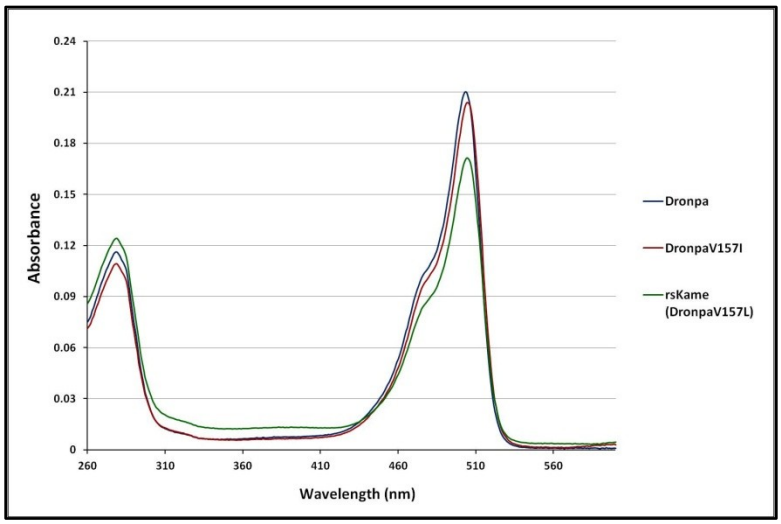

B

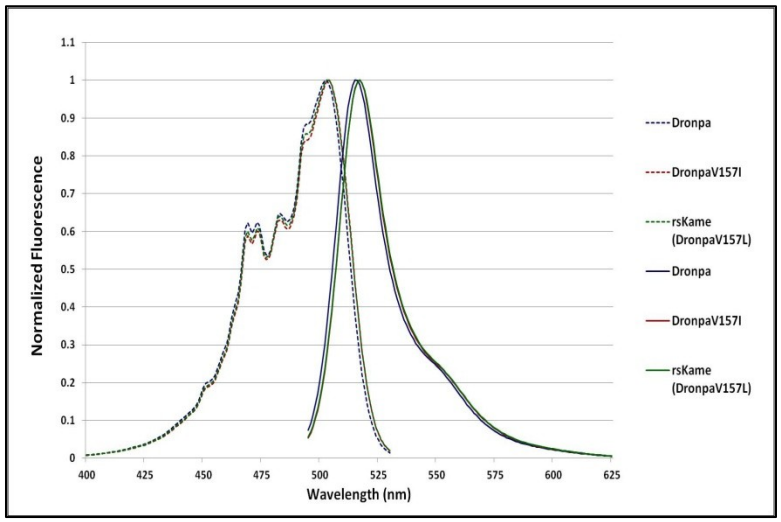

Figure 17: Absorbance, excitation, and emission spectra for DronpaV157X mutant series. A) The absorbance spectrum of each purified DronpaV157X protein sample was taken continuously from 260 nm to 600 nm in duplicate. The average absorbance at 278 nm was used to determine protein concentration. B) The excitation spectrum of each purified DronpaV157X protein sample was taken from 400 nm to 530 nm with an emission wavelength of 525 nm. The emission spectrum of each purified DronpaV157X protein sample was taken from 495 nm to 625 nm with 488 nm excitation.

In order to calculate the molar extinction coefficient (ε), and the quantum yield, the absorption spectra is necessary along with the emission spectra. The absorption spectrum is a measure of the absorption of specific wavelengths of light by a protein sample. Samples were loaded onto a spectrophotometer (Varian Cary 50 Bio UV/Visible) in a 10 mm quartz cuvette. Protein concentrations were determined within each individual spectrum by taking the absorbance of the sample at 278 nm. Spectra were taken in duplicate and averaged. Absorption spectra were taken continuously from 260 nm to 600 nm (Figure 17a). The published ε and quantum yield of Dronpa were used as the standards as were the experimentally obtained spectra. The molar extinction coefficients, quantum yields, and brightness of the Dronpa mutants were determined using the protocols from Stefan Jakobs group. (Personal communication)[141] Molar extinction coefficients were determined using the formula described below.

$$\varepsilon_{x} = (\text{Abs}_{X} / \text{Abs}_{\text{REFERENCE}}) * (\varepsilon_{\text{REFERENCE}})$$

The absorption spectra were first corrected by baseline subtraction and then normalized for protein concentration by dividing the corrected spectra by the absorbance at 278 nm. The maximal absorbance was then divided by the reference maximal absorbance of the reference protein ($\text{Abs}_{X} / \text{Abs}_{\text{REFERENCE}}$). This number is sample concentration dependent. We then multiplied by the published ε of the reference protein.[139] Quantum yield were calculated by using the formula described below.

$$QY_{X} = QY_{\text{REFERENCE}} * (\text{Integral}_{X} / \text{Integral}_{\text{REFERENCE}}) * (\text{Abs}_{\text{REFERENCE}} / \text{Abs}_{X})$$

We first integrated the total area under the curve of the emission spectra taken at the same excitation wavelength as the absorption spectra. Next we divided that by the integral of the reference protein ($\text{Integral}_{X} / \text{Integral}_{\text{REFERENCE}}$). We then divided the original measured absorbance of the reference protein by the original measured absorbance of the sample ($\text{Abs}_{\text{REFERENCE}} / \text{Abs}_{X}$). We multiplied these two parameters with the published quantum yield of the reference protein.[154] The brightness is determined by the below formula.

$$\text{Brightness} = ((QY_{X} * \varepsilon_{x})/(QY_{EGFP} * \varepsilon_{EGFP}))*100$$

To calculate the brightness, we multiplied the quantum yield of the sample and the molar extinction coefficient ($QY_{X} * \varepsilon_{x}$). Since brightness is generally compared to EGFP, we also multiplied the quantum yield of the sample and the molar extinction coefficient of EGFP ($QY_{EGFP} * \varepsilon_{EGFP}$). We divided the sample brightness by the EGFP brightness. In order to obtain the percentage of brightness as compared to EGFP, we multiplied by 100. The $\varepsilon_{\text{REFERENCE}}$ of Dronpa is 95,000 M^{-1} cm^{-1} and the $QY_{\text{REFERENCE}}$ is 0.85.[155] The $\varepsilon_{\text{REFERENCE}}$ of EGFP is 56,000 M^{-1} cm^{-1} and the $QY_{\text{REFERENCE}}$ is 0.60.[155] After calculations, the ε_{x} of DronpaV157I is 98,000 M^{-1} cm^{-1} and the $QY_{\text{REFERENCE}}$ is 0.88. The ε_{x} of rsKame is 72,000 M^{-1} cm^{-1} and the QY_{x} is 0.86. The brightness of Dronpa is 240. The brightness of DronpaV157I is 257. The brightness of rsKame is 184. These differences illustrate the effect of the mutations on the Dronpa chromophore. Though brightness is reduced for rsKame, the overall brightness is still sufficient for PALM imaging, as demonstrated previously (Table 1).

Table 1: Bulk spectroscopy of DronpaV157X mutant series

Fluorescent Protein	Excitation Maximum	Emission Maximum	ε M^{-1} cm^{-1}	Quantum Yield	Brightness
Dronpa	503nm	515nm	95,000	0.85	240
DronpaV157I	504nm	517nm	98,000	0.88	257
rsKame	503nm	517nm	72,000	0.86	184

Single Molecule Photophysics of Dronpa, DronpaV157I, and rsKame

The bulk data indicated a few minor changes in rsKame from Dronpa, but none that were significant other than the change in brightness. However, this alone could not account for the improved imaging observed with rsKame. Therefore we needed to examine rsKame at the single molecule level or, more simply, to examine individual rsKame proteins. The single molecule photophysical characterization protocol for fluorescent proteins that we used was developed in our lab by Jae Yen Shin and Sanghyuk Lee.[130] The basic protocol is briefly described below.

1. Stringently wash glass slides.
2. Expose ions on glass surface via silane treatment.
3. Passivate glass slides with m-polyethylene glycol (mPEG)/Biotin-polyethylene glycol (Bio-PEG).
4. Build an imaging chamber with epoxy.
5. Bind Bio-PEG with neutravidin.
6. Immobilize small amounts of biotin bound 100nm gold fiducial markers.
7. Immobilize purified biotinylated protein.
8. Wash thoroughly and take PALM data.

The most important variable, when examining single molecule photophysics, is background. Any stray bit of dust or other marginally fluorescent or reflective molecule can be mistaken for an actual fluorescent molecule and can introduce a substantial amount of error to our final calculations. We prevented this by using a stringent cleaning protocol for the glass slides. Glass slides (#1.5) were separated in a rack in a clean glass beaker and rinsed with double distilled filtered H_2O (ddH_2O) and reagent grade acetone. The slides were sonicated in reagent grade acetone and then washed and sonicated in reagent grade 200-proof ethanol. Glass slides were then boiled in 1M KOH. Afterwards the slides were cooled and rinsed in ddH_2O. Next, highly corrosive piranha solution (H_2O_2:H_2SO_4) was added to the slides and the reaction allowed to proceed. Slides were rinsed in ddH_2O and reagent grade acetone. It was critical to have clean reagents and to use the same tweezers to manipulate the slides and slide holders. It was also important to keep the tweezers clean by never allowing them to touch outside surfaces. Instead the tweezers were held in a sterile plastic conical between uses.

In order to coat the glass slides with mPEG, the glass was silanized with 3-aminopropyltriethoxysilane. This left a "sticky" surface of amines for the polyethylene glycol (PEG) to bind to. A solution of m-polyethylene glycol/biotin-polyethylene glycol (mPEG/Bio-PEG) dissolved in 0.1 M sodium carbonate was added. Small amounts of Bio-PEG were

included with the mPEG solution (1:9 w/w ratios). This small amount ensures that the Bio-PEG molecules will be spatially distant from each other, which is critical for downstream applications. The PEG-ylated surface is passivated and will not bind molecules. The Bio-PEG can be bound with neutravidin and then can bind other biotinylated molecules. A secondary critical factor for making ultra clean PEG-ylated slides was using new mPEG/Bio-PEG. mPEG and Bio-PEG will degrade over time. The degraded mPEG/Bio-PEG has a background that shows up in the green emission channel when illuminated by 488 nm laser. The slides were then washed and stored in ddH_2O. Slides can be stored for up to two months in ddH_2O.

Ultraclean PEG-ylated slides were prepared for PALM data accumulation by first drying with N_2 gas and creating a well with epoxy. As before the slides were only handled with the clean tweezers from the glass cleaning step. After the epoxy dried, the bottom of the well was coated with neutravidin diluted in 0.2 μm filtered buffer to 10 μg/mL in single molecule imaging buffer (150 mM Tris pH 7.4, 50 mM NaCl). The neutravidin acted as a binding partner linking the Bio-PEG to other biotinylated molecules (Figure 18). Excess neutravidin was washed clear with buffer. Small amounts (1:50,000 dilution of OD 50) of biotin coated 100 nm Au particles were immobilized on the glass surface. Excess gold was washed away with buffer. Finally 0.1 nM of purified protein was immobilized on the surface, ensuring that single molecules are at least 300 nm apart. Excess protein was washed away with buffer and the slide was loaded in a slide holder for PALM imaging.

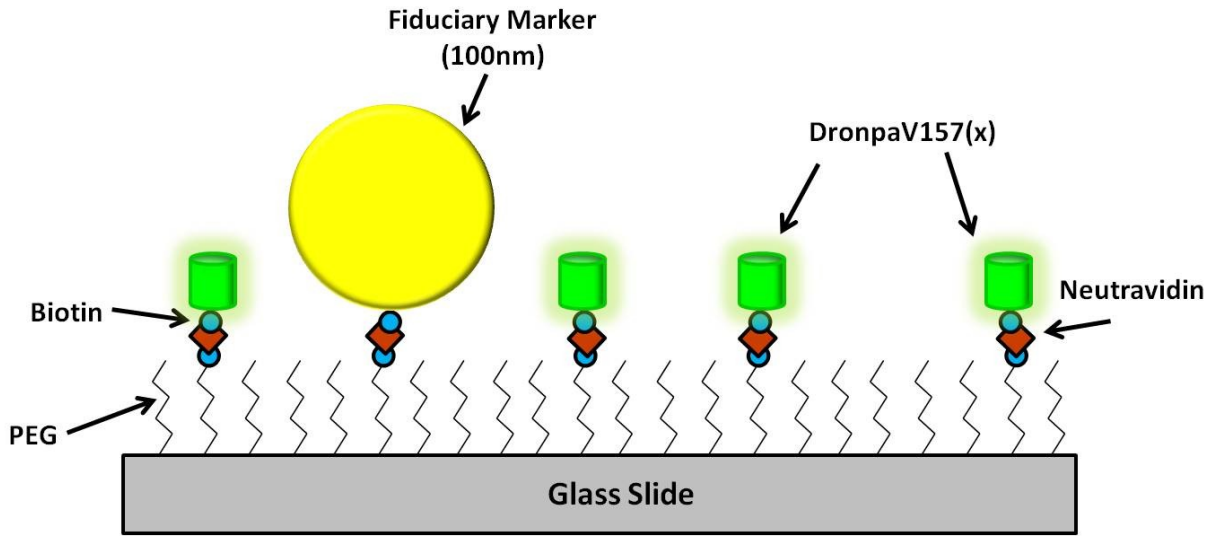

Figure 18: Diagram of slide preparation for examination single molecule photophysics of DronpaV157X mutant series. Ultra clean glass slides were predominantly PEG-ylated with small amounts of biotin-PEG. Slides were treated with neutravidin (10 μg/mL) and biotinylated 100 nm fiducial markers (1:50,000, OD 50) before 0.1 nm of purified protein was immobilized.

Single molecule data was taken on the PALM microscopy under several different conditions (Table 2). A single sample illuminating laser angle for TIRF was set for all conditions and samples. The imaging method for all samples was kept identical. After the focal plane and sample illuminating laser angle were set at the beginning of the experiment, a new field of view was chosen. The camera was turned on immediately prior to turning on the lasers. The excitation laser was turned on immediately afterwards. Three seconds after exposing the sample to the excitation laser, the activation laser was turned on. The reasons for this delay were to photobleach any background molecules and reduce added background error. PALM data was collected with a 525 nm emission filter (range 25 nm) until the entire field of view was bleached. The experiment was repeated eight times per sample + condition combination.

Table 2: Single molecule experiment parameters

Condition	Sample	488 nm laser power density (W/mm^2)	405 nm laser power density (mW/mm^2)
1	Dronpa	0.32	0.00
2	Dronpa	0.32	0.61
3	Dronpa	0.32	1.56
4	Dronpa	0.32	3.46
5	Dronpa	0.32	7.28
6	Dronpa	0.54	0.00
7	Dronpa	0.54	0.61
8	Dronpa	0.54	1.56
9	Dronpa	0.54	3.46
10	Dronpa	0.54	7.28
11	Dronpa	5.87	0.00
12	Dronpa	5.87	0.61
13	Dronpa	5.87	1.56
14	Dronpa	5.87	3.46
15	Dronpa	5.87	7.28
16	DronpaV157I	0.32	0.00
17	DronpaV157I	0.32	0.61
18	DronpaV157I	0.32	1.56
19	DronpaV157I	0.32	3.46
20	DronpaV157I	0.32	7.28
21	DronpaV157I	0.54	0.00
22	DronpaV157I	0.54	0.61
23	DronpaV157I	0.54	1.56
24	DronpaV157I	0.54	3.46
25	DronpaV157I	0.54	7.28
26	DronpaV157I	5.87	0.00
27	DronpaV157I	5.87	0.61
28	DronpaV157I	5.87	1.56
29	DronpaV157I	5.87	3.46
30	DronpaV157I	5.87	7.28
31	rsKame	0.32	0.00
32	rsKame	0.32	0.61
33	rsKame	0.32	1.56
34	rsKame	0.32	3.46
35	rsKame	0.32	7.28
36	rsKame	0.54	0.00
37	rsKame	0.54	0.61
38	rsKame	0.54	1.56
39	rsKame	0.54	3.46
40	rsKame	0.54	7.28
41	rsKame	5.87	0.00
42	rsKame	5.87	0.61
43	rsKame	5.87	1.56
44	rsKame	5.87	3.46
45	rsKame	5.87	7.28

PALM images were analyzed using the threshold levels of 6 (peak to background) and 2000 (total photon count) for PALM analysis to select for fluorescent molecules. The first 100 frames of each image were discarded to remove photobleached background from the analysis. For each image a region of interest (ROI) was drawn in the most evenly illuminated area of the entire frame. The ROI was 256 x 256 pixels or 27 μm x 27 μm. The same ROI was used for all images. We confirmed that all single molecules are at least 300 nm apart. The data for all eight images for each condition were combined and plotted. (Appendix A: Table 6)

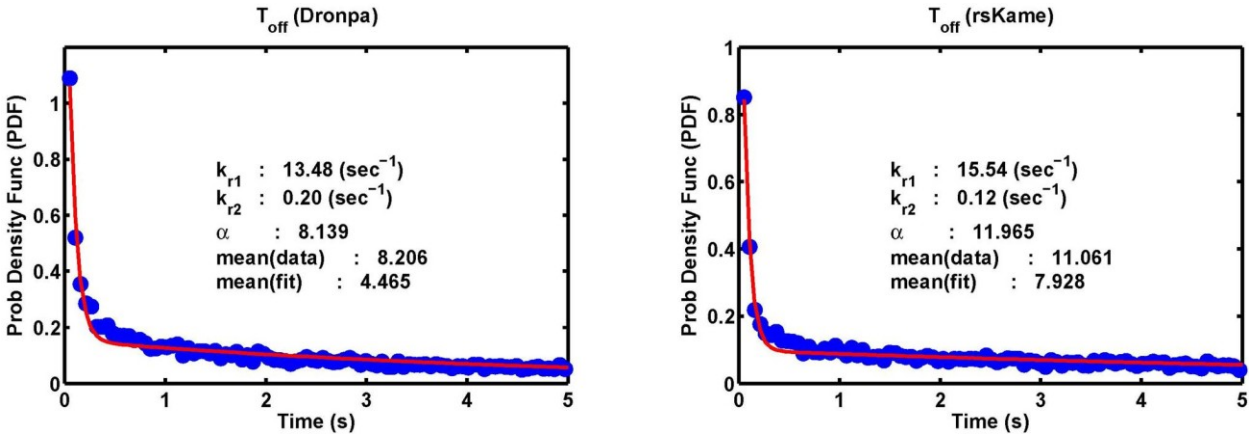

Figure 19: Sample T_{OFF} probability distribution fit with a double exponential. The isomerization of the chromophore from trans to cis is controlled by two photoactivation (recovery) kinetic rate constants, k_{r1} and k_{r2}. The fast photoactivation rate constant is k_{r1} and the slow recovery rate constant is k_{r2}. The ratio of the populations with the trans to cis switching rate of k_{r2} versus k_{r1} is denoted as α. (488 nm = 0.54 W/mm^2, 405 nm = 0 mW/mm^2)

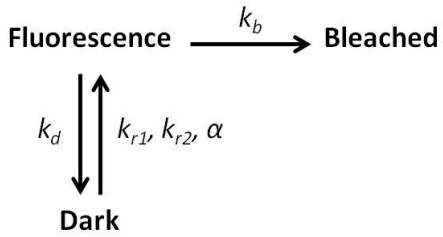

Figure 20: DronpaV157X mutant series proposed kinetic model fit with a double exponential decay for the recovery rate. Proposed kinetic model shows three possible states for a single DronpaV157X protein. DronpaV157X can be in its dark state, fluorescent state, or photobleached state. The recovery rates were fit to a double exponential decay.

We wanted to understand the effect of increased steric hindrance around the Dronpa chromophore. This necessitates a definitive kinetic model for the photoswitching of Dronpa. We propose a kinetic model where the Dronpa molecule can exist in three states: the dark state, the fluorescent state, or the photobleached state. Between the fluorescent and dark states the Dronpa chromophore undergoes a cis to trans or trans to cis isomerization. Our kinetic model is validated by quantifying three different variables of the single Dronpa molecule emission traces. We measured the number of times a single molecule photoswitches (N_{Blink}), the time spent in the fluorescent state (T_{ON}), and the time spent in the dark state (T_{OFF}). For the moment, we will discuss the analysis of T_{OFF}, then return to T_{ON} and N_{Blink} to validate our model.

The T_{OFF} is described by several interdependent fluorescence recovery rates of varying degrees of contribution. In a double exponential decay fit, two different rate constants (k_{r1} and k_{r2}) make up the overall rate of switching from trans to cis, or from the dark state to the fluorescing state, and is described by $p(t) = (k_{r1}e^{-k_{r1}t} + \alpha k_{r2}e^{-k_{r2}t})/(1 + \alpha)$ (Figure 19). The ratio of the populations with the trans (OFF) to cis (ON) switching rate k_{r2} versus k_{r1} is called α (Figure 20).

However, if we take a deeper look at the T_{OFF} data of Dronpa and rsKame, we note that the data is better fit by a triple exponential decay than by a double exponential decay (Figure 21). A triple exponential decay fit would suggest that Dronpa and/or rsKame actually have three rate constants (k_{r1}, k_{r2}, and k_{r3}). The ratio of the populations with the trans to cis switching rate k_{r3} versus k_{r2} is termed β and α for k_{r2} versus k_{r1}. This fit is described by $p(t) = (k_{r1}e^{-k_{r1}t} + \alpha k_{r2}e^{-k_{r2}t} + \beta k_{r3}e^{-k_{r3}t})/(1 + \alpha + \beta)$. This would suggest that the switching model of the chromophores of Dronpa and rsKame has several intermediate steps during trans to cis isomerization (Figure 22).

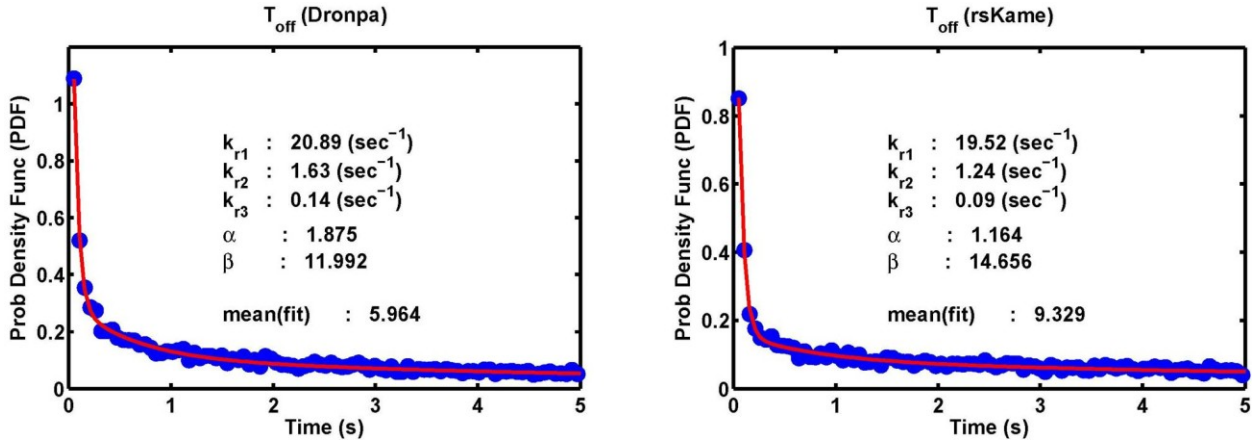

Figure 21: Sample T_{OFF} probability distribution fit with a triple exponential decay. The isomerization of the chromophore from trans to cis is controlled by potentially three photoactivation (recovery) kinetic rate constants: k_{r1}, k_{r2}, and k_{r3}. Under the triple exponential model, the fast photoactivation rate constant is still k_{r1} but now there are two slow recovery rate constants: k_{r2} and k_{r3}. The ratio of the populations with the trans to cis switching rate of k_{r2} versus k_{r1} is denoted as α and k_{r3} versus k_{r2} as β. (488 nm = 0.54 W/mm^2, 405 nm = 0 mW/mm^2)

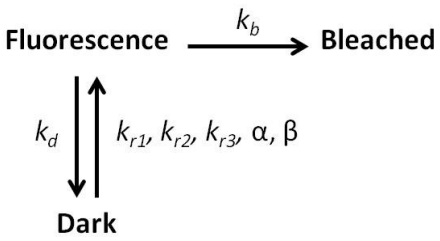

Figure 22: DronpaV157X mutant series proposed kinetic model fit with a triple exponential decay for the recovery rate. Proposed kinetic model shows three possible states for a single DronpaV157X protein. DronpaV157X can be in its dark state, fluorescent state, or photobleached state. The recovery rates were fit to a triple exponential decay.

The probability distributions of N_{Blink}, T_{ON}, and T_{OFF} support our second proposed kinetic model with three interdependent fluorescence recovery rates for Dronpa, DronpaV157I, and rsKame (Figure 23). N_{Blink} is the measure of the number of times chromophore switches from the dark to fluorescent states prior to photobleaching. The N_{Blink} probability distributions are well fit with geometric distributions described by $k_d/(k_d + k_b)$. The T_{ON} is the measure of the time spent in the cis isomerization or fluorescent state. The T_{ON} distributions are well fit with a single exponential decay described by $(k_d + k_b)$. The T_{OFF} is a measure of the time spent in the trans isomerization or the dark state and, as described previously, is better fit with a triple exponential decay and described by $p(t) = (k_{r1}e^{-k_{r1}t} + \alpha k_{r2}e^{-k_{r2}t} + \beta k_{r3}e^{-k_{r3}t})/(1 + \alpha + \beta)$. Using N_{Blink} and T_{ON}, we can determine the k_d and k_b for each fluorescent protein and each dual illumination condition. These random variables, N_{Blink}, T_{ON}, and T_{OFF}, and the fits of their probability distributions were consistent for wild type Dronpa as well as the two mutant variants, DronpaV157I and DronpaV157L, demonstrating the validity of the second proposed kinetic model (Figure 23).

The kinetic rates demonstrated several important facets of Dronpa and the mutants that were heretofore unknown and explained both the difficulties we faced with Dronpa and the success of rsKame. The rates for DronpaV157I also illustrated the same properties as rsKame but to a lesser degree of significance. Because we used only rsKame for later experiments, we will discuss only the kinetic rates for Dronpa and rsKame to examine the effects of increased steric hinderance around the chromophore and varying laser power densities.

A comparison of the T_{ON} between Dronpa and rsKame showed no significant difference at any given combination of 488 nm and 405 nm laser power densities, demonstrating that the T_{ON} was not affected by the increased steric hindrance of the leucine side chain. The T_{ON} of both Dronpa and rsKame was not affected by the power density of the 405 nm activation laser. The T_{ON} of both fluorescent proteins was significantly decreased by an increased 488 nm excitation laser power density. T_{ON} is influenced by both the k_d and k_b. Either or both could be altering the T_{ON}. The N_{Blink} was significantly decreased by increased 488 nm laser power density for both Dronpa and rsKame and was affected by the increased steric hindrance of rsKame but not significantly. Since both T_{ON} and N_{Blink} were affected by an increase in 488 nm laser power density, we examined the k_b and k_d to determine which rate constant is affected (Figure 24). The

k_d was not significantly changed by increased steric hindrance about the chromophore, or differences in the 488 nm or 405 nm laser power densities. The k_b was significantly increased with increased 488 nm laser power densities but unaffected by increasing 405 nm laser power densities or increased steric hindrance about the chromophore. This is as expected considering 488 nm is the excitation wavelength. The lack of effect on the k_d by the 488 nm and 405 nm laser power densities indicates that neither illumination plays an active role in driving the chromophore from the cis (ON) to the trans (OFF) conformation. Therefore, the chromophore must either spontaneously "relax" from the cis to the trans conformation or another unknown variable is driving the transition.

The T_{OFF} of Dronpa and rsKame are significantly altered by all three variables, the 405 nm laser power density, the 488 nm laser power density, and the increased steric hindrance of the leucine as position 157. The overall T_{OFF} of both proteins significantly decreases as the 405 nm laser power density increases. The increased steric hindrance of rsKame significantly increases the T_{OFF} and is most pronounced below 2 mW/mm^2 of 405nm laser power density. The T_{OFF} of both fluorescent proteins is significantly decreased by increased 488 nm. The T_{OFF} of rsKame is significantly greater, by 50% or more, than Dronpa, even at increased 488 nm laser power densities. Cumulative probability distributions of Dronpa and rsKame at various 488 nm and 405 nm laser power densities further demonstrate the effects of each illumination on T_{OFF}. We also noted that both Dronpa and rsKame could be activated by illumination with the 488 nm wavelength in the absence of 405 nm illumination. The cumulative probability distributions also demonstrate that increased steric hindrance about the chromophore will reduce the activation effect of 488 nm to different degrees (Figure 25). The interdependence of the three recovery rates may in part be due to the co-activation of the chromophore's trans to cis isomerization by both 488 nm and 405 nm illumination.

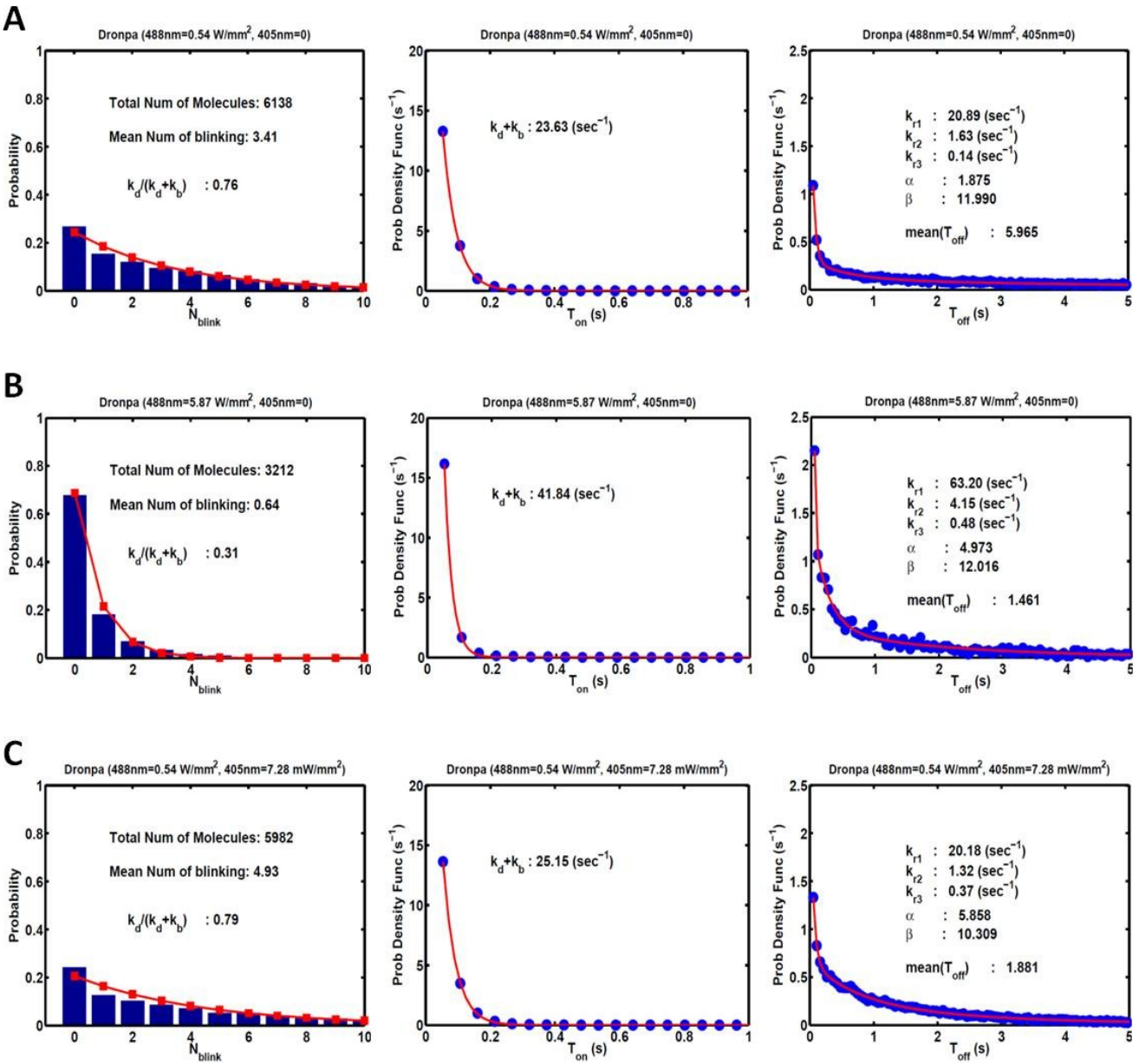
A
Dronpa (488nm=0.54 W/mm², 405nm=0)
Total Num of Molecules: 6138
Mean Num of blinking: 3.41
kd/(kd+kb) : 0.76
Probability
Nblink
kd+kb : 23.63 (sec⁻¹)
Prob Density Func (s⁻¹)
Ton (s)
kr1 : 20.89 (sec⁻¹)
kr2 : 1.63 (sec⁻¹)
kr3 : 0.14 (sec⁻¹)
α : 1.875
β : 11.990
mean(Toff) : 5.965
Toff (s)
B
Dronpa (488nm=5.87 W/mm², 405nm=0)
Total Num of Molecules: 3212
Mean Num of blinking: 0.64
kd/(kd+kb) : 0.31
kd+kb : 41.84 (sec⁻¹)
kr1 : 63.20 (sec⁻¹)
kr2 : 4.15 (sec⁻¹)
kr3 : 0.48 (sec⁻¹)
α : 4.973
β : 12.016
mean(Toff) : 1.461
C
Dronpa (488nm=0.54 W/mm², 405nm=7.28 mW/mm²)
Total Num of Molecules: 5982
Mean Num of blinking: 4.93
kd/(kd+kb) : 0.79
kd+kb : 25.15 (sec⁻¹)
kr1 : 20.18 (sec⁻¹)
kr2 : 1.32 (sec⁻¹)
kr3 : 0.37 (sec⁻¹)
α : 5.858
β : 10.309
mean(Toff) : 1.881

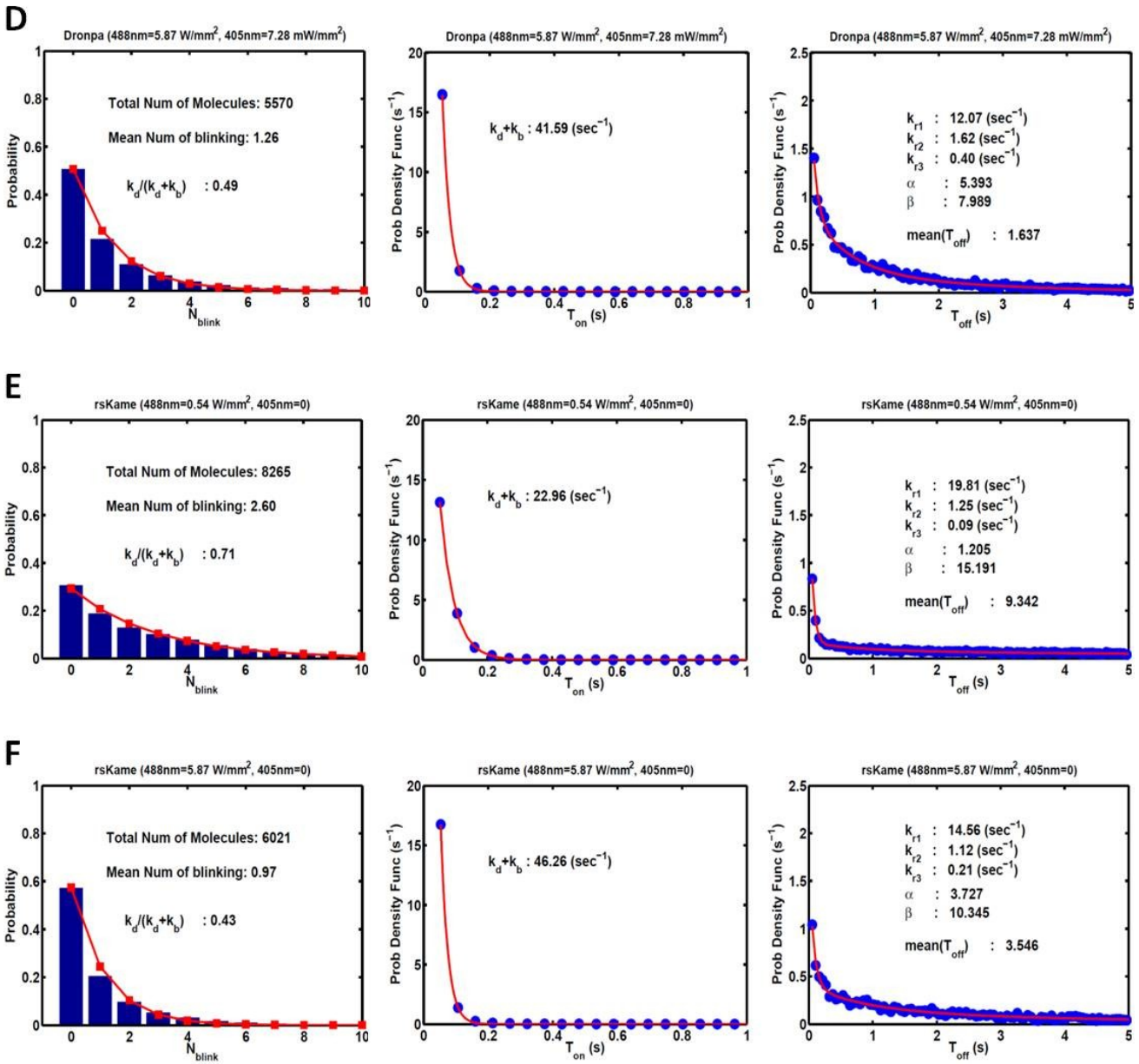
D
Dronpa (488nm=5.87 W/mm², 405nm=7.28 mW/mm²)
Total Num of Molecules: 5570
Mean Num of blinking: 1.26
k_d/(k_d+k_b) : 0.49
Probability
N_blink
k_d+k_b : 41.59 (sec^-1)
Prob Density Func (s^-1)
T_on (s)
k_r1 : 12.07 (sec^-1)
k_r2 : 1.62 (sec^-1)
k_r3 : 0.40 (sec^-1)
α : 5.393
β : 7.989
mean(T_off) : 1.637
T_off (s)
E
rsKame (488nm=0.54 W/mm², 405nm=0)
Total Num of Molecules: 8265
Mean Num of blinking: 2.60
k_d/(k_d+k_b) : 0.71
k_d+k_b : 22.96 (sec^-1)
k_r1 : 19.81 (sec^-1)
k_r2 : 1.25 (sec^-1)
k_r3 : 0.09 (sec^-1)
α : 1.205
β : 15.191
mean(T_off) : 9.342
F
rsKame (488nm=5.87 W/mm², 405nm=0)
Total Num of Molecules: 6021
Mean Num of blinking: 0.97
k_d/(k_d+k_b) : 0.43
k_d+k_b : 46.26 (sec^-1)
k_r1 : 14.56 (sec^-1)
k_r2 : 1.12 (sec^-1)
k_r3 : 0.21 (sec^-1)
α : 3.727
β : 10.345
mean(T_off) : 3.546

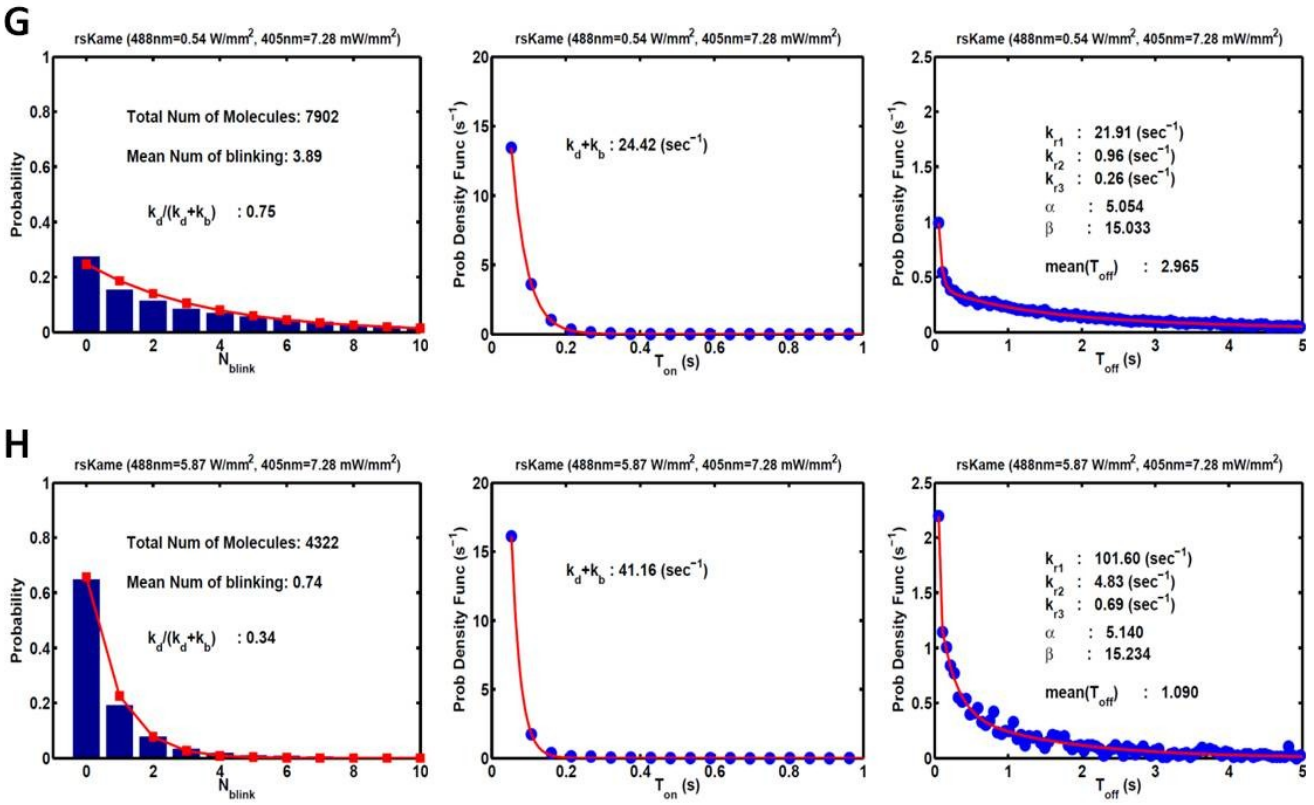

Figure 23: Quantification of the isomerization and photobleaching rates of Dronpa and rsKame. Each row contains three probability distributions (N_{Blink}, T_{ON}, T_{OFF}) describing three measured variables used to determine the kinetic rates. Each row also represents a different set of imaging conditions and/or protein sample. For all conditions, N_{Blink} is fit well by a geometric distribution. T_{ON} is fit well by a single exponential decay. T_{OFF} is better fit by a triple exponential decay. A) Dronpa illuminated with 488 nm (0.54 W/mm^2) and 405 nm (0 mW/mm^2). B) Dronpa illuminated with 488 nm (5.87 W/mm^2) and 405 nm (0 mW/mm^2). C) Dronpa illuminated with 488 nm (0.54 W/mm^2) and 405 nm (7.28 mW/mm^2). D) Dronpa illuminated with 488 nm (5.87 W/mm^2) and 405 nm (7.28 mW/mm^2). E) rsKame illuminated with 488 nm (0.54 W/mm^2) and 405 nm (0 mW/mm^2). F) rsKame illuminated with 488 nm (5.87 W/mm^2) and 405 nm (0 mW/mm^2). G) rsKame illuminated with 488 nm (0.54 W/mm^2) and 405 nm (7.28 mW/mm^2). H) rsKame illuminated with 488 nm (5.87 W/mm^2) and 405 nm (7.28 mW/mm^2).

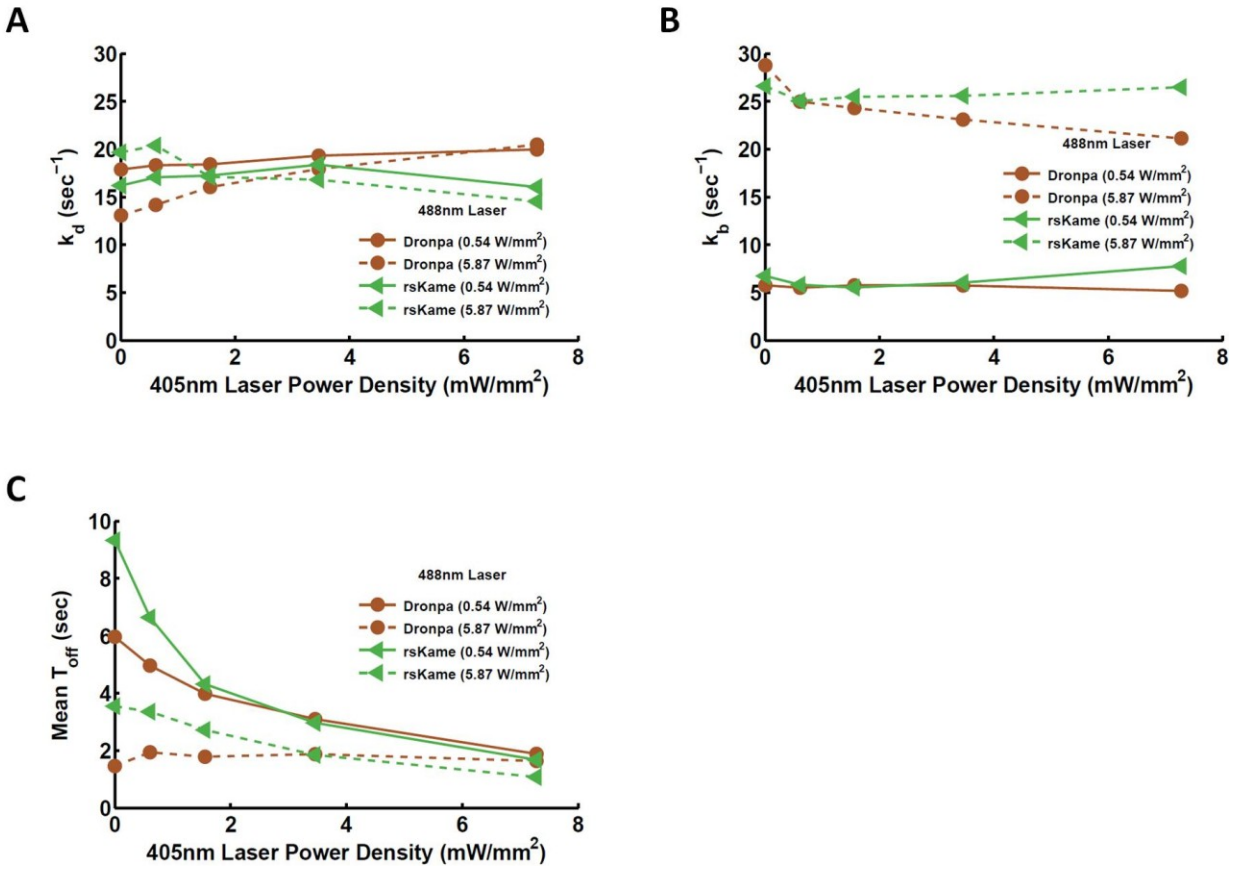

Figure 24: Summary and comparison of isomerization to the dark state, photobleaching, and recovery rates between rsKame and Dronpa. Single molecule samples were excited with either 5.87 W/mm^2 (dotted line) or 0.54 W/mm^2 (solid line) 488 nm laser power and activated over a range of 405 nm laser power densities (0.0-8.0 mW/mm^2). A) The k_d is a measure of the rate at which the Dronpa/rsKame chromophore isomerizes from the cis to the trans state (ON to OFF). The k_d is relatively unaffected by changes in 488 nm and 405 nm laser power densities and the increased steric hindrance around the chromophore between Dronpa and rsKame B) The k_b is a measure of the rate at which Dronpa/rsKame is photobleached. The k_b is not significantly affected by increased 405 nm laser power density or increased steric hindrance between Dronpa and rsKame. The k_b is significantly increased with increased 488 nm laser power density. C) The T_{OFF} is a measure of the time spent in the dark state and its probability distribution is described by three intertwined recovery rate constants. The mean T_{OFF} was significantly increased with increased steric hindrance around the rsKame chromophore and significantly decreased with increasing 488 nm excitation and 405 nm activation laser power densities. The difference is most pronounced below 405 nm activation laser power density of 2.0 mW/mm^2. Most importantly, significant activation of the Dronpa and rsKame chromophores was noted in the absence of the 405 nm laser, demonstrating that illumination with 488 nm can both excite and activate the Dronpa and rsKame chromophores.

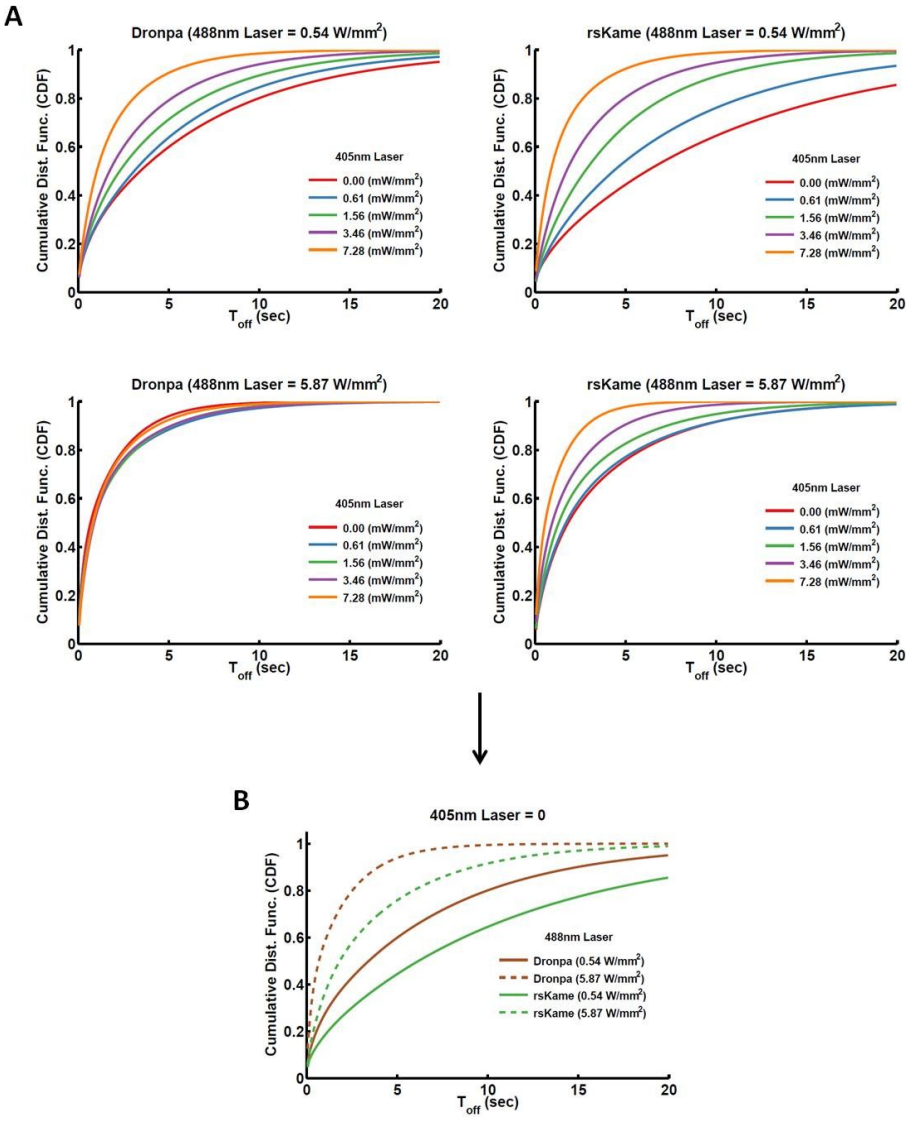

Figure 25: Cumulative probability distributions for T_{OFF} demonstrate photoactivation by 488 nm illumination for both Dronpa and rsKame. The cumulative probability distributions result from measured recovery rates across 405 nm laser power densities ranging from 0-8 mW/mm^2. A) Distributions were obtained for four excitation conditions: Dronpa [488 nm (0.54 W/mm^2)], Dronpa [488 nm (5.87 W/mm^2)], rsKame [488 nm (0.54 W/mm^2)], rsKame [488 nm (5.87 W/mm^2)]. The distributions show an increased probability of shorter T_{OFF}s with increasing 488 nm and 405 nm laser power densities. The values of T_{OFF} are increased with the increased steric hindrance between Dronpa and rsKame. B) Cumulative probability distributions of Dronpa and rsKame at 405 nm (0 mW/mm^2) demonstrate photoactivation of the two fluorescent proteins even in the absence of the purported 405 nm photoactivation light but in the presence of 488 nm excitation light. The 488 nm-only-induced photoactivation effect is reduced in rsKame when compared to Dronpa. The effect is also reduced with decreased 488 nm laser power density (0.54 W/mm^2 vs. 5.87 W/mm^2).

Two important observations were made from the single molecule data. The increased steric hindrance of the leucine at position 157 in rsKame resulted in an increased T_{OFF}. A protein with an increased T_{OFF} will spend more time in the dark state, effectively "slowing" the trans to cis switching of the chromophore. In addition, we were able to collect PALM data for both Dronpa and rsKame when the fluorescent proteins were excited by 488 nm and not activated by 405 nm illumination. The T_{ON} and N_{Blink} were not affected by the addition of 405 nm illumination. Therefore, Dronpa and rsKame can be both excited and activated by 488 nm laser illumination. In addition, at higher 488 nm laser power densities, the addition of the 405 nm laser power densities becomes almost negligible. These results provide an explanation for the effects we observed when attempting to use Dronpa initially. The initial 488 nm exposure step in the published protocol was not only exciting molecules already in the activated state but also activating molecules in the dark state and then exciting them as well.[148] This explains both the "shimmering" phenomenon, as large populations of Dronpa were activated and excited at once, and the bleaching effect of the initial 488 nm exposure step. The results also demonstrate that the activation of the Dronpa chromophore is dominated by 488 nm illumination. The increased steric hindrance of rsKame "slows" the trans to cis isomerization of the chromophore by at least 50%, a margin that allows for 488 nm activation effect to be mitigated enough for successful PALM imaging. We now had both a red and a green PA-FP that are useful for PALM imaging.

PA-mCherry1, an Alternate Red Fluorescent Photoactivatable Fluorescent Protein

We also examined the photophysics of PAmCherry1 as a potential PALM PA-FP and as a point of comparison for rsKame. PAmCherry1 was purified using the same vector construct and purification protocol as Dronpa and rsKame (Figure 26). Purified PAmCherry1 was successfully obtained (Figure 27). We did not examine bulk spectroscopic properties of PAmCherry1 because the fluorescent protein was already well characterized in literature.

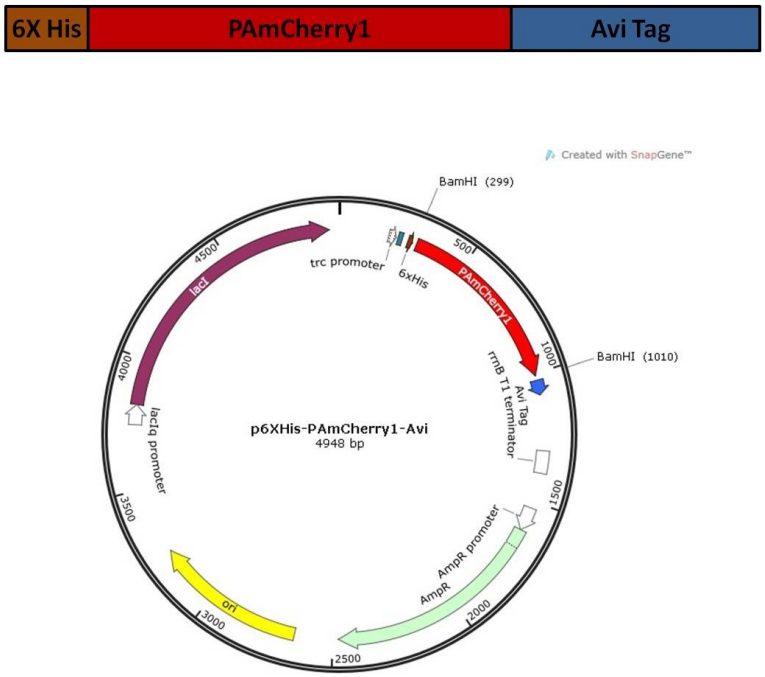

Figure 26: Genetic construct and cloning map of PAmCherry1 for purification.
PAmCherry1 was inserted into the pJY00 bacterial expression vector with BamHI between an N-terminal 6XHis tag and a C-terminal avidin sequence. pJY00 has an IPTG inducible promoter.

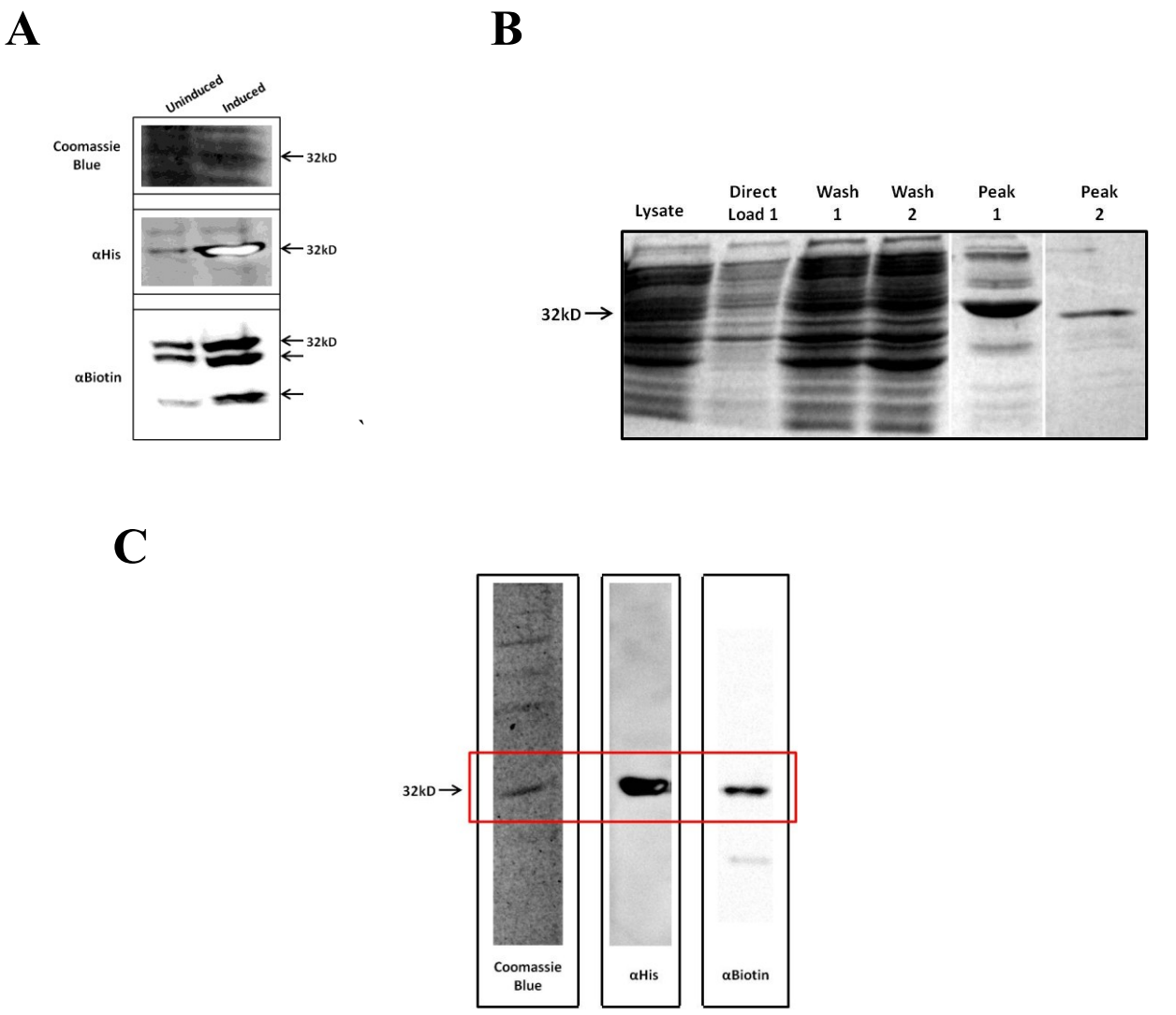

Figure 27: Expression and purification of PAmCherry1. A) AvB101 *E. coli* cells transformed with p6XHis-PAmCherry1-Avi were induced and cultured with 1 μg/mL IPTG and 0.5 μM biotin for 12 hours prior to purification. Uninduced lanes were cultured with biotin but not IPTG. Samples were run on an SDS-PAGE gel and stained with Coomassie Blue for overall protein content or probed with αHis and Streptavidin-HRP conjugated antibodies. B) Cell lysate ("Lysate") of the induced AvB101 p6XHis-PAmCherry1-Avi cells was loaded on to a nickel column ("Direct Load1/2"). Unbound protein was washed away ("Wash1/2") with excess lysis buffer and eluted off the column with a gradient elution of increasing imidazole concentration in elution buffer in two peaks ("Peak 1/2") (Table 5). Samples from each step were loaded onto a polyacrylimide denaturing gel and stained with Coomassie Blue showing increasing purity of the PAmCherry1 protein sample. C) Purified samples of PAmCherry1 from the second peak fractions were pooled and dialyzed to remove the imidazole. Samples of each purified protein were run on an SDS-PAGE gel and stained with Coomassie Blue for overall protein content or probed with αHis and Streptavidin-HRP conjugated antibodies. The samples showed high purity as well as robust biotinylation.

We examined the photophysics of PAmCherry1 using the same slide preparation protocol with a different imaging protocol. For imaging, focal planes and sample illuminating laser angles for TIRF were set as described previously. The 561 nm excitation laser was turned on and left on for 30 seconds to photobleach any potential background. We then turned on the camera, followed by activation 405 nm laser illumination. We took PALM data until the field of view was entirely photobleached. We tested the conditions detailed in Table 3.

Table 3: Single molecule kinetic data for DronpaV157X mutant series

Condition	Sample	561 nm laser power density (W/mm^2)	405 nm laser power density (W/mm^2)
1	PAmCherry1	22	0.00
2	PAmCherry1	22	0.60
3	PAmCherry1	22	1.26
4	PAmCherry1	22	2.83
5	PAmCherry1	22	6.14

We calculated the photoactivation rates of PAmCherry1 over various 405 nm laser power densities (0-6.14 W/mm^2). We found that the photoactivation rates followed first order rate kinetics and can be defined as $e^{-k_a T}$. Therefore, based on a linear regression of the photoactivation rates versus 405 nm laser power density, we are able to calculate the photoactivation rate of PAmCherry1 at 7.28 mW/mm^2, the highest photoactivation laser power density used when activating rsKame (Figure 28). At 7.28 mW/mm^2, PAmCherry1 has a k_a of $8.4*10^{-5}$ s^{-1}. Therefore, over a 5 minute experiment, the average time for imaging rsKame, less than 2.5% of PAmCherry1 molecules would be activated. We decided to use PAmCherry1 for our future PALM imaging both for this reason and because it lacked the residual green background that was problematic with mEos2 and Dendra2.

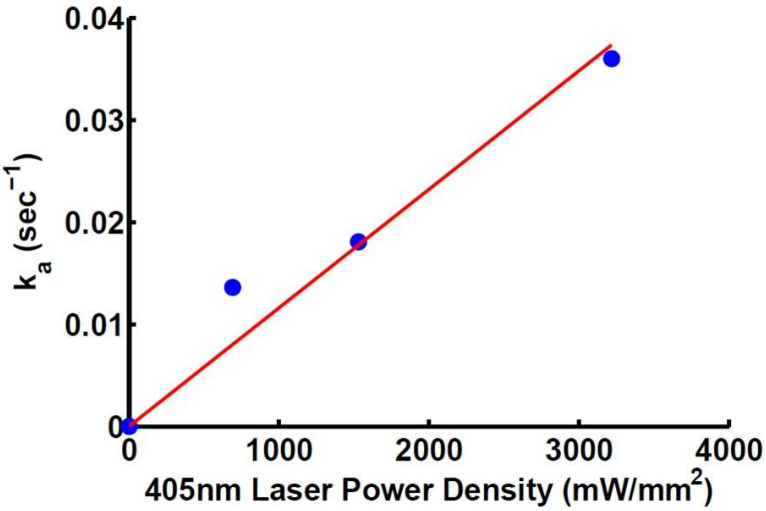

Figure 28: Photoactivation rate of PAmCherry1 vs. 405 nm laser power density. Photactivation (k_a) rates were calculated from single molecule data with activation laser powers ranging from 0-7 W/mm^2. A linear regression of the data allows for the calculation of the percent of PAmCherry1 molecules activated at a given activation laser power density over time.

After the single molecule studies, we had two PA-FPs useful for PALM imaging, PAmCherry1 and rsKame. We used the two PA-FPs for our subsequent work with two-color PALM and mitochondrial fission.

FUTURE DIRECTIONS

PHOTOSWITCHABLE CHROMOPHORE ISOMERIZATION

An rsKame Cis to Trans/Trans to Cis Isomerization Model

Our photophysical data clearly demonstrated that the increased steric hindrance of the leucine at position 157 in rsKame increases the T_{OFF} and inhibits the trans to cis switching of the chromophore. There are several published models of the chromophore's cis to trans/trans to cis isomerization movement based on crystal structures of Dronpa in both the fluorescent (PDB 2IE2 (cis/ON)) and dark (PDB 2POX (trans/OFF)) states.[134,137,138] We used the Andreson model in combination with Stefan Jakobs group's work on rsFastLime as the basis for our mutations.[134] The Andreson model details an isomerization model where the chromophore movement is heavily influenced by the side chains of surrounding amino acids: H193, S142, R66, and V157. The model specifically details a sequence of events where the valine sidechain has to move outward from the chromophore in order for isomerization to take place.[134] However, when we modeled a leucine in the place of valine in position 157 we found that, based solely on steric interactions predicted by the Pymol software, the leucine sidechain most likely interferes with the movement of serine 142 (Figure 29).

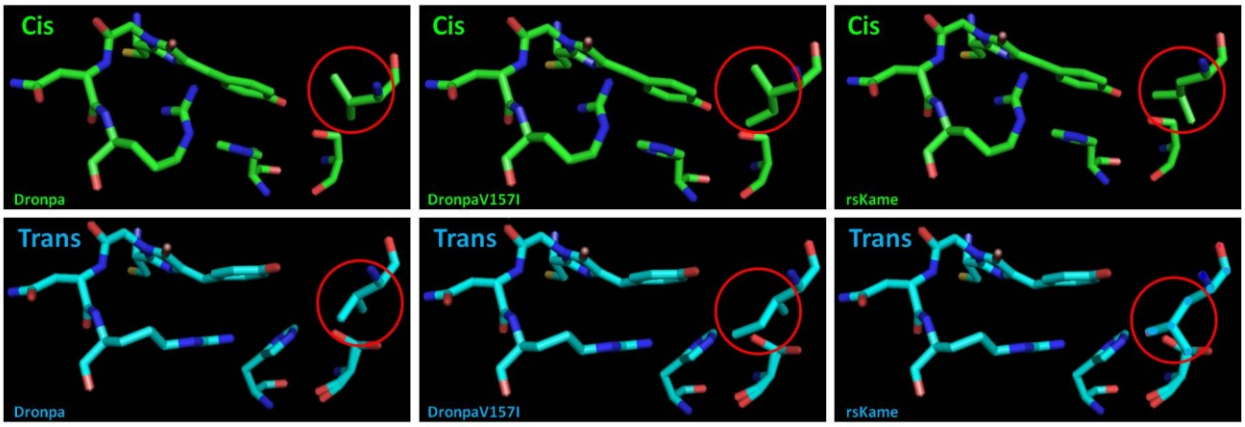

Figure 29: PyMol modeling of the DronpaV157X mutant series' chromophores and the surrounding interacting amino acid side chains. Using Dronpa crystal structure PDB files 2IE2 (cis/ON) and 2POX (trans/OFF), the Val at position 157 was substituted with Ile or Leu (red circle). Ile and Leu residues were placed in the confirmation that was most probable based on Van der Waals interactions and hydrophobic forces. Modeling suggests that the amino acid sidechain at position 157 does not interact directly with the chromophore, but instead interacts with the Ser at position 142. The Ser sidechain hydroxyl does interact directly with hydroxyl on the tyrosine of the chromophore. Part of the chromophore isomerization involves the formation and breaking of the hydrogen bonds between the chromophore tyrosine and Ser142. Delaying or partially inhibiting the bond formation may be the cause of the increased T_{OFF} observed in rsKame single molecule photophysical studies.

Based on the Andreson model, the S142 movement is critical to the formation of the hydrogen bond between it and the hydroxyl group on the side chain of tyrosine 64, the final step for creating the cis positioned fluorescent chromophore.[134] Regardless of the actual sequence of events, our Pymol modeling shows the leucine side chain seems to have a greater capacity to transiently sterically inhibit the formation of the hydrogen bond between the S142 and the tyrosyl oxygen. Of course, the Pymol modeling is no substitute for actual crystal structures. To elucidate the actual change in the formation of the fluorescent chromophore in rsKame, crystal structures of rsKame in both the fluorescent and dark state are necessary. In addition, we note that the observed three recovery rates of Dronpa and rsKame may give insight into the chromophore switching mechanism but would require either novel mutations with T_{OFF} of a different kinetic order and crystal structures thereof.

MATERIALS AND METHODS

STANDARD TECHNIQUES AND STARTING MATERIALS

Molecular biology techniques that are considered standard were performed as are commonly described. These include polymerase chain reaction (PCR), restriction digest, ligation, and transformation. Minipreps of plasmid DNA from DH5α *E. coli* were performed using the Zippy Plasmid Miniprep Kit from Zymo Research and gel extractions were performed using the Zymoclean Gel DNA Recovery Kit from Zymo Research. All sequencing was performed using non-premixed sequencing reactions through Sequetech, Inc. All PCR, mutagenesis, and sequencing primers were synthesized through Integrated DNA Technologies, Inc. PCR and sequencing primers are listed in the Table 4. All enzymes used for molecular cloning were purchased from New England Biolabs. The base materials for LB broth, solid media plates, and the antibiotics were purchased from Sigma Aldrich. LB broth consisted of 10 g/L bacto-peptone, 5 g/L yeast extract, and 10 g/L NaCl. The solid media plates were made with LB and 1.5% (w/v) agar. The antibiotics used were appropriate to the *E. coli* being cultured. The antibiotics and concentrations used were 100 mg/L ampicillin and 30 mg/L kanamycin. Buffers are detailed in Table 5.

Table 4: Cloning and sequencing primers

Name	Sequence 5' → 3'
mEos2 6XHis Fwd	ATGCATCATCACCATCACCACAGTGCGATTAAGCCAGAC
6X His EcoRI Kozak Fwd	AAAAGAATTCGACACCATGCATCATCACCATCACCAC
mEos2 Linker 1 Rv	GAAGCTTGAGCTCGAGACATGTTTAGATCCCCTAATCGTC TGGC
Linker 2 Rv	CCGTCGACTGCAGAATTCGAAGCTTGAGCTCGAGACATG
Linker 3 Rv	ATCCCGGGCCCGCGGTACCGTCGACTGCAGAATTC
Linker 4 Rv	TTTCCGGCTCTCGGTGGCGATGGATCCCGGGCCCG
Linker 5 Rv	TTGAAGCGCTCCTGGCCTTTCCGGCTCTCGGTG
BclXl Extension 2 Rv	CAGGAACCAGCGGTTGAAGCGCTCCTGGCCTTTC
BclXl Extension 3 Rv	ACCAGCCACAGTCATGCCCGTCAGGAACCAGCG
BclXl Extension 4 Rv	GAGTGAGCCCAGCAGAACCACACCAGCCACAG
BclXl Extension 4 NotI Rv	GCGGCCGCTCACTTCCGACTGAAGAGTGAGCCCAG
Linker 1 PstI Fwd	AAAACTGCAGGATCTAAACATGTCTCGAGCTCAAGC
Linker 2 Fwd	CATGTCTCGAGCTCAAGCTTCGAATTCAGCAG
Linker 3 Fwd	CAGCAGTCGACGGTACCGCGGGCCCGGGATCCATC
Linker 4 mEos2 Fwd	CCCGGGATCCATCGCCACCAGTGCGATTAAG
mEos2 6XHis Rv	TTAGTGGTGATGGTGATGATGCCCTAATCGTCTGGC
6XHis NotI Rv	AAAAGCGGCCGCTTAGTGGTGATGGTGATGATG
6XHis EcoRI Kozak Fwd	AAAAGAATTCGACACCATGCATCATCACCATCACCAC
mEos2 Sequencing Fwd	TGCATTGCCAGAAACGACATAACAATGG
mEos2Sequencing Rv	GTTCTGAAGTCACATCGGTAATGGGC
Linker 4 Dronpa Fwd	CCCGGGATCCATCGCCACCAGTGTGATTAAACC
Dronpa 6XHis Rv	TTAGTGGTGATGGTGATGATGTCTAGATAACTTGGCCTG
Dronpa 6XHis Fwd	ATGCATCATCACCATCACCACAGTGTGATTAAACCAGAC
Dronpa Linker 1 Rv	AGCTCGAGACATGTTTAGATCTCTAGATAACTTGGCC

Dronpa Sequencing Fwd	TGTAACGCGACAAACGACATAACCC
Dronpa Sequencing Rv	GAAGTCACATCGGTAATGGCCACC
HsBCS1L EcoRI Kozak Fwd	AAAAGAATTCGACACCATGCCACTTTCAGACTTTATTC
HsBCS1L PstI Rv	CTGCAGGGCCAGTGCTCGAGCTTC
COX5A AflII Kozak Fwd	AAAACTTAAGGACACCATGCTGGGCGCCGCTCTC
COX5A NotI Rv	GCGGCCGCCACTTTGTCAAGGCCCAG
Dronpa NotI Fwd	GCGGCCGCAAGTGTGATTAAACCAGAC
Dronpa XbaI Rv	AAAATCTAGATAACTTGGCCTGCCTCGGCAG
DronpaV157I Mutagenesis Fwd	GGAGTGCTGAAGGGTGATATTAACATGGCTCTGTCGC
DronpaV157L Mutagenesis Fwd	GGAGTGCTGAAGGGTGATCTGAACATGGCTCTGTCGC
DronpaV157F Mutagenesis Fwd	GGAGTGCTGAAGGGTGATTTCAACATGGCTCTGTCGC
DronpaV157I Mutagenesis Rv	GCGACAGAGCCATGTTAATATCACCCTTCAGCACTCC
DronpaV157L Mutagenesis Rv	GCGACAGAGCCATGTTCAGATCACCCTTCAGCACTCC
DronpaV157F Mutagenesis Rv	GCGACAGAGCCATGTTGAAATCACCCTTCAGCACTCC
Dronpa BamHI Fwd	AAAAGGATCCAGTGTGATTAAACCAGACATGAAG
Dronpa BamHI Rv	AAAAGGATCCCTTGGCCTGCCTCGGCAGCTC
6XHis Kozak PmeI Fwd	AAAATTTAAAGACACCATGCATCATCACCATCACCAC
6XHis PmeI Rv	CGCGCCTTTAAATTAGTGGTGATGGTGATGATG
BCS1L Kozak PmeI Fwd	GGAATTTAAAGACACCATGCCATTTTCAGACTTTGTTC
HsBCS1L Kozak PmeI Fwd	GGAATTTAAAGACACCATGCCACTTTCAGACTTTATTC
BclXl PmeI Rv	AAAATTTAAATCACTTCCGACTGAAGAGTGAGCCCAG
PAmCherry1 BamHI Fwd	AAAAGGATCCGTGAGCAAGGGCGAGGAG
PAmCherry1 BamHI Rv	AAAAGGATCCCTTGTACAGCTCGTCCATGCCG
PAmCherry1 6XHis Fwd	ATGCATCATCACCATCACCACGTGAGCAAGGGCGAG
PAmCherry Linker 1 Rv	AGCTCGAGACATGTTTAGATCCTTGTACAGCTCGTCC
PAmCherry1 Sequencing Fwd	GACTACTTTAAGCTGTCCTTCCCCGAG
PAmCherry1 Sequencing Rv	GTCCTTCAGCTTCACTCTGGGCTTG
rsKame AflII Kozak Fwd	AAAACTTAAGGACACCATGAGTGTGATTAAACCAGAC
rsKame NotI Rv	AAAAGCGGCCGCCTTGGCCTGCCTCGGCAGCTC
Drp1 Linker NotI Fwd	CAAGGCGGCCGCAGGAGGGGGATCTGGAGGCGGATCTG GCGGAGGAGAGGCGCTAATTC
Drp1 ApaI Rv	AAAAGGGCCCTCACCAAAGATGAGTCTCCCGG
Drp1 Sequencing Primer	CAAGAGAGGTAGATCCAGATGGTCGCAGAACCC
PAmCherry1(N) Kozak KpnI Fwd	AAAAGGTACCGACACCATGGTGAGCAAGGGCGAG
PAmCherry1(N) XhoI Rv	AAAACTCGAGCCGCCGTCCTCGGGGTACATC
PAmCherry1(C) Linker XhoI Fwd	AAAACTCGAGCGGAGGGGGAGGCTCTGGAGGCGGAGGA GTGAGCAAGGGCGAG
PAmCherry1(C) ApaI Rv	AAAAGGGCCCTTACTTGTACAGCTCGTCCATGCCG
Dendra2(N) Kozak KpnI Fwd	AAAAGGTACCGACACCATGAACACCCCGGGAATTAACC
Dendra2(N) XhoI Rv	AAAACTCGAGCCGCCGTCGCGCACGTGCAGC
Dendra2(C) Linker XhoI Fwd	AAAACTCGAGCGGAGGGGGAGGCTCTGGAGGCGGAGGA CTGCTGGTGGGC
Dendra2(C) ApaI Rv	AAAAGGGCCCTTACCACACCTGGCTGGGCAGG
rsKame(N) Kozak KpnI Fwd	AAAAGGTACCGACACCATGAGTGTGATTAAACCAG
rsKame(N) XhoI Rv	AAAACTCGAGCCTCCATCACGCACATAC
rsKame(C) Linker XhoI Fwd	AAAACTCGAGCGGAGGGGGAGGCTCTGGAGGCGGAGGA GTGCTGAAGGGTG
rsKame(C) ApaI Rv	AAAAGGGCCCTTACTTGGCCTGCCTCGGCAGCTC
mEos2(N) Kozak KpnI Fwd	AAAAGGTACCGACACCATGAGTGCGATTAAGCCAG
mEos2(N) XhoI Rv	AAAACTCGAGCCTCCATCACGCACATAC
mEos2(C) Linker XhoI Fwd	AAAACTCGAGCGGAGGGGGAGGCTCTGGAGGCGGAGGA

	GTGCTGACGGGTG
mEos2(C) ApaI Rv	AAAAGGGCCCTTATCGTCTGGCATTGTCAGG
EGFP Kozak KpnI Fwd	AAAAGGTACCGACACCATGGTGAGCAAGGGCGAG
EGFP XhoI Rv	AAAAGAGCCCTTGTACAGCTCGTCCATGCC
EGFP Linker XhoI Fwd	AAAACTCGAGCGGAGGGGGAGGCTCTGGAGGCGGAGGA GTGAGCAAGGGCGAGGAGC
EGFP ApaI Rv	AAAAGGGCCCTTACTTGTACAGCTCGTCCATGCCG
TagBFP Kozak KpnI Fwd	AAAAGGTACCGACACCATGAGCGAGCTGATTAAGG
TagBFP XhoI Fwd	AAAACTCGAGCGGAGGGGGAGGCTCTGGAGGCGGAGGA AGCGAGCTG
TagBFP XhoI Rv	AAAACTCGAGCCATTAAGCTTGTGCCCCAG
TagBFP ApaI Rv	AAAAGGGCCCTTAATTAAGCTTGTGCCCCAG
ATP5F1 Kozak AflII Fwd	AAAACTTAAGGACACCATGCTGTCCCGGGTGGTACTTTCC
PAmCherry(C) Lk XhoI Fwd	AAAACTCGAGCGGAGGGGGAGGCTCTGGAGGCGGAGGA GCCCTGAAGGGCGAGGTCAAG
ATP5F1 XhoI Rv	AAAACTCGAGCCCATAACTGGCTGTGCTTGAGCC
IRES BamHI Fwd	AAAAAAAGGATCCGCCCCTCTCCCTCCCCCC
PAmCherry1(C) BamHI (IRES) Rv	AAAAGGATCCTTACTTGTACAGCTCGTCCATGCC
ATP5O Kozak NotI Fwd	AAAAGCGGCCGCGACACCATGGCTGCCCCAGCAGTGTCC
IRES NotI Rv	AAAAGCGGCCGCGGCCATATTATCATCGTG
Cherry (N) Lk XhoI Fwd	AAAACTCGAGCGGAGGGGGAGGCTCTGGAGGCGGAGGA GTGAGCAAGGGCGAGGAGG
ATP5O XhoI Rv	AAAACTCGAGCCGACAATCTCCCGCATAGCCC
Cherry (N) XbaI Rv	AAAATCTAGATTAGCCGTCCTCGGGGTACATCC

Table 5: Buffers

Buffer	Composition
1X Phosphate Buffered Saline	137 mM NaCl 2.7 mM KCl 10 mM Na_2HPO_4 * 2 H20 2.0 mM KH_2PO_4 pH 7.4
1X Lysis Buffer	50 mM Na2HPO_4 pH 7.4 300 mM NaCl 10 mM Imidazole 5% glycerol
1X Elution Buffer	50 mM Na_2HPO_4 pH 7.4 300 mM NaCl 300 mM Imidazole 5% glycerol
1X Dialysis Buffer	50 mM Na_2HPO_4 pH 7.4 300 mM NaCl 5% glycerol
1X Single Molecule Imaging Buffer	150 mM Tris pH 7.4 50 mM NaCl
1X PHEM	60 mM PIPES 25 mM HEPES 10 mM EGTA 2.0 mM $MgCl_2$

CLONING OF MAMMALIAN EXPRESSION VECTORS

Two mammalian expression vectors were used: pCMV Kan/Neo from Origene and pcDNA5/TO from Invitrogen. Photoactivatable fluorescent proteins (PA-FPs) used for the studies were mEos2, DronpaV157X, and PAmCherry1. PAmCherry1 was a generous gift from the Liphardt lab (University of California, Berkeley). All cloning techniques including primer synthesis and sequencing confirmations were done as described in Standard Techniques and Starting Materials as is the list of cloning primers (Table 4). A Kozak consensus sequence GACACC was added directly N-terminal of the ATG start codon in all constructs to promote translation.

To create pBCS1L-Lk-PA-FP-6XHis, murine *BCS1L* was purchased in the pCMV Kan/Neo vector backbone from Origene. In the pBCS1L (CMV Kan/Neo) commercial vector, *BCS1L* is

cloned into the backbone with EcoRI and NotI. The 25 amino acid linker (Lk) DLNMSRAQASNSAVDGTAGPGSIAT was added to the N-terminal of a PA-FP using nesting PCR. A 6XHis C-terminal tag and restriction sites PstI and NotI were added by PCR. The final vector product pBCS1L(1-160)-Lk-PA-FP-6XHis was made by cloning one of the Lk-PA-FP-6X-His PCR constructs into pBCS1L (CMV Kan/Neo) using the PstI site found mid gene and the C-terminal NotI site.

To build p6XHis-PA-FP-Lk-BclXl(201-233), the Lk and BclXl(201-233) was added to the C-terminal of the PA-FPs with nesting PCR. A 6XHis N-terminal tag and restriction sites EcoRI and NotI were added by PCR. The PCR product 6XHis-PA-FP-Lk-BclXl(201-233) was cloned into pCMV Kan/Neo using EcoRI and NotI, creating the final vector product p6XHis-PA-FP-Lk-BclXl(201-233).

To build the DronpaV157X mutant series mammalian expression vector p6XHis-DronpaV157X-Lk-BclXl(201-233), the PCR product 6XHis-DronpaV157X-Lk-BclXl(201-233) was created using nesting PCR. Restrictions sites EcoRI and NotI were added by PCR. The product was cloned into pCMV Kan/Neo. The same PCR product had the restriction sites AflII and NotI added to it by PCR instead of EcoRI and NotI and was cloned into pcDNA5/TO to create p(TO)6XHis-DronpaV157X-Lk-BclXl(201-233).

To build the DronpaV157X mutant series mammalian expression vector pBCS1L(1-160)-Lk-DronpaV157X-6XHis, the PCR product BCS1L(1-160)-Lk-DronpaV157X-6XHis was built in two parts. First, BCS1L(1-160) was PCR'd with added EcoRI and PstI restriction sites. Second, Lk-DronpaV157X-6XHis was built by nesting PCR. Restrictions sites PstI and NotI were added with PCR. BCS1L(1-160) and Lk-DronpaV157X-6XHis were digested with PstI, ligated together. The ligated BCS1L(1-160)-Lk-DronpaV157X-6XHis was PCR'd with added restriction sites EcoRI and NotI. The full length PCR product was cloned into pCMV Kan/Neo with EcoRI and NotI, resulting in pBCS1L(1-160)-Lk-DronpaV157X-6XHis. The same full length PCR product was re-PCR'd with restriction sites AflII and NotI and cloned into pcDNA5/TO with AflII and NotI, resulting in p(TO)BCS1L(1-160)-Lk-DronpaV157X-6XHis.

To create pCox5A-DronpaV157X mutant series, the original genetic construct to serve as a template for site directed mutagenesis was created in two steps. First, Dronpa was PCR'd with the addition of NotI and XbaI restriction sites and the absence of an ATG start codon. The construct was cloned into pcDNA5/TO with NotI and XbaI to create pDronpa-N. The restriction sites AflII and NotI were added to full length *COX5A* by PCR. *COX5A* cDNA was purchased from Open Biosystems. *COX5A* was cloned N-terminal to Dronpa into pDronpa-N with AflII and NotI, resulting in pCox5A-Dronpa. The pCox5A-Dronpa was the template plasmid for site directed mutagenesis of Dronpa at V157.

SITE DIRECTED MUTAGENESIS

Site directed mutagenesis of Dronpa at V157 was performed using the Quikchange Mutagenesis kit and protocol from Agilent Technologies. Primers were designed according to the Quikchange Mutagenesis protocol specifications and detailed in Table 4. Full length vector constructs as described in Cloning of Mammalian Expression Vectors were replicated and mutagenized by PCR with PfuUltra DNA polymerase from Agilent. Template plasmid isolated from DH5α *E. coli* is methylated and, after the PCR step, destroyed by digestion with DpnI. Nicked circular mutant plasmids were directly transformed into DH5α *E. coli* cells, where the native cell ligases seal the nicks and replicate the DNA plasmids. DNA purification and

sequencing confirmation for successful mutagenesis were performed as described in Standard Techniques and Starting Materials. Mutagenesis primers altered Val157 to Ile157, Leu157, or Phe157.

CELL CULTURE

Three different cell types were used: murine C2C12 (muscle), murine EpH4 (mammary gland epithelial), and *Homo sapiens* T-Rex HeLa (cervical cancer) cells. C2C12 cells were obtained from ATCC. EpH4 cells were originally isolated by C. Roskelley.[156] Cells were already in house. T-Rex HeLa cells were purchased from Invitrogen. C2C12 cells were cultured in Dulbeccos' Modified Eagle's Medium (DMEM) and 10% fetal bovine serum. All cell reagents were purchased from University of California, San Francisco Cell Culture Facility. The EpH4 cells were cultured in DMEM with 2% FBS with added 5 mg/L of insulin and 50 mg/L gentamycin. T-Rex HeLa cells were cultured in Modified Eagle's Medium (MEM) with10% tetracycline free FBS, 1% penicillin/streptomycin, and 5 mg/L blasticidin to maintain the stably transfected tetracycline repressor gene. Cells were grown at 37ºC with 5% CO_2.

CELL TRANSFECTION

Mammalian cells were transfected with one of two lipid based commercial transfection reagents. C2C12 and EpH4 cells were transfected with Lipofectamine2000 (Invitrogen). Cells could be transfected in media with serum or without with little change in efficiency. Cells were transfected for 4-8 hours and then incubated for at least 12 hours at 37ºC and 5% CO_2 prior to imaging. T-Rex HeLa cells were transfected with Xfect (Clontech). Cells could be transfected in media with serum, which is important because HeLa cells died quickly in the absence of serum. Cells were again transfected for 48 hours and then incubated for at least 12 hours at 37ºC and 5% CO_2 prior to imaging.

Prior to transfection, T-Rex HeLa cells were plated on acid washed fibronectin coated #1.5 glass slides (Warner Instruments) and grown to ~70% confluency (24-48 hours) at 37ºC in growth media with blasticidin selection (10 μg/mL, Invitrogen). T-Rex HeLa cells were co-transfected with Xfect (Clontech). Cells were transfected in media with serum. Cells were transfected for 4-8 hours and then incubated for at 24-48 hours at 37ºC and 5% CO_2 prior to imaging. Post transfection and at least 12 hours prior to imaging, cells were fed FBS coated 40 nm Au particles (60,000 particles/mL, Microspheres-Nanospheres).

LIVE CELL IMAGING WITH SCANNING CONFOCAL MICROSCOPE

Cells were imaged on the Nikon Eclipse TE2000-S scanning confocal microscope (Nikon Instruments Inc.). Cells were plated on MatTek imaging tissue culture plates (MatTek Corporation). MatTek imaging tissue culture plates have a #1.5 glass slide in the center of the plate for high quality imaging. Cells were imaged *in vivo* and in growth media. When necessary, mitochondrial networks were labeled with MitoTracker Red CMXRos (Life Technologies/Invitrogen) at 30 nM concentrations. MitoTracker Red CMXRos labeled cells were imaged by laser excitation at 561 nm and the fluorescence was collected with a 663-738 nm emission filter. Cells transfected with nonactivated mEos2 were imaged by laser excitation at

488 nm and the fluorescence was collected with a 510-560 nm emission filter. Cells transfected with Dronpa or one of our DronpaV157X mutant variants were activated with 15 second 405 nm mercury arc lamp activation prior to laser excitation at 488 nm and fluorescence was collected with a 510-560 nm emission filter. When both the PA-FP and MitoTracker Red CMXRos are imaged in the same cells, the different excitations were taken consecutively. Images were analyzed and overlaid using ImageJ.

PALM INSTRUMENTATION AND IMAGING

Prior to fixation, cells were plated on fibronectin coated acid washed 25 mm round #1.5 glass slides. Twelve hours prior to fixation, cells were fed 100 nm or 40 nm Au fiducial markers coated in FBS (60,000 particles/mL). Cells were fixed with 1% formalin (Sigma Aldrich) in 1X PBS or 1X PHEM (Table 5) for 10 minutes then washed five times with 0.2 μm filtered 1X PHEM. Fixed cells were imaged in 1X PHEM.

The PALM microscope was built in house by Sanghyuk Lee (Bustamante Lab).[130] The commercial platform base was an Olympus IX71 UAPO150xO/TIRFM-SP N.A. 1.45 objective. A 55 μm x 55 μm sample area is illuminated by the laser and the Z drift was automatically corrected using a piezo-stage (CRIFF, ASI) controlled active feedback. Fluorescence images were collected with an electron multiplying charge coupled camera (DV887ECS-BV; Andor). The image rate is 20 Hz.

Prior to imaging, sample illuminating laser angle for pseudo-TIRF were set for the focal plane. Angles were set to evenly illuminate the area in question while achieving as close to TIRF as possible. Cells transfected with mEos2 fused constructs were imaged using increasing activation at 405 nm (0.6-6.0 W/mm^2) and excitation at 561 nm (22 W/mm^2) with a mEos2 emission filter (588-621 nm). Cells transfected with Dronpa or DronpaV157X variants were imaged using combinations of increasing activation at 405 nm (0.61-7.28 mW/mm^2) and excitation at 488 nm (0.32-5.87 W/mm^2) with a Dronpa emission filter (525 nm, range 25 nm). Cells were imaged until all fluorescent molecules were photobleached.

PALM DATA ANALYSIS

Individual fluorescent events were determined by setting two parameter thresholds. The parameter 1 threshold is the X fold brightness of individual pixels over the total background per frame. The parameter 2 threshold is the sum of the number of photons collected in the 7 x 7 pixel square centered on each pixel identified with parameter 1. Fluorescent events identified by both parameters are considered real and are compiled frame by frame. Each pixel equals 106.6 nm; therefore, by applying the total photon count threshold, each event's PSF center is separated spatially by at least 700 nm. Events that pass both thresholds are considered real and the 7 x 7 pixel square is fit by a 2-D Gaussian PSF. From these PSFs, the inferred position of the single PA-FP molecule was calculated. The XY drift of all identified events are corrected by tracking the drift of the 100 nm or 40 nm Au fiducial marker through the PALM movie data. The sum of all XY drift corrected identified fluorescent events is the final analyzed PALM image. Sanghyuk Lee designed the MATLAB based software used for this analysis termed "peakfindtool" and "palmplot".[130]

PROTEIN EXPRESSION AND IN VIVO BIOTINYLATION

Dronpa, Dronpa V157X, and PAmCherry1 were PCR'd with added BamHI restrictions sites and cloned into pJY00. Cloning in frame into the BamHI sites of pJY00 resulted in the genetic construct with an N-terminal 6XHis and a C-terminal avidin tag, p6XHis-DronpaV157X-Avi.

Dronpa and DronpaV157X mutant variants are transformed into AvB101 *E. coli* cells and selected with ampicillin (Amp, 100 μg/mL) and chloramphenicol (Cam, 10 μg/mL). AvB101 cells are transformed with pBirACm. pBirACm is IPTG inducible and has the BirA gene that will biotinylate avidin tags on proteins when biotin is available. Starter cultures of 50 mL LB and antibiotics were inoculated with one colony and incubated overnight at 37°C with agitation. A one liter LB culture with ampicillin only was inoculated to an OD_{600} of 0.1 with the starter culture. Cells were grown to an OD_{600} of 0.7 at 37°C with agitation then induced with 1 mM IPTG. At the time of induction biotin was added to a 50 μM concentration. Proteins were induced for 12 hours then collected by centrifugation. The cell pellet was washed in lysis buffer (Table 5) three times and then either stored at -80°C or immediately purified.

PROTEIN PURIFICATION

Affinity chromatography using nickel coated sepharose beads (His-trap HP) from GE was used to purify His-tagged Dronpa, DronpaV157X mutant variants, and PAmCherry1. Purification was done by fast protein liquid chromatography on an FPLC instrument (ÄKTAFPLC, GE Healthcare Life Scienes). Buffers are described in Table 5. Cell pellets were resuspended in 30 mL of lysis buffer and lysed via sonication at 18 mW (five 20 second pulses with 1 minute intervals). The His-trap HP columns were equilibriated with 10 mL of lysis buffer at a rate of 1.0 mL/min. Cell lysate was loaded onto the column at a rate of 0.5 mL/min and washed with 10 mL of lysis buffer at a rate of 0.5 mL/min. All column bound proteins were eluted off using a gradient elution with elution buffer. The gradient elution was set to reach 100% in 90 minutes and loaded onto the column at 0.5 mL/min. 1.5 mL fractions were collected and analyzed. Samples of the cell lysate, direct load onto the column, and flow-throughs were collected for purity analyses. The fractions containing DronpaV157X were collected, concentrated, and dialyzed to remove imidazole using dialysis buffer and centrifugation in size exclusion columns with 15 kDa filters. Purified protein was snap frozen in liquid nitrogen and stored at -80°C. Protein purity and biotinylation was examined by running denatured purified samples on a polyacrylimide denaturing gel (SDS-PAGE) and staining for total protein with Coomassie blue or transferring the protein onto a nitrocellulose membrane and probing for histidine with a HRP-conjugated αHis and for biotinylation with a HRP-conjugated streptavidin (Western blot analysis). Samples taken throughout the purification process were also run on a SDS-PAGE gel and stained with Coomassie Blue to examine increasing protein purity. Protein samples were quantified using a BCA Assay (Pierce).

BULK SPECTROSCOPY

For excitation and emission spectra, purified protein samples were diluted to 1 μM in a 10 mm quartz cuvette. For the excitation spectra, the cuvette was loaded onto the fluorimeter (QuantaMaster 30, Photon Technology International) and an emission wavelength of 525 nm

was chosen. The sample was bombarded with excitation wavelengths from 400 nm to 530 nm. The emission spectra of the same sample were taken by bombarding the sample with an excitation wavelength of 488 nm and the emission spectrum was collected from 495 nm to 625 nm. For the absorbance spectra, purified protein samples of approximately 3 μM were loaded in a 10 mm quartz cuvette and loaded onto the Varian Cary 50 Bio UV/Visible spectrophotometer. The absorbance of the sample was continuously taken from 260 nm to 600 nm in duplicate. Measurements from the excitation, emission, and absorbance spectra were used to calculate the quantum yield, molar extinction co-efficient and brightness of each DronpaV157X mutant variant.

SINGLE MOLECULE PALM IMAGING

Glass slides (25 mm, #1.5) were loaded onto a glass slide holder for separation. Slides were first immersed in acetone and sonicated for 30 minutes. Next the slides were sonicated in ethanol for 15 minutes and rinsed in Milli-Q filtered water. The slides were boiled in 1 M KOH for 30 minutes. After cooling, the slides were rinsed in Milli-Q water and then left in piranha solution (solution of H_2O_2 and H_2SO_4 in a 4:9 v/v ratio) for 60 minutes. Slides were rinsed in first Milli-Q water then acetone. Fresh acetone was added along with 3-aminopropyl triethoxysilane (Sigma Aldrich) to a final concentration of 1% for 30 minutes. The slides were rinsed in acetone and sonicated in acetone for 5 minutes, 5 times. The slides were then rinsed with Milli-Q water multiple times and then dried with N_2 gas. Slides were PEGylated with 20 μL of an mPEG-SCM-5000: Biotin-PEG-SC-5000 (Laysan Bio, Inc.) solution (9:1, w/w) in 0.1 M $NaHCO_3$, pH 8.0 sandwiched between two slides. Slides were incubated overnight in a humid chamber. Following incubation, the slides were rinsed thoroughly with Milli-Q water and stored at room temperature in Milli-Q water.

Single molecule experiment sample slides for protein immobilization were prepared by drying a PEGylated ultra clean glass slide with N_2 gas. A small well was built on the slide with epoxy. The slide was incubated with neutravidin (Invitrogen, 10 μg/mL) diluted in dialysis buffer for 10 minutes, and then excess neutravidin was rinsed away with dialysis buffer. Next, 100 nm biotin conjugated Au fiducial markers (OD 50, Nanopartz Inc.) were diluted 1:50,000 in dialysis buffer and incubated on the slide for 5 minutes. Excess fiducial markers were washed away. Finally, 0.1 nM of purified protein diluted in dialysis buffer was incubated on the slide for 10 minutes and then excess protein is washed away with dialysis buffer. The sample is now ready for imaging.

The sample was loaded onto the PALM microscope and the focal plane was set to the bottom of the glass slide using the fiducial markers. The sample illuminating laser angle for TIRF was set for even illumination in the field of view. Samples were imaged under a variety of fluorescent conditions but the general procedure was the same for all. For the DronpaV157X series samples, a field of view was established with fiducial markers under 561 nm (22 W/mm^2) laser illumination and the sample was illuminated with 488 nm excitation laser (0.32-5.87 W/mm^2) for 3 seconds prior to activation with 405 nm laser (0-7.28 mW/mm^2). The first 100 frames of each image were discarded from each movie during analysis. Each sample movie was taken for 5000 frames (until the sample was photobleached) at 20 Hz. Each imaging condition was imaged over 8 fields of view. For the PAmCherry1 samples, a field of view was established with fiducial markers with 561 nm laser illumination. Samples were imaged one of two ways: either the sample was co-illuminated with 561 nm (22 W/mm^2) and 405 nm (0.0-6.0 W/mm^2)

and imaged at 20 Hz until the sample was completely photobleached; or the sample was pre-activated with 405 nm laser illumination (6.0 W/mm^2) and then illuminated with 561 nm (22 W/mm^2) and imaged at 20 Hz until the sample was completely photobleached.

SINGLE MOLECULE PHOTOPHYSICAL DATA ANALYSIS

Individual proteins were picked out using the PALM software and the two parameters discussed previously. The peak to background threshold was set at 6 and the total photon count threshold was set at 2000. A region of interest (ROI) in the central part of each analyzed image was set. The data for each fluorescent event for all events in the 8 PALM images per imaging condition (488 nm and 405 nm laser power densities) were combined. Data plots, fits, and various kinetic data were analyzed using MATLAB based algorithms as part of the software "palmplot".[130]

Chapter 3: Development of a Two Color PALM Imaging Protocol

Introduction

In order for PALM imaging to be biologically relevant in general and useful for our studies in mitochondrial fission in particular, clear two-color PALM is essential. We have already demonstrated that the published two-color protocol with mEos2 and Dronpa was not effective in our hands. Previously established two-color PALM protocols were insufficient because Dronpa can be activated by 488 nm wavelength as well as the 405 nm wavelength, and because the Dronpa chromophore photoswitches too rapidly for our 20 Hz camera. In addition to the issues with Dronpa, mEos2 has a residual green background that we found impossible to bleach away completely. This residual green background combined with the green autofluorescence of mitochondria, due to the high NADH content, made imaging Dronpa or rsKame difficult. With such a high background, the signal to noise ratio was unfavorable for super resolution imaging. Therefore we developed a protocol making use of our new green fluorescent protein, rsKame, which was characterized extensively in the Chapter 2, and PAmCherry1, a dark to red PA-FP, that has no residual green background

Previous Two-Color PALM Protocols

Several published protocols for two-color PALM already exist in the literature. Eric Betzig described a two color protocol for tdEos2 and Dronpa in 2007.[148] In that protocol, tdEos2 molecules are imaged first. The cell sample is illuminated by strong 561 nm excitation laser to eliminate any pre-activated molecules. Next, the camera is turned on and the 405 nm activation laser is turned on at low power. The sample is imaged with both lasers until all the tdEos2 fluorescent molecules are activated, excited, and imaged. The camera is turned off and the sample is once again illuminated with a strong 561 nm excitation laser to photobleach any remaining tdEos2 molecules. The sample is then illuminated with strong a 488 nm excitation laser to return any pre-activated Dronpa molecules to the dark state. Next the camera is turned on and the 405 nm activation laser is turned on at low power. The sample is imaged until all Dronpa molecules are activated, excited, and imaged. The camera is turned off, finishing the image. The image is analyzed and corrected for drift using 100 nm Au fiducial markers. The technique is limited by labeling density and sample thickness.

In 2008, Eric Betzig and Jennifer Lippincott-Schwartz published a method that allowed for tracking of single photoactivatable fluorescent proteins or protein fusions in live cells.[157] Using the methodology of PALM, extremely small stochastic populations were activated and excited. This was done with very low intensity activation illumination and a higher intensity excitation illumination to promote photobleaching. Fluorescent proteins were imaged at slow camera rates of approximately 20 frames per second. During analysis, individual fluorescent proteins were tracked frame by frame, building a path of movement. Single fluorescent proteins were considered individual if they appeared in successive frames and did not exhibit movement of greater than 300 nm from the previous frame. They termed this method sptPALM. A detailed methodology of sptPALM imaging and analysis was published in 2009.

Jennifer Lippincott-Schwartz and Vladislav Verkhusha published a two-color PALM imaging method using PAmCherry1 and PA-GFP in 2009.[158] The protocol combined sptPALM with multiple fluorophores. The PALM imaging methodology was based on Eric Betzig's protocol with one significant difference. The PA-GFP and PAmCherry1 were imaged simultaneously using a Dual-View Imaging System from Photometrics. The cell sample was hit with three lasers simultaneously: the 405 nm activation laser at low to increasing intensity and two excitation lasers (488 nm and 561 nm) with middling intensities. The overall photon emissions were directed through two different emission filters, specific to the emission spectra of PA-GFP or PAmCherry1. This allowed for the imaging of both fluorescent proteins concurrently. They performed their experiments in live cells and used slow camera speeds (20 frames per second or below) to track individual molecules.

Lippincott-Schwartz and Verkusha have continued their research into two-color sptPALM, publishing a new red photoactivatable fluorescent protein, PATagRFP, in 2010.[159] They repeated similar two-color sptPALM experiments to that of PAmCherry1 and PA-GFP, replacing PAmCherry1 with PATagRFP. Since PATagRFP was a brighter fluorescent molecule, their sptPALM imaging produced more efficient molecule tracking over a longer time course. Their imaging methodology and analysis was unchanged.

As discussed previously, Betzig's two-color PALM protocol was unsuccessful in our hands due to the "shimmering" effect of Dronpa and the residual green fluorescent background of mEos2. In fact, in a personal communication with Betzig, he acknowledged the issue and suggested using thin sectioned samples for effective imaging, in order to better separate the molecules physically since we could not do so temporally. Thin sectioning is a difficult technical skill and requires comparatively harsh sample preparation, which can fragment mitochondrial networks. We also attempted to use PA-GFP as described previously and had difficulties with dimness of PA-GFP and its "shimmering" effect as well. Since we were able to solve our imaging difficulties with green fluorescent proteins by developing rsKame, we also had to develop a new imaging protocol.

RESULTS AND DISCUSSION

EXPRESSION AND IMAGING OF rsKAME AND PAmCHERRY1 IN A SINGLE CELL

Molecular Cloning and Expression of Mitochondrial Membrane Targeted rsKame and PAmCherry1

We previously described genetic constructs that allowed us to specifically localize PA-FPs to either the OMM or the IMM and embed them in the membrane (Chapter 2). Using the cloning methods described previously, we constructed p6XHis-PAmCherry1-Lk-BclXl(201-233), pHsBCS1L(1-160)-Lk-rsKame-6XHis, and p(TO)HsBCS1L(1-160)-Lk-rsKame-6XHis.

Figure 30: Genetic constructs and cloning maps of mitochondria membrane localized rsKame and PAmCherry1. BCS1L(1-160) was replaced by HsBCS1L(1-160) to build p(Hs)BCS1L-Lk-rsKame-6XHis and p(TO)HsBCS1L-Lk-rsKame-6XHis. 6XHis-PAmCherry1-BclXl(201-233) was inserted into pCMV Kan/Neo with EcoRI and NotI.

Because we chose to use both *Homo sapiens* and murine cell lines for these experiments, we had to create two more constructs: pHsBCS1L(1-160)-Lk-rsKame-6XHis and p(TO)HsBCS1L(1-160)-Lk-rsKame-6XHis (Figure 30). HsBCS1L is the *Homo sapiens* homologue of murine BCS1L. The construct pBCS1L(1-160)-Lk-rsKame-6XHis did not localize to the mitochondria (data not shown) when transfected in T-Rex HeLa cells. We

surmised correctly that the problem was likely the organism of origin of the BCS1L sequence and solved the issue by using the *Homo sapiens* homologue. BCS1L(1-160) on pBCS1L(1-160)-Lk-rsKame and p(TO)BCS1L(1-160)-Lk-rsKame (Chapter 2) was substituted with HsBCS1L(1-160) to build pHsBCS1L(1-160)-Lk-rsKame and p(TO)HsBCS1L(1-160)-Lk-rsKame.

We confirmed the corrected localization of the PA-FPs to the mitochondria in T-Rex HeLa cells with HsBCS1L(1-160) by creating pHsBCS1L(1-160)-Lk-mEos2-6XHis. T-Rex HeLa cells plated on MatTek imaging plates were transfected with pHsBCS1L(1-160)-Lk-mEos2-6XHis. The mitochondrial network was labeled with MitoTracker Red CMXRos. We imaged the cells with a scanning confocal microscope (Figure 31). The HsBCS1L(1-160) fused fluorescent protein and the MitoTracker Red CMXRos overlaid perfectly, confirming correct localization to the mitochondria.

Prior to attempting two-color imaging, we confirmed the localization and suitability of both rsKame and PAmCherry1 for PALM imaging (Figure 32). EpH4 or HeLa cells were transfected with p(TO)HsBCS1L(1-160)-Lk-rsKame or p6XHis-PAmCherry1-Lk-BclXl(201-233). HeLa cells transfected with p(TO)HsBCS1L(1-160)-Lk-rsKame were induced with doxycycline (4 hours, 1 μg/mL) Cells were PALM imaged and analyzed as described in Chapter 2 (Figure 33).

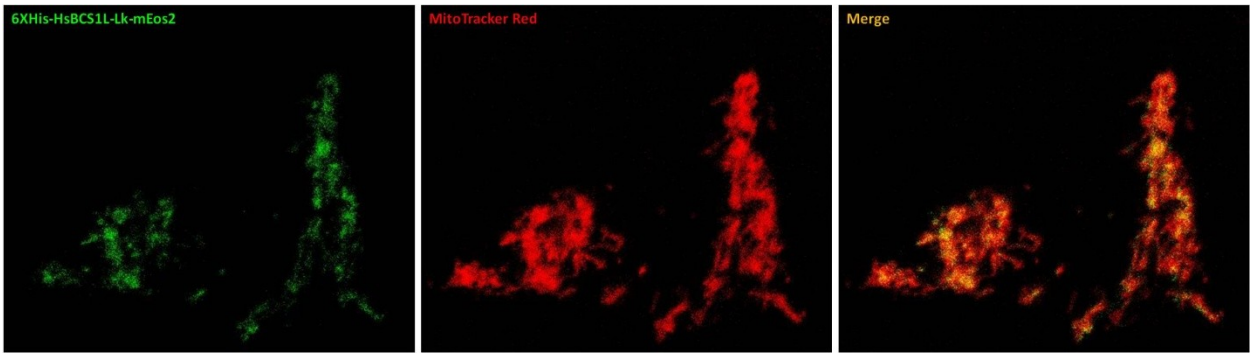

Figure 31: Replacing BCS1L(1-160) with HsBCS1l(160) results in correct PA-FP localization to mitochondria in T-Rex HeLa cells. Murine BCS1L (1-160) was replaced with *Homo sapiens* BCS1L(1-160) in pBCS1L(1-160)-Lk-PA-FP-6XHis for expression in T-Rex HeLa cells. T-Rex HeLa cells were transfected with pHsBCS1L(1-160)-Lk-mEos2-6XHis and mitochondria were labeled with MitoTracker Red. Cells were imaged by scanning confocal microscopy and analyzed in ImageJ.

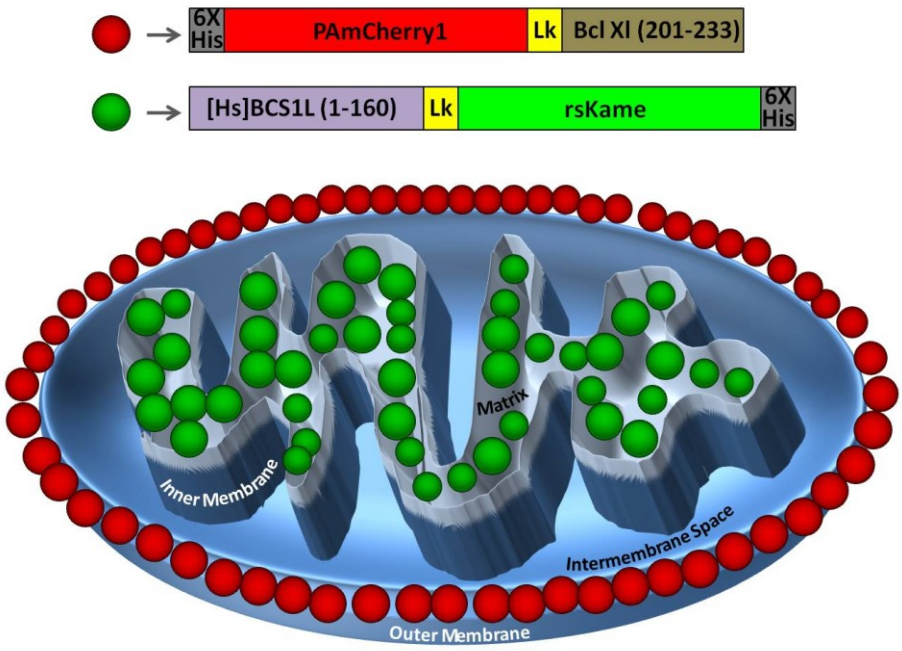

Figure 32: Localization of mitochondrial membrane targeted PAmCherry1 and rsKame. 6XHis-PAmCherry1-Lk-BclXl(201-233) is localized to the mitochondrial outer membrane. (Hs)BCS1L-Lk-rsKame-6XHis is localized to the mitochondrial inner membrane. The amount of (Hs)BCS1L-Lk-rsKame-6XHis protein expression can be controlled depending on its vector backbone.

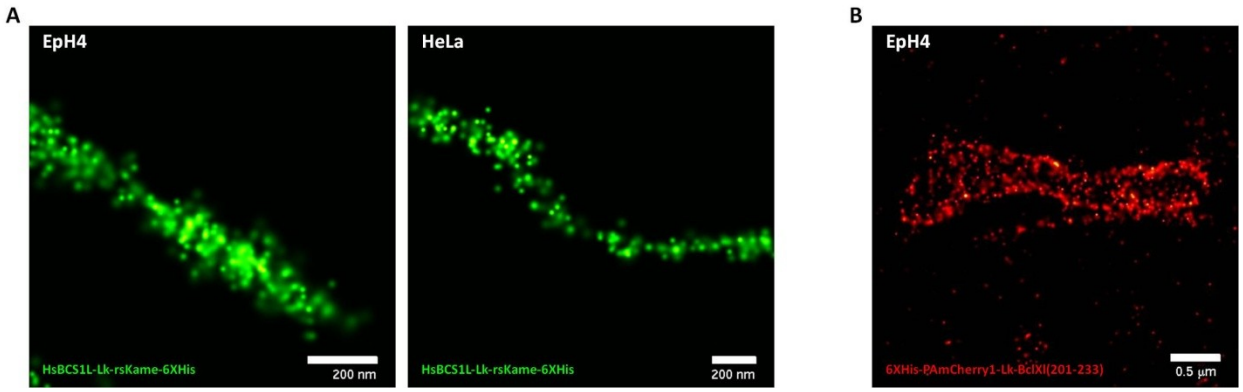

Figure 33: Mitochondrial cristae can be delineated by targeted rsKame and mitochondrial outer membranes can be delineated by targeted PAmCherry1. EpH4 or HeLa cells were transfected with A) p(TO)HsBCS1L(1-160)-Lk-rsKame or B) p6XHis-PAmCherry1-Lk-BclXl(201-233) and PALM imaged. HeLa cells were induced for 4 hours with 1 µg/mL doxycycline. A) rsKame localizes to and delineates the inner membrane structure. B) PAmCherry1 localizes to and delineates the outer mitochondrial membrane structure.

PROTOCOL DEVELOPMENT FOR TWO-COLOR PALM IMAGING AND ANALYSIS

Two-Color PALM Imaging Protocol

Both the murine EpH4 cell line and the T-Rex HeLa cell line were used in the following studies. Cells were plated on #1.5 acid washed fibronectin coated glass coverslips 12-48 hours prior to transfection. EpH4 cells were co-transfected with p6XHis-PAmCherry1-Lk-BclXl(201-233) and pBCS1L(1-160)-Lk-rsKame-6XHis with Lipofectamine. T-Rex HeLa cells were co-transfected with p6XHis-PAmCherry1-Lk-BclXl(201-233) and either pHsBCS1L(1-160)-Lk-rsKame-6XHis or p(TO)HsBCS1L(1-160)-Lk-rsKame-6XHis for inducibile expression. Both sets of constructs were transfected with Xfect. Cells were grown for 24-48 hours post transfection at 37ºC. Cells were fed FBS coated 100 nm and 40 nm Au fiducial markers >12 hours prior to imaging. T-Rex HeLa cells transfected with p(TO)HsBCS1L(1-160)-Lk-rsKame-6XHis were induced with 1.0 μg/mL doxycycline for 4 hours prior to fixation. Cells were prepared for imaging by washing 3-5 times with 1X PHEM, then fixation in 1% formalin in 1X PHEM for 10 minutes. Cells were washed >5 times in 1X PHEM before imaging. All buffers were filtered through 0.2 μm sterile filter flasks prior to use.

Cells were imaged using the basic protocol detailed below.

1. Set focal plane and TIRF angle.
2. Image rsKame.
3. Switch lasers and channels.
4. Image PAmCherry1.
5. Merge images by direct overlay.

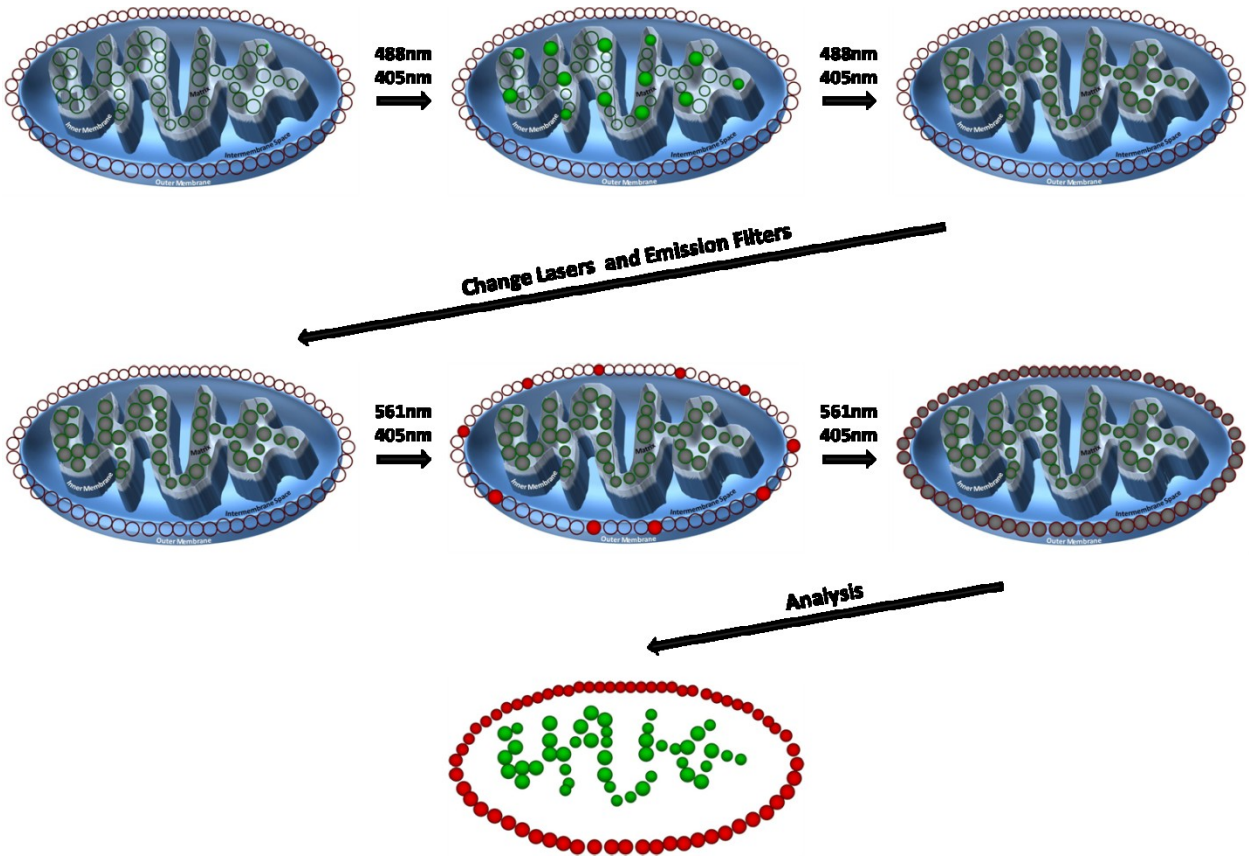

Figure 34: Two-color PALM imaging method model. Prior to activation, both rsKame and PAmCherry1 are in the dark or nonactivated state. To image rsKame, samples are activated with 405 nm and excited/activated with 488 nm. The sample is imaged until all of the rsKame is photobleached. Lasers and filters are changed and a second image is started. To image PAmCherry1, samples are activated with 405 nm and excited with 561 nm until all the PAmCherry1 is photobleached. The two separate images are analyzed and overlaid to produce the final two-color super resolution PALM image.

We set the focal plane by finding the best field of view of the mitochondria using the mercury arc lamp with 488 nm excitation and 525 nm emission wavelengths. We then set the sample illumination laser angle for pseudo-TIRF using the 561 nm laser, the 588-621 nm emission filter, and Au fiducial markers. We attempted to achieve as close to TIRF as possible, but inevitabley ended in pseudo-TIRF. Pseudo-TIRF will result in a propagating wave that is larger than 100 nm. We were then ready to begin imaging the sample. We chose to image rsKame first because the 405 nm laser power density required to activate rsKame will only activate less than 2.5% of PAmCherry1 fluorescent molecules (Chapter 2). This is useful because we could image all of rsKame while activating only a negligible amount of PAmCherry1. When we began the data collection, we turned on the 488 nm excitation laser at

5.87 W/mm^2 and immediately turned on the camera. We then set the vertical (Z) feedback on the stage and turned on the 405 nm activation laser at 0.61 mW/mm^2. We collected PALM data until all molecules were photobleached. We did not raise the 405 nm activation laser power density above 1.56 mW/mm^2. In order to change lasers and filters for imaging PAmCherry1, we turned off the Z feedback for the stage before turning off the 488 nm excitation and 405 nm activation lasers. We turned off the camera immediately after turning off the Z feedback but before the lasers were turned off. We changed emission filters from 525 nm to 588-621 nm and began a new imaging data file. To image PAmCherry1, we turned on the 561 nm excitation laser (22 W/mm^2) and the camera immediately afterwards. The Z feedback for the stage was set. We then turned on the 405nm activation laser, starting at 0.60 W/mm^2. We slowly increased the 405 nm laser power over time in order to maintain a visually constant rate of events throughout the data collection. We continued imaging and data collection until all molecules were photobleached. The Z feedback was turned off before turning off the camera or the lasers. The camera was turned off followed by the lasers (Figure 34).

Two-Color PALM Image Analysis

PALM data analysis of dual color images was done in a step-wise fashion. Each two-color image was actually composed of two PALM imaging files; one for rsKame (green emission channel) and one for PAmCherry1 (red emission channel). The files are analyzed separately and then overlaid using a software program, "dualpalmplot", designed in the Bustamante lab by postdoctoral fellow Sanghyuk Lee. The rsKame and PAmCherry1 imaging files were analyzed using MATLAB based software "peakfindtool". Fluorescent "events" were selected based on two parameters. Parameter 1 was the threshold of individual pixel X fold brightness over total background (peak to background). Parameter 2 was the threshold of the sum of photons within the surrounding 7 x 7 pixels centered on the pixels identified with parameter 1 (total photon count). Both thresholds can be set manually. rsKame events were selected using a peak to background threshold of 6 fold and a total photon count threshold of approximately 2000. PAmCherry1 events were selected using a peak to background threshold of 6 fold and a total photon count threshold of approximately 2200. XY drift was tracked and correct using Au fiducial marker tracking as described previously (Chapter 2). All the fluorescent events for either rsKame or PAmCherry1 were compiled into two respective images. These images were directly overlaid using MATLAB based software "dualpalmplot".

Observable Mitochondrial Morphology via Two-Color PALM

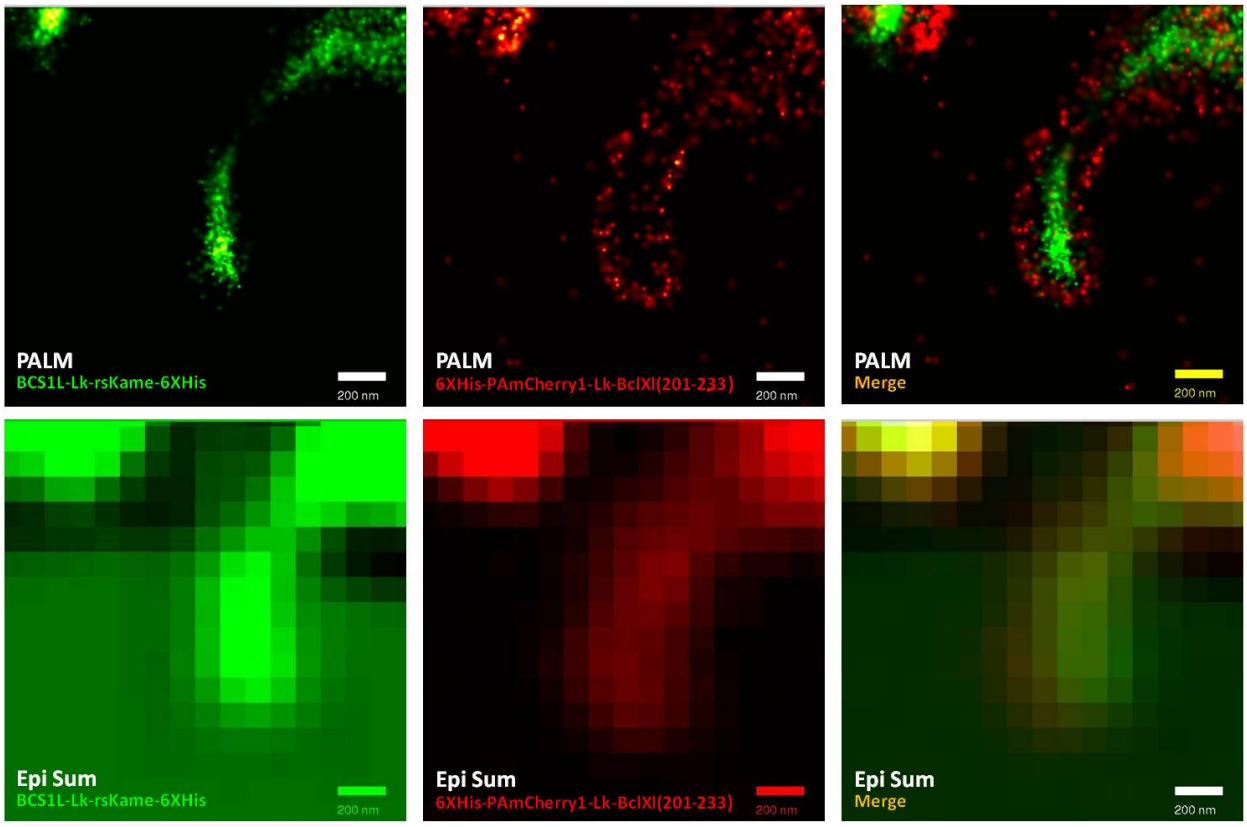

Figure 35: Two-color super resolution PALM image of distinct mitochondrial membranes. EpH4 cells were co-transfected with pBCS1L-Lk-rsKame-6XHis and p6XHis-PAmCherry1-BclXl(201-233) and incubated for 24 hours prior to imaging. Cells were PALM imaged using the two-color method, analyzed, and directly overlaid. *(Top row)* A mitochondrion imaged with the novel two-color PALM image allows for visualization of the two distinct mitochondrial membranes. *(Bottom row)* Diffraction limited summed epifluoresence (Epi Sum) of the same image, lacking distinct visual differentiation between mitochondrial membranes.

Using our new two color PALM protocol, we were able to easily elucidate the inner mitochondrial membrane from the outer mitochondrial membrane in both EpH4 cells and T-Rex HeLa cells (Figure 35). We were able to examine both punctate and elongated mitochondrial morphologies. We observed outer mitochondrial membranes in large rounded morphologies, in long tubular morphologies, and in branches. Outer membrane diameters can be clearly measured and range from <200 nm to >1.0 μm. Inner membrane morphologies showed a great variety as well. A large number of inner mitochondrial membrane morphologies showed the clear lines associated with the cristae. Some mitochondrial inner membranes only partially filled the outer mitochondrial membrane compartments. Still other mitochondrial inner membrane morphologies seemed disorganized. The inner mitochondrial membranes that showed clear cristae morphologies were most often associated with elongated outer mitochondrial membranes (Figure 36). The disorganized inner mitochondrial membranes were most often associated with the large rounded punctate outer mitochondrial membranes. The outer mitochondrial membranes that branched or had intermediate morphologies between elongated or punctate were often associated with only a partial filling of the compartment with the inner mitochondrial membrane of varying observed degrees of organization.

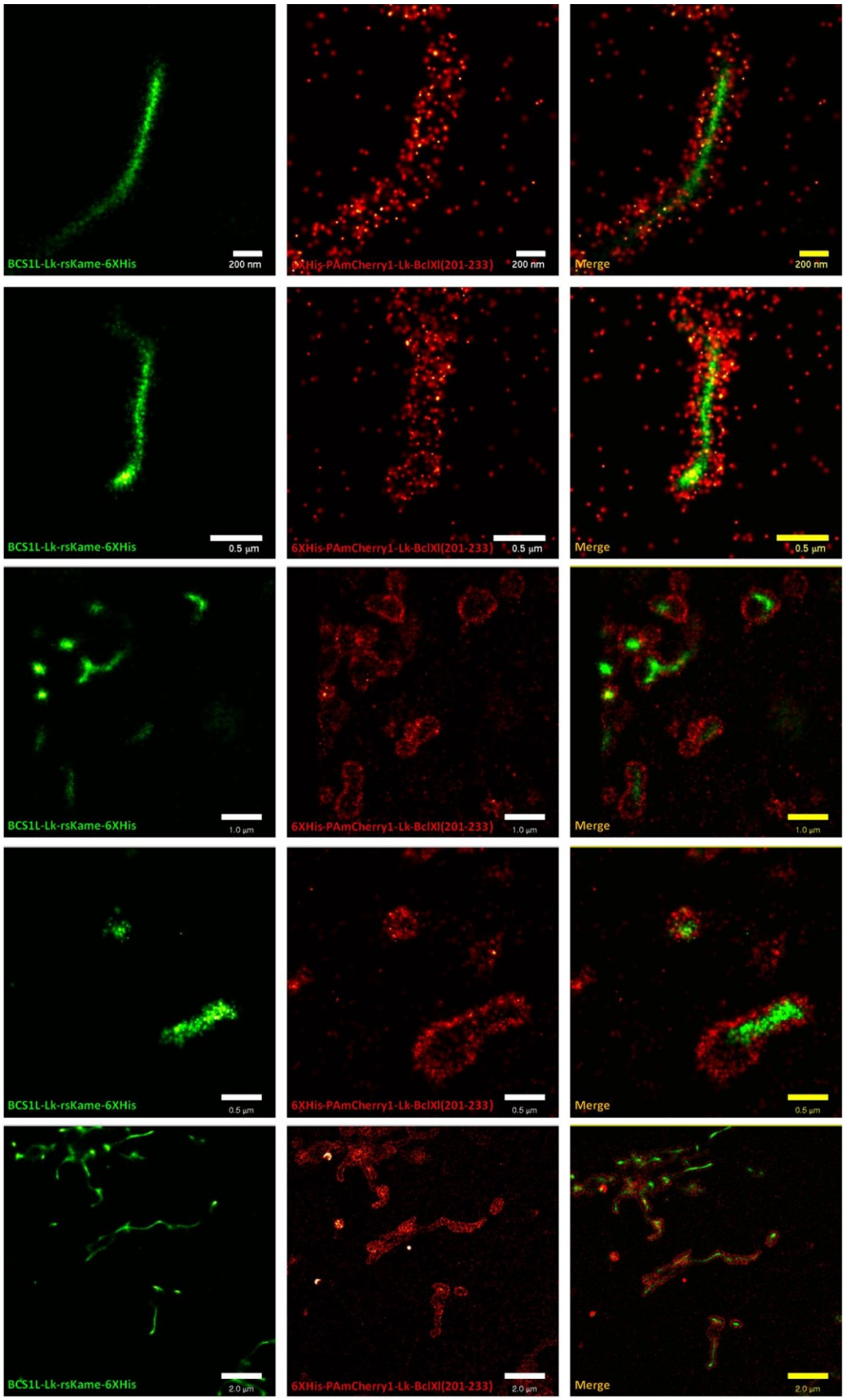
BCS1L-Lk-rsKame-6XHis
200 nm
6XHis-PAmCherry1-Lk-BclXl(201-233)
200 nm
Merge
200 nm
BCS1L-Lk-rsKame-6XHis
0.5 μm
6XHis-PAmCherry1-Lk-BclXl(201-233)
0.5 μm
Merge
0.5 μm
BCS1L-Lk-rsKame-6XHis
1.0 μm
6XHis-PAmCherry1-Lk-BclXl(201-233)
1.0 μm
Merge
1.0 μm
BCS1L-Lk-rsKame-6XHis
0.5 μm
6XHis-PAmCherry1-Lk-BclXl(201-233)
0.5 μm
Merge
0.5 μm
BCS1L-Lk-rsKame-6XHis
2.0 μm
6XHis-PAmCherry1-Lk-BclXl(201-233)
2.0 μm
Merge
2.0 μm

Figure 36: Two-color PALM imaging of mitochondrial membranes show various outer and inner membrane morphologies. EpH4 cells or HeLa cells were co-transfected with p(Hs)BCS1L-Lk-rsKame-6XHis and p6XHis-PAmCherry1-BclXl(201-233) and incubated for 24 hours prior to imaging. Cells were PALM imaged using the two-color method, analyzed, and directly overlaid. Extensive inner membrane remodeling is noted. The outer membrane adopts various shapes including punctate, elongated, and branched.

We now had all three components necessary for PALM imaging: a red PA-FP (PAmCherry1), a green PA-FP (rsKame), and a working protocol. We were, at last, able to begin tackling our original biological question, which was to examine the structural characteristics of mammalian Drp1 oligomerization during mitochondrial fission *in situ*.

FUTURE DIRECTIONS

SUPER RESOLUTION METHOD IMPROVEMENTS

Live Cell and Three Dimensional PALM Imaging

One of the holy grails of super resolution imaging is the ability to image dynamic processes in live cells. Super resolution would allow the most accurate visualization of live cell activities to date. Most super resolution microscopic techniques are limited by the time necessary to take an image and the stability of the fluorophores. Most dynamic changes in the cell occur on a time scale of seconds or a few minutes. Even organelles exhibit considerable movement within a few minutes. Current PALM imaging methods are much too slow. One method available in the literature is short high speed imaging combined with reversibly switchable dyes or fluorescent proteins of live proteins. By taking temporally short images at high speed imaging rates, the movement of the cellular components is mitigated. Further studies into live cell PALM imaging are warranted. Three dimensional PALM imaging has been detailed in the literature using combinations of analysis algorithms, two-photon illumination, and confocal scanning technology. However, the method can use considerable improvement to become more ubiquitous and also warrants further study.

Shortened Experiment Times via Simultaneous Imaging

One of the limitations of two-color PALM imaging is the necessity of consecutive imaging of the different colors. Simultaneous imaging of multiple colors could shorten the imaging time of each sample by half. In order to image two colors concurrently, the sample would need to be illuminated with two excitation laser wavelengths and one activation wavelength. The light emitting from the sample would need to be split and directed through two different emission filters before hitting one or two detectors. The photoactivation strength needed for both fluorophores would need to be fairly similar or else the concurrent setup would not allow for a shortened imaging time. The setup could be expanded to additional colors via additional fluorophores, emission filters, and/or excitation wavelengths.

Multicolor PALM Imaging

Our two-color PALM method has allowed for clean, unambiguous, super resolution imaging of up to two proteins at any given time. However, increasing the number of colors available for imaging as well as increasing the number of colors able to be imaged per sample could vastly improve the usability of the PALM technology.

There are severe limitations in the development of new photoactivatable fluorescent protein colors. Any fluorophore that is excited close to the commonly used 405 nm activation wavelength is going to undergo similar problems as we experienced with Dronpa. Photoactivatable fluorescent proteins in the far red spectra are limited by the mutations necessary for photoactivatablility. The mutations necessary for achieving the far red spectrum are often at the same location as the mutations necessary for photoactivation and incompatible with each other. However, we can use existing photoactivatable proteins, dyes, and small molecules with overlapping emission spectra if we have emission filters with very narrow wavelength bands. If their excitation spectra also overlap, then we can use the previously mentioned concurrent imaging and detection theories to expand the number of colors we can image. For example, we could potentially image rsKame, mEos2, and PAmCherry1 using three narrow emission filters, sequential imaging of rsKame and mEos2/PAmCherry1, and concurrent imaging of mEos2 and PAmCherry1. Expanding the color palette of PALM fluorophores by emission filters, illumination strategies, or additional dyes are crucial for expanding the biological use of PALM imaging.

MATERIAL AND METHODS

STANDARD TECHNIQUES AND STARTING MATERIALS

Molecular biology techniques that are considered standard were performed as are commonly described. These include polymerase chain reaction (PCR), restriction digest, ligation, and transformation. Minipreps of plasmid DNA from DH5α *E. coli* were performed using the Zippy Plasmid Miniprep Kit from Zymo Research and gel extractions were performed using the Zymoclean Gel DNA Recovery Kit from Zymo Research. All sequencing was performed using non-premixed sequencing reactions through Sequetech, Inc. All PCR, mutagenesis, and sequencing primers were synthesized through Integrated DNA Technologies, Inc. PCR and sequencing primers are listed in the Table 4. All enzymes used for molecular cloning were purchased from New England Biolabs. The base materials for LB broth, solid media plates, and the antibiotics were purchased from Sigma Aldrich. LB broth consisted of 10 g/L bacto-peptone, 5 g/L yeast extract, and 10 g/L NaCl. The solid media plates were made with LB and 1.5% (w/v) agar. The antibiotics used were appropriate to the *E. coli* being cultured. The antibiotics and concentrations used were 100 mg/L ampicillin and 30 mg/L kanamycin.

CLONING OF MAMMALIAN EXPRESSION VECTORS

Two mammalian expression vectors were used: pCMV Kan/Neo from Origene and pcDNA5/TO from Invitrogen. Photoactivatable fluorescent proteins (PA-FPs) used for the studies were rsKame and PAmCherry1. PAmCherry1 was a generous gift from the Liphardt lab (University of California, Berkeley). All cloning techniques including primer synthesis and

sequencing confirmations were done as described in Standard Techniques and Starting Materials and the list of cloning primers is detailed on Table 4. A Kozak consensus sequence GACACC was added directly N-terminal of the ATG start codon in all constructs to promote translation.

p6XHis-PAmcherry1-Lk-BclXl(201-233) had already been built in Chapter 2. pBCS1L-Lk-rsKame-6XHis and p(TO)BCS1L-Lk-rsKame-6XHis had already been built in Chapter 2 under the names pBCS1L-Lk-DronpaV157L-6XHis and p(TO)BCS1L-Lk-DronpaV157L-6XHis. *Homo sapiens BCS1L* was obtained from Open Biosystems. pHsBCS1L-Lk-rsKame-6XHis and p(TO)HsBCS1L-Lk-rsKame-6XHis was built by removing murine BCS1L(1-160) from pBCS1L-Lk-rsKame-6XHis via digestion with EcoRI and PstI or PmeI and PstI respectively and replacing it with *Homo sapiens* BCS1L(1-160) (HsBCS1L(1-160)). Prior to insertion, restriction sites EcoRI and PstI were added to HsBCS1L(1-160) by PCR. The same process was repeated to create pHsBCS1L-Lk-mEos2-6XHis from pBCS1L-Lk-mEos2-6XHis.

CELL CULTURE

Two different cell types were used: murine EpH4 (mammary gland epithelial) and *Homo sapiens* T-Rex HeLa (cervical cancer). EpH4 cells were originally isolated by C. Roskelly. Cells were already in house. T-Rex HeLa cells were purchased from Invitrogen. All cell reagents were purchased from University of California, San Francisco Cell Culture Facility. The EpH4 cells were cultured in DMEM with 2% FBS with added 5 mg/L of insulin and 50 mg/L gentamycin. T-Rex HeLa cells were cultured in Modified Eagle's Medium (MEM) with10% tetracycline free FBS, 1% penicillin/streptomycin, and 5 mg/L blasticidin to maintain the stably transfected tetracycline repressor gene. Cells were grown at 37ºC with 5% CO_2.

CELL TRANSFECTION AND INDUCTION

Mammalian cells were transfected with one of two lipid based commercial transfection reagents. EpH4 cells were transfected with Lipofectamine2000 (Invitrogen). Cells could be transfected in media with serum or without with little change in efficiency. Cells were transfected for 4-8 hours and then incubated for at least 24 hours at 37ºC and 5% CO_2 prior to imaging. T-Rex HeLa cells were transfected with Xfect (Clontech). Cells could be transfected in media with serum, important because HeLa cells died quickly in the absence of serum. Cells were again transfected for 4-8 hours and then incubated for at least 24 hours at 37ºC and 5% CO_2 prior to imaging. T-Rex HeLa cells transfected with genetic constructs on the pcDNA5/TO backbone were induced with 1 μg/mL doxycycline (Invitrogen/Life Technologies) in growth media for 4 hours prior to fixation.

LIVE CELL IMAGING WITH SCANNING CONFOCAL MICROSCOPE

Cells were imaged on the Nikon Eclipse TE2000-S scanning confocal microscope (Nikon Instruments Inc.). Cells were plated on MatTek imaging tissue culture plates (MatTek Corporation). MatTek imaging tissue culture plates have a #1.5 glass slide in the center of the plate for high quality imaging. Cells were imaged *in vivo* and in growth media. When necessary, mitochondrial networks were labeled with MitoTracker Red CMXRos (Life Technologies/Invitrogen) at 30 nm concentration. MitoTracker Red CMXRos labeled cells were

imaged by laser excitation at 561 nm and the fluorescence was collected with a 663-738nm emission filter. Cells transfected with rsKame were imaged by laser excitation at 488nm and the fluorescence was collected with a 510-560 nm emission filter. When both the PA-FP and MitoTracker Red CMXRos are imaged in the same cells, the different excitations were taken consecutively. Images were analyzed and overlaid using ImageJ.

SAMPLE PREPARATION AND TWO-COLOR PALM IMAGING

Prior to fixation, cells were plated on fibronectin coated acid washed 25 mm round #1.5 glass slides. Twelve hours prior to fixation, cells were fed 100 nm or 40 nm Au fiducial markers coated in FBS (60,000 particles/mL). Cells were fixed with 1% formalin (Sigma Aldrich) in 1X PBS or 1X PHEM (see Table 5) for 10 minutes then washed five times with 0.2 μm filtered 1X PHEM. Fixed cells were imaged in 1X PHEM.

The mitochondrial focal plane was set using 488 nm mercury arc lamp excitation. The sample illumination laser angle for TIRF or pseudo-TIRF was set by illumination of the 100 nm or 40 nm Au fiducial markers (Microspheres-Nanospheres) with 561 nm laser (22 W/mm^2). To first image rsKame the sample was illuminated with 488 nm excitation/activation laser (5.87 W/mm^2) and the piezo-stage controlled Z feedback was set. The sample was then co-illuminated with the 405 nm activation laser at 0.61 mW/mm^2. Fluorescent data was collected at 20 Hz with the 525 nm emission filter (range 25 nm) until all molecules were photobleached. This concluded the first (green) image of the two-color set. Before changing excitation lasers and emission filters for PAmCherry1 imaging, the Z feedback was turned off prior to stopping the 488 nm and 405 nm lasers. The emission filter was changed to the 588-612 nm emission filter. To image PAmCherry1, the sample was illuminated with the 561 nm excitation laser (22 W/mm^2) and the Z feedback for the stage was set. The 405 nm activation laser was turned on at 0.6 W/mm^2 and slowly increased to 6.0 W/mm^2 over time in order to maintain a visually constant number of events throughout the data collection. Fluorescence data was collected at 20 Hz until all molecules were photobleached. The Z feedback was turned off before turning the lasers off. This concluded the second (red) image of the two-color set.

TWO-COLOR PALM ANALYSIS

Each of the two PALM imaging movies per two-color PALM image is analyzed separately and then overlaid using the MATLAB based software program "dualpalmplot" (designed in the Bustamante lab by Sanghyuk Lee). The individual imaging files were analyzed using a MATLAB based software "peakfindtool". Fluorescent "events" were selected based on the two parameter thresholds for individual pixel brightness over background and 7 x 7 pixel sum of photons centered on pixels identified with the first parameter threshold respectively. Each pixel equals 106.6 nm; therefore, each event's PSF center is separated spatially by 700 nm. rsKame events were selected using a peak to background threshold of 6 fold and a total photon count threshold of approximately 2000. PAmCherry1 events were selected using a peak to background threshold of 6 fold and a total photon count threshold of approximately 2200. XY drift was tracked and corrected using Au fiducial marker tracking as described previously (Chapter 2). All the fluorescent events for either rsKame or PAmCherry1 were compiled into two respective images. These images were directly overlaid using MATLAB based software "dualpalmplot".

Chapter 4: Determination of Structural Characteristics of Drp1 Fission Rings *In Situ*

INTRODUCTION

Mammalian dynamin related protein 1 (Drp1) is the key dynamic player in mitochondrial fission. During mitochondrial fission, Drp1 is recruited to the mitochondrial constriction sites through unknown mechanisms and forms an oligomeric helical ring around the mitochondrial outer membrane. Dynamic constriction is driven by GTP hydrolysis, resulting in the scission of the mitochondrial outer membrane and the division of one mitochondrial tubule into two.[73] Using the novel PALM protocol developed in Chapter 3, we chose to examine the structural properties of Drp1 helical rings during the fission process *in situ*.

DYNAMIN-RELATED GTPase (Dnm1) and DYNAMIN RELATED PROTEIN 1 (Drp1)

A brief overview of mitochondrial fission and fusion was previously described in Chapter 1. Here we will discuss further mitochondrial fission and the role of dynamin related protein 1 (Drp1). Dynamins are GTPase proteins responsible for the scission of vesicles formed at the cellular or organelle membranes during endocytosis or vesicle movement from one organelle to another.[160] In *Saccharomyces cerevisiae*, the dynamin-related GTPase (Dnm1) protein is responsible for mitochondrial fission and was characterized by Janet Shaw in 1998.[161] Dnm1 has an N-terminal GTPase and a C-terminal GED with coiled coil domains in the middle of the protein. Disruption of Dnm1 resulted in an interconnected or collapsed mitochondrial net. Overexpression of Dnm1 resulted in a wild type mitochondrial morphology. GFP tagged Dnm1 co-localized with labeled mitochondria, a subcellular localization that was confirmed biochemically. Dnm1 is found predominantly associated with mitochondria. Loss of Dnm1 showed no effect on other organelles or endocytosis.[161,162] Dnm1 localization to mitochondrial constrictions sites was first characterized by immunogold labeling and later by time lapse confocal microscopy.[71,162] Not every Dnm1 puncta resulted in mitochondrial fission, though a significant subset did. Dnm1 helical ring self assembly around the mitochondrial outer membrane has been shown by direct imaging of dividing mitochondria using electron microscopy and *in vitro* self assembly of helical ring formation with purified Dnm1, and is dependent on GTP binding.[73,163] GTP binding promotes a conformational change in Dnm1 that allows for self assembly into helical rings. Recently, *in vitro* Dnm1 helical structures around liposomes examined with cryo-EM have be shown to have a novel two start helical arrangement with a helical pitch of approximately 30 nm.[84] The base assembly unit of Dnm1 is a tetramer, as opposed to the dimer base assembly unit of dynamin. Dynamin assembles as a single start helix.[84] The *in vitro* self assembled helical purified Dnm1 rings around liposomes were caused to further constrict by the addition of GTP and subsequent GTP hydrolysis, changing the outer diameter of the ring from a mean of 111 nm in the absence of GTP to a mean of 71 nm in the presence of GTP, a dynamic change of 40 nm.[84,163]

Mammalian Drp1 was first described by Kazuhisa Nakayama in 1997 and characterized by Alexander van der Bliek in 1998.[164,165] Drp1 is characterized by its N-terminal GTPase domain,

its C-termimal GED, and middle coiled coil domains. The middle part of the protein gives the overall structure to the protein. Loss of Drp1 results in a highly interconnected mitochondrial network, demonstrating a disruption of mitochondrial fission. Overexpression of Drp1 results in a highly fragmented mitochondrial network, demonstrating an overall increase in mitochondrial fission.[78] Drp1 has also been implicated in perixosome and vesicle formation but its role is controversial. YFP tagged Drp1 has been shown to localize to the mitochondrial network, though the majority was localized to the cytosol.[78] Drp1 actively cycles between the cytoplasm and mitochondrial tubules during the fission processes of healthy cells.[166] Drp1 translation to mitochondria *in vivo* is regulated by the phosphorylation or dephosphorylation of Ser637 (*Homo sapiens*).[167] Drp1, in response to cytosolic cyclic AMP levels, is phosphorylated by cyclic AMP-dependent protein kinase, also denoted protein kinase A (PKA).[168] Drp1 is dephosphoylated by calcineurin in response to cystosolic Ca^{+2} ion levels. Dephosphorylated Drp1 predominantly localizes to mitochondria; whereas, phosphorylated Drp1 is maintained in the cytosol.[169] During apoptosis amd in the presence of Bcl-2-assocated X protein (Bax) at the fission site, Drp1 is sumolyated and stably associates with the mitochondrial tubule, promoting increased fission.[166]

Purified Drp1 has been shown to form self assembled helical rings in the presence and absence of liposomes *in vitro*. Ring and helix formation is dependent on GTP binding. Those same helical rings will undergo constriction with increased GTP and the forward movement of GTP hydrolysis.[61,170] Drp1 is recruited to the mitochondria by an unknown mechanism. Stimulation of Drp1 recruitment to the mitochondria includes various apoptotic stimuli as well as unknown homeostatic factors. However, whether Dnm1 or Drp1 self assembled helical rings are sufficient for fully completing membrane scission is still controversial, as there has been no evidence of liposome scission in the *in vitro* experiments with purified Dnm1 or Drp1, though there is significant membrane constriction observed when GTP hydrolysis is active.[78,84] This may be due to the ability of liposomes to stretch. For membrane scission with Dnm1 or Drp1 to take place, it is likely that regulation of the size of the helical ring is critical for there to be enough membrane curvature for scission to occur.[15] Other fission machinery components clearly have important roles to play.

ADDITIONAL MITOCHONDRIAL FISSION MACHINERY COMPONENTS

The additional fission machinery components vary significantly between *Saccharomyces cerevisiae* and mammalian systems. The additional fission machinery of yeast has been well characterized, up to and including a crystal structure of the mitochondrial membrane bound portion of the machinery.[171] The additional components of the yeast fission machinery are fission protein 1 (Fis1), mitochondrial division protein 1 (Mdv1), and CCR4-associated factor 4 (Caf4).[83,163,172] Caf4 is considered interchangeable with Mdv1. Fis1 is a small C-terminally anchored protein. The 18 kDa protein's N-terminus is located in the cytoplasm and is made of six alpha-helices. In yeast, Fis1 is found randomly and uniformly distributed on the outer mitochondrial membrane and can serve as the platform for Mdv1 and Dnm1.[83] Mdv1 is localized near the mitochondria but not membrane bound. The 80 kDa protein has an N-terminal domain that interacts with Fis1 and a C-terminal domain that interacts with Dnm1.[172] Caf4 is a paralogue of Mdv1 that can replace Mdv1 but is otherwise nonessential.[171] The overall mechanism of interaction between Dnm1 and Mdv1 is unknown, but continued interaction between Dnm1 and Mdv1 throughout the completion of fission is necessary.[172]

Mammalian fission machinery components are less well understood and additional components are continuously being discovered. The majority of the mammalian fission machinery was discussed in detail in Chapter 1. The mammalian fission machinery has two direct homologues to yeast Dnm1 and Fis1, which are Drp1 and hFis1. However, hFis1 does not seem to play the same role in the mammalian system as in the yeast. In fact, it is controversial as to what role hFis1 plays in mitochondrial fission at all. Several studies have examined the knockdown and over expression of hFis1 and come up with competing results. Some studies find that the knockdown of hFis1 disrupts mitochondrial fission and other studies find no effect. Some studies find over expression of hFis1 increases mitochondrial fragmentation and other studies again show no effect on mitochondrial morphology.[60,65,77,173] Mitochondrial fission factor (Mff) is a recently characterized 38 kDa mitochondrial fission protein that seems to play a more definitive role in mitochondrial fission. Knockdowns of Mff show a clear disruption of mitochondrial fission and highly interconnected mitochondrial networks. Overexpression of Mff results in an extensive increase in mitochondrial fission. Labeled Mff and Drp1 co-localize with each other as punctate spots.[65,76,174] MiD49/51 and Endophilin B1 are both additional mitochondrial fission components that are not well understood. MiD49/51 are 49 kDa and 51 kDa proteins that have been recently characterized to play a role in mitochondrial fission but their role or mechanism is, as yet, unknown.[82] Endophilin B1 likely plays a role after Drp1 is recruited to constriction sites. The 41 kDa protein likely stabilizes or increases membrane curvature at already constricted sites on the mitochondrial outer membrane.[74] Though there is evidence that an inner mitochondrial membrane fission machinery exists, the components of that machinery and the mechanism are still unknown for both yeast and mammalian systems.[83]

ROLE OF THE ENDOPLASMIC RETICULUM IN MITOCHONDRIAL FISSION

Recently, the role of the endoplasmic reticulum (ER) in mitochondrial fission has become more prominent. It has long been known that the mitochondrial network and endoplasmic reticulum make frequent contacts to exchange calcium ions, lipids, etc., but it now seems that the ER has an additional mechanical role in mitochondrial fission.[175] The laboratories of Gia Voeltz and Jodi Nunnari have recently shown that the ER actually wraps around the mitochondrial outer membrane, physically constricting the membrane down to approximately 109 nm.[71] This has been demonstrated in both mammalian and yeast systems and fits well with what has been observed with the measured diameters of *in vitro* self assembled helical rings of Drp1/Dnm1 pre-constriction around liposomes (~109 nm). They also demonstrated through time lapse confocal microscopy of labeled mitochondrial and ER networks that mitochondrial fission occurs at puncta where the ER network wraps around mitochondrial tubules. In addition, they showed that Drp1 localized to these junctions as well.[71] Xiaowei Zhuang showed mitochondrial constriction by the ER using two-color super resolution imaging with small molecule organelle dyes.[176] It now seems definitive that physical constriction of the mitochondrial outer membrane is necessary for mitochondrial fission by Drp1 or Dnm1.

CURRENT MITOCHONDRIAL FISSION MODELS

In *Saccharomyces cerevisiae*, the fission mechanical model is as follows. The endoplasmic reticulum wraps around the mitochondria and physically constricts the mitochondrial tubule. Dnm1 is recruited to the constriction site and interacts with the Fis1 bound Mdv1. GTP

hydrolysis proceeds, causing a conformational change in the Dnm1 helical ring that results in further constriction of the outer mitochondrial membrane until membrane scission occurs.[83] In the less well understood mammalian system, the endoplasmic reticulum again physically constricts the mitochondrial tubule. Drp1 is recruited to the constriction site to form a helical ring by an unknown mechanism. At the site, Drp1 interacts with Mff and potentially hFis1 as well as MiD49/51. GTP hydrolysis proceeds, causing a conformational change in the ring, constricting the membrane further until membrane scission occurs.[15]

RESULTS AND DISCUSSION

EXPRESSION AND PALM IMAGING OF Drp1 FISSION RINGS

Molecular Cloning and Expression of rsKame tagged Drp1

In live growing cells, Drp1 is most commonly found in cytoplasm in dimers and tetramers.[163] During mitochondrial fission, the Drp1 is recruited to the mitochondria and forms helical rings. Drp1 helical rings on mitochondria have been examined in live cells via confocal microscopy and in fixed samples by electron microscopy.[78] However, the confocal microscopic studies are limited by the diffraction limit and the electron microscopic studies of mitochondria can cause mitochondrial morphological changes. In order to examine the structural properties of Drp1 helical rings *in situ*, we strove to visualize the helical ring at super resolution while maintaining the native mitochondrial network morphology via gentle sample preparation (Figure 37). For that we chose our previously described (Chapter 3) two-color PALM imaging protocol.

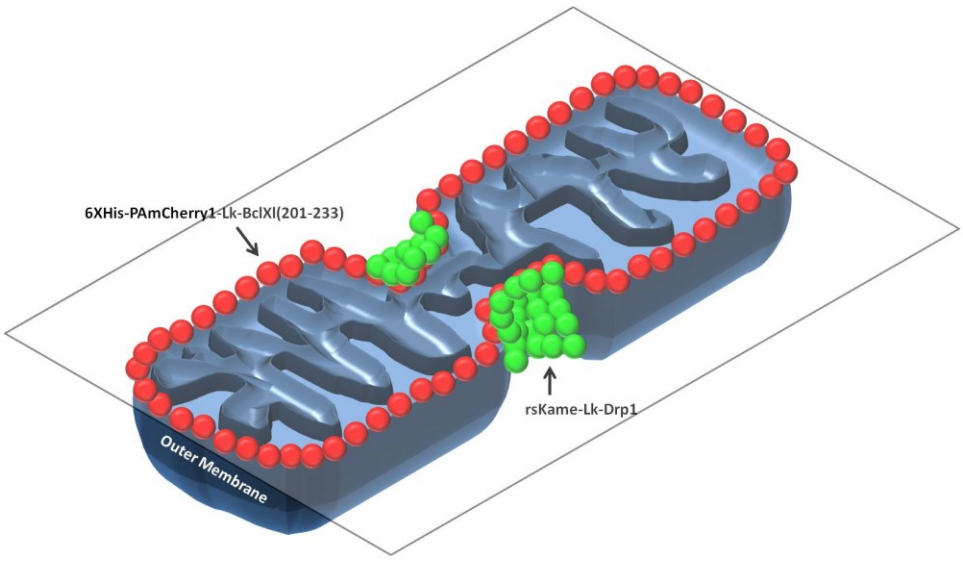

Figure 37: Model of two-color PALM imaging scheme Drp1 oligomeric helical rings constricting the mitochondrial outer membrane. The mitochondrial outer membrane is decorated with targeted and membrane embedded PAmCherry1. Drp1 is C-terminally fused to rsKame with a linker to prevent rsKame from interfering with Drp1 oligomerization or GTPase activity.

We set out to image Drp1 rings by labeling the outer mitochondrial membrane with PAmCherry1 and fusing Drp1 to rsKame. We already had a functional and characterized genetic construct for labeling the outer mitochondrial membrane with PAmCherry1 (p6XHis-PAmCherry1-Lk-BclXl(201-233)). Therefore, we only had to build a genetic construct to label Drp1 without interfering with function. We chose to use an inducible promoter and the TetOn system from Invitrogen. The TetOn system involved the T-Rex HeLa cell line, which, as mentioned previously, has a stably transfected tetracycline repressor maintained by blasticidin selection. We used the pcDNA 5/TO plasmid from the same system as our vector backbone. pcDNA 5/TO has 2 tetracycline (Tet) repressor binding sites on a CMV promoter. When a T-Rex HeLa cell is transfected with a genetic construct on the pcDNA 5/TO backbone, the Tet repressors bind to the repressor binding sites and prevent RNA polymerase from binding and transcribing the gene. However, when tetracycline or its analogue, doxycycline, are added to the cell, the antibiotics bind to the Tet repressor molecules and prevent the molecules from binding to the Tet repressor binding sites. The gene can then be expressed. The amount of added antibiotic and the time of expression determine the amount of protein that is expressed. The actual amount of expressed protein varies from cell to cell. Previous work in the literature has shown the localization of Drp1 fused to GFP is improved when GFP is fused to the N terminus of Drp1.[78] Based on this information, we also chose to fuse rsKame to the N-terminus of *Homo sapiens* Drp1 (Figure 38). We began with an initial construct of rsKame fused to Drp1 with a three amino acid linker but had difficulties with Drp1 localization in downstream applications. (Data not shown) We chose instead to use a fourteen amino acid flexible linker (AAAGGGSGGGSGGG) between rsKame and Drp1 in order to prevent rsKame from

interfering with the function of Drp1. A fourteen amino acid linker will add negligible error to our downstream measurements. We cloned rsKame into pcDNA 5/TO. The fourteen amino acid linker was added via PCR to the N-terminal end of *DRP1*. *DRP1* was then cloned into the prsKame-5/TO creating prsKame-lk-Drp1-5/TO.

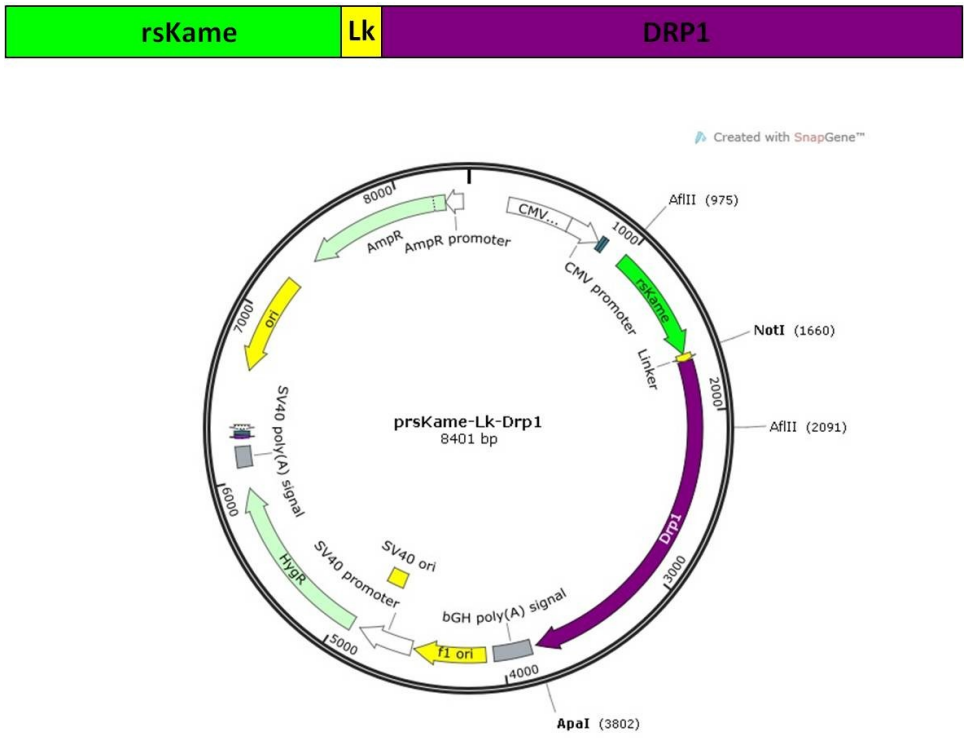

Figure 38: Genetic construction and cloning map of Drp1 fused to the C-terminal of rsKame and separated by a short flexible linker. rsKame was inserted into pcDNA5/TO with AflII and NotI creating prsKame. The short flexible linker was added to the N-terminus of *DRP1* by PCR and inserted into prsKame with NotI and ApaI to create prsKame-Lk-Drp1.

Drp1 Two-Color PALM Imaging Protcol

During our initial attempts of imaging, T-Rex HeLa cells were plated 12-24 hours prior to transfection on acid washed fibronectin coated #1.5 glass slides. Cells were co-transfected with prsKame-lk-Drp1-5/TO and p6XHis-PAmCherry1-Lk-BclXl(201-233) via X-fect. Cells were fed FBS coated 40 nm Au particles (60,000 particles/mL) and grown for 36 hours post transfection at 37°C prior to imaging. prsKame-lk-Drp1-5/TO was expressed by the addition of 1 µg/mL Dox for 4 hours. Cells were washed in 1X PHEM and fixed for 10 minutes in 1% formalin in 1X PHEM. Cells were washed again in 1X PHEM and imaged using the two-color PALM protocol described in Chapter 3. Most of the rsKame-Drp1 protein was still localized in

the cytoplasm. This high cytoplasmic percentage made determining Drp1 rings around the mitochondria delineated in PAmCherry1 impossible.

We consulted with the Nunnari lab at University of California, Davis and, upon their advice, added two additional reagents to our sample preparation for our second imaging attempt: staurosporine and z-vad-fmk. Staurosporine is a chemical that induces apoptosis. During apoptosis, mitochondrial fission is greatly increased and larger portions of the cytoplasmic Drp1 populations are recruited to the mitochondria. If apoptosis is allowed to continue to completion, the cell dies. Dead cell or cells close to death are very difficult to image due to their rounded cell morphology. In addition, apoptotic cells will exhibit extremely punctate mitochondrial morphologies. In order to mitigate the downstream apoptotic effects like rounding of the cell and death, we inhibited the caspases released by the staurosporine induced apoptosis by pre-treating the transfected cells with a caspase inhibitor, z-vad-fmk. Our new pre-imaging treatment is briefly described below.

1. Plate T-Rex HeLa cells 24-48 hours prior to transfection.
2. Co-transfect cells with prsKame-lk-Drp1-5/TO and p6XHis-PAmCherry1-Lk-BclXl(201-233).
3. Incubate cells 24-36 hours.
4. Add doxycycline and caspase inhibitors and incubate at 37°C for 110 minutes.
5. Add staurosporine and incubate at 37C for another 100 minutes.
6. Label mitochondria with MitoTracker Deep Red
7. Wash cells.
8. Fix cells.
9. Wash cells.
10. Image.

T-Rex HeLa cells were plated on acid washed fibronectin coated #1.5 glass slides and grown to ~70% confluency (24-48 hours) at 37°C in growth media with blasticidin selection. Cells were co-transfected with prsKame-lk-Drp1-5/TO and p6XHis-PAmCherry1-Lk-BclXl(201-233) with Xfect. A total of 6 µg of DNA was transfected per slide. Post transfection, cells were fed FBS coated 40 Au fiducial markers (60,000 particles/mL). Cells were incubated at 37°C for 24-36 hours post transfection with blasticidin selection. Approximately four hours prior to imaging, doxycycline and z-vad-fmk were added to the total growth media to final concentrations of 0.75 µg/mL and 20 mM respectively. Cells were incubated for 110 minutes at 37°C. Staurosporine was then added to the media to a final concentration of 1 µM and cells were incubated for another 100 minutes at 37°C. Immediately after the total 3.5 hours of doxycycline induction, caspase inhibitor treatment, and staurosporine treatment, mitochondria were labeled with MitoTracker Deep Red at a final concentration of 30 nM. Treated cells were washed 3-5 times in 1X PHEM then fixed in 1% formalin in 1X PHEM for 10 minutes at room temperature. Post fixation, cells were washed 5-7 times in 1X PHEM. Cells were imaged using the two-color PALM protocol as described in Chapter 3.

In order to clearly image the Drp1 ring formation on mitochondria during fission, we needed an induced protein level that ensured a high level of rsKame fused Drp1 incorporation in the rings. However, we had to keep the expression levels of rsKame fused Drp1 low enough such

that the cytoplasmic rsKame fused Drp1 would not create a high background. We accomplished this mostly by using a shorter induction time with a medium concentration of doxycycline. We labeled the mitochondrial organelle network with MitoTracker Deep Red in order to set the focal planes during imaging. Because the mitochondrial outer membrane was delineated in PAmCherry1, which is a dark to red PA-FP, we had no method of setting the focal plane to best image the mitochondrial network. MitoTracker Deep Red is shifted to the far red spectra and does not have overlapping emission spectra with PAmCherry1. Therefore, in cells with mitochondria labeled with MitoTracker Deep Red and delineated in PAmCherry1, we could set the focal plane using the mercury arc lamp with an excitation of 561 nm and a far red 607-636 nm emission filter. The PALM imaging of PAmCherry1 is unaffected by the MitoTracker Deep Red labeling or the setting of the focal plane.

STRUCTURAL ANALYSIS OF Drp1 FISSION RING

PALM Image Analysis and Drp1 Fission Ring Identification, Structural Analysis, and Quantification

PALM analysis was completed as described in Chapter 3. After initial analysis, individual cells were screened by eye for PAmCherry1 delineated mitochondria that showed clear membrane boundaries. Post PALM analyses, approximately 36 cells (2/3 of cells imaged) were useful for further analysis. In each of the screened cells, the rsKame-lk-Drp1 image was overlaid over the PAmCherry1 labeled mitochondria image.

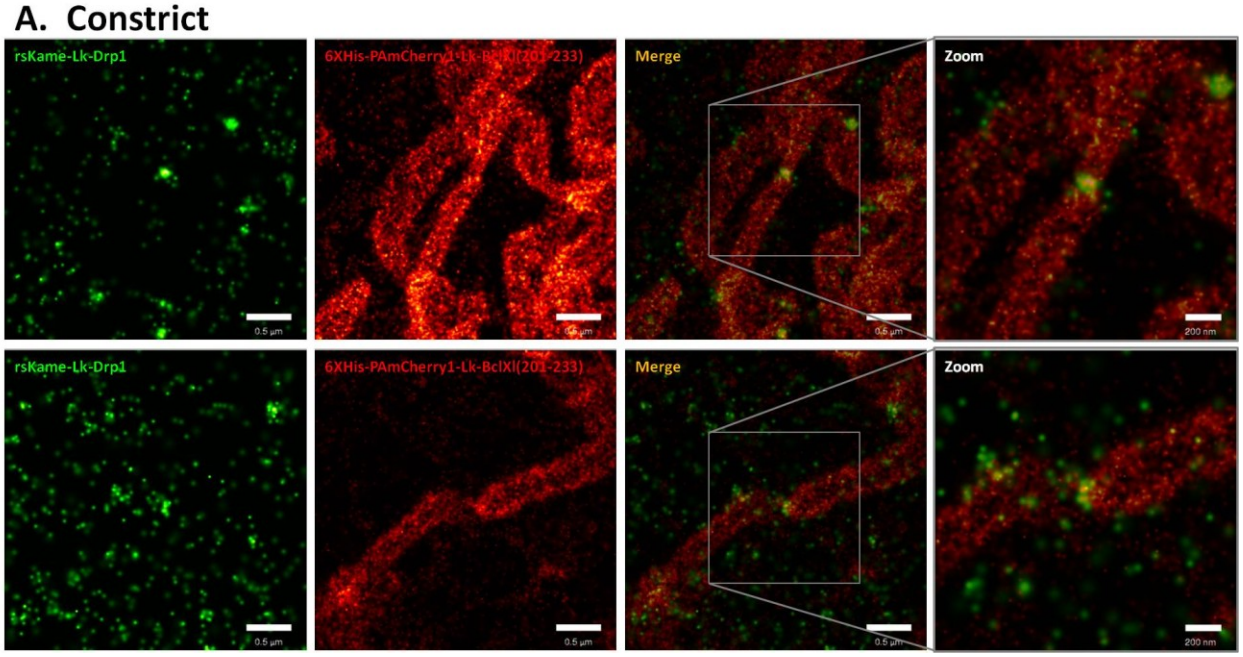

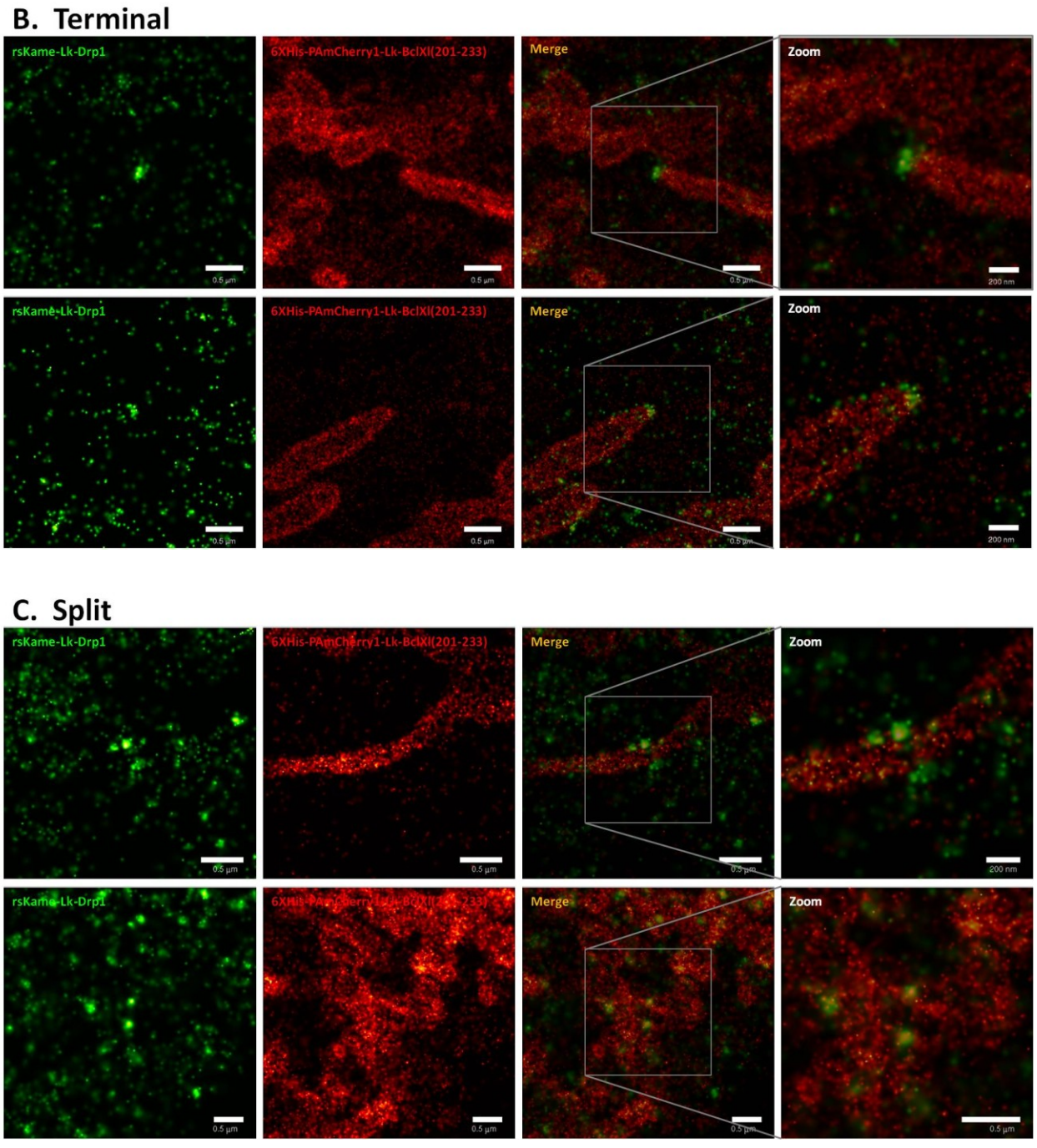

Figure 39: Drp1 adopts three different helical ring morphologies on mitochondria. Three different Drp1 morphologies were observed on mitochondria. A) The Drp1 "Constrict" morphology encircled the mitochondria at various stages of constriction. B) The Drp1 "Terminal" morphology was observed at the ends of mitochondria and was considered the end structure of the Drp1 helical ring directly following fission. C) The Drp1 "Split" morphology is a novel morphology observed as two Drp1 foci flanking the mitochondrial outer membrane but not fully encircling the mitochondria tubule.

Drp1 helical rings on mitochondria were classified in three different ways. Drp1 helical rings were termed "Constrict" if they completely encircled a mitochondrion, both at clear points of membrane constriction or completely circling unconstricted mitochondrial membrane (Figure 39a). We made the assumption the "Constrict" Drp1 rings were at various stages of mitochondrial fission. Drp1 helical rings were termed "Terminal" if they were observed at the ends of mitochondrion (Figure 39b). Based on the localization we made the assumption that "Terminal" Drp1 helical rings had completed mitochondrial fission. A third surprising morphology of Drp1 that was observed was the "Split "morphology (Figure 39c). We observed numerous events of mitochondria flanked by two small patches of Drp1 in line with each other on either side of the membrane. These were commonly found on mitochondria with larger diameters. These Drp1 helical rings were termed "Split".

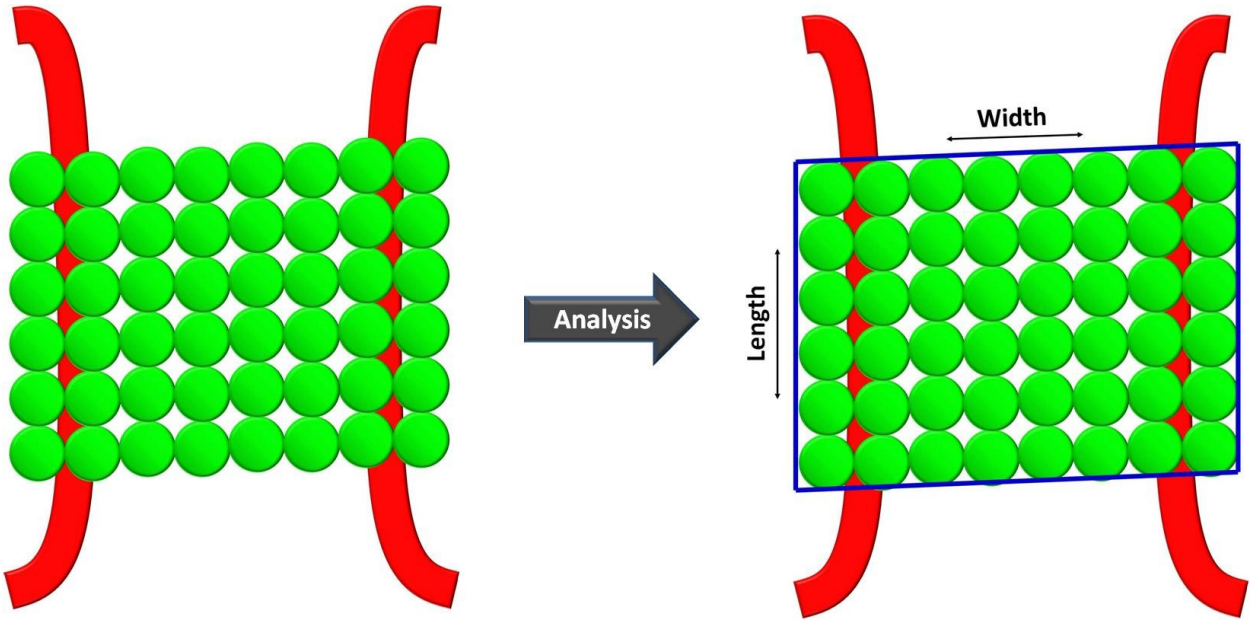

Figure 40: The diameter and length of the Drp1 fission structure was measured using a defined box. Drp1 fission structures were analyzed by drawing a box directly around the structure as defined by its super resolution fluorescence. Measuring the length and width of the box gives quantifiable structural data of each Drp1 fission structure.

Using the "box" tool in the MATLAB based software "dualpalmplot"; we outlined each Drp1 fission structure with a box (Figure 40). Side one measured the length of the Drp1 helical ring and side two measured the outer diameter of the Drp1 helical ring. We compiled the Drp1 helical rings from thirty six different cells. We measured N = 117 Drp1 structures with a "Constrict" morphology, N = 121 Drp1 structures with a "Terminal" morphology, and N = 54 Drp1 structures with a "Split" morphology. The means of the respective individual data sets were calculated using a Gaussian distribution as were the standard errors of mean (σ_M). The

medians were calculated directly from the individual data sets. The "Constrict" width mean is 201.4 nm ± 2.2 nm and has a median of 191.6 nm. The "Constrict" length mean is 137.5 ± 24 nm and has a median of 131.3 nm. The "Terminal" width mean is 161.3 nm ± 2.2 nm and has a median of 153.6 nm. The "Terminal" length mean is 116.6 nm ± 1.6 nm and has a median of 111.4 nm. The "Split" width mean is 395.4 nm ± 7.3 nm and has a median of 386.1 nm. The "Split" length mean is 134.8 nm ± 2.2 nm and has a median of 132.1 nm (Figure 41c).

A

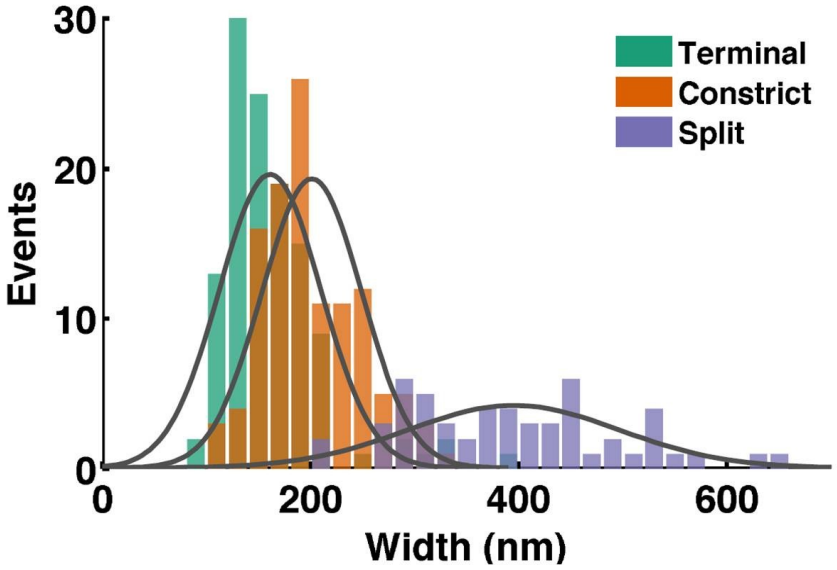

B

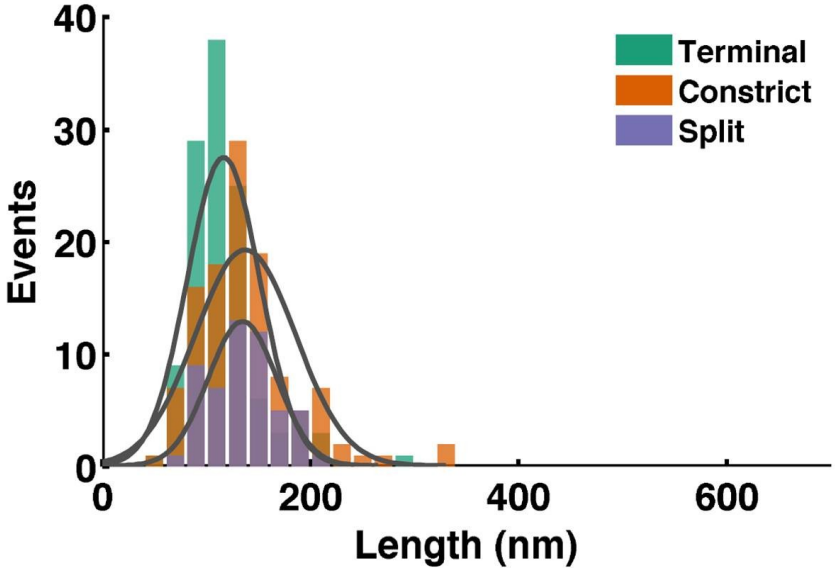

C

N	Drp1 Width	Mean $\pm$ σ_M	Median
117	Constriction	201.4 nm $\pm$ 2.2	191.6 nm
121	Terminal	161.3 nm $\pm$ 2.2	153.6 nm
54	Split	395.4 nm $\pm$ 7.3	386.1 nm

Drp1 Length	Mean $\pm$ σ_M	Median
Constriction	137.5 nm $\pm$ 2.2	131.3 nm
Terminal	116.6 nm $\pm$ 1.6	111.4 nm
Split	134.8 nm $\pm$ 2.2	132.1 nm

Figure 41: Quantification of Drp1 fission structure diameter and length. Thirty six cells were analyzed for the study. A) Drp1 helical ring diameter for three different morphologies (Constrict, Terminal, and Split) was quantified. The mean diameter for the Terminal morphology is decreased by 40 nm as compared to the mean diameter for the Constrict morphology. The Split morphology had the widest distribution of diameters. B) Drp1 helical length for the three morphologies (Constrict, Terminal, and Split) was quantified. The Constrict and Split morphologies had very similar mean lengths and standard errors of mean. The Terminal morphology had a slightly decreased length, consistent with Drp1 helical ring degradation post completion of mitochondrial fission. C) The three Drp1 fission structure morphologies were quantified. The means and standard errors of mean of the diameter and length distributions were calculated from the normal Gaussian fit. The medians of each data set are also calculated separately to account for any skew in the histogram of each distribution.

Our mean "Constrict" Drp1 helical ring diameter measurements are approximately 70 nm larger than published Dnm1 *in vitro* helical ring diameters visualized by electron microscopy prior to the addition of GTP. The same is true for the mean "Terminal" Drp1 helical ring diameter as compared to published Dnm1 *in vitro* helical ring diameters visualized by electron microscopy after the addition of GTP (Figure 41a). We hypothesize that the differences in absolute diameter is the result of the limits of PALM resolution (~25-30 nm) plus the bulk of the fluorescent protein itself (~1-3 nm) and possibly the linker to a small degree (~1-2 nm). This potentially added approximately 35 nm to either side of the Drp1 helical ring, explaining the differences in absolute measurement. This is likely the reason why both the "Constrict" and the "Terminal" Drp1 ring structures are increased by a similar amount. In addition, the size of the distributions of the "Constrict" and "Terminal" morphologies give additional information. The "Constrict" distribution spans a much larger diameter range, consistent with the fixation of Drp1 helical ring membrane constriction at various timepoints during mitochondrial fission. In contrast, the "Terminal" morphology distribution spans a much smaller diameter range, consistent with the morphology representing the end point of mitochondrial fission, post membrane scission. Regardless of the potential overestimation and operating under the hypothesis that the "Constrict" structures are immobilized at various stages of fission and the "Terminal" structures have fully completed fission and membrane scission, we were able to determine a clear dynamic change of approximately 40 nm in mean diameter between the "Constrict" structures and the "Terminal" structures. This change in mean diameter is consistent with published data on dynamic changes observed *in vitro* on purified Dnm1 helices on

liposomes examined with electron microscopy.[84] The mean measured length of the Drp1 helices was altered between the "Constrict" and "Terminal" structures but not significantly (Figure 41b). The slight reduction observed in "Terminal" Drp1 structures is most likely due to degradation post fission and membrane scission. Because of the uncertainty due to the limits of PALM resolution, we cannot make absolute measurements of the helical length. However, if we accept a 70 nm in total resolution error as previously proposed for the diameter measurements, and based on the *in vitro* measurements of Dnm1 assembled on liposomes (~30 nm helical pitch), we can estimate a mean of 2 helical turns for a two start Drp1 fission ring.[84] It is probable that Drp1 also forms a two start helix similar to the structure observed for Dnm1 and may also have a tetramer base assembly unit. Drp1 is known to form primarily tetramers in the cytoplasm.[78,84] In addition, based on the narrowness of our distribution, we can conclude that length of the Drp1 helix in fission is consistent. The "Split" structural morphologies also had a mean length consistent with "Constrict" and "Terminal" structures. This consistency in length leads us to believe that the "Split" morphology is not simply an artifact of the imaging or of apoptosis. We do not fully understand the "Split" morphology or what its role in mitochondrial fission may be. It does not fit with the current theory that Drp1 is recruited to the sites on the mitochondria that are constricted by the endoplasmic reticulum. Further study on these "Split" morphologies may be warranted.

FUTURE DIRECTIONS

FURTHER STUDIES ON DRP1 RELATED FISSION MECHANISM

Split Morphology

Perhaps one of the most unexpected results of the Drp1 PALM imaging was the visualization of the Drp1 morphology we termed "Split". As mentioned in the Results and Discussion section, we noticed a consistent feature in our images, where the mitochondrial outer membrane was flanked by two punctate spots of Drp1 on either side of the membrane. These spots were always directly across from each other in a line perpendicular to the line of the membrane tubule. The distance between the two spots varied with the diameter of the mitochondrion. However, the mean length of the Split morphology was consistent with that of the Terminal and Constrict morphologies. The Split morphology (N = 54) was less common than the total of Terminal and Constrict morphologies (N = 238), providing approximately 20% of the total morphologies noted. This unexpected split morphology throws into question the currently accepted fission mechanism. The presently understood mechanism describes a process where the ER constricts the mitochondrial tubule before Drp1 is recruited to the mitochondria.[71] However, in the Split morphology, the membrane is clearly not constricted prior to the presence of Drp1. It is also noted that the ER contacts the mitochondria at locations that do not result in fission, opening the question to the mechanism by which the ER choose to simply contact the mitochondria for content exchanges or to wrap around the tubules and physically constrict them.[175] Perhaps these small patches of Drp1, potentially not able to be visualized by confocal microscopy, mark future fission sites.

One way to test whether the Split morphology has any relation to marking fission sites is to image the ER, the mitochondrial outer membrane, and Drp1 all at once. This three color super resolution imaging is possible if we combine our PALM imaging protocol with the new super

resolution imaging with small molecule dyes recently published by Xiaowei Zhuang's group.[176] The imaging would require a camera able to image at faster rates with precise and narrow emission filters. With that additional equipment, we could label the ER with a small molecule dye in addition to our previous Drp1/mitochondrial outer membrane imaging protocol to image all three colors sequentially and merge them into an overall image. The visual combination of ER, mitochondrial outer membrane, and Drp1 in various stages of fission, including the Split morphology, could give a clearer perspective onto the beginning mechanism of mitochondrial fission, and perhaps novel insights into Drp1 recruitment to constrictions sites and how constriction sites are determined in general.

Force and Membrane Scission

An interesting and pronounced difference between Dnm1/Drp1 helical ring formation on liposomes *in vitro* and actual mitochondria *in vivo* or *in situ* is the lack of membrane scission when the Dnm1/Drp1 rings are formed on liposomes. Dnm1/Drp1 helical rings have not been shown to complete membrane scission on liposomes and often seem to form longer helices than are seen *in vivo* or *in situ*.[84,163] This is likely because a certain amount of membrane curvature is necessary for scission and the liposomes are too flexible. Another possibility is force. Liposomes are generally empty vesicles of a non viscous fluid and can be quite malleable. Mitochondria are full of membranes, proteins, fluids, etc. and therefore can only adopt a limited number of shapes. Perhaps the force generated by the pressure of the constriction of a single mitochondrion aides in increasing membrane curvature and driving forward membrane scission. Though a measurement of the force and pressure inside a single constricted mitochondrion would be very difficult to ascertain, it is still a question worth pursuing.

Regulation of Helical Length

The length of Dnm1/Drp1 helical rings is closely tied to membrane scission. The helical ring must be long enough to allow room for division. However, too long a helical ring will result in insufficient membrane curvature for successful scission. The regulatory mechanisms for the Dnm1/Drp1 helical rings are currently unknown. Our studies showed a narrow range of helical length consistent with tight regulation. Classic biochemical studies on over expression and knocked down expression on potential regulatory partners such as hFis1, Mff, or MiD49/51 are warranted.

Further Studies on Mechanisms and Interactions between Fission Machinery Components

Mff and hFis1 Interactions

The relative roles of Mff and hFis1 in the mammalian mitochondrial fission machinery are generally unknown. Mff has no direct homologue in the yeast mitochondrial fission machinery, whereas hFis1 is a direct homologue of Fis1. However, hFis1 does not seem to play the same role in mitochondrial fission as Fis1 and there are not direct homologues for Mdv1 or Caf4. The evidence that Mff plays a significant role in mitochondrial fission, based on overexpression and knockdown studies on Mff itself and co-localization studies of Mff with Drp1, is

conclusive.[65,76,174] Evidence that hFis1 plays a significant role in mammalian mitochondrial fission is more opaque. The effect of hFis1 overexpression and/or knockdowns seems to vary somewhat from study to study. However, since it is a direct homologue and is localized to the mitochondrial outer membrane, it seems likely that it must have some purpose in the fission machinery.[60,80,173] Elucidating the interaction between Mff and hFis1 could give insight on the current fission mechanism or regulation, and may also give some indication of the evolutionary path from the simpler yeast fission system to the more complex mammalian one. Crosslinking experiments between Mff and hFis1 have yielded mixed results with some studies showing successful pulldown of one with the other, and alternate studies showing no detectable interaction between the two.[76,80] One method of examining the question *in situ* is to label both proteins with PALM photoactivatable fluorescent proteins and image them under conditions that promote fission to examine potential co-localization. A better study for stable interaction would be to use a similar imaging method but with the bifurcation/complementation photoactivatable fluorescent proteins that will be described in Chapter 5.

Bax and Drp1 Interactions

Recently there has been increased interest in the interactions between Bcl-2-assocated X protein (Bax) and Drp1. Bax is a pro-apoptotic protein, predominantly found in the cytosol. However, upon initiation of apoptosis, Bax is recruited to the mitochondrial outer membrane via a conformational change. It was thought that Bax functioned in the membrane permeabilization of mitochondria and the release of cytochrome *c*.[177] More recently, there is evidence showing that Bax may not permeabilize the mitochondrial outer membranes but instead coordinate with Drp1 in some manner to promote apoptosis. There has been evidence showing the Drp1 may increase Bax oligomerization on the mitochondrial membranes and there is also evidence that activation of Bax might increase Drp1 recruitment and stabilization at mitochondrial fission sites.[61,166,170] The actual interactions of Bax and Drp1 have yet to be fully elucidated. Super resolution imaging studies of overall Bax localization and co-localization with Drp1 could give greater insight into the role of Bax in fission.

MATERIALS AND METHODS

STANDARD TECHNIQUES AND STARTING MATERIALS

Molecular biology techniques that are considered standard were performed as are commonly described. These include polymerase chain reaction (PCR), restriction digest, ligation, and transformation. Minipreps of plasmid DNA from DH5α *E. coli* were performed using the Zippy Plasmid Miniprep Kit from Zymo Research and gel extractions were performed using the Zymoclean Gel DNA Recovery Kit from Zymo Research. All sequencing was performed using non-premixed sequencing reactions through Sequetech, Inc. All PCR, mutagenesis, and sequencing primers were synthesized through Integrated DNA Technologies, Inc. PCR and sequencing primers are listed in the Table 4. All enzymes used for molecular cloning were purchased from New England Biolabs. The base materials for LB broth, solid media plates, and the antibiotics were purchased from Sigma Aldrich. LB broth consisted of 10 g/L bacto-peptone, 5 g/L yeast extract, and 10 g/L NaCl. The solid media plates were made with LB and 1.5% (w/v)

agar. The antibiotics used were appropriate to the *E. coli* being cultured. The antibiotics and concentrations used were 100 mg/L ampicillin and 30 mg/L kanamycin.

CLONING OF MAMMALIAN EXPRESSION VECTORS

All cloning techniques including primer synthesis and sequencing confirmations were done as described in Standard Techniques and Starting Materials as is the list of cloning primers (Table 4). A Kozak consensus sequence GACACC was added directly N-terminal of the ATG start codon in all constructs to promote translation.

p6XHis-PAmcherry1-Lk-BclXl(201-233) had already been built in Chapter 2. To create prsKame-Lk-Drp1, rsKame was inserted into pcDNA5/TO backbone using AflII and NotI. *Homo sapiens DRP1* was a generous gift from Jodi Nunnari (University of California, Davis). A fourteen amino acid flexible linker (AAAGGGSGGGSGGG) was added to the N-terminus of *DRP1* by PCR. Restriction sites NotI and ApaI were also added to *DRP1* by PCR and the construct Lk-Drp1 then cloned into the prsKame-5/TO with NotI and ApaI creating prsKame-Lk-Drp1.

CELL CULTURE AND CELL TRANSFECTION

Homo sapiens T-Rex HeLa (cervical cancer) cells were used for these studies. T-Rex HeLa cells were purchased from Invitrogen. All cell reagents were purchased from University of California, San Francisco Cell Culture Facility. T-Rex HeLa cells were cultured in Modified Eagle's Medium (MEM) with10% tetracycline free FBS, 1% penicillin/streptomycin, and 5 mg/L blasticidin to maintain the stably transfected tetracycline repressor gene. Cells were grown at 37ºC with 5% CO_2.

Prior to transfection, T-Rex HeLa cells were plated on acid washed fibronectin coated #1.5 glass slides (Warner Instruments) and grown to ~70% confluency (24-48 hours) at 37ºC in growth media with blasticidin selection (10 μg/mL, Invitrogen). T-Rex HeLa cells were co-transfected with Xfect (Clontech). Cells were transfected in media with serum. Cells were transfected for 4-8 hours and then incubated for at 24-48 hours at 37ºC and 5% CO_2 prior to imaging. Post transfection and at least 12 hours prior to imaging, cells were fed FBS coated 40 nm Au particles (60,000 particles/mL, Microspheres-Nanospheres).

CELL SAMPLE PREPARATION

Approximately four hours prior to imaging, doxycycline (Invitrogen) and z-vad-fmk (Promega) were added to the total growth media to final concentrations of 0.75 μg/mL and 20 mM respectively. Cells were incubated for 110 minutes at 37ºC. Staurosporine (Cell Signaling Technologies) was then added to a final concentration of 1 μM and cells were incubated for another 100 minutes at 37ºC. Immediately following the total 3.5 hours of doxycycline induction, caspase inhibitor treatment, and staurosporine treatment, mitochondria were labeled with MitoTracker Deep Red (Life Technologies/Invitrogen) at a final concentration of 30 nM. Treated cells were washed 3-5 times in 1X PHEM then fixed in 1% formalin (Sigma-Aldrich) in 1X PHEM for 10 minutes at room temperature. Post fixation, cells were washed 5-7 times in 1X

PHEM. Fixed cells were imaged in 1X PHEM. All buffers are detailed in Table 5 and were filtered through a 0.2 μm filter.

PALM IMAGING AND DATA ANALYSIS

Samples were imaged using the two-color PALM protocol as described in Chapter 3 with one alteration. Mitochondrial focal planes were set using mercury arc lamp excitation of the MitoTracker Deep Red. Initial two-color PALM analysis of samples was performed as described in Chapters 2 and 3. After initial analysis, two-color PALM images were examined by eye for mitochondrial networks with clear delineation of the outer mitochondrial membranes. Cells that passed the initial inspection were then further examined by eye for Drp1 fission structures on mitochondria. Drp1 fission structures were quantified by drawing a "box" closely around the Drp1 fission structure. The length and the width of the box equaled the length and the diameter of the Drp1 fission structures respectively and were quantified. The measured length and diameter distributions were plotted as histograms and fit to a normal Gaussian curve. The mean and standard error of mean of each distribution were calculated from the Gaussian fit. The median of each data set was also calculated separately to account for any skew in the overall data.

Chapter 5: Collateral Science: BiFC-PALM and the Solution to PALM Co-Localization

INTRODUCTION

Sometimes the pursuit of one scientific path turns up alternate paths and sometimes thinking creatively to solve a scientific difficulty turns up a novel solution to problem. We affectionately term these side discoveries "collateral science". When developing our methodology for two-color PALM imaging of Drp1, we were confronted with the difficulties attendant to attempting to image Drp1 localized to mitochondria among a much larger cytoplasmic population. Therefore, we attempted to come up with a method that would only allow fluorescent proteins to be activatable when the proteins were localized to the mitochondria. Since Drp1 exists in dimers and tetramers in the cytoplasm, fluorescence resonance energy transfer (FRET) was not possible.[178] We therefore expanded our investigations and came across the bimolecular fluorescence complementation technique (BiFC) first described by Lynne Regan in 2000.[179] The technique involves the bifurcation or splitting of GFP into two halves and then allowing them to complement back into a fully excitable fluorescent protein.[180] We theorized that if photoactivatable fluorescent proteins could be bifurcated, complement, and still maintain their photoactivatability, termed "BiFC PA-FPs", then we could fuse Drp1 to one half of a BiFC PA-FP and the ER membrane to the other half of BiFC PA-FP. When the ER constricted the mitochondrial tubule, the two BiFC PA-FPs halves would be able to complement, creating a fully functional PA-FP. The complementation would only happen at the constriction sites, not in the cytoplasm, eliminating the background. Though our other imaging methodology proved useful and was resolved much more quickly, we realized that the BiFC PA-FP technology had greater implications than we realized, including the solution to the difficulties in determining accurate co-localization of proteins using PALM imaging methodology.

BIMOLECULAR FLUORESCENCE COMPLEMENTATION

Bimolecular fluorescence complementation makes use of the structure of most fluorescent proteins, a β-barrel surrounding a hydrophobic core. For bifurcation, a single fluorescent protein is divided into two halves, each of which is fused with a short linker to one of two interacting proteins. When the two proteins interact stably in an *in vivo* or *in vitro* situation, the two halves of the bifurcated fluorescent protein fold into the correct conformation via hydrophobic forces.[181] Successfully bifurcated and complemented fluorescent proteins share several common features. They are all bifurcated between β sheets 7 and 8 and require low temperatures and stable close proximity for a significant amount of time in order for complementation to take place.[181] A linker of at least five amino acids in length is also necessary for the two bifurcated halves to find their proper orientation. The two halves complement through hydrophobic interactions of the core. The complementation is currently thought to be irreversible. The efficiency of the complementation and the resultant brightness is dependent on the fluorescent protein that was bifurcated and complemented. The specificity of the bifurcated halves is also dependent on the individual proteins. Multi-color BiFC imaging is possible but requires significant controls for each study to confirm true specificity.[181] Bimolecular fluorescence complementation has been

reported to have a resolution limit close to that of fluorescence resonance energy transfer (FRET), approximately 5-10 nm based on linker length.[178,182] Bimolecular fluorescence complementation of multiple fluorescent proteins across the spectra have been characterized, but to date no reported attempt of bimolecular fluorescence complementation with a photoactivatable fluorescent protein has been published.

FLUORESCENCE RESONANCE ENGERY TRANSFER

Fluorescence resonance energy transfer (FRET) describes the mechanism by which the energy emitted by one chromophore can be used to excite the other chromophore. FRET requires a chromophore pair where one chromophore acts as the donor molecule and one chromophore acts as the acceptor molecule.[178] For a fluorescent molecule, the pair requires that the donor molecule's emission spectrum overlap with the excitation spectrum of the acceptor molecule. When the donor molecule is excited, its energy is transferred to its acceptor molecule by dipole-dipole coupling instead of emitting photons. The fluctuations in detectable emission of the donor and acceptor fluorescent molecules are a measure of the proximity of the two molecules to each other.[183] The efficiency of FRET is dependent on the distance between the donor and acceptor molecules and the amount of overlap of donor emission spectrum and the acceptor excitation spectrum. FRET is generally used to show protein or protein subunit proximity, enzyme dynamics, or transient protein-protein or protein subunit interactions.[98]

MAMMALIAN F_1F_0-ATP Synthase

F_1F_0-ATP synthase is a ubiquitous enzyme complex spanning the mitochondrial inner membrane and is responsible for the production of adenosine triphosphate (ATP) from adenosine diphosphate (ADP) and free phosphate.[51] ATP synthase is made up of two dynamic sectors (F_1 and F_0). The F_1 sector is found in the matrix and is responsible for the synthesis of ATP. The F_0 is found embedded in the membrane. The dynamic rotation of the F_0 subunit is driven by a proton pump that also drives proton flow across the inner membrane from the intermembrane space to the matrix. The dynamic rotation of the F_0 sector is transferred to the F_1 sector through a connecting stalk, causing conformational changes in the subunits of F_1 and allowing for ATP synthesis.[51,52] The F_1 and F_0 sectors are also connected by a static stator sector that is thought to prevent F_0 rotation due to F_1 subunit conformational changes, and to perhaps stabilize the interactions between F_1 and F_0 sectors in the face of membrane distortion.[50] In the mitochondria, abundant ATP synthase enzyme complexes are found predominantly on the cristae and there is evidence that the ATP synthase enzymes complex clusters determine the tubular structure of the mitochondrial cristae.[53,184]

PALM CO-LOCALIZATION AND BIMOLECULAR FLUORESCENCE COMPLEMENTATION

A major issue for the biological research relevance of PALM imaging is determining true co-localization as opposed to mere proximity. Prior to super resolution microscopy, the diffraction limit was approximately 250 nm and any fluorescently tagged proteins that were within that proximity were considered co-localized. However, 250 nm is still a very large

cellular distance. With PALM and its resolution limit of 25 nm, co-localization of molecules has to be revisited. PALM allows us to determine an absolute localization of each individually tagged protein. To determine co-localization, we had hypothesized that by using computer algorithms to overlap Gaussian distributions of each protein we could determine what measure of overlap was considered "real" co-localization. However, that idea is full of potential pitfalls in regards to XY drift, PA-FP blinking, and percentage of overlap, etc. The BiFC technique would allow for a 7 nm relative localization within a 25 nm absolute localization "spot" (Figure 42). Therefore, for each 25 nm PALM "spot" or event, we could confirm that there are two proteins interacting with each other within a 7 nm proximity, solving the PALM co-localization difficulties.

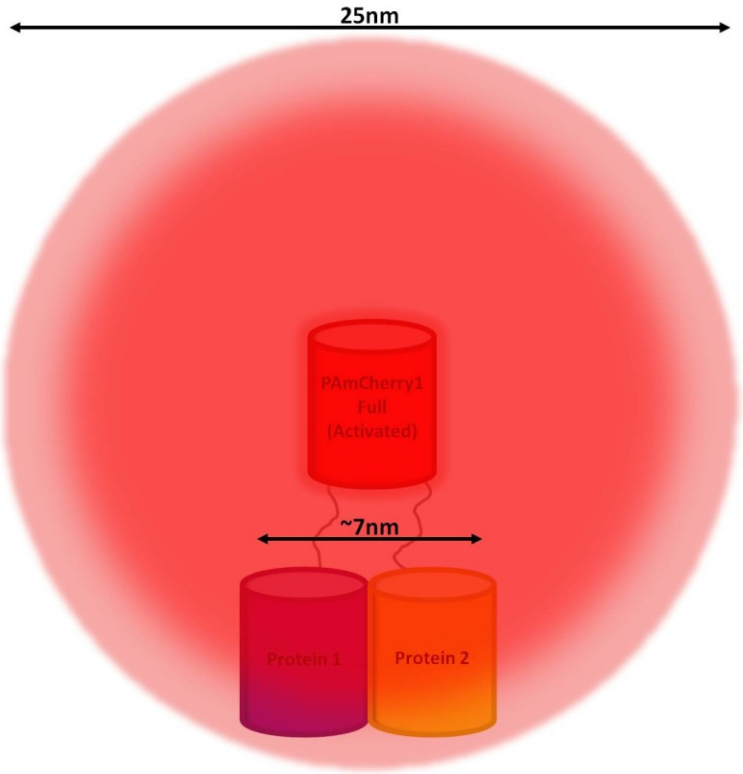

Figure 42: Model of protein-protein co-localization with BiFC PALM. Two stably interacting proteins allow for complementation between two bifurcated halves of PAmCherry1 (or Dendra2 or rsKame). Upon activation and PALM imaging, individual fluorescent events with a point spread function diameter of approximately 25 nm. Two proteins interacting within approximately 7 nm are contained within each 25 nm point spread function diameter.

RESULTS AND DISCUSSION

DEVELOPMENT OF BIFURCATED FLUORESCENT COMPLEMTATION COMPATIBLE PHOTOACTIVATABLE FLUORESCENT PROTEINS

Molecular Cloning and Expression of Bifurcated PAmCherry1

We began by replicating published work on the bifurcation and complementation of mCherry (Figure 43).[182] We noted that, like most BiFC fluorescent proteins, BiFC mCherry1 gave the greatest fluorescence upon complementation when split between β sheets 7 and 8.[182] PAmCherry1 is a mutant variant of mCherry1. However, all the mutations involved in the photoactivatability of the chromophore are specific to the chromophore and are not involved in folding kinetics or the β barrel structure. We decided to split PAmCherry1 at the same bifurcation point, between amino acids 160 and 161. PAmCherry1(1-160) was renamed PAmCherry1(N). PAmCherry1(161-236) was renamed PAmCherry1(C). We fused the respective halves of PAmCherry1 to the N or C terminal of EGFP with a twelve amino acid flexible linker (GSSGGGGSGGGG) cloned in frame between the two genes (Figure 44). BiFC halves were fused to EGFP due to its ability to dimerize when highly expressed.

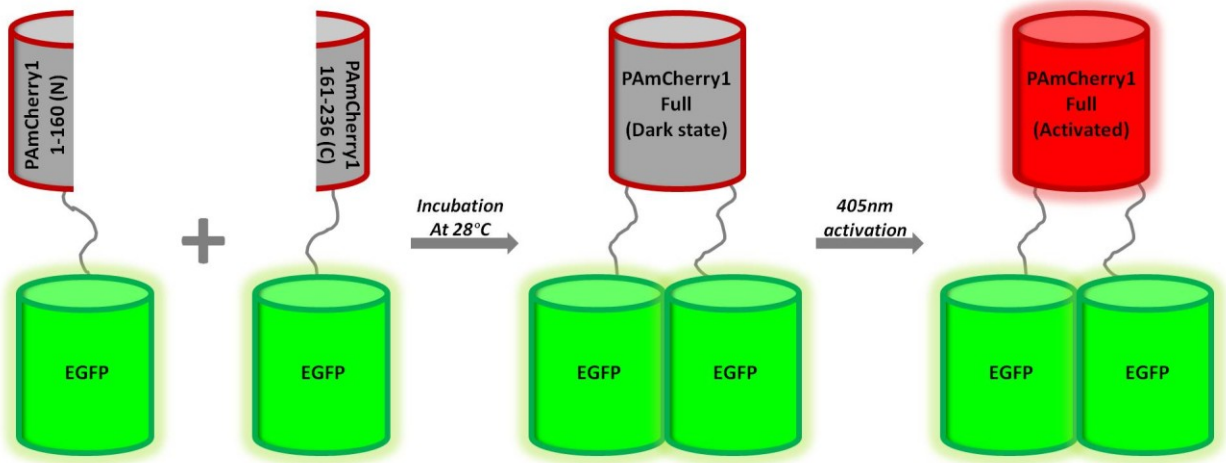

Figure 43: Model of bifurcation and complementation of PAmCherry1. PAmCherry1 was bifurcated between sheets β7 and β8. The two halves were fused to EGFP via a flexible linker, which dimerizes at high concentrations. When EGFP dimerizes, the two halves of PAmCherry1 are close enough in proximity to complement into a functional photoactivatable fluorescent protein. Post complementation and with 405 nm activation, PAmCherry1 fluoresces.

PAmCherry1(N) was cloned into pcDNA5/TO. The 12 amino acid flexible linker was added via PCR to the N terminus of EGFP. Lk-EGFP was cloned into pPAmCherry1(N)-5/TO to create pPAmCherry1(N)-Lk-EGFP. To create its bifurcation partner, the 12 amino acid flexible linker was added to the N terminal of PAmCherry1(C) via PCR and cloned into pcDNA5/TO. EGFP was cloned at the N-terminal of pLk-PAmCherry1(C)-5/TO to create pEGFP-Lk-PAmCherry1(C).

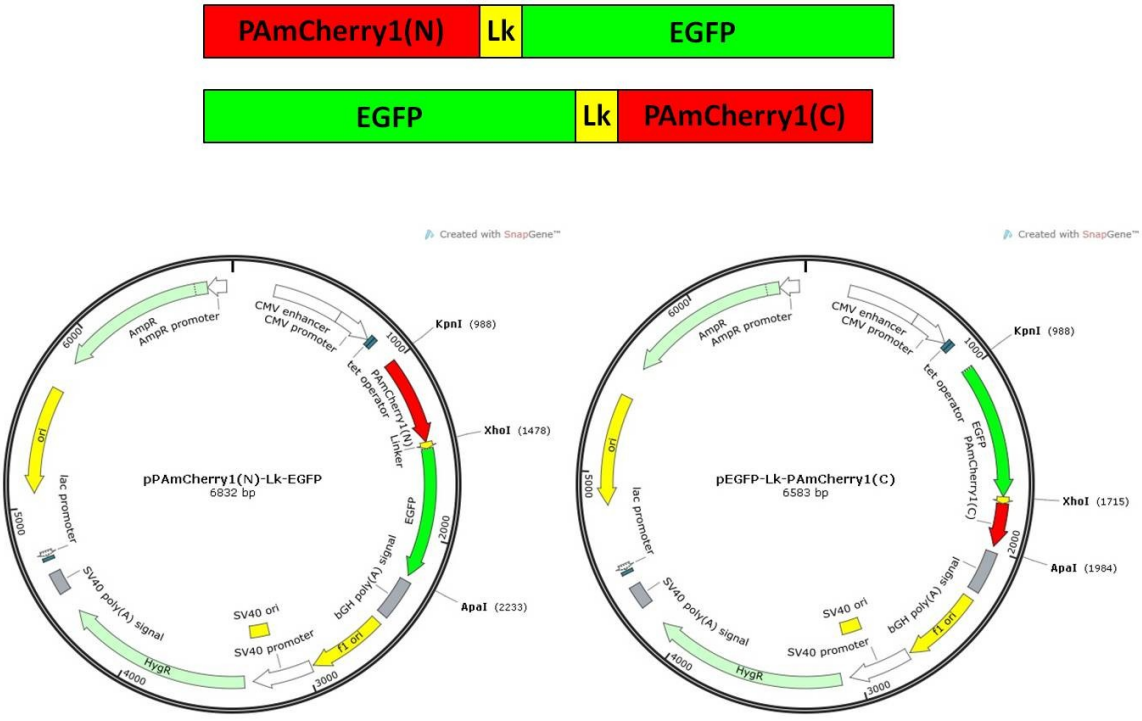

Figure 44: Genetic constructs and cloning maps of the bifurcated halves of PAmCherry1 fused to EGFP with a flexible linker. PAmCherry1(N) was inserted into pcDNA5/TO with KpnI and XhoI. The flexible linker was added to the N terminus of EGFP. Lk-EGFP was cloned into pPAmCherry1(N)-5/TO with XhoI and ApaI to create pPAmCherry1(N)-Lk-EGFP. To create pEGFP-Lk-PAmCherry1(C), the flexible linker was added to the N terminus of PAmCherry1(C) and inserted into pcDNA5/TO via XhoI and ApaI. EGFP was inserted at the N-terminal of Lk-PAmCherry1(C) into pLk-PAmCherry1(C)-5/TO with KpnI and XhoI to finish pEGFP-Lk-PAmCherry1(C).

To test for expression and successful complementation, EpH4 cells were plated on MatTek imaging plates 24 hours prior to transfection. Cells were transfected with pPAmCherry1(N)-Lk-EGFP, pEGFP-Lk-PAmCherry1(C), or both. Cells were incubated for 12-24 hours at 37°C and then incubated for another 12 hours at 25°C. Cells were imaged with the confocal microscope. Transfected cells were identified by EGFP expression. Extra bright cells in the co-transfection

condition were likely to have both constructs. These cells were first imaged for EGFP using the 488 nm excitation laser and a 520 nm emission filter. The cells were also imaged for PAmCherry1 using the 561 nm excitation laser and the 663-738 nm emission filter. Then cells were exposed to 405 nm activation via the mercury arc lamp for approximately 20 seconds. The cells were then re-imaged for EGFP and PAmCherry1 under the same conditions prior to activation.

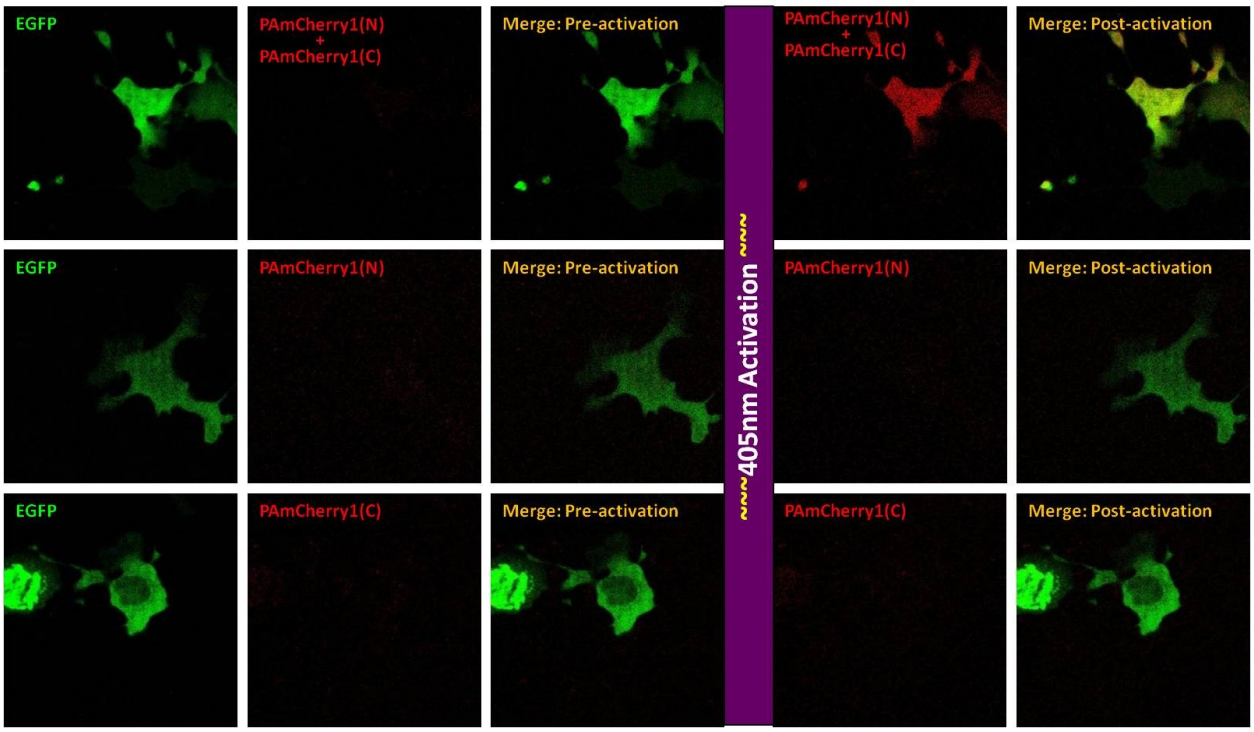

Figure 45: PAmCherry1 maintains its photoactivatability after bifurcation and complementation. EpH4 cells were co transfected with pPAmCherry1(N)-Lk-EGFP and pEGFP-Lk-PAmCherry1(C). Transfection with one of the two constructs singly was used as a negative control. Bright EGFP expression was used to identify cells that have both constructs. These cells were imaged for EGFP using the 488 nm excitation laser, then for PAmCherry1 using the 561 nm excitation laser. Next, cells were exposed to 405 nm mercury arc lamp activation for 20s. The cells were re-imaged for EGFP and PAmCherry1.

Image analysis was performed by overlaying the EGFP and PAmCherry1 pre-activation and post-activation images respectively directly in ImageJ. There was little to no red fluorescence observable in transfected cells prior to activation. Post activation, however, there was significant red fluorescence observed. This confirmed that bifurcated PAmCherry1 could complement and maintain its photoactivatability. In both samples that were singly transfected with one half of the BiFC PAmCherry1, no red fluorescence was observed in EGFP expression cells (Figure 45). In

addition, we imaged the same samples on the PALM microscope to observe BiFC PAmCherry1 as a potential PALM protein. Initially, cells were exposed to continuous excitation with the 561 nm laser (22 W/mm^2). During the continuous excitation, co-transfected cells were then exposed to activation with the 405 nm laser (3.46 W/mm^2). Individual PAmCherry1 PALM events were clearly visible upon but not prior to activation. These results confirm that bifurcated PAmCherry1, upon complementation, maintains photoactivatability and is a viable PALM PA-FP (Figure 48).

Molecular cloning and expression of BiFC Dendra2 and rsKame

After the success of BiFC PAmCherry1, we decided to test other PA-FPs for maintenance of photoactivatable fluorescence upon bifurcation and complementation. Other successful BiFC PA-FPs would widen the palette of these specialized fluorescent proteins for downstream imaging applications. We chose to bifurcate mEos2, Dendra2, and rsKame (Figure 46). We followed the same molecular cloning setup as described above, again bifurcating all three fluorescent proteins between β sheets 7 and 8. Both mEos2 and Dendra2 were fused to EGFP, but rsKame was fused to TagBFP. This is because rsKame and EGFP have overlapping excitation and emission spectra and cannot be distinguished from one another.

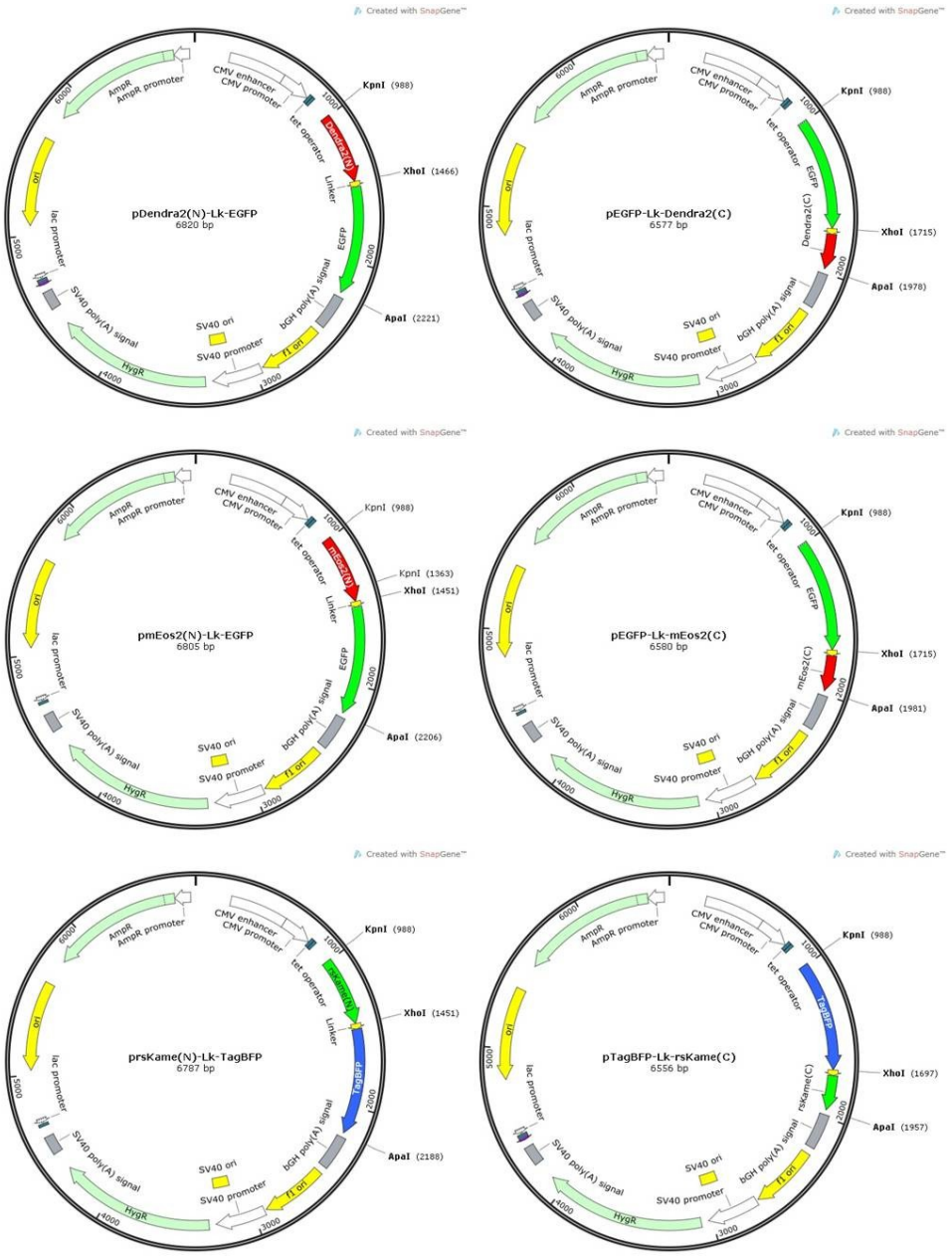

Figure 46: Cloning maps of the bifurcated halves of photoactivatable fluorescent proteins (PA-FPs) Dendra2, mEos2, and rsKame fused to EGFP or TagBFP with a flexible linker. Dendra2(N), mEos2(N), and rsKame(N) were inserted into pcDNA5/TO with KpnI and XhoI to create pPA-FP(N)-5/TO. The flexible linker was added to the N terminus of EGFP or TagBFP. Lk-EGFP or Lk-TagBFP were inserted into pPA-FP(N)-5/TO with XhoI and ApaI to create pPA-FP(N)-Lk-EGFP or pPA-FP(N)-Lk-TagBFP. To build pEGFP-Lk-PA-FP(C) and pTagBFP-Lk-PA-FP(C), the flexible linker was added to the N termini of Dendra2(C), mEos2(C), or rsKame(N) and inserted into pcDNA5/TO via XhoI and ApaI to create pLk-PA-FP(C)-5/TO. EGFP or TagBFP was inserted at the N-terminus of Lk-PA-FP(C) into pLk-PA-FP(C)-5/TO with KpnI and XhoI to finish pEGFP-Lk-PA-FP(C) and pTagBFP-Lk-PA-FP(C).

Cells were transfected and treated as described previously, including similar controls. For bifurcated mEos2 and Dendra2, imaging was performed as described previously. Bifurcated rsKame was imaged by first determining transfected cells by excitation with the 405 nm mercury arc lamp. Cells with bright blue fluorescence were considered transfected with both bifurcation plasmids. These cells were first imaged by excitation with the 488 nm laser and a 520 nm emission filter for rsKame green fluorescence. Cells were then excited and activated by exposure to the 405 nm laser. Blue fluorescence was collected with a 435-485 nm filter. The cells were then excited with the 488 nm laser and green fluorescence was collected with a 520 nm emission filter. Post imaging analysis was performed as described previously.

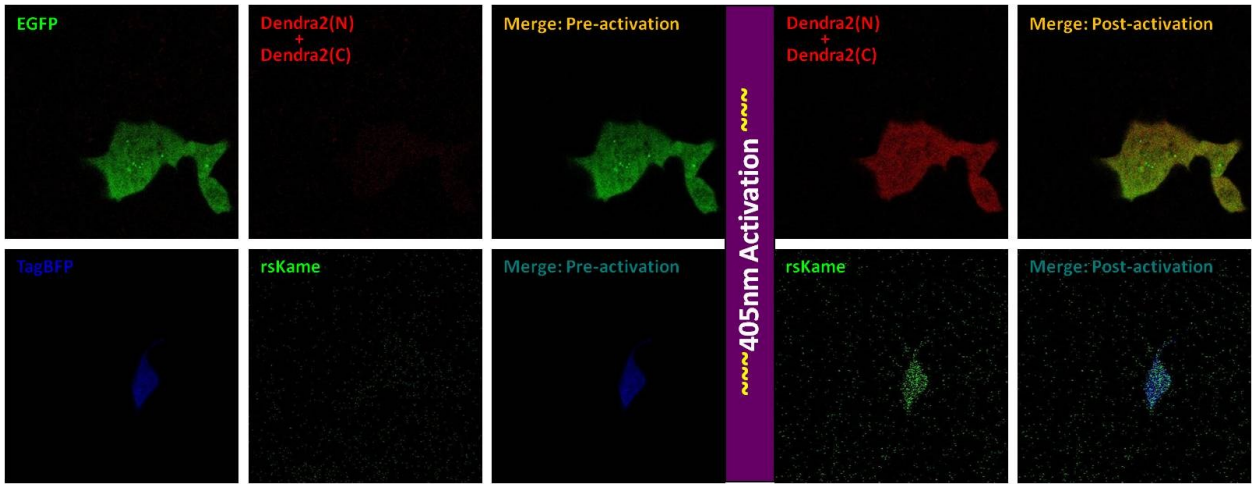

Figure 47: Dendra2 and rsKame maintain photoactivatability and photoswitchability respectively after bifurcation and complementation. EpH4 cells were co-transfected with pDendra2(N)-Lk-EGFP and pEGFP-Lk-Dendra2(C) or prsKame(N)-Lk-TagBFP and pTagBFP-Lk-rsKame(C). Bright EGFP or TagBFP expression was used to identify cells that have both constructs. Cells containing the bifurcated Dendra2 were imaged for EGFP using the 488 nm excitation laser and then for Dendra2 using the 561 nm excitation laser. Next cells were exposed to 405 nm mercury arc lamp activation for 20 seconds. The cells were re-imaged for EGFP and Dendra2. Cells containing the bifurcated rsKame were first imaged for TagBFP using the 405 nm excitation laser, and then inactivated by mercury arc lamp illumination at 488 nm. Next cells were exposed to 405 nm mercury arc lamp activation for 20 seconds. The cells were imaged rsKame using the 488 nm excitation laser and subsequently re-imaged for TagBFP.

We observed red fluorescence and green fluorescence upon complementation and activation in cells co-transfected with the two halves of Dendra2 and rsKame respectively. Neither BiFC PA-FP showed observable fluorescence without activation, indicating that they maintain their photoactivatable properties. No singly transfected sample for either Dendra2 or rsKame showed any observable red or green fluorescence post complementation and activation. mEos2 did not show any red fluorescence upon bifurcation and complementation. Whether this is because the chromophore is affected by the bifurcation/complementation or the photoactivatability is inhibited, we do not know. However because we now had a green to red BiFC PA-FP (Dendra2) and a dark to green reversibly switchable BiFC PA-FP (rsKame), we chose not to pursue future investigations with mEos2 (Figure 47). We took the cells co-expressing both halves of BiFC Dendra2 or BiFC rsKame to the PALM scope to examine fitness for PALM imaging. Samples with BiFC Dendra2 were exposed to continuous illumination with an excitation 561 nm laser and a 663-738 nm emission filter. During this continuous illumination, the activation 405 nm laser was added. Upon activation, clear photoactivatable fluorescent events were observed. The same was true for samples with BiFC rsKame, though in that setup, the excitation laser is 488 nm and the emission filter is 522 nm (Figure 48). These results confirm bifurcated Dendra2 and rsKame, upon complementation, maintain photoactivatability and are viable PALM PA-FPs.

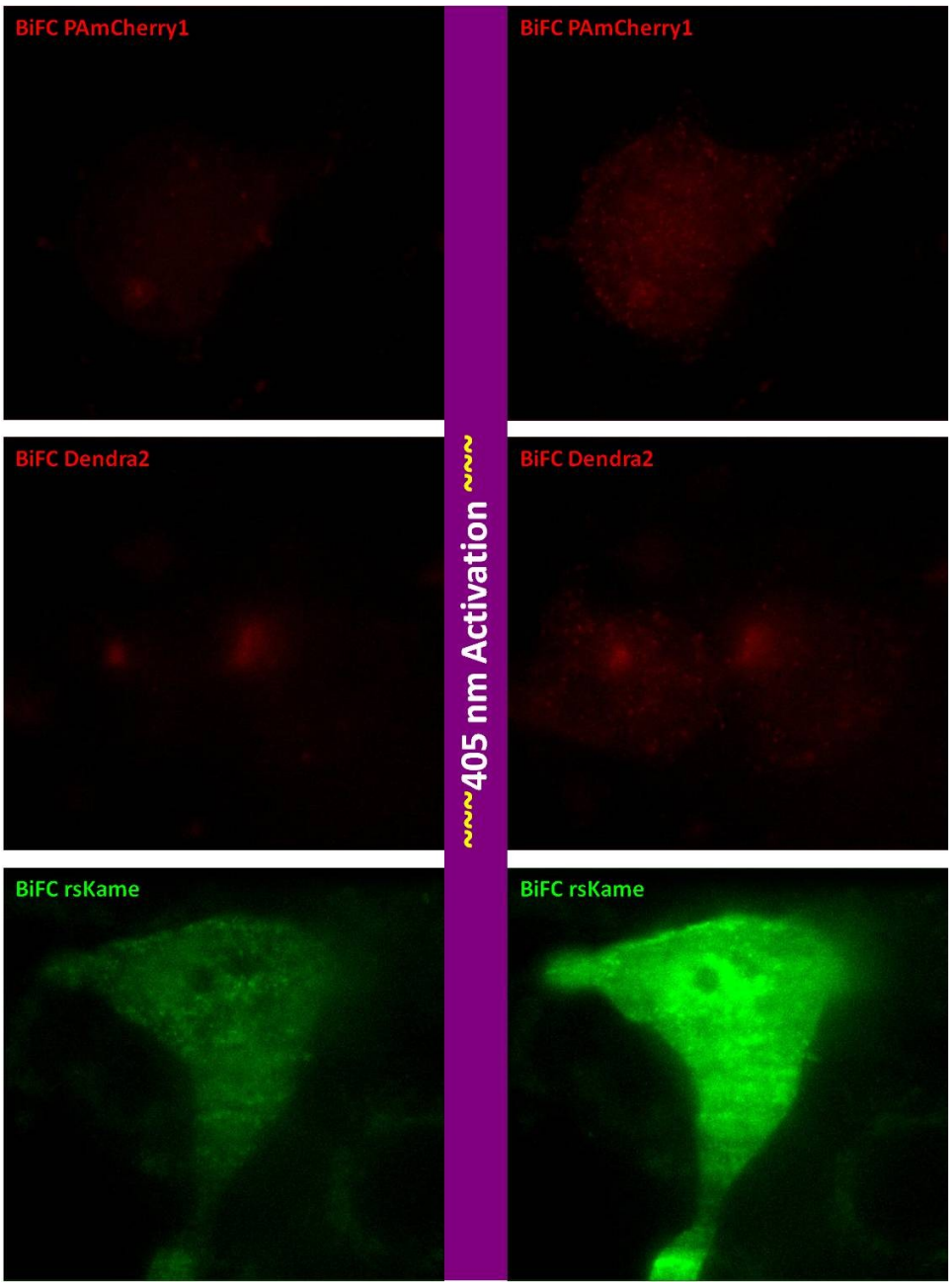

Figure 48: Bifurcated and complemented PAmCherry1, Dendra2, and rsKame maintain photoactivatability during PALM imaging conditions. EpH4 cells were co-transfected with pPAmCherry1(N)-Lk-EGFP and pEGFP-Lk-PAmCherry1(C), pDendra2(N)-Lk-EGFP and pEGFP-Lk-Dendra2(C), or prsKame(N)-Lk-TagBFP and pTagBFP-Lk-rsKame(C). Cells were imaged on the PALM microscope at 20 Hz. Cells were excited with 561 nm at 22 W/mm^2 (PAmCherry1, Dendra2) or 488 nm at 5.87 W/mm^2 (rsKame) (*left column*). Cells were illuminated with the 405 nm activation laser at 2.83 W/mm^2 (PAmCherry1, Dendra2) or 3.46 mW/mm^2 (rsKame) (*right column*). Figure images are stills taken from PALM movies.

FUTURE DIRECTIONS

PALM IMAGING OF BIFURCATED FLUORESCENT COMPLEMTATION COMPATIBLE PHOTOACTIVATABLE FLUORESCENT PROTEINS

Molecular cloning of ATP synthase subunits fused to BiFC PAmCherry1 halves

In order for bifurcated and complemented photoactivatable flouorescent protein (BiFC PA-FP) to be a useful biological tool to allow for the measure of protein-protein co-localization in the context of PALM imaging, the technique must be demonstrated in a biological system. To that end, we have chosen to label two stator subunits of the mammalian mitochondrial F_1F_0-ATP synthase: ATP5F1 and ATP5O.[50] We chose ATP5F1 and ATP5O based on published FRET studies of the *Saccharomyces cerevisiae* homologues (subunit b (*ATP4*) and oligomycin sensitivity-conferring protein (*ATP5*) respectively). In these published studies, the two subunits were labeled with the FRET donor acceptor pair BFP/YFP and demonstrated stable FRET interactions.[50] We chose to fuse the *Homo sapiens* homologues ATP5F1 and ATP5O to one of each of the PAmCherry1 bifurcated halves. This is ongoing research.

We chose to place the final construct on a pcDNA5/TO backbone in order to allow for inducible expression in later studies if needed. The two fusion proteins were placed under the same promoter and separated by the consensus sequence for an internal ribosome entry site (IRES). This allows for the co-expression of two different genetic constructs off the same mRNA. We chose this method so as to be confident that both fusion proteins were expressed in the same cell and at similar expression levels. Both subunits have published instances of having previously been fused to fluorescent proteins, so we were confident the addition of our bifurcation halves would not interfere with localization or function. The bifurcated PAmCherry1 halves and ATP5F1 or ATP5O were separated by the 12 amino acid flexible linker described previously.

We built pATP5F1-PAmCherry1(C)-IRES-ATP5O-PAmCherry1(N) by inserting three smaller genetic constructs, ATP5F1-Lk-PAmCherry1(C), IRES, and ATP5O-Lk-PAmCherry1(N) into pcDNA5/TO (Figure 49). ATP5F1-Lk-PAmCherry1(C) was created by adding the linker to the N-terminus of PAmCherry1(C) through PCR, then ligating it to the C-terminus of *ATP5F1*. ATP5O-Lk-PAmCherry1(N) was created by adding the linker to the N-terminus of PAmCherry1(N) through PCR, then ligating it to the C-terminus of *ATP5O*. Restriction sites were added to IRES. Because of the unique restriction sites, all three smaller genetic constructs were inserted into pcDNA5/TO in one step to finish pATP5F1-PAmCherry1(C)-IRES-ATP5O-PAmCherry1(N).

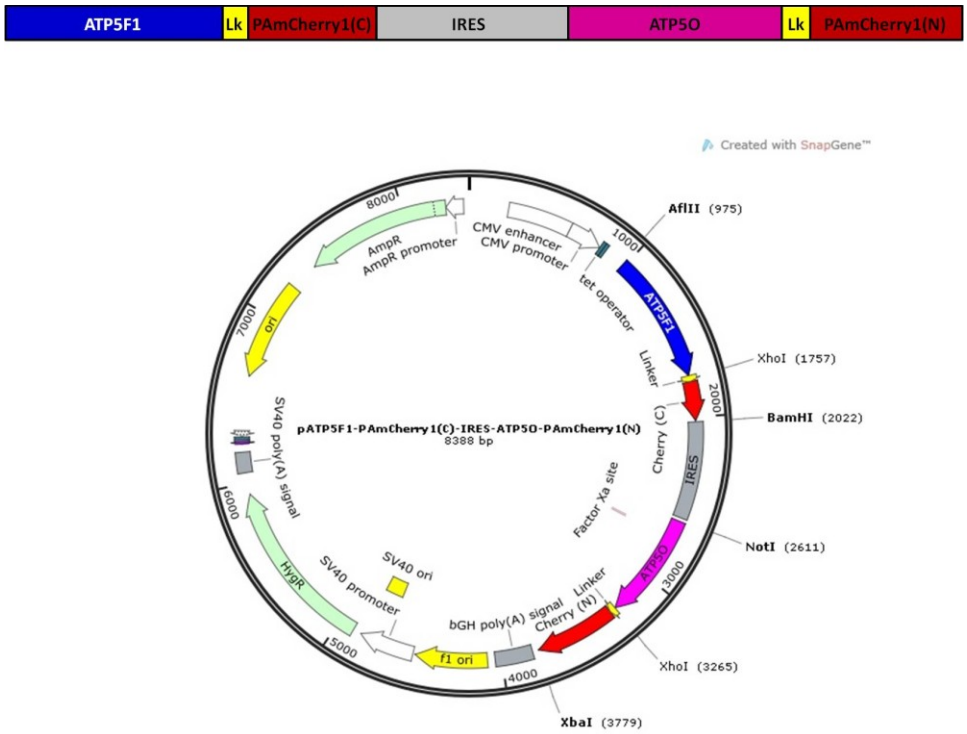

Figure 49: Genetic construction and cloning map of ATPF1 and ATP5O fused to bifurcated halves of PAmCherry1 with a flexible linker. pATP5F1-PAmCherry1(C)-IRES-ATP5O-PAmCherry1(N) was created by inserting three smaller genetic constructs, ATP5F1-Lk-PAmCherry1(C), IRES, and ATP5O-Lk-PAmCherry1(N), into pcDNA5/TO. ATP5F1-Lk-PAmCherry1(C) was built by adding the linker to the N-terminus of PAmCherry1(C), then ligating Lk-PAmCherry1(C) to the C-terminus of *ATP5F1* by XhoI. Restriction sites AflII and BamHI were added. ATP5O-Lk-PAmCherry1(N) was built by adding the linker to the N-terminus of PAmCherry1(N), then ligating Lk-PAmCherry1(N) to the C-terminus of *ATP5O* by XhoI. Restriction sites NotI and XbaI were added. Restriction sites BamHI and NotI were added to IRES. All three smaller genetic constructs were inserted into pcDNA5/TO.

PALM Imaging and Analysis of BiFC-PAmCherry1 fused to ATP5F1 and ATP5O

EpH4 cells will be transfected with the pATP5F1-PAmCherry1(C)-IRES-ATP5O-PAmCherry1(N) and PALM imaged as described in Chapter 2 and 3. PALM images will be analyzed at described in Chapter 2.

CONTROLS, SPECIFICITY, AND RESOLUTION

Negative Controls

The first experiments to confirm complementation dependent on protein-protein co-localization is the development of the negative control. We propose to disrupt the interaction between ATP5F1 and ATP5O by mutating the conserved Gly184 on ATP5O to Asn. This mutation and its disruption of rat ATP5O incorporation into yeast F_1F_0-ATP synthase have been previously documented.[50] Cells expressing the mutant ATP5O G184N fused to a bifurcated half of PAmCherry1 are expected to show no observable fluorescence upon activation when paired with functional ATP5F1 fused to the complementary half of PAmCherry1. This negative control could also be used for examination of BiFC PA-FP specificity or linker length effects in later studies.

Specificity

In order to perform BiFC PALM with more than one BiFC PA-FP, the specificity of each PA-FPs halves to themselves must be determined. Due to the photoactivatable or photoswitchable properties, it is likely that PA-FPs halves will be highly specific to themselves. The photoactivation mechanism of PAmCherry1 and Dendra2 is similar and involves a chemical change around the chromophore. The photoswitching mechanism of rsKame involves an isomerization of the chromophore. Since PAmCherry1 and Dendra2 have a similar photoactivation method, it is possible that PAmCherry1 and Dendra2 may have some cross specificity. Since the photoactivation mechanism of PAmCherry1 and Dendra2 is incompatible with the photoswitching mechanism of rsKame, it is unlikely there will be cross specificity between rsKame and PAmCherry1 or Dendra2. However, all combinations should be tested. The easiest way to test specificity is to fuse the respective bifurcated halves to known interacting protein partners, then transfect cells with various N and C bifurcated half combinations and examine for photoactivatable for photoswitchable fluorescence.

Resolution

BiFC resolution is dependent on the linker length separating the BiFC fluorescent protein half and protein of interest. Shortening or lengthening the linker should increase or decrease the relative resolution of protein-protein interaction. However, a flexible linker is necessary for the BiFC halves to have enough rotational freedom to find the complementation orientation. Therefore, there is likely a limit as to how short the linker can be before complementation no longer occurs. On the other side of the equation, a long linker will likely result in complementations between non-interacting proteins, creating false positives. The limits to the short linker length can be examined by creating BiFC halves fused to known interacting proteins with various short linker lengths. When photoactivatable fluorescence is no longer able to be visualized, the shortest linker limit has been reached. The limits to the long linker length can be identified by creating BiFC halves fused to known noninteracting proteins with various long linker lengths. When photoactivatable fluorescence appears, the longest linker length has been reached. Identifying the short and long linker parameters will give information on the relative

resolution capabilities of BiFC, critical to protein-protein co-localization studies with BiFC PALM.

SINGLE MOLECULE STUDIES

Single molecule studies of complementation kinetics and hydrophobic forces

The time necessary for complementation to occur is a limiting factor for any protein-protein interaction study *in vivo* or *in situ*. In addition, the complementation time seems to be dependent on the fluorescent protein. Therefore, investigations into the kinetics of complementation could prove very informative for BiFC PALM studies. Our lab is uniquely set up to examine complementation kinetics using fluorescent optical tweezers. Fluorescent optical tweezers combine a fluorescent microscopy with an optical trap setup. Two beads are held apart with a laser and pipette with a biological molecule or amalgamation of molecules attached to and held between the beads. The movement of the bead in and out of the laser provides a measure of the force between the two beads. This setup is placed in the path of an activation and/or excitation laser and an emission filter and CCD camera. To examine the complementation kinetics, two versions of a strongly dimerizing protein could be fused to one of each of the two bifurcated halves of a PA-FP like PAmCherry1 (or any bifurcated fluorescent protein). Those protein fusions could be attached to DNA tethers and bound to the two respesctive beads. When the strongly dimerizing proteins interact, a measurable force will be introduced into the system. At this time, the sample should be illuminated with both activation and excitation wavelengths. When the two bifurcated PA-FP halves complement and mature, then there will be detectable fluorescence, allowing us to calculate a global kinetic rate of complementation/maturation. Prior to complementation and maturation, there should be no visible fluorescence. This *in vitro* setup mimics the BiFC process *in vivo*. Variables like salt concentration, pH, and temperature can be examined in this setup.

In addition, the complementation of two bifurcated halves is considered irreversible and can potentially trap two transiently interacting proteins together. It is generally thought that the interaction between the two bifurcated halves is based on hydrophobic forces. To study the strength of these forces, a bifurcated and complemented fluorescent protein can be held between two beads and force applied until the two halves separate. A measure of the hydrophobic forces between the bifurcated and complemented halves could potentially predict the trapping effect that BiFC fluorescent proteins may have on proteins in a cell.

MATERIALS AND METHODS

STANDARD TECHNIQUES AND STARTING MATERIALS

Molecular biology techniques that are considered standard were performed as are commonly described. These include polymerase chain reaction (PCR), restriction digest, ligation, and transformation. Minipreps of plasmid DNA from DH5α *E. coli* were performed using the Zippy Plasmid Miniprep Kit from Zymo Research and gel extractions were performed using the Zymoclean Gel DNA Recovery Kit from Zymo Research. All sequencing was performed using non-premixed sequencing reactions through Sequetech, Inc. All PCR, mutagenesis, and sequencing primers were synthesized through Integrated DNA Technologies, Inc. PCR and

sequencing primers are listed in the Table 4. All enzymes used for molecular cloning were purchased from New England Biolabs. The base materials for LB broth, solid media plates, and the antibiotics were purchased from Sigma Aldrich. LB broth consisted of 10 g/L bacto-peptone, 5 g/L yeast extract, and 10 g/L NaCl. The solid media plates were made with LB and 1.5% (w/v) agar. The antibiotics used were appropriate to the *E. coli* being cultured. The antibiotics and concentrations used were 100 mg/L ampicillin and 30 mg/L kanamycin.

CLONING OF MAMMALIAN EXPRESSION VECTORS

All bifurcated PA-FP halves are separated from the interacting proteins by an amino acid flexible linker (GSSGGGGSGGGG). The flexible linkers are added to the genetic construction by PCR. All genetic constructs were inserted into the pcDNA5/TO vector backbone. Restriction sites are added via PCR.

PAmCherry1(N) is PAmCherry1(1-160). PAmCherry1(C) is PAmCherry1(161-236). PAmCherry1(N) was inserted into pcDNA5/TO with KpnI and XhoI to build pPAmCherry1(N)-5/TO. The linker was added to the N terminus of EGFP. Lk-EGFP was cloned into pPAmCherry1(N)-5/TO with XhoI and ApaI to build pPAmCherry1(N)-Lk-EGFP. To build pEGFP-Lk-PAmCherry1(C), the linker was added to the N terminal of PAmCherry1(C) via PCR and inserted into pcDNA5/TO via XhoI and ApaI to create pLk-PAmCherry1(C)-5/TO. EGFP was cloned at the N-terminal of pLk-PAmCherry1(C)-5/TO with KpnI and XhoI to build pEGFP-Lk-PAmCherry1(C).

Dendra2(N) is Dendra2(1-156). Dendra2(C) is Dendra2(157-230). Dendra2(N) was inserted into pcDNA5/TO with KpnI and XhoI to build pDendra2(N)-5/TO. The linker was added to the N terminus of EGFP. Lk-EGFP was cloned into pDendra2(N)-5/TO with XhoI and ApaI to build pDendra2(N)-Lk-EGFP. To build pEGFP-Lk-Dendra2(C), the linker was added to the N terminal of Dendra2 (C) via PCR and inserted into pcDNA5/TO via XhoI and ApaI to create pLk-Dendra2 (C)-5/TO. EGFP was cloned at the N-terminal of pLk-Dendra2(C)-5/TO with KpnI and XhoI to build pEGFP-Lk-Dendra2(C).

mEos2(N) is mEos2(1-151). mEos2(C) is mEos2(152-226). mEos2(N) was inserted into pcDNA5/TO with KpnI and XhoI to build pmEos2(N)-5/TO. The linker was added to the N terminus of EGFP. Lk-EGFP was cloned into pmEos2(N)-5/TO with XhoI and ApaI to build pmEos2(N)-Lk-EGFP. To build pEGFP-Lk-mEos2(C), the linker was added to the N terminal of mEos2(C) via PCR and inserted into pcDNA5/TO via XhoI and ApaI to build pLk-mEos2(C)-5/TO. EGFP was cloned at the N-terminal of pLk-mEos2(C)-5/TO with KpnI and XhoI to build pEGFP-Lk-mEos (C).

rsKame(N) is rsKame(1-151). rsKame(C) is rsKame(152-224). rsKame(N) was inserted into pcDNA5/TO with KpnI and XhoI to build prsKame(N)-5/TO. The linker was added to the N terminus of TagBFP. Lk-TagBFP was cloned into prsKame(N)-5/TO with XhoI and ApaI to create prsKame(N)-Lk-TagBFP. To build pTagBFP-Lk-rsKame(C), the linker was added to the N terminal of rsKame(C) via PCR and inserted into pcDNA5/TO via XhoI and ApaI to build pLk-rsKame(C)-5/TO. TagBFP was cloned at the N-terminal of pLk-rsKame(C)-5/TO with KpnI and XhoI to build pTagBFP-Lk-rsKame(C).

pATP5F1-PAmCherry1(C)-IRES-ATP5O-PAmCherry1(N) was built by inserting three smaller genetic constructs, ATP5F1-Lk-PAmCherry1(C), IRES, and ATP5O-Lk-PAmCherry1(N) into pcDNA5/TO. ATP5F1-Lk-PAmCherry1(C) was synthesized by adding the linker to the N-terminus of PAmCherry1(C) through PCR, then ligating it to the C-terminus

of *ATP5F1* by XhoI. Restriction sites AflII and BamHI were added to the full length construct by PCR. ATP5O-Lk-PAmCherry1(N) was synthesized by adding the linker to the N-terminus of PAmCherry1(N) through PCR, then ligating it to the C-terminus of *ATP5O* by XhoI. Restriction sites NotI and XbaI were added to the full length construct by PCR. Restriction sites BamHI and NotI were added to IRES. Because of the unique restriction sites, all three smaller genetic constructs were inserted into pcDNA5/TO in a one step ligation to finish pATPF1-PAmCherry1(C)-IRES-ATP5O-PAmCherry1(N).

CELL CULTURE

Two different cell types were used: murine EpH4 (mammary gland epithelial), and *Homo sapiens* T-Rex HeLa (cervical cancer) cells. EpH4 cells were originally isolated by C. Roskelly. Cells were already in house. T-Rex HeLa cells were purchased from Invitrogen. All cell reagents were purchased from University of California, San Francisco Cell Culture Facility. The EpH4 cells were cultured in DMEM with 2% FBS with added 5 mg/L of insulin and 50 mg/L gentamycin. T-Rex HeLa cells were cultured in Modified Eagle's Medium (MEM) with10% tetracycline free FBS, 1% penicillin/streptomycin, and 5 mg/L blasticidin to maintain the stably transfected tetracycline repressor gene. Cells were grown at 37°C with 5% CO_2.

CELL TRANSFECTION AND COMPLEMENTATION PROTOCOL

Mammalian cells were transfected with one of two lipid based commercial transfection reagents. EpH4 cells were transfected with Lipofectamine2000 (Invitrogen). Cells could be transfected in media with serum or without serum with little change in efficiency. Cells were transfected for 4-8 hours and then incubated for at least 24 hours at 37°C and 5% CO_2 prior to imaging. T-Rex HeLa cells can be transfected with Xfect (Clontech) in media with serum. Cells will be transfected for 4-8 hours and then incubated for at least 12 hours at 37°C and 5% CO_2 prior to imaging. To promote complementation of bifurcated fluorescent protein halves, cells are incubated at 25°C for 10-24 hours post transfection and initial 24 hour incubation at 37°C.

LIVE CELL IMAGING WITH SCANNING CONFOCAL MICROSCOPE

Cells were imaged on the Nikon Eclipse TE2000-S scanning confocal microscope (Nikon Instruments Inc.). Cells were plated on MatTek imaging tissue culture plates (MatTek Corporation). Cells were imaged *in vivo* and 1X PHEM. Images were analyzed and overlaid using ImageJ. Cells co-transfected with pPAmCherry1(N)-Lk-EGFP and pEGFP-Lk-PAmCherry1(C) were imaged for EGFP using the 488 nm excitation laser then for PAmCherry1 using the 561 nm excitation laser. Cells were exposed to 405 nm mercury arc lamp activation for 20 seconds, and then re-imaged for EGFP and PAmCherry1. Cells co-transfected with pDendra2(N)-Lk-EGFP and pEGFP-Lk-Dendra2(C) were imaged for EGFP using the 488 nm excitation laser then for Dendra2 using the 561 nm excitation laser. Cells were exposed to 405 nm mercury arc lamp activation for 20 seconds. The cells were re-imaged for EGFP and Dendra2. Cells co-transfected with prsKame(N)-Lk-TagBFP and pTagBFP-Lk-rsKame(C) were first imaged for TagBFP using the 405 nm excitation laser then inactivated by mercury arc lamp illumination at 488nm. Cells were exposed to 405 nm mercury arc lamp activation for 20

seconds. The cells were imaged rsKame using the 488 nm excitation laser and subsequently re-imaged for TagBFP.

PALM IMAGING AND ANALYSIS

Prior to imaging, cells were plated on fibronectin coated acid washed 25 mm round #1.5 glass slides (Warner Instruments). Cells were washed 5-7 times and imaged in 1X PHEM. All buffers were filtered through a 0.2 μm filter and are detailed in Table 5.

To image BiFC PAmCherry1, the sample was illuminated with the 561 nm excitation laser (22 W/mm^2). The 405 nm activation laser was turned on at 2.83 W/mm^2 and fluorescence data was collected at 20 Hz. To image BiFC Dendra, the sample was illuminated with the 561 nm excitation laser (22 W/mm^2). The 405 nm activation laser was turned on at 2.83 W/mm^2 and fluorescence data was collected at 20 Hz. To image BiFC rsKame, the sample was illuminated with the 488 nm excitation laser (5.87 W/mm^2). The 405 nm activation laser was turned on at 3.46 mW/mm^2 and fluorescence data was collected at 20 Hz. Stills from the PALM movies were used for the demonstration of activation.

Chapter 6: Conclusion

We set out to answer a simple biological question: what are the high resolution structural properties of Drp1 helical rings that constrict mammalian mitochondria during fission *in vivo*? We sought to answer this simple biological question in the absence of morphological artifacts produced by sample preparation and beneath the limits of diffraction. We chose a more recent but established method of super resolution visualization, PALM, in the hopes that the sub-diffraction resolution would show quantifiable structural detail. What we found was that PALM, specifically two-color PALM, had not quite reached its purported biological relevance in regards to cellular imaging and protein-protein co-localization. A biological question was needed to direct innovative solutions towards functional use of two-color PALM imaging in the context of fluorescently exploring a single mammalian cell. Our biological question served that purpose.

In the course of our research and this thesis, we discovered that the published two-color PALM protocols were not adequate or indeed functional in our hands. This necessitated a change in course from simply answering our question concerning mitochondrial fission to the development of a novel photoswitchable fluorescent protein and Dronpa variant, raKame, and a re-development of the two-color PALM imaging method as a whole. In Chapter 2 we detailed the process of characterizing rsKame and developed a kinetic model for both rsKame and Dronpa. Important observations were made about the photoactivation of Dronpa and our variants, namely that Dronpa and our variants were not perfectly photoswitchable fluorescent proteins. Instead of pure activation by 405 nm illumination, Dronpa and our variants could be excited as well as activated by 488 nm illumination. In fact, the activation effect by 488 nm illumination was far stronger than that of the 405 nm illumination. Because of this activation by 488 nm illumination, high resolution PALM imaging of Dronpa proved nearly impossible. In addition, we demonstrated that the cis (ON) to trans (OFF) isomerization of the Dronpa/rsKame chromophore is not driven by 405 nm or 488 nm illumination; therefore, the chromophore either spontaneously relaxes to the trans conformation or is affected by an unknown variable. Our novel mutant, rsKame, had two major improvements as compared to Dronpa. First rsKame had a significantly increased T_{OFF} time (by at least 50%) that better separated fluorescent events temporally; and second, rsKame showed a significant decrease in 488 nm activation, though not to zero. The combination of these two improvements made rsKame a useful photoswitchable fluorescent protein for super resolution PALM imaging. The large difference in 405 nm photoactivation rates between rsKame and PAmCherry1 combined with the lack of associated residual green fluorescencemade PAmCherry1 a good imaging partner for rsKame.

With our palette now complete, in Chapter 3 we developed a novel two-color PALM imaging protocol for examining the two separate mitochondrial membranes *in situ*. Our method is functionally the reverse of established protocols, though the basic PALM imaging theory remains unchanged. With our novel protocol and palette, we were able to obtain super resolution images of mitochondrial inner and outer membranes, showing distinct morphological differences between the two membranes reminiscent of mitochondrial images obtained with electron microscopy.

In Chapter 4 we returned at last to our simple biological question with our improved PALM methodology and novel photoswitchable green fluorescent protein, rsKame. Drp1 monomers were fused to rsKame and the mitochondrial outer membrane was densely decorated with PAmCherry1. Cells were prepared for imaging by gentle fixation. The obtained super resolution images showed Drp1 helical rings with a high enough resolution that quantifiable structural

information about the helical rings could be measured, though we were still bound by resolution limits of approximately 25 nm. Our absolute mean diameter measurements of the Drp1 helical rings, both during mitochondrial membrane constriction and post membrane scission, were significantly larger than published measurements of *in vitro* Dnm1 helical rings; however, this is likely due to the differences in resolution limits between electron microscopy and PALM microscopy as well as our described sources of measurement error from the PA-FP itself and/or the linker.[84,163] We were able to observe a 40 nm decrease in mean diameter between Drp1 helical rings during mitochondrial outer membrane constriction and post membrane scission. This observation is consistent with a dynamic change in Drp1 helical ring diameter during mitochondrial fission and consistent with the published fission ring diameter decrease of *in vitro* Dnm1.[84,163] The Drp1 helical ring mean length remains predominantly consistent during membrane constriction and scission. The Drp1 helical length distribution is tightly clustered pointing to a small range of helical ring lengths unlike published observations of assembled *in vitro* Dnm1.[84] This may point to a regulatory mechanism of the Drp1 ring length *in vivo* mitochondrial fission that is not present during *in vitro* studies. We also observed a novel Drp1 morphology showing two Drp1 foci flanking the mitochondrial outer membrane. Though the diameter of these foci varied widely, the length was tightly clustered and consistent with the helical length observed for Drp1 fission rings that completely encircled the mitochondria. Because of this consistency, we believe this novel morphology warrants further investigation.

The scientific path often leads to unexpected observations, or what we affectionately term "collateral science". In Chapter 5 we investigated bifurcation and complementation of fluorescent proteins as a possible method for imaging Drp1 fission rings sans the background from the cytoplasmic population of Drp1. At the time, no photoactivatable or photoswitchable fluorescent proteins had been bifurcated. We demonstrated that three PA-FPs, PAmCherry1, Dendra2, and rsKame, could be bifurcated and still maintain photoactivatability or photoswitchability. We have begun studies using BiFC PAmCherry1 to PALM image the stable interactions between mitochondrial F_1F_0-ATP synthase stator subunits (ATP5F1 and ATP5O). This work is novel, ongoing, and still needs significant research to develop negative controls, examine specificity and the effect of linker length. There is also potential for interesting examination of the complementation kinetics and hydrophobic forces by optical tweezer studies.

Two major results of this thesis have further reaching importance than quantifying the structural characteristics of Drp1 helical rings during mammalian mitochondrial fission. Without the ability to image in multiple colors, PALM loses much of its biological research relevance. The development of rsKame and a functioning two-color PALM method allows for the super resolution exploration of proteins or cellular structures that can be successfully fused to rsKame, PAmCherry1, or other photoactivatable fluorescent proteins. There is much information to be gained from clearer pictures of cellular structures and functions. Without a definitive method of determining protein-protein co-localization in PALM imaging, proximity versus interaction would constantly a source for debate. The development of BiFC PALM has the potential to solve this issue for stably interacting proteins by defining relative resolution within approximately 7 nm with a physical tether and an absolute resolution of the protein-protein interaction within the cell itself.

This thesis and my work contained herein represent six years of extensive training in basic molecular biology, cell culture, biochemistry, microscopy, and data analysis. But more importantly, I was forced time and again to think creatively, to put disparate puzzle pieces

together in unexpected ways, and to prove my ideas would work by obtaining hard data. I learned more about the physics of light and microscopy then I ever thought I would need to know. Two beautiful aspects of this work were particularly inspiring: PALM microscopy allowing for clearer views of cellular structures and the mitochondrial network itself in its almost maddening complexity.

When I was a little girl, I wanted to know everything that happened in our body. When I was an undergraduate, I wanted to know everything that happened in a single cell. Now, I would happily settle for clearly understanding this one fascinating organelle.

"There are all kinds of interesting questions that come from a knowledge of science, which only adds to the excitement and mystery and awe of a flower." -Richard Feynman

Or in my case, a mitochondrion.

Works Cited

1. Fuchs, G. Alternative pathways of carbon dioxide fixation: insights into the early evolution of life? *Annual Review of Microbiology* **65**, 631–58 (2011).

2. Gray, M. W., Burger, G. & Lang, B. F. The origin and early evolution of mitochondria. *Genome Biology* **2**, 1018.1-1018.5 (2001).

3. Wang, C. & Youle, R. J. The role of mitochondria in apoptosis. *Annual Review of Genetics* **43**, 95–118 (2009).

4. Gulbins, E., Dreschers, S. & Bock, J. Special Review Series – Biogenesis and Physiological Adaptation of Mitochondria Role of mitochondria in apoptosis *Experimental Physiology : General aspects of apoptosis* **88.1**, 85-90 (2003).

5. Green, D. R. & Reed, J. C. Mitochondria and Apoptosis. *Science* **281**, 1309 (1998).

6. Kowald, A. & Kirkwood, T. B. L. Evolution of the mitochondrial fusion-fission cycle and its role in aging. *Proceedings of the National Academy of Sciences of the United States of America* **108**, 10237–42 (2011).

7. Wallace, D. C. A mitochondrial paradigm of metabolic and degenerative diseases, aging, and cancer: a dawn for evolutionary medicine. *Annual Review of Genetics* **39**, 359–407 (2005).

8. Margulis, L. Genetic and evolutionary consequences of symbiosis. *Experimental Parasitology* **39**, 277–349 (1976).

9. Gray, M. W. Mitochondrial evolution. *Cold Spring Harbor Perspectives in Biology* **4**, 1-16 (2012).

10. Leary, S. C. & Sasarman, F. Mitochondrial DNA. *Methods in Molecular Biology* **554**, 143–162 (2009).

11. Parone, P. A. *et al.* Preventing mitochondrial fission impairs mitochondrial function and leads to loss of mitochondrial DNA. *PloS One* **3**, e3257 (2008).

12. Trappe, S. J. Transfection of mitochondria : strategy towards a gene therapy of mitochondrial DNA diseases. *Gene* **23**, 10–17 (1995).

13. Malka, F. *et al.* Separate fusion of outer and inner mitochondrial membranes. *EMBO reports* **6**, 853–9 (2005).

14. Berman, S. B., Pineda, F. J. & Hardwick, J. M. Mitochondrial fission and fusion dynamics: the long and short of it. *Cell death and differentiation* **15**, 1147–52 (2008).

15. Chan, D. C. Mitochondrial fusion and fission in mammals. *Annual Review of Cell and Developmental Biology* **22**, 79–99 (2006).

16. Wurm, C. A. & Jakobs, S. Differential protein distributions define two sub-compartments of the mitochondrial inner membrane in yeast. *FEBS Letters* **580**, 5628–34 (2006).

17. Rabl, R. *et al.* Formation of cristae and crista junctions in mitochondria depends on antagonism between Fcj1 and Su e/g. *The Journal of Cell Biology* **185**, 1047–63 (2009).

18. Logan, D. C. The mitochondrial compartment. *Journal of Experimental Botany* **57**, 1225–43 (2006).

19. Mannella, C. A. Structure and dynamics of the mitochondrial inner membrane cristae. *Biochimica et Biophysica Acta* **1763**, 542–8 (2006).

20. Chvanov, M. Metabolic control of elastic properties of the inner mitochondrial membrane. *The Journal of Physical Chemistry* **110**, 22903–9 (2006).

21. State, F. & Model, S. S. Supramolecular Structure of the Mitochondrial Oxidative Phosphorylation System. *Journal of Biological Chemistry* **282**, 1–4 (2007).

22. Goffart, S., Martinsson, P., Malka, F., Rojo, M. & Spelbrink, J. N. The Mitochondria of Cultured Mammalian Cells. *Methods in Molecular Biology* **372**, 3–16 (2007).

23. Wallace, D. C., Stugard, C., Murdock, D., Schurr, T. & Brown, M. D. Ancient mtDNA sequences in the human nuclear genome : A potential source of errors in identifying pathogenic mutations. *Proceedings of the National Academy of Sciences of the United States of America* **94**, 14900-14905 (1997).

24. Shadel, G. S. & Seidel-rogol, B. L. Diagnostic Assays for Defects in mtDNA Replication and Transcription in Yeast and Humans. *Methods in Cell Biology* **80**, 465–479 (2001).

25. Ekstrand, M. I. *et al.* Mitochondrial transcription factor A regulates mtDNA copy number in mammals. *Human Molecular Genetics* **13**, 935–944 (2004).

26. Gaspari, M., Larsson, N. & Gustafsson, C. M. The transcription machinery in mammalian mitochondria. *Biochimica et Biophysica Acta* **1659**, 148 – 152 (2004).

27. Lunt, S. Y. & Vander Heiden, M. G. Aerobic glycolysis: meeting the metabolic requirements of cell proliferation. *Annual Review of Cell and Developmental Biology* **27**, 441–64 (2011).

28. Gilkerson, R. W., Selker, J. M. L. & Capaldi, R. A. The cristal membrane of mitochondria is the principal site of oxidative phosphorylation. *FEBS Letters* **546**, 355–358 (2003).

29. Balaban, R. S. Regulation of oxidative phosphorylation in the mammalian cell of oxidative phosphorylation in the mammalian cell. *American Journal of Physiology-Cell Physiology* **258**, C377-C389 (1990).

30. Papa, S. *et al.* The Oxidative Phosphorylation System in Mammalian Mitochondria. *Advances in Mitochondrial Medicine* **942**, 3–37 (2012).

31. Chen, H. & Chan, D. C. Mitochondrial dynamics--fusion, fission, movement, and mitophagy--in neurodegenerative diseases. *Human Molecular Genetics* **18**, R169–76 (2009).

32. Cardaci, S. & Ciriolo, M. R. TCA Cycle Defects and Cancer: When Metabolism Tunes Redox State. *International Journal of Cell Biology* **2012**, 161837 (2012).

33. Schägger, H. *et al.* Significance of respirasomes for the assembly/stability of human respiratory chain complex I. *The Journal of Biological Chemistry* **279**, 36349–53 (2004).

34. Leary, S. C. & Sasarman, F. Oxidative phosphorylation: synthesis of mitochondrially encoded proteins and assembly of individual structural subunits into functional holoenzyme complexes. *Methods in Molecular Biology)* **554**, 143–62 (2009).

35. Muster, B. *et al.* Respiratory chain complexes in dynamic mitochondria display a patchy distribution in life cells. *PloS One* **5**, e11910 (2010).

36. Dudkina, N. V., Sunderhaus, S., Boekema, E. J. & Braun, H.-P. The higher level of organization of the oxidative phosphorylation system: mitochondrial supercomplexes. *Journal of Bioenergetics and Biomembranes* **40**, 419–24 (2008).

37. Sazanov, L. A. Current Topics Respiratory Complex I : Mechanistic and Structural Insights Provided by the Crystal Structure of the Hydrophilic Domain. *American Chemical Society* **46**, 2275-2288 (2007).

38. Schägger, H. & Pfeiffer, K. Supercomplexes in the respiratory chains of yeast and mammalian mitochondria. *The EMBO Journal* **19**, 1777–83 (2000).

39. Acín-Pérez, R. *et al.* Respiratory complex III is required to maintain complex I in mammalian mitochondria. *Molecular Cell* **13**, 805–15 (2004).

40. Efremov, R. G., Baradaran, R. & Sazanov, L. The architecture of respiratory complex I. *Nature* **465**, 441–5 (2010).

41. Dudkina, N. V., Eubel, H., Keegstra, W., Boekema, E. J. & Braun, H. Structure of a mitochondrial supercomplex formed by respiratory-chain complexes I and III. *PNAS* **102**, 3225–3229 (2005).

42. Lenaz, G. & Genova, M. L. Kinetics of integrated electron transfer in the mitochondrial respiratory chain: random collisions vs. solid state electron channeling. *American Journal of Physiology-Cell Physiology* **292**, C1221–39 (2007).

43. Figueroa, P. *et al.* The four subunits of mitochondrial respiratory complex II are encoded by multiple nuclear genes and targeted to mitochondria in Arabidopsis thaliana. *Plant Molecular Biology* **50**, 725–34 (2002).

44. Cecchini, G. Function and structure of complex II of the respiratory chain. *Annual Review of Biochemistry* **72**, 77–109 (2003).

45. Ho, S. H. & Rieske, J. S. Differential labeling of the subunits of respiratory complex III with [3H]succinic anhydride, [14C]succinic anhydride, and p-diazobenzene-[35S]sulfonate. *Journal of Bioenergetics and Biomembranes* **17**, 333–48 (1985).

46. Khalimonchuk, O. & Rödel, G. Biogenesis of cytochrome c oxidase. *Mitochondrion* **5**, 363–88 (2005).

47. Fontanesi, F., Soto, I. C., Horn, D. & Barrientos, A. Assembly of mitochondrial cytochrome c-oxidase, a complicated and highly regulated cellular process. *American Journal of Physiology-Cell Physiology* **291**, C1129–47 (2006).

48. Chen, Z. X. & Pervaiz, S. Involvement of cytochrome c oxidase subunits Va and Vb in the regulation of cancer cell metabolism by Bcl-2. *Cell Death and Differentiation* **17**, 408–20 (2010).

49. Schmidt, T. R. *et al.* Rapid electrostatic evolution at the binding site for cytochrome c on cytochrome c oxidase in anthropoid primates. *Proceedings of the National Academy of Sciences of the United States of America* **102**, 6379–84 (2005).

50. Gavin, P. D., Devenish, R. J. & Prescott, M. FRET reveals changes in the F1–stator stalk interaction during activity of F1F0-ATP synthase. *Biochimica et Biophysica Acta (BBA) - Bioenergetics* **1607**, 167–179 (2003).

51. Baker, L. a, Watt, I. N., Runswick, M. J., Walker, J. E. & Rubinstein, J. L. Arrangement of subunits in intact mammalian mitochondrial ATP synthase determined by cryo-EM. *Proceedings of the National Academy of Sciences of the United States of America* **109**, 11675–80 (2012).

52. Boyle, G. M., Roucou, X., Nagley, P., Devenish, R. J. & Prescott, M. Modulation at a distance of proton conductance through the *Saccharomyces cerevisiae* mitochondrial F1F0-ATP synthase by variants of the oligomycin sensitivity-conferring protein containing substitutions near the C-terminus. *Journal of Bioenergetics and Biomembranes* **32**, 595–607 (2000).

53. Faccenda, D. & Campanella, M. Molecular Regulation of the Mitochondrial F(1)F(o)-ATPsynthase: Physiological and Pathological Significance of the Inhibitory Factor 1 (IF(1)). *International Journal of Cell Biology* **2012**, 367934 (2012).

54. Wang, X. The expanding role of mitochondria in apoptosis The expanding role of mitochondria in apoptosis. *Genes and Development* **15**, 2922–2933 (2001).

55. Ghochani, M. Experimental And Theoretical Study Of Mitochondrial Inner Membrane Conformation : Electron Microscope Tomography and Thermodynamics. *Physics Department, San Diego State University* (2010).

56. Elmore, S. Apoptosis: a review of programmed cell death. *Toxicologic Pathology* **35**, 495–516 (2007).

57. Otera, H. & Mihara, K. Mitochondrial dynamics: functional link with apoptosis. *International Journal of Cell Biology* **2012**, 821676 (2012).

58. Zorzano, A., Liesa, M., Palaci, M. & Liesa, M. Mitochondrial Dynamics in Mammalian Health and Disease. *Physiology Review* **89**, 799–845 (2009).

59. Shi, Y. A structural view of mitochondria-mediated apoptosis. *Nature Structural Biology* **8**, 394–401 (2001).

60. Yu, T., Fox, R. J., Burwell, L. S. & Yoon, Y. Regulation of mitochondrial fission and apoptosis by the mitochondrial outer membrane protein hFis1. *Journal of Cell Science* **118**, 4141–51 (2005).

61. Wu, S., Zhou, F., Zhang, Z. & Xing, D. Bax is essential for Drp1-mediated mitochondrial fission but not for mitochondrial outer membrane permeabilization caused by photodynamic therapy. *Journal of Cellular Physiology* **226**, 530–41 (2011).

62. Cassidy-Stone, A. *et al.* Chemical inhibition of the mitochondrial division dynamin reveals its role in Bax/Bak-dependent mitochondrial outer membrane permeabilization. *Developmental Cell* **14**, 193–204 (2008).

63. Chen, H. & Chan, D. C. Emerging functions of mammalian mitochondrial fusion and fission. *Human Molecular Genetics* **14**, R283–9 (2005).

64. Chen, H. & Chan, D. C. Emerging functions of mammalian mitochondrial fusion and fission. *Human molecular genetics* **14**, R283–9 (2005).

65. Hoppins, S. & Nunnari, J. Cell Biology. Mitochondrial dynamics and apoptosis--the ER connection. *Science* **337**, 1052–4 (2012).

66. Otera, H. & Mihara, K. Discovery of the membrane receptor for mitochondrial fission GTPase Drp1. *Small GTPases* **2**, 167–172 (2011).

67. Olichon, A. *et al.* The human dynamin-related protein OPA1 is anchored to the mitochondrial inner membrane facing the inter-membrane space. *FEBS Letters* **523**, 171–176 (2002).

68. Olichon, A. *et al.* Loss of OPA1 perturbates the mitochondrial inner membrane structure and integrity, leading to cytochrome c release and apoptosis. *The Journal of Biological Chemistry* **278**, 7743–6 (2003).

69. Knott, A. Bossy-Wetzel, E. Impairing the Mitochondrial Fission and Fusion Balance: Mechanism of Neurodegeneration. *Annals New York Academy of Sciences* **1147**, 283–292 (2009).

70. Darshi, M. *et al.* ChChd3, an inner mitochondrial membrane protein, is essential for maintaining crista integrity and mitochondrial function. *The Journal of Biological Chemistry* **286**, 2918–32 (2011).

71. Friedman, J. R. *et al.* ER tubules mark sites of mitochondrial division. *Science* **334**, 358–62 (2011).

72. Huang, P., Galloway, C. A. & Yoon, Y. Control of mitochondrial morphology through differential interactions of mitochondrial fusion and fission proteins. *PloS One* **6**, e20655 (2011).

73. Smirnova, E., Griparic, L., Shurland, D.-L. & van der Bliek, A. M. Dynamin-related Protein Drp1 Is Required for Mitochondrial Division in Mammalian Cells. *Mol. Biol. Cell* **12**, 2245–2256 (2001).

74. Karbowski, M., Jeong, S.-Y. & Youle, R. J. Endophilin B1 is required for the maintenance of mitochondrial morphology. *The Journal of Cell Biology* **166**, 1027–39 (2004).

75. Palmer, C. S. *et al.* MiD49 and MiD51, new components of the mitochondrial fission machinery. *EMBO Reports* **12**, 565–73 (2011).

76. Otera, H. *et al.* Mff is an essential factor for mitochondrial recruitment of Drp1 during mitochondrial fission in mammalian cells. *The Journal of Cell Biology* **191**, 1141–58 (2010).

77. Koch, A., Yoon, Y., Bonekamp, N. A., McNiven, M. A. & Schrader, M. A role for Fis1 in both mitochondrial and peroxisomal fission in mammalian cells. *Molecular Biology of the Cell* **16**, 5077–86 (2005).

78. Smirnova, E., Griparic, L., Shurland, D. L. & van der Bliek, A. M. Dynamin-related protein Drp1 is required for mitochondrial division in mammalian cells. *Molecular Biology of the Cell* **12**, 2245–56 (2001).

79. Pitts, K. R., Yoon, Y., Krueger, E. W. & McNiven, M. A. The dynamin-like protein DLP1 is essential for normal distribution and morphology of the endoplasmic reticulum and mitochondria in mammalian cells. *Molecular Biology of the Cell* **10**, 4403–17 (1999).

80. Yoon, Y., Krueger, E. W., Oswald, B. J. & McNiven, M. A. The Mitochondrial Protein hFis1 Regulates Mitochondrial Fission in Mammalian Cells through an Interaction with the Dynamin-Like Protein DLP1. *Molecular and Cellular Biology* **23**, 5409–5420 (2003).

81. McMahon, H. T. & Gallop, J. L. Membrane curvature and mechanisms of dynamic cell membrane remodelling. *Nature* **438**, 590–6 (2005).

82. Palmer, C. S. *et al.* MiD49 and MiD51, new components of the mitochondrial fission machinery. *EMBO Reports* **12**, 565–73 (2011).

83. Hoppins, S., Lackner, L. & Nunnari, J. The machines that divide and fuse mitochondria. *Annual Review of Biochemistry* **76**, 751–80 (2007).

84. Mears, J. A. *et al.* Conformational changes in Dnm1 support a contractile mechanism for mitochondrial fission. *Nature Structural & Molecular Biology* **18**, 20–6 (2011).

85. Brown, T. A., Fetter, R. D., Tkachuk, A. N. & Clayton, D. A. Approaches toward super-resolution fluorescence imaging of mitochondrial proteins using PALM. *Methods* **51**, 458-463 (2010).

86. Owen, D. M. *et al.* PALM imaging and cluster analysis of protein heterogeneity at the cell surface. *Journal of Biophotonics* **3**, 446–54 (2010).

87. York, A. G., Ghitani, A., Vaziri, A., Davidson, M. W. & Shroff, H. Confined activation and subdiffractive localization enables whole-cell PALM with genetically expressed probes. *Nature Methods* **8**, 327–33 (2011).

88. Shroff, H., White, H. & Betzig, E. Photoactivated localization microscopy (PALM) of adhesion complexes. *Current Protocols in Cell Biology* **Chapter 4**, Unit 4.21 (2008).

89. Leung, B. O. & Chou, K. C. Review of super-resolution fluorescence microscopy for biology. *Applied Spectroscopy* **65**, 967–80 (2011).

90. Ellinger, B. Y. P. Fluorescence Microscopy In Biology. *Biological Reviews* **15**, 323-347 (1940).

91. Ghiran, I. C. Light Microscopy. *Methods in Molecular Biology* **689**, 93–136 (2011).

92. Huang, B., Bates, M. & Zhuang, X. Super-resolution fluorescence microscopy. *Annual Review of Biochemistry* **78**, 993–1016 (2009).

93. Tsien, R. Y. The green fluorescent protein. *Annual Review of Biochemistry* **67**, 509–44 (1998).

94. Tsien, R. Y. The green fluorescent protein. *Annual Review of Biochemistry* **67**, 509–44 (1998).

95. Heim, R., Prasher, D. C. & Tsien, R. Y. Wavelength mutations and posttranslational autoxidation of green fluorescent protein. *Proceedings of the National Academy of Sciences of the United States of America* **91**, 12501–4 (1994).

96. Shaner, N. C., Patterson, G. H. & Davidson, M. W. Advances in fluorescent protein technology. *Journal of Cell Science* **120**, 4247–60 (2007).

97. Davidson, M. W. & Campbell, R. E. Engineered fluorescent proteins: innovations and applications. *Nature Methods* **6**, 713–717 (2009).

98. Chudakov, D. M., Matz, M. V., Lukyanov, S. & Lukyanov, K. A. Fluorescent Proteins and Their Applications in Imaging Living Cells and Tissues. *Physiological Review* **90**, 1103–1163 (2010).

99. Shimomura, O. Discovery of green fluorescent protein. *Methods of Biochemical Analysis* **47**, 1–13 (2006).

100. Shaner, N. C., Steinbach, P. A. & Tsien, R. Y. Advances in fluorescent protein technology. *Journal of Cell Science* **120**, 4247–4260 (2007).

101. St Croix, C. M., Shand, S. H. & Watkins, S. C. Confocal microscopy: comparisons, applications, and problems. *BioTechniques* **39**, S2–5 (2005).

102. Patel, D. V. & McGhee, C. N. J. Contemporary in vivo confocal microscopy of the living human cornea using white light and laser scanning techniques: a major review. *Clinical & Experimental Ophthalmology* **35**, 71–88 (2007).

103. Jenne, C. N., Wong, C. H. Y., Petri, B. & Kubes, P. The use of spinning-disk confocal microscopy for the intravital analysis of platelet dynamics in response to systemic and local inflammation. *PloS One* **6**, e25109 (2011).

104. Stehbens, S., Pemble, H., Murrow, L. & Wittmann, T. Imaging intracellular protein dynamics by spinning disk confocal microscopy. *Methods in Enzymology* **504**, 293–313 (2012).

105. Haraguchi, T. Live cell imaging: approaches for studying protein dynamics in living cells. *Cell Structure and Function* **27**, 333–4 (2002).

106. Schmidt, R. *et al.* Spherical nanosized focal spot unravels the interior of cells. *Nature Methods* **5**, 539–44 (2008).

107. Neumann, D., Bückers, J., Kastrup, L., Hell, S. W. & Jakobs, S. Two-color STED microscopy reveals different degrees of colocalization between hexokinase-I and the three human VDAC isoforms. *PMC Biophysics* **3**, 4 (2010).

108. Petford-Long, A. K. & Chiaramonti, A. N. Transmission Electron Microscopy of Multilayer Thin Films. *Annual Review of Materials Research* **38**, 559–584 (2008).

109. Wang, Z. L. New Developments in Transmission Electron Microscopy for Nanotechnology. *Advanced Materials* **15**, 1497–1514 (2003).

110. Rose, H. H. Optics of high-performance electron microscopes. *Science and Technology of Advanced Materials* **9**, 014107 (2008).

111. Russell, S. D. & Daghlian, C. P. Scanning electron microscopic observations on deembedded biological tissue sections: Comparison of different fixatives and embedding materials. *Journal of Electron Microscopy Technique* **2**, 489–495 (1985).

112. Bogner, a, Jouneau, P.-H., Thollet, G., Basset, D. & Gauthier, C. A history of scanning electron microscopy developments: towards "wet-STEM" imaging. *Micron* **38**, 390–401 (2007).

113. Suzuki, E. High-resolution scanning electron microscopy of immunogold-labelled cells by the use of thin plasma coating of osmium. *Journal of Microscopy* **208**, 153–7 (2002).

114. Hirst, E. M. A. An Easy Method for Orientated Embedding Tissue Culture-Cell Monolayers in LR White Resin for Postem bedding Immunocytochemistry. *Journal of Electron Microscopy Technique* **458**, 456–458 (1991).

115. Denham, S. & Cutchey, D. High Contrast Imaging of Surface Events. *Imaging & Microscopy* **11**, 54–55 (2009).

116. Denham, S. & Cutchey, D. Total Internal Reflection Fluorescence (TIRF) Microscopy. *Imaging & Microscopy* **11**, 54–55 (2009).

117. Betzig, E. *et al.* Proteins at Nanometer Resolution. *Science* **1642**, (2009).

118. Betzig, E. *et al.* Imaging intracellular fluorescent proteins at nanometer resolution. *Science* **313**, 1642–5 (2006).

119. Shroff, H. *et al.* Dual-color superresolution imaging of genetically expressed probes within individual adhesion complexes. *Proceedings of the National Academy of Sciences of the United States of America* **104**, 20308–13 (2007).

120. Rust, M. J., Bates, M. & Zhuang, X. imaging by stochastic optical reconstruction microscopy (STORM). *Nature Methods* **3(10)**, 793-795 (2006).

121. Huang, B., Jones, S. A., Brandenburg, B. & Zhuang, X. Whole-cell 3D STORM reveals interactions between cellular structures with nanometer-scale resolution. *Nature Methods* **5**, 1047–52 (2008).

122. Hess, S. T., Girirajan, T. P. K. & Mason, M. D. Ultra-high resolution imaging by fluorescence photoactivation localization microscopy. *Biophysical Journal* **91**, 4258–72 (2006).

123. Lichtman, J. W. & Conchello, J. Fluorescence microscopy. *Nature Methods* **2**, 910-919 (2005).

124. Ha, T. & Tinnefeld, P. Photophysics of fluorescent probes for single-molecule biophysics and super-resolution imaging. *Annual Review of Physical Chemistry* **63**, 595–617 (2012).

125. Henderson, J. N. *et al.* Structure and mechanism of the photoactivatable green fluorescent protein. *Journal of the American Chemical Society* **131**, 4176–7 (2009).

126. Mckinney, S. A., Murphy, C. S., Hazelwood, K. L., Davidson, M. W. & Looger, L. L. BRIEF COMMUNICATIONS A bright and photostable photoconvertible fluorescent protein. *Nature Methods* **6**, 131–133 (2009).

127. Patterson, G. H. & Lippincott-Schwartz, J. A photoactivatable GFP for selective photolabeling of proteins and cells. *Science* **297**, 1873–7 (2002).

128. Adam, V. *et al.* Rational design of photoconvertible and biphotochromic fluorescent proteins for advanced microscopy applications. *Chemistry & Biology* **18**, 1241–51 (2011).

129. Chudakov, D. M., Lukyanov, S. & Lukyanov, K. A. Tracking intracellular protein movements using photoswitchable fluorescent proteins PS-CFP2 and Dendra2. *Nature Protocols* **2**, 2024–32 (2007).

130. Lee, S.-H., Shin, J. Y., Lee, a. & Bustamante, C. Counting single photoactivatable fluorescent molecules by photoactivated localization microscopy (PALM). *Proceedings of the National Academy of Sciences* **190**, 17436–17441 (2012).

131. Subach, F. V. *et al.* Photoactivation mechanism of PAmCherry based on crystal structures of the protein in the dark and fluorescent states. *Proceedings of the National Academy of Sciences of the United States of America* **106**, 21097–102 (2009).

132. Subach, F. V. *et al.* Photoactivatable mCherry for high-resolution two-color fluorescence microscopy. *Nature Methods* **6**, 153–9 (2009).

133. Mizuno, H. *et al.* Light-dependent regulation of structural flexibility in a photochromic fluorescent protein. *Proceedings of the National Academy of Sciences of the United States of America* **105**, 9227–32 (2008).

134. Andresen, M. *et al.* Structural basis for reversible photoswitching in Dronpa. *Proceedings of the National Academy of Sciences of the United States of America* **104**, 13005–9 (2007).

135. Habuchi, S. *et al.* Reversible single-molecule photoswitching in the GFP-like fluorescent protein Dronpa. *Proceedings of the National Academy of Sciences of the United States of America* **102**, 9511–6 (2005).

136. Dedecker, P. *et al.* Fast and reversible photoswitching of the fluorescent protein dronpa as evidenced by fluorescence correlation spectroscopy. *Biophysical Journal* **91**, L45–7 (2006).

137. Stiel, A. C. *et al.* 1.8 A bright-state structure of the reversibly switchable fluorescent protein Dronpa guides the generation of fast switching variants. *The Biochemical journal* **402**, 35–42 (2007).

138. Wilmann, P. G. *et al.* The 1.7 A crystal structure of Dronpa: a photoswitchable green fluorescent protein. *Journal of Molecular Biology* **364**, 213–24 (2006).

139. Andresen, M. *et al.* Photoswitchable fluorescent proteins enable monochromatic multilabel imaging and dual color fluorescence nanoscopy. *Nature Biotechnology* **26**, 1035–40 (2008).

140. Moors, S. L. C. *et al.* How Is cis−trans Isomerization Controlled in Dronpa Mutants? A Replica Exchange Molecular Dynamics Study. *Journal of Chemical Theory and Computation* **4**, 1012–1020 (2008).

141. Andresen, M. *et al.* Photoswitchable fluorescent proteins enable monochromatic multilabel imaging and dual color fluorescence nanoscopy. *Nature Biotechnology* **26**, 1035–40 (2008).

142. Brouwer, A. M. Standards for photoluminescence quantum yield measurements in solution (IUPAC Technical Report). *Pure and Applied Chemistry* **83**, 2213–2228 (2011).

143. Remington, S. J. Fluorescent proteins: maturation, photochemistry and photophysics. *Current Opinion in Structural Biology* **16**, 714–21 (2006).

144. Kaufmann, T. *et al.* Characterization of the signal that directs Bcl-x(L), but not Bcl-2, to the mitochondrial outer membrane. *The Journal of Cell Biology* **160**, 53–64 (2003).

145. Stan, T., Brix, J., Schneider-mergener, J., Pfanner, N. & Neupert, W. Mitochondrial Protein Import : Recognition of Internal Import Signals of BCS1 by the TOM Complex. *Molecular and Cellular Biology* **23**, 2239-2250 (2003).

146. Chithrani, B. D. & Chan, W. C. W. Elucidating the mechanism of cellular uptake and removal of protein-coated gold nanoparticles of different sizes and shapes. *Nano Letters* **7**, 1542–50 (2007).

147. Schmidt, R. *et al.* Mitochondrial Cristae Revealed with Focused Light 2009. *Nano* **9**, 2508-2510 (2009).

148. Shroff, H. *et al.* Dual-color superresolution imaging of genetically expressed probes within individual adhesion complexes. *Proceedings of the National Academy of Sciences of the United States of America* **104**, 20308–13 (2007).

149. Shroff, H. *et al.* Dual-color superresolution imaging of genetically expressed probes within individual adhesion complexes. *Proceedings of the National Academy of Sciences of the United States of America* **104**, 20308–13 (2007).

150. Huang, B., Bates, M. & Zhuang, X. Super-resolution fluorescence microscopy. *Annual Review of Biochemistry* **78**, 993–1016 (2009).

151. Fornuskova, D. *et al.* Novel insights into the assembly and function of human nuclear-encoded cytochrome c oxidase subunits 4, 5a, 6a, 7a and 7b. *The Biochemical journal* **428**, 363–74 (2010).

152. Huh, W.-K. *et al.* Global analysis of protein localization in budding yeast. *Nature* **425**, 686–91 (2003).

153. Sauer, M. Reversible molecular photoswitches: a key technology for nanoscience and fluorescence imaging. *Proceedings of the National Academy of Sciences of the United States of America* **102**, 9433–4 (2005).

154. Ando, R., Flors, C., Mizuno, H., Hofkens, J. & Miyawaki, A. Highlighted generation of fluorescence signals using simultaneous two-color irradiation on Dronpa mutants. *Biophysical Journal* **92**, L97–9 (2007).

155. Nikon MicroscopyU | Introduction to Fluorescent Proteins. at <http://www.microscopyu.com/articles/livecellimaging/fpintro.html>

156. Montesano, R., Soriano, J. V., Fialka, I. & Orci, L. Isolation of EpH4 mammary epithelial cell subpopulations which differ in their morphogenetic properties. *In vitro Cellular & Developmental Biology-Animal* **34**, 468–77 (1998).

157. Manley, S. *et al.* High-density mapping of single-molecule trajectories with photoactivated localization microscopy. *Nature Methods* **5**, 155–7 (2008).

158. Subach, F. V. *et al.* Photoactivatable mCherry for high-resolution two-color fluorescence microscopy. *Nature Methods* **6**, 153–160 (2009).

159. Subach, F. V., Patterson, G. H., Renz, M., Lippincott-Schwartz, J. & Verkhusha, V. V. Bright monomeric photoactivatable red fluorescent protein for two-color super-resolution sptPALM of live cells. *Journal of the American Chemical Society* **132**, 6481–91 (2010).

160. Hinshaw, J. E. Dynamin and its role in membrane fission. *Annual Review of Cell and Developmental Biology* **16**, 483–519 (2000).

161. Otsuga, D. The Dynamin-related GTPase, Dnm1p, Controls Mitochondrial Morphology in Yeast. *The Journal of Cell Biology* **143**, 333–349 (1998).

162. Bleazard, W. *et al.* The dynamin-related GTPase Dnm1 regulates mitochondrial fission in yeast. *Nature Cell Biology* **1**, 298–304 (1999).

163. Ingerman, E. *et al.* Dnm1 forms spirals that are structurally tailored to fit mitochondria. *The Journal of Cell Biology* **170**, 1021–7 (2005).

164. Shin, H. W., Shinotsuka, C., Torii, S., Murakami, K. & Nakayama, K. Identification and subcellular localization of a novel mammalian dynamin-related protein homologous to yeast Vps1p and Dnm1p. *Journal of Biochemistry* **122**, 525–30 (1997).

165. Smirnova, E., Shurland, D. L., Ryazantsev, S. N. & van der Bliek, a M. A human dynamin-related protein controls the distribution of mitochondria. *The Journal of Cell Biology* **143**, 351–8 (1998).

166. Wasiak, S., Zunino, R. & McBride, H. M. Bax/Bak promote sumoylation of DRP1 and its stable association with mitochondria during apoptotic cell death. *The Journal of Cell Biology* **177**, 439–50 (2007).

167. Jahani-Asl, A. & Slack, R. S. The phosphorylation state of Drp1 determines cell fate. *EMBO Reports* **8**, 912–3 (2007).

168. Chang, C.-R. & Blackstone, C. Cyclic AMP-dependent protein kinase phosphorylation of Drp1 regulates its GTPase activity and mitochondrial morphology. *The Journal of Biological Chemistry* **282**, 21583–7 (2007).

169. Cereghetti, G. M. *et al.* Dephosphorylation by calcineurin regulates translocation of Drp1 to mitochondria. *Proceedings of the National Academy of Sciences of the United States of America* **105**, 15803–8 (2008).

170. Montessuit, S. *et al.* Membrane remodeling induced by the dynamin-related protein Drp1 stimulates Bax oligomerization. *Cell* **142**, 889–901 (2010).

171. Zhang, Y., Chan, N. C., Ngo, H. B., Gristick, H. & Chan, D. C. Crystal structure of mitochondrial fission complex reveals scaffolding function for mitochondrial division 1 (Mdv1) coiled coil. *The Journal of Biological Bhemistry* **287**, 9855–61 (2012).

172. Naylor, K. *et al.* Mdv1 interacts with assembled dnm1 to promote mitochondrial division. *The Journal of Biological Chemistry* **281**, 2177–83 (2006).

173. Yoon, Y., Krueger, E. W., Oswald, B. J., Mcniven, A. & Mcniven, M. A. The Mitochondrial Protein hFis1 Regulates Mitochondrial Fission in Mammalian Cells through an Interaction with the Dynamin-Like Protein DLP1. *Molecular and Cell Biology* **23**, 5409-5420 (2003).

174. Gandre-Babbe, S. & van der Bliek, A. M. The novel tail-anchored membrane protein Mff controls mitochondrial and peroxisomal fission in mammalian cells. *Molecular Biology of the Cell* **19**, 2402–12 (2008).

175. Mironov, S. L., Ivannikov, M. V. & Johansson, M. [Ca2+]i signaling between mitochondria and endoplasmic reticulum in neurons is regulated by microtubules. From mitochondrial permeability transition pore to Ca2+-induced Ca2+ release. *The Journal of Biological Chemistry* **280**, 715–21 (2005).

176. Shim, S.-H. *et al.* Super-resolution fluorescence imaging of organelles in live cells with photoswitchable membrane probes. *Proceedings of the National Academy of Sciences of the United States of America* **109**, 13978–83 (2012).

177. Cassidy-Stone, A. *et al.* Chemical inhibition of the mitochondrial division dynamin reveals its role in Bax/Bak-dependent mitochondrial outer membrane permeabilization. *Developmental Cell* **14**, 193–204 (2008).

178. Piston, D. W. & Kremers, G.-J. Fluorescent protein FRET: the good, the bad and the ugly. *Trends in Biochemical Sciences* **32**, 407–14 (2007).

179. Ghosh, I., Hamilton, A. D., Regan, L. & Haven, N. 5658 Antiparallel Leucine Zipper-Directed Protein Reassembly : Application to the Green Fluorescent Protein. *Journal of the American Chemical Society* **122**, 5658–5659 (2000).

180. Barnard, E., McFerran, N. V., Trudgett, A., Nelson, J. & Timson, D. J. Development and implementation of split-GFP-based bimolecular fluorescence complementation (BiFC) assays in yeast. *Biochemical Society Transactions* **36**, 479–82 (2008).

181. Kerppola, T. K. Bimolecular fluorescence complementation (BiFC) analysis as a probe of protein interactions in living cells. *Annual Review of Biophysics* **37**, 465–87 (2008).

182. Fan, J. *et al.* Split mCherry as a new red bimolecular fluorescence complementation system for visualizing protein–protein interactions in living cells. *Biochemical and Biophysical Research Communications* **367**, 47–53 (2008).

183. Chudakov, D. M., Lukyanov, S. & Lukyanov, K. a Fluorescent proteins as a toolkit for in vivo imaging. *Trends in Biotechnology* **23**, 605–13 (2005).

184. Hoppins, S. *et al.* A mitochondrial-focused genetic interaction map reveals a scaffold-like complex required for inner membrane organization in mitochondria. *The Journal of Cell Biology* **195**, 323–40 (2011).

Appendix A:

Table 6: Single molecule kinetic data for DronpaV157X mutant series

Sample	488 nm laser power density (W/mm^2)	405 nm laser power density (mW/mm^2)	k_d (s^{-1})	k_b (s^{-1})	k_{r1} (s^{-1})	k_{r2} (s^{-1})	k_{r3} (s^{-1})	α	β	$<T_{ON}>$ (s)	$<T_{OFF}>$ (s)	$<N_{Blink}>$
Dronpa	0.32	0.00	13.71	6.90	23.24	2.40	0.12	1.15	10.36	20.61	7.13	2.97
Dronpa	0.32	0.61	14.99	6.31	23.87	2.15	0.15	1.05	9.42	21.30	5.36	3.81
Dronpa	0.32	1.56	15.52	5.20	25.79	2.92	0.22	1.16	11.69	20.72	3.87	4.90
Dronpa	0.32	3.46	16.20	6.46	22.10	1.49	0.28	1.65	9.71	22.65	2.95	4.77
Dronpa	0.32	7.28	16.40	6.56	21.53	1.21	0.34	5.13	7.12	22.97	1.92	5.16
Dronpa	0.54	0.00	17.87	5.76	20.89	1.63	0.14	1.88	11.99	23.63	5.96	3.41
Dronpa	0.54	0.61	18.31	5.51	20.96	2.47	0.17	1.39	13.04	23.82	4.96	3.82
Dronpa	0.54	1.56	18.41	5.76	20.75	1.32	0.20	1.92	10.32	24.17	3.98	4.17
Dronpa	0.54	3.46	19.32	5.74	19.29	1.14	0.25	3.42	11.59	25.06	3.10	4.52
Dronpa	0.54	7.28	19.97	5.18	20.18	1.32	0.37	5.86	10.31	25.15	1.88	4.93
Dronpa	5.87	0.00	13.07	28.77	63.21	4.15	0.48	4.97	12.02	41.84	1.46	0.64
Dronpa	5.87	0.61	14.17	24.97	14.98	1.55	0.29	3.40	4.25	42.14	1.94	0.72
Dronpa	5.87	1.56	16.04	24.30	18.79	1.98	0.34	4.89	8.11	40.34	1.78	0.86
Dronpa	5.87	3.46	17.93	23.10	20.23	1.45	0.31	7.34	8.01	41.02	1.87	1.07
Dronpa	5.87	7.28	20.48	21.12	12.15	1.64	0.40	5.41	8.09	41.59	1.63	1.26
DronpaV157I	0.32	0.00	11.16	6.83	23.85	2.22	0.14	0.99	6.27	17.83	5.59	3.14
DronpaV157I	0.32	0.61	12.43	5.02	25.81	3.13	0.17	0.82	7.69	17.45	4.72	4.04
DronpaV157I	0.32	1.56	12.55	5.55	23.90	2.12	0.21	0.91	7.35	18.10	3.78	4.29
DronpaV157I	0.32	3.46	13.67	5.99	23.32	1.48	0.28	1.77	7.23	19.66	2.66	4.82
DronpaV157I	0.32	7.28	14.18	6.38	22.12	1.26	0.33	3.71	5.00	20.56	1.88	4.99
DronpaV157I	0.54	0.00	14.82	4.07	20.96	1.42	0.16	1.84	11.74	18.89	5.00	3.86
DronpaV157I	0.54	0.61	16.21	4.41	20.80	1.79	0.19	1.88	12.55	20.62	4.33	4.07
DronpaV157I	0.54	1.56	16.97	4.35	19.61	1.05	0.21	3.46	13.04	21.32	3.82	4.55
DronpaV157I	0.54	3.46	16.84	4.63	19.28	1.04	0.25	4.03	9.99	21.47	2.96	4.47
DronpaV157I	0.54	7.28	17.30	5.24	19.01	1.13	0.30	6.32	7.28	22.55	2.05	4.60
DronpaV157I	5.87	0.00	17.06	21.38	12.67	1.26	0.28	3.20	3.85	38.44	2.01	1.08
DronpaV157I	5.87	0.61	21.79	18.00	18.47	1.43	0.27	7.54	6.93	39.78	1.98	1.40
DronpaV157I	5.87	1.56	23.60	16.29	11.66	1.16	0.20	6.70	4.63	38.89	2.33	1.57
DronpaV157I	5.87	3.46	22.95	17.71	8.28	1.12	0.20	4.91	3.13	40.65	2.24	1.50
DronpaV157I	5.87	7.28	20.78	18.73	13.91	1.45	0.28	7.83	6.25	39.51	1.85	1.32

rsKame	0.32	0.00	11.57	7.64	22.68	1.51	0.08	0.75	8.88	19.21	10.63	2.14
rsKame	0.32	0.61	13.16	6.03	27.12	2.86	0.13	0.82	11.56	19.19	6.75	3.34
rsKame	0.32	1.56	13.81	6.89	21.71	0.97	0.17	1.51	9.26	20.70	4.80	3.57
rsKame	0.32	3.46	14.41	5.90	20.94	0.86	0.25	3.40	8.98	20.31	2.70	4.37
rsKame	0.32	7.28	14.46	6.84	22.26	1.34	0.38	5.37	7.21	21.51	1.71	4.16
rsKame	0.54	0.00	16.20	6.74	19.52	1.24	0.09	1.16	14.66	22.93	9.33	2.61
rsKame	0.54	0.61	17.05	5.81	22.08	1.29	0.13	1.58	18.48	22.86	6.64	3.35
rsKame	0.54	1.56	17.24	5.53	26.82	2.25	0.21	1.94	24.17	22.77	4.32	3.74
rsKame	0.54	3.46	18.38	6.04	21.91	0.96	0.26	5.05	15.04	24.42	2.97	3.89
rsKame	0.54	7.28	16.04	7.76	20.61	1.37	0.38	5.78	7.30	23.80	1.68	3.18
rsKame	5.87	0.00	19.67	26.59	14.57	1.12	0.21	3.73	10.36	46.26	3.55	0.97
rsKame	5.87	0.61	20.38	25.05	16.69	0.92	0.20	3.92	7.78	45.43	3.35	1.06
rsKame	5.87	1.56	17.10	25.48	14.69	1.15	0.24	5.64	8.89	42.57	2.72	0.85
rsKame	5.87	3.46	16.80	25.58	22.16	2.04	0.39	3.68	9.43	42.38	1.85	0.87
rsKame	5.87	7.28	14.54	26.48	37.88	4.29	0.69	5.14	14.15	41.02	1.08	0.75